ABSTRACT

Application of Ab Initio Theory to the Chemistry of Ultrathin Films

Paul A. Brown, Ph.D.

Mentor: Kevin L. Shuford, Ph.D.

In this work, we investigate a number of important nanosheets, e.g., graphene, haeckelites, and titanium disulfide for the expressed purpose of tuning the electronic ground state properties. We employ condensed matter techniques to interrogate realized and theoretically postulated ultrathin films to mine ground state properties that may bolster established, or nascent nanotechnologies. In this regard, a number of ultrathin films are *tuned* to induce new material properties that are not intrinsic to the original crystal. We show that chemical modification with extrinsic substitutional pnictogen dopants placed within the crystal lattice of graphene can functionalize the basal plane of graphene to obtain potentially catalytic properties. Furthermore, an alternative doping strategy, less intensive than pnictogenic substitutions, including halogen diatomic molecules were introduced as adsorbates on monolayer, bilayer, and multilayer graphenes of different polymorphism to influence the ground state of the graphitic nanosheets. We observed the induction of a band gap of controllable size as a function of halogen and polymorphism. Consequently, the semimetallic graphene

systems formed a p-type semiconductor, which enables field-dependent control of Dirac carriers within the ultrathin films. Each of these studies take advantage of the orbital and lattice degrees of freedom enabling tunability of this monoelemental nanosheet. Furthermore, the authors postulate theorized ultrathin films dubbed Archimedean ultrathin films. These nanosheets form a unique semiregular polygonal (4,8)-tessellated configuration. This configuration was extended to bulk crystals where we show the potential for forming ultrathin films that contain this unique symmetry. Two groups were studied: the boron pnictides, and the aluminum pnictides. The ground states featured indirect band gap semiconductors, where it was discovered that the boron-pnictides, in particular the planar configurations, possessed a double band gap. Subsequently, the optical response of the boron pnictides were revealed within linear response time-dependent density functional theory, which showed that the planar ultrathin films displayed strong optical response from the UV to the IR. Finally, the electronic ground state of 1T-TiS_2 was mechanically strained to induce phase transitions converting this nanosheet into a direct band gap semiconductor. Hence, we demonstrate the tunability of material properties for a series of ultrathin films, whose material properties could provide or support existing and nascent nanotechnologies for the 21^{st}-century.

Application of Ab Initio Theory to the Chemistry of Ultrathin Films

by

Paul A. Brown, B.A., B.S., M.S.

A Dissertation

Approved by the Department of Chemistry & Biochemistry

_____

Patrick J. Farmer, Ph.D., Chairperson

Submitted to the Graduate Faculty of
Baylor University in Partial Fulfillment of the
Requirements for the Degree
of
Doctor of Philosophy

Approved by the Dissertation Committee

_____

Kevin L. Shuford, Ph.D., Chairperson

_____

Darrin J. Bellert, Ph.D.

_____

Carlos E. Manzanares, Ph.D.

_____

Caleb D. Martin, Ph.D.

_____

Enrique Blair, Ph.D.

Accepted by the Graduate School
August 2018

_____

J. Larry Lyon, Ph.D., Dean

Page bearing signatures is kept on file in the Graduate School.

TABLE OF CONTENTS

LIST OF FIGURES

LIST OF TABLES

ACKNOWLEDGMENTS

My academic pursuits would not be possible without the support of my family, friends, and colleagues. I extend my warm gratitude to Baylor University, whom through their stewardship have formed exceptional facilities to promote the highest quality of research for which this document serves as a testament. I would like to thank the department of chemistry and biochemistry, for being in their company these six years have been the most impactful in shaping who I am as a scientist. Furthermore, I would like to thank my former advisor Dr. Michael Messina for introducing me to theoretical chemistry and encouraging me to pursue a career in this highly diverse field. I would like to also thank my committee Dr. Darrin J. Bellert, Dr. Carlos E. Manzanares, Dr. Caleb D. Martin, and Dr. Enrique Blair. Next, I would like to specially thank my advisor Dr. Kevin L. Shuford. Dr. Shuford is the consummate "do it yourself" advisor. Working for Kevin has been a wonderful experience, with his empowerment approach to research, "get out in the world" attitude, and ever refulgent personality, my life and knowledge have been irrevocably changed. I extend my deepest gratitude to him, for my life will never be the same. I would like to also thank my family and friends. My wife Karen, whose persistent encouragement and belief in me has enabled me to realize this great achievement. I would like to also thank my father Garry S. Brown, and my mother Cecilia Wilson for their constant support and encouragement. Moreover, I would like to thank my siblings Judson G. Brown and Bruce S. Brown for their persistent encouragement. I would like to specially thank my grandmother whom a decade ago suggested I take a college course. Next, I would like to thank my extended family, e.g., Greg and Sherry Brown, their son and daughter-in-law Chris and Katie Brown, Walker Brown and his daughter Cora Brown, my mother-in-law Susan Yarbrough, and her son and daughter-in-law

Collin and Ginger Yarbrough for their companionship all of which have made this achievement possible. I would to especially acknowledge my colleague Zack Theis, whose circuitous conversations on the minutia of quantum matter were enjoyable and creative. And I would like to thank my fellow group members Emvia Calixte and Andrew Smith for thoughtful and engaging discussions on life and science. Finally, I would like to thank my fellow physical chemistry colleagues for their thoughtful conversations.

To my family

CHAPTER ONE

Introduction

Civilizations have characterized themselves by the materials they shape and the technologies they derive from them. The ability to utilize emerging technologies in novel or unexpected ways has been an incessant pursuit by mankind. The human epochs of the Stone, Bronze, Iron, Nuclear, and Silicon ages have marked significant societal expansions, whose technologies have propelled human beings to dominate the earth. However, the preeminence of the world's civilizations are replete with growing challenges that endanger its very existence. Rising populations, greater energy demands, higher demand for information capacity, agricultural security, national security, and greenhouse emissions are currently the challenges faced by the world's civilizations. The necessity to redress these prescient challenges has become an imperative need for all nations. Great promise in addressing all of these challenges may originate from nanochemistry.

The nanoscale is a new frontier of intense research that is dedicated to absolute control of one-billionth of a meter. The ability to control matter in such a way to tailor nascent nanotechnologies to the needs (challenges) alluded to above is a tantalizing prospect. Moreover, the ability to *tune* material properties will enable a seemingly infinite number of possible technologies for a myriad societal challenges, which will extend to medical, industrial, information, military, and agricultural areas so important for society. In particular, the discovery of graphene in 2004, a one atom thick sheet of carbon, marks a new frontier in nanoscience ripe with possibilities.[6,7] This incredible discovery, for which Geim and Novoselov received the Noble prize in 2010, presented remarkable properties never observed in existing materials to date. Monolayer graphene, *material suprema*, was found to have the largest known

surface area ($\sim 3000 m^2/g$), highest known thermal conductivity (higher than diamond), strongest material in the universe (Young's modulus of $1TPa$), stiffest known material (stiffer than diamond), most stretchable material (20% elasticity), highest current density at room temperature ($\sim$ 1000 times of Cu), impermeable (even to helium), highest intrinsic mobility (100 times of silicon), conducts electricity in the limit of no electrons, lightest charge carriers (zero rest mass), and, finally, the longest mean free path at room temperature ($\sim 1\mu$m).[8] These superlative material properties propelled the field of ultrathin films, which began from pencil lead (1564) or graphite a material known for centuries! Since the discovery of graphene, and the erosion of scientific dogma that ultrathin films cannot exist, new families of two-dimensional materials have been discovered holding new possibilities for technological application. In fact, over the past 14 years graphene has been extended to new nanotechnologies such as an electrode material, catalyst, resonant tunneling transistors, light emitting diodes, photovoltaics, and heterostructures, where even proof-of-concept nanoassemblies feature record breaking results.[9–18] However, the proliferation of single-atom thick nanosheets have been limited by two factors: the rate of production with specific sheet thicknesses, e.g., monolayer over bilayer, etc., and the quality of the nanosheets, or the presence of defects and impurities that vitiate intrinsic material properties.[19] In fact, the first two-dimensional material to be isolated was achieved with Scotch tape, which remains the best method for avoiding impurities and defects.[6] Regardless of these (mass) production limitations ultrathin films continue to thrive with new discoveries every year.[20–28] Furthermore, as new ultrathin films are discovered, characterizing their electronic properties will be critical especially for tailoring ultrathin films for given applications.

Every material carries with it quantum degrees-of-freedom that are derived from the elements forming the material. Specifically, each ultrathin film possesses orbital, spin, charge, topological, and lattice degrees-of-freedom.[29] Hence, these degrees-of-freedom form the foundation for *tuning* material properties for electrical, light, magnetism, heat, and mechanical applications, see Figure 8.1. In this manuscript, we investigate the chemical and physical properties of a series of ultrathin films using an *ab initio* condensed matter perspective. This approach is suitable for crystalline systems such as ultrathin films, which form periodic arrangements of atoms on a lattice. This research exploits condensed matter theoretical tools applied to the investigation of ultrathin films ranging from well known graphene to unknown haeckelite ultrathin films, and titanium disulfide, see Chapters three-seven. In Chapter one, we exploit graphene's sensitivity to chemical modifications, whereby graphene is perforated with a single vacancy or monovacancy defect state, which accommodates pnictogen dopants to observe periodic chemical trends. This work demonstrates the ability to chemically modify graphene into a functional material, where the basal plane of monolayer graphene is technically chemically inert. Furthermore, experimental evidence has demonstrated this to be possible.[30–35] Blistering graphene is one way to *tune* the material properties of graphene, yet a viable alternative to physically altering the lattice could be achieved with halogen adsorbates, Chapter four. In Chapter four, the introduction of halogen diatoms enabled the formation of a band gap, a major limitation in controlling Dirac carriers in graphene, which converted monolayer and multilayer graphene into a small gap p-doped semiconductor making field-dependent charge carriers possible in a otherwise semimetal. Furthermore, it was found that each diatom species induced different band gap sizes, which appeared to be intimately related to the contact distances of a given diatomic molecule. Moreover, unnoticed in the original study, a topological Mexican-hat bandstructure forms in these doped systems, in particular, the multilayer cases, which has become an intense area of research.

These observations were corroborated in earlier experiments that involved bromine and iodine gas, that is, band gap formation.[36] Interestingly, a similar observation was discovered in the newly theorized haeckelite materials of Chapter five. In Chapter five, newly theorized (4,8)-tessellated nanosheets were derived from bulk crystals that contained the requisite intrinsic symmetries of the ultrathin films. In this work, group-III and group-V elements were placed at the vertices of a (4,8)-tessellation lattice, and their electronic properties fully determined. A number of notable observations were made: one, the ability to form a ultrathin film from the bulk crystals appeared possible from changes in the energy of formation and low cohesive energies; second, the boron group formed unique Mexican hat bandstructures, which were accompanied with van Hove singularities in the projected density of states hinting to significant optical activity; third, *H*-BSb ultrathin film was found to be unstable due to a unique boron-boron bond that formed from charge transfer from antimony atoms; fourth, all ultrathin films tended to form indirect bandgap semiconductors; finally, two competing configurations were predicted, where a planar geometry is possible and, a more stable, buckled configuration was found. Unlike earlier chapters, Chapter five focused on both lattice and elemental degrees-of-freedom. Furthermore, because of the unique bandstructures observed in the planar boron-pnictogen ultrathin films, Chapter six focused on the optical response of these nanosheets. Chapter six, showed that each planar haeckelite could potentially support very strong optical response, which extends from the IR to the UV. This exciting prospect points to the possibility of photovoltaic applications, where a haeckelite ultrathin film could act as a tandem with another material to absorb IR light, where approximately 54% of solar irradiance is emitted from the sun. Much more research is required, however, for the newly proposed Archimedean nanosheets to understand their behavior, for instance, substrate interactions. Finally, in Chapter seven, the transition metal dichalcogenide 1T-TiS_2 polymorph was mechanically strained to observe potential phase transitions

in the ground state electronic structure. In this study, the semimetal 1T-TiS_2 was mechanically stretched and compressed to induce the formation of a band gap, which upon tensile of the nanosheet an indirect band gap appeared and later transitioned to a direct band gap at higher tensile strain. Consequently, the semimetal 1T-TiS_2 was converted into a moderate band gap semiconductor from mechanical strain of its lattice degree-of-freedom. Hence, 1T-TiS_2 could potentially be implemented for optoelectronic applications where the material could be mechanically strained to induce a band gap. Consequently, this body of research demonstrates the impact of *tuning* in condensed matter, and, perhaps most importantly, the implications for technological impact utilizing the thinnest known materials and the degrees-of-freedom they support.

1.1 Attribution

The work published herein was conducted chiefly by the authors listed. Chapters three, five, and six were carried out by the first author, whose data and manuscript were gathered and formed. This work was subsequently edited by the coauthors, and submitted for peer review. Chapters four and seven were spear-headed by Dr. Chengyong Xu (first author). The coauthors subsequently revised, extended, and authenticated results produced by Dr. Xu. The subsequent articles were edited and submitted by the authors for peer review.

CHAPTER TWO

The Many-Body Problem & Ground-Excited State Density Functional Theory

2.1 The Many-Body Problem

Electronic structure theory contains within it many approximations made necessary because of the intractability of the full Hamiltonian. The full nonrelativistic Hamiltonian of an electronic system is given by the following expression,

$$\hat{\mathcal{H}} = \sum_I \Big[-\frac{\hbar^2}{2M_I}\nabla_I^2 + \frac{1}{2}\frac{e^2}{4\pi\epsilon_0}\sum_{I\neq J}\frac{Z_I^{val}Z_J^{val}}{|\mathbf{R}_I-\mathbf{R}_J|}\Big] + \sum_i \Big[-\frac{\hbar^2}{2m_e}\nabla_i^2 + \frac{e^2}{4\pi\epsilon_0}\sum_{i\neq j}\frac{1}{|\mathbf{r}_i-\mathbf{r}_j|}\Big] - \frac{e^2}{4\pi\epsilon_0}\sum_I\sum_i\frac{Z_I^{val}}{|\mathbf{R}_I-\mathbf{r}_i|}, \quad (2.1)$$

where this expression can be more succinctly written in operator form as,

$$\hat{\mathcal{H}} = \hat{\mathcal{T}}_I + \hat{\mathcal{V}}_{II} + \hat{\mathcal{T}}_e + \hat{\mathcal{V}}_{ee} + \hat{\mathcal{V}}_{eI}. \quad (2.2)$$

This expression contains the kinetic energy of the nuclei, $\hat{\mathcal{T}}_I$, the potential energy of the nuclei, $\hat{\mathcal{V}}_{II}$, the kinetic energy of the electrons, $\hat{\mathcal{T}}_e$, the potential energy of the electrons, $\hat{\mathcal{V}}_{ee}$, and the potential energy of the electron-ion interaction, $\hat{\mathcal{V}}_{eI}$, for a collection of electrons, $\mathbf{r} = \{\mathbf{r}_i\}$, and nuclei, $\mathbf{R} = \{\mathbf{R}_I\}$, degrees of freedom.[37] This expression can be adapted to include the influence of electric fields, magnetic fields, and hyperfine interactions, and relativistic effects such as spin-orbit coupling as well.[37] Including the above electronic Hamiltonian into the time-dependent Schrödinger equation,

$$i\hbar\frac{\partial\Phi}{\partial t} = \hat{\mathcal{H}}\Phi(\{\mathbf{r}_i\},\{\mathbf{R}_J\},t), \quad (2.3)$$

and evolving the full wavefunction (nuclei and electrons), $\Phi(\{\mathbf{r}_i\},\{\mathbf{R}_J\},t)$, in time permits a complete description of quantum matter. In fact, all of chemistry can be

understood with the above expressions. Unfortunately, the full Hamiltonian , Equation 2.1, is intractable to solve for any reasonably sized system of practical chemical significance. For instance, if one wanted to determine the total wavefunction of benzene with 42 total electrons in a discretized box of 10 Å with 50 grid-points for a molecule approximately 4.5 Å across; this would require 50^{126} operations of Equation 2.1- 2.3 for many time-steps. The computation of the full electronic problem on the fastest computers reaching approximately 10^{18} floating-point operations per second will require 3.73x10^{188} years to compute! This is known as the "dimensional wall" or "exponential wall" for wavefunction based methods commonly encountered in electronic structure theory.[37,38] Because of the deleterious scaling of computational effort in computing the full Hamiltonian we are forced to introduce soluble approximations for predictions of chemically relevant phenomena.

2.1.1 Born-Oppenheimer Approximation

The simplest approximation takes advantage of the mass disparity between the electrons and the nuclei. In fact, the mass ratio of an electron to nuclei ranges $\frac{m_e}{M} \approx \frac{1}{2000} - \frac{1}{500{,}000}$, hence the motion of the electrons relative to the nuclei appears instantaneous.[39] To decouple the above Equation 2.1 we must employ the ansatz introduced by Born (1951),

$$\Phi(\{\mathbf{r_i}\},\{\mathbf{R_I}\};t) = \sum_{l=0}^{\infty} \Psi_l(\{\mathbf{r_i}\},\{\mathbf{R_I}\})\chi_l(\{\mathbf{R_I}\};t), \tag{2.4}$$

here $\chi_l(\{\mathbf{R_I}\};t)$ is the time-dependent nuclear wavefunction or coefficients of the full wavefunction expansion, and $\Psi_l(\{\mathbf{r_i}\},\{\mathbf{R_I}\})$ is the electronic wavefunction.[37] It is important to note that the full wavefunction, Φ, obeys orthogonality $< \Psi_k|\Psi_l >= \delta_{kl}$. Substituting Equation 2.4 into Equation 2.3 and project from the left $\Psi_l^*(\{\mathbf{r_i}\},\{\mathbf{R_I}\})$

integrating over all space yields a set of coupled differential equations,

$$\Big[-\sum_I \frac{\hbar^2}{2M_I}\nabla_I^2 + E_k(\{\mathbf{R_I}\})\Big]\chi_k + \sum_l \mathcal{C}_{kl}\chi_l = i\hbar\frac{\partial \chi_k}{\partial t}, \tag{2.5}$$

where

$$\mathcal{C}_{kl} = \int d^3r \Psi_k^* \Big[-\sum_I \frac{\hbar^2}{2M_I}\nabla_I^2\Big]\Psi_l + \frac{1}{M_I}\sum_I \Big\{ \int d^3r \Psi_k^*[-i\hbar\nabla_I]\Psi_l \Big\}[-i\hbar\nabla_I], \tag{2.6}$$

which is the time-dependent Schrödinger equation for coupled electron and nuclear dynamics.[37] The $\mathcal{C}_{kl}$ is the *nonadiabatic coupling* operator for the kinetic energy of the nuclei (first term in Equation 2.6) and the nuclear dependence of their momenta.[37] If we treat only the diagonal terms of the nonadiabatic coupling operator, $\mathcal{C}_{kk} = -\sum_I \frac{\hbar^2}{2M_I}\int d^3r \Psi_k^* \nabla_I^2 \Psi_k$, we introduce the "adiabatic approximation" because the diagonal terms only consider an adiabatic wavefunction in a single state, Ψ_k, and precludes the possibility of electronic excitations resulting from the motion of the nuclei. This yields the following set of decoupled equations,

$$\Big[-\sum_I \frac{\hbar^2}{2M_I}\nabla_I^2 + E_k(\{\mathbf{R_I}\}) + \mathcal{C}_{kk}(\{\mathbf{R_I}\})\Big]\chi_k = i\hbar\frac{\partial \chi_k}{\partial t}, \tag{2.7}$$

where the wavefunction can be decoupled by introducing the product wavefunction, $\Phi(\{\mathbf{r_i}\},\{\mathbf{R_I}\};t) \approx \Psi_k(\{\mathbf{r_i}\},\{\mathbf{R_I}\})\chi_k(\{\mathbf{R_I}\};t)$ Equation 2.7 leads to the expression,

$$\Big[-\sum_I \frac{\hbar^2}{2M_I}\nabla_I^2 + E_k(\{\mathbf{R_I}\})\Big]\chi_k = i\hbar\frac{\partial \chi_k}{\partial t}, \tag{2.8}$$

which yields the well-known "Born-Oppenheimer" approximation. Here the $E_k(\{\mathbf{R_I}\})$ are the adiabatic energies of the electrons parametrically dependent on the nuclear positions. From Equation 2.8, the nuclear wavefuction moves in a field of electrons in the state k. Hence, the motion of the nuclei has no influence on the electronic wavefuctions, or the nuclei do not induce transitions between electronic

states. Therefore, Equation 2.8 defines the physical ground state, excluding degeneracy, for which the electrons instanteously occupy. In the limit of clamped-nuclei the time-dependence of the nuclear wavefunction vanishes. Therefore, the Born-ansatz becomes a time-independent wavefunction of the product of nuclear and electron wavefunctions, e.g., $\Phi \sim \chi_k(\mathbf{R}_I)\Psi_k(\mathbf{r}_i;\mathbf{R}_I)$. Substituting this expression into the full Hamiltonian, $\hat{\mathcal{H}} \mapsto \hat{H}(\mathbf{r},\mathbf{R})$ (Equation 2.1) for stationary solutions yields,

$$[\hat{\mathcal{H}}_e + \mathcal{V}_{II}(\mathbf{R})]\Psi_k(\mathbf{r};\mathbf{R}) = E_k(\mathbf{R})\Psi_k(\mathbf{r};\mathbf{R}), \tag{2.9}$$

where the kinetic energy of the nuclei is zero, the nuclear coefficients have been reduced, and the electronic Hamiltonian, $\hat{\mathcal{H}}_e$, operates on all electron degrees of freedom. The nuclear-nuclear potential energy can be included into the external potential, $\mathcal{V}_{eI}$, as a pertubation on the ground state of the subsystem of electrons; therefore, we arrive at the time-independent Schrödinger equation for the parametrically dependent electrons,

$$\hat{H}\Psi_k(\mathbf{r};\mathbf{R}) = E_k(\mathbf{R})\Psi(\mathbf{r};\mathbf{R}). \tag{2.10}$$

This expression is an eigenvalue equation of motion for all adiabatic electron degrees of freedom for a single equilibrium nuclear configuration, hence we can drop the parametric dependence leaving the simpler expression, $\hat{H}\Psi_k(\mathbf{r}) = E_k\Psi_k(\mathbf{r})$. Equation 2.10 forms the starting point for the subsequent formulation of Density Functional theory for the motion of electrons moving in a field of quasi-static nuclei.

2.2 Ground-State Density Functional Theory

Ground state density functional theory (DFT) is an exact treatment of the many-body fermionic system, but the only unknown in the Kohn-Sham equations of motion is the correlation energy.[2] It is important to emphasize that DFT is formulated for the computational ease of solving the expression discussed below (and

above), and to overcome the *dimensional wall* associated with wavefunction based formulations. Moreover, we shall see that the triumph of DFT is rooted in the Levy-Lieb constrained search approach, which permits a variational solution of the Kohn-Sham equations that arrived 14 years later after the Nobel paper of Kohn and Sham.[2,38] With the constrained search approach we shall see that the remaining limitation of the Kohn-Sham equations rests on the exchange-correlation energy density per particle. This term is the elusive enigma in the DFT formalism that continues to be the source of intense research, for complete knowledge of this term would open the possibility of computing exactly all observables of a given system of interest; moreover, with the exact exchange-correlation energy term the Kohn-Sham equations would be complete, but the exact expression remains unknown. Hence, the necessity of approximations to the exchange-correlation energy per particle is widely employed in two broad categories, that is, semiempirical and pure exchange-correlation functionals. As examined below, the exchange-correlation functionals are formed in various ways, but the use of exact-constraints based on fundamental (well-known) properties of nature serves as the best way forward for systematic predictions of the correlated many-body system. We will examine in detail the fundamental expression for DFT, the ground-state energy, which can be formed as a functional of the electron density.

The time-independent Schrödinger equation contains all of the necessary information to describe the motion of electrons on a Born-Oppenheimer potential energy surface for a given many-body system. It would be instructive to expand the expression into the essential terms for describing the density of electrons as a functional of each term in Equation 2.10. Moreover, we will use spatial-spin coordinates for generality, $\mathbf{x} = (\mathbf{r_i}, \sigma)$, where σ is for spin-up ($\uparrow$) and/or spin-down ($\downarrow$) electrons obeying half-integer Fermi-Dirac statistics, $s = \frac{1}{2}$. Furthermore, we will determine the expectation of each operator contributing to Equation 2.10, which can be related to the ground state energy for a given system. First we must define what the (spin)

electron density, $n_\sigma(\mathbf{x})$, is for a many-body system of electrons. The electron density, for a given system, has the following form,

$$\begin{aligned} n_\sigma(\mathbf{x}) &= N \sum_{\sigma\sigma'} \int \prod_{i=2}^{N} d^3\mathbf{r}_i \theta(\mu - \epsilon_{i\sigma}) \Psi^*_{i\sigma}(\mathbf{x}, \mathbf{x}_2, ..., \mathbf{x}_N) \Psi_{i\sigma'}(\mathbf{x}, \mathbf{x}_2, ..., \mathbf{x}_N) \\ &= \sum_{i\sigma} \theta(\mu - \epsilon_{i\sigma}) |\Psi_{i\sigma}(\mathbf{x})|^2, \end{aligned} \tag{2.11}$$

here i is a composite index for $i \equiv (\mathbf{R}, n, l, m_l)$, which are the ion positions, principle quantum number, angular momentum quantum number, and azimuthal quantum number respectively. The Heaviside step-function, $\theta(\mu - \epsilon_{i\sigma})$, guarantees that for $\Psi_{i\sigma}$ with $\epsilon_{i\sigma} < \mu$ are occupied states, and $\epsilon_{i\sigma} > \mu$ are unoccupied states for chemical potential, μ. The chemical potential is selected so long as the sum rule (normalization) applies, $\int d^4x n(\mathbf{x}) = N$.[40] Moreover, because the electron density is spin-dependent the total electron density can be formed by summing both spin-up and spin-down densities, $n(\mathbf{r}) = n^\uparrow(\mathbf{r}) + n^\downarrow(\mathbf{r})$. Throughout this chapter we will presume that only Kohn-Sham wavefunctions are discussed, which are not to be construed as the *true* ground state wavefunctions. The electron density, presented above, can be shown to be a functional for all terms in Equation 2.10. The kinetic energy of the electrons has the following form in DFT,

$$\begin{aligned} \hat{\mathcal{T}}_e = \hat{T}_s[n_\uparrow, n_\downarrow] &= -\frac{\hbar^2}{2m_e} \sum_\sigma \sum_i \theta(\mu - \epsilon_{i\sigma}) \Psi^*_{i\sigma}(\mathbf{x}) \nabla_i^2 \Psi_{i\sigma}(\mathbf{x}) \\ &= \frac{\hbar^2}{2m_e} \sum_\sigma \sum_i \theta(\mu - \epsilon_{i\sigma}) |\nabla_i \Psi_{i\sigma}(\mathbf{x})|^2, \end{aligned} \tag{2.12}$$

where we have added the notation for the Kohn-Sham noninteracting kinetic energy, $\hat{T}_s$. The external potential energy, $\mathcal{E}_{eI} \equiv E_{eI}[n_\uparrow, n_\downarrow](\mathbf{r}) = E_{ext}[n](\mathbf{r}) = \langle V_{ext}[n](\mathbf{r}) \rangle$,

resulting from the attractive interaction between electrons and ions takes the form,

$$\begin{aligned} E_{ext}[n] &= -\frac{e^2}{4\pi\epsilon_0}\sum_{i,\sigma}\sum_{I}\int d^3\mathbf{r}\theta(\mu-\epsilon_{i\sigma})\Psi^*_{i\sigma}(\mathbf{x})\frac{Z_I^{val}}{|\mathbf{R_I}-\mathbf{r}_i|}\Psi_{i\sigma}(\mathbf{x}) \\ &= -\frac{e^2}{4\pi\epsilon_0}\sum_{i,\sigma}\sum_{I}\int d^3\mathbf{r}\theta(\mu-\epsilon_{i\sigma})\frac{Z_I^{val}}{|\mathbf{R_I}-\mathbf{r}_i|}|\Psi_{i\sigma}(\mathbf{x})|^2 \\ &= \int d^3\mathbf{r}v_{ext}(\mathbf{r})n_\sigma(\mathbf{x}), \end{aligned} \tag{2.13}$$

which is just the interaction of the ground state electron density with the external potential energy provided by the nuclei. The ion-ion electrostatic interaction, $\mathcal{E}_{II}$, is similar to Equation 2.13 with an electron density term included; however, we are assuming ion-clamped approximation (*Born-Oppenheimer*) for this term and will forego writing this expression here, so we will presume it forms a portion of the external interaction potential in Equation 2.13. The electron-electron interaction, $\mathcal{E}_{ee} \equiv E_{ee}[n_\uparrow, n_\downarrow] = E_{ee}[n] = \langle V_{ee}[n](\mathbf{r})\rangle$, has the following density functional dependence,

$$\begin{aligned} &E_{ee}[n] = \\ &\frac{1}{2}\frac{e^2}{4\pi\epsilon_0 m_e}\sum_{\sigma\sigma'}\int\int d^3\mathbf{r}d^3\mathbf{r}'\theta(\mu-\epsilon_{i\sigma})\theta(\mu-\epsilon_{j\sigma})\Psi^*_{i\sigma'}(\mathbf{x}')\Psi^*_{j\sigma}(\mathbf{x})\frac{1}{|\mathbf{r}-\mathbf{r}'|}\Psi_{j\sigma'}(\mathbf{x}')\Psi_{i\sigma}(\mathbf{x}), \end{aligned} \tag{2.14}$$

where the electron-electron energy contains all of the complex quantum effects, such as exchange and correlation, among the electrons. The electron-electron interaction

can be expanded to account for the antisymmetry of the fermionic wavefunctions into,

$$E_{ee}[n] = \frac{1}{2}\frac{e^2}{4\pi\epsilon_0}\sum_{\sigma\sigma'}\int\int d^3\mathbf{r}d^3\mathbf{r}'\theta(\mu-\epsilon_{i\sigma})\theta(\mu-\epsilon_{j\sigma})$$
$$[\Psi_{j\sigma}(\mathbf{x})\Psi^*_{j\sigma'}(\mathbf{x}')\frac{1}{|\mathbf{r}-\mathbf{r}'|}\Psi^*_{i\sigma'}(\mathbf{x}')\Psi_{i\sigma}(\mathbf{x}) - \Psi^*_{i\sigma'}(\mathbf{x}')\Psi^*_{j\sigma}(\mathbf{x})\frac{1}{|\mathbf{r}-\mathbf{r}'|}\Psi_{j\sigma'}(\mathbf{x}')\Psi_{i\sigma}(\mathbf{x})]$$
$$= \frac{1}{2}\frac{e^2}{4\pi\epsilon_0}\sum_{\sigma\sigma'}\int\int d^3\mathbf{r}d^3\mathbf{r}'\theta(\mu-\epsilon_{i\sigma})\theta(\mu-\epsilon_{j\sigma})$$
$$\Big[\frac{n_{\sigma'}(\mathbf{x})n_{\sigma}(\mathbf{x}')}{|\mathbf{r}-\mathbf{r}'|} - \frac{n_{\sigma}(\mathbf{x})n_{XC}(\mathbf{x},\mathbf{x}')}{|\mathbf{r}-\mathbf{r}'|}\Big] \tag{2.15}$$

where we have taken advantage of the antisymmetry of the ground state Kohn-Sham wavefunction to express the electron-electron energy in terms of the Hartree energy, $U_H[n]$, and the exchange-correlation energy, $E_{XC}[n]$, shown below. The $n_{XC}(\mathbf{r},\mathbf{r}')$ is commonly known as the exchange-correlation *hole* for fermions, which will become clear in Section 2.2.3 below. This expression can be further reduced to simply a spin-dependent second-order pair density, $n(\mathbf{x},\mathbf{x}')$, via

$$E_{ee}[n] = \frac{1}{2}\frac{e^2}{4\pi\epsilon_0}\sum_{\sigma\sigma'}\int\int d^3\mathbf{r}d^3\mathbf{r}'\theta(\mu-\epsilon_{i\sigma})\theta(\mu-\epsilon_{j\sigma})\frac{n(\mathbf{x},\mathbf{x}')}{|\mathbf{r}-\mathbf{r}'|}$$
$$= U_H[n] + E_{XC}[n]. \tag{2.16}$$

Here we have introduced a second-order correlation function, $n(\mathbf{x},\mathbf{x}') = n_{\sigma}(\mathbf{x})n_{\sigma'}(\mathbf{x}') - n_{XC}(\mathbf{x},\mathbf{x}')n_{\sigma'}(\mathbf{x}')$, to account for exchange and correlation between electron densities within a many-body system.[2] The correlation function is related to another important quantity known as the pair-correlation function, $g(\mathbf{x},\mathbf{x}')$, often expressed as, $n_{XC}(\mathbf{x},\mathbf{x}') = [g(\mathbf{x},\mathbf{x}')-1]n_{\sigma'}(\mathbf{x}')$.[2] The pair-correlation function is a measure of correlation for a given system. The electron-electron energy effectively contains all of the essential ingredients of static and dynamical interactions between electrons for a given atom, molecule, or solid. If we combine all of the expressions above and group

them together we arrive at the energy as a functional of the ground state density,

$$E_{KS}[n] = T_s[n] + U_H[n] + E_{XC}[n] + \int d^3\mathbf{r} n_\sigma(\mathbf{x}) v_{ext}(\mathbf{r}), \tag{2.17}$$

where we have omitted the ion-ion electrostatic energy for a single fixed system in its ground state. The first three terms are the *noninteracting* Kohn-Sham kinetic energy density, the Hartree energy, and the exchange-correlation energy. The last term is the external energy for the attraction of nuclei and electrons, which is system dependent. However, the first three terms in Equation 2.17 are completely determined from the interactions among electrons, hence these terms can be succinctly written as,

$$E_{KS}[n] = F[n] + \int d^3\mathbf{r} n_\sigma(\mathbf{x}) v_{ext}(\mathbf{r}), \tag{2.18}$$

where $F[n] = T_s[n] + U_H[n] + E_{XC}[n]$ is a *universal* functional of all electrons. As alluded to above, this expression forms the basis of DFT, and the exchange-correlation energy, $E_{XC}[n]$, is the only unknown. But if exchange-correlation were known exactly, then it would be possible to compute all properties of any system with Equation 2.18 exactly. Unfortunately, the exact expression for $E_{XC}[n]$ is unknown; consequently, this term is approximated with various exact constraints based on the homogeneous electron gas or inclusion of exact-exchange energy to enable better predictions. Thus, the $E_{XC}[n]$ is the source of intense research culminating into a set of approximations gradually improving over the well-known local density approximation (LDA), otherwise known as Jacob's ladder, see Figure 2.1. In Figure 2.1 the simplest approximation is to neglect the exchange-correlation term, which is the Hartree-Fock approximation; above this is the LDA, the generalized gradient approximation (GGA) which includes the gradient of the density such as the PBE functional, meta-GGA includes the kinetic energy of the ground-state electron density such as the SCAN

functional, hybrid approximation includes an add-mixture (a_0 in the figure) of exact exchange (EXX) such as the HSE06 functional, and higher rungs including the random-phase approximation (RPA) or the inclusion of unoccupied states for configuration interaction, Figure 2.1.[41–53] Jacob's ladder forms the paradigmatic structure of DFT, which is the quintessence of current density functional approximations to the exchange-correlation energy of the many-body ground state. However, how can we know that a solution to the Kohn-Sham equation of motion can be found in terms of the density? In the next section, we explore the existence of such a solution proving the possibility for formulating the many-body problem in terms of the density alone without the need of multivariate wavefunctions.

2.2.1 Hohenberg-Kohn Theorems

Kohn-Sham theory is a theory for describing correlated quantum systems.[2] A central axiom in DFT is that all of the many-body interactions can be predicted from knowledge of a single scalar-function, the ground-state electron density, $n_0(\mathbf{r})$.[2,37] We shall see that the electron density is a functional of the ground state total energy, which permits the formation of a variational solution of the Kohn-Sham equations that enables the *ab initio* predictions commonly reported in the literature and within this work. But first we must show that there exist a unique solution for the ground state density within the framework of DFT, otherwise the density, which is the solution to the many-body system, would not be unique for a given correlated system of electrons; hence, there would exist many possible ground state densities that would be used for predictions of observables and, yet, we could not distinguish what outcomes are legitimate for a given many-body system. Nevertheless, the Hohenberg-Kohn theorems will show that for a nonrelativistic nondegenerate electron gas, the ground state electron density can uniquely determine the external potential and, subsequently, the ground state energy of a given atom, molecule, or solid. Here will will state and prove the Hohenberg-Kohn theorems of DFT:

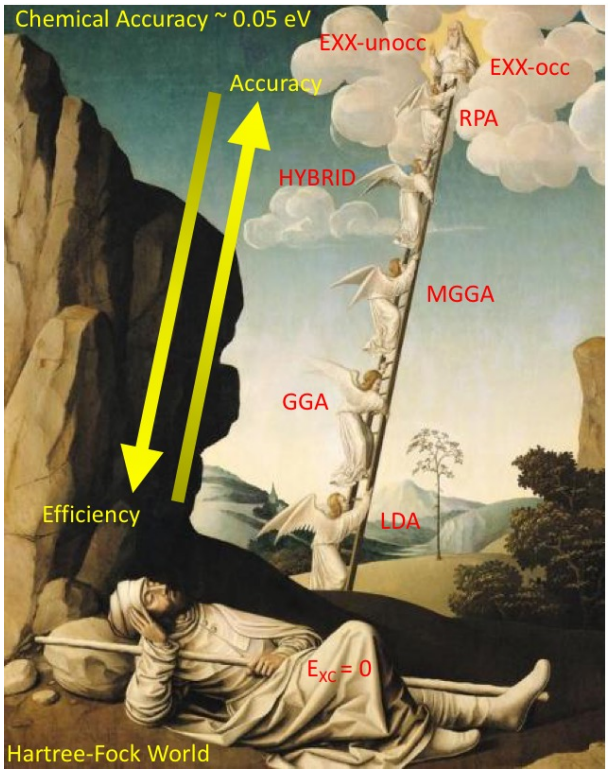

$$E_{XC}^{HYBRID}[n] = E_{XC}^{GGA/L(S)DA} + a_0 E_{XX}$$

$$E^{MGGA}{}_{XC}[n] = \int d^4x\, n_{\downarrow,\uparrow}(x)\varepsilon_{xc}(r, \nabla n_{\downarrow}, \nabla n_{\uparrow}, \tau_{\downarrow}, \tau_{\uparrow})$$

$$E^{GGA}{}_{XC}[n] = \int d^4x\, n_{\downarrow,\uparrow}(x)\varepsilon_{xc}(r, \nabla n_{\downarrow}, \nabla n_{\uparrow})$$

$$E^{LDA}{}_{XC}[n] = \int d^4x\, n_{\downarrow,\uparrow}(x)\varepsilon_{xc}(r)$$

Figure 2.1. Jacob's ladder provides a measure of the pedigree of approximation to the $E_{XC}[n]$ in Equation 2.18. Each rung of the ladder includes additional exact constraints to improve upon the predictions of the $E_{XC}[n]$ term. Jacob's ladder shows the predictive power of various approximations starting from the simplest (Hartree-Fock) to the most computationally demanding with exact-exchange (EXX) with occupied and/or unoccupied states. Adapted from Jacob's ladder c.1490 French School.[1]

HK.1 For any system of interacting particles in an external potential, $v_{ext}(\mathbf{r})$, the potential is uniquely determined, except for an additive constant, e.g., $v_{ext}^{(1)} - v_{ext}^{(2)} = constant$, by the ground state electron density, $n_0(\mathbf{r})$, where the density is constrained $\int d^3\mathbf{r} n(\mathbf{r}) = N$ (N is the total number of electrons) and depends on the ground-state antisymmetric wavefunction, $\Psi_{i\sigma}$.[2,54]

Proof. The proof of **HK.1** can be completed by *reductio ad absurdum*. First we use the Hamiltonian of the electrons in Equation 2.10 for the time-independent nonrelativistic Schödinger equation. We suppose that there exist two external potentials, $v_{ext}^{(1)}$

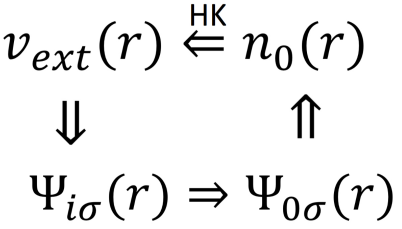

Figure 2.2. Diagrammatic representation of the Hohenberg-Kohn existence theorems, which is the upper portion of the diagram (labeled "HK"). The lower portion of the diagram shows that the many-body wavefunctions, $\Psi_{i\sigma}(r)$, is determined by the external potential, $v_{ext}(r)$, including the ground-state wavefunction, $\Psi_{0\sigma}(r)$, which subsequently yields the ground state density, $n_0(r)$. Here the index σ is meant to include spin for generality.[2]

and $v_{ext}^{(2)}$, whose density and ground state energy are equivalent. We will further assume that the external potential energies differ by more than a constant. Moreover, the external potentials will have two different Hamiltonians, $\hat{H}^{(1)}$ and $\hat{H}^{(2)}$, along with two different many-body wavefunctions , $\Psi_{i\sigma}^{(1)}$ and $\Psi_{i\sigma}^{(2)}$, which lead to the same ground state density, $n_0(\mathbf{r}r)$, Figure 2.2. Because $\Psi_{i\sigma}^{(2)}$ is not the ground state of $\hat{H}^{(1)}$ then,

$$E^{(1)} = \left\langle \Psi_{i\sigma}^{(1)} \middle| \hat{H}^{(1)} \middle| \Psi_{i\sigma}^{(1)} \right\rangle < \left\langle \Psi_{i\sigma}^{(2)} \middle| \hat{H}^{(1)} \middle| \Psi_{i\sigma}^{(2)} \right\rangle, \tag{2.19}$$

where

$$\begin{aligned} \left\langle \Psi_{i\sigma}^{(2)} \middle| \hat{H}^{(1)} \middle| \Psi_{i\sigma}^{(2)} \right\rangle &= \left\langle \Psi_{i\sigma}^{(2)} \middle| \hat{H}^{(2)} \middle| \Psi_{i\sigma}^{(2)} \right\rangle + \left\langle \Psi_{i\sigma}^{(2)} \middle| \hat{H}^{(1)} - \hat{H}^{(2)} \middle| \Psi_{i\sigma}^{(2)} \right\rangle \\ &= E^{(2)} + \int d^3\mathbf{r} \Big[v_{ext}^{(1)} \text{ - } v_{ext}^{(2)} \Big] n_0(\mathbf{r}), \end{aligned} \tag{2.20}$$

hence

$$E^{(1)} < E^{(2)} + \int d^3r \Big[v_{ext}^{(1)} - v_{ext}^{(2)} \Big] n_0(\mathbf{r}), \tag{2.21}$$

likewise for $E^{(2)}$ we arrive at the following,

$$E^{(2)} = \left\langle \Psi_{i\sigma}^{(2)} \middle| \hat{H}^{(2)} \middle| \Psi_{i\sigma}^{(2)} \right\rangle < \left\langle \Psi_{i\sigma}^{(1)} \middle| \hat{H}^{(2)} \middle| \Psi_{i\sigma}^{(1)} \right\rangle, \tag{2.22}$$

where

$$\left\langle \Psi_{i\sigma}^{(1)} \middle| \hat{H}^{(2)} \middle| \Psi_{i\sigma}^{(1)} \right\rangle = \left\langle \Psi_{i\sigma}^{(1)} \middle| \hat{H}^{(1)} \middle| \Psi_{i\sigma}^{(1)} \right\rangle + \left\langle \Psi_{i\sigma}^{(1)} \middle| \hat{H}^{(2)} - \hat{H}^{(1)} \middle| \Psi_{i\sigma}^{(1)} \right\rangle$$
$$= E^{(1)} + \int d^3\mathbf{r} \Big[v_{ext}^{(2)} \text{ - } v_{ext}^{(1)} \Big] n_0(\mathbf{r}), \quad (2.23)$$

hence

$$E^{(2)} < E^{(1)} + \int d^3\mathbf{r} \Big[v_{ext}^{(2)} - v_{ext}^{(1)} \Big] n_0(\mathbf{r}). \quad (2.24)$$

If we add Equations 2.21 and Equation 2.24, then we arrive at the contradictory statement, $E^{(1)} + E^{(2)} < E^{(1)} + E^{(2)}$. Hence, there cannot exist two external potentials that are more than an additive constant which yields the same nondegenerate ground state electron density. Thus, the ground state density uniquely determines the external potential, and the reverse is true as well, Figure 2.2. Therefore, all properties of a many-body correlated system can be determined with the ground state density yielding N, $\hat{H}$, and $\Psi_{i\sigma}$ from $n_0(\mathbf{r})$, *quod erat demonstrandum* (*Q.E.D.*).[2,54] We now prove the second Hohenberg-Kohn theorem.

HK.2 A *universal* functional for the energy functional $E[n]$ defined in terms of the density, $n(\mathbf{r})$, and is valid for any external potential, $v_{ext}(r)$, exist. For any particular $v_{ext}(\mathbf{r})$, the *exact* ground state energy is the global minimum of this functional, and $n(\mathbf{r})$ is the exact ground state density that minimizes this functional.[2,54]

Proof. We will assume only "v-representable" densities to be a functional of the ground state energy. The electron density, in this case, is associated with the ground state energy for a given Hamiltonian and external potential for an antisymmetric wavefunction, $\Psi_{i\sigma}$. The variational solution can be applied here to show that the Kohn-Sham ground state energy is a minimum for electron density (**HK.1**), $n(\mathbf{r})$. Because the kinetic energy and potential energies entering the electronic Hamiltonian are uniquely determined by the ground state electron density, then each term can be

viewed as a functional of the electron density,

$$\begin{aligned} E_{HK}[n] &= T[n] + E_{int}[n] + \int d^3\mathbf{r} n(r) v_{ext}(\mathbf{r}) + E_{II} \\ &\equiv F_{HK}[n] + \int d^3\mathbf{r} n(\mathbf{r}) v_{ext}(\mathbf{r}) + E_{II}, \end{aligned} \tag{2.25}$$

where the E_{II} is the ion-ion (electrostatic) potential energy interaction, $F_{HK}[n] = T[n] + E_{int}[n]$, is a *universal* functional of (*only*) the interacting kinetic energy of the electrons and their pair-wise interactions. (we will define explicitly the terms in Equation 2.25 later) It is important to note that $F_{HK}[n]$ is applicable for all external potentials and number of particles. We must show that Equation 2.25 is a minimum by recognizing,

$$\begin{aligned} E_{HK}[n] &= \left\langle \Psi_{i\sigma} \middle| \hat{H} \middle| \Psi_{i\sigma} \right\rangle \\ &= F_{HK}[n] + \int d^3\mathbf{r} n(\mathbf{r}) v_{ext}(\mathbf{r}) + E_{II} \\ &\geq F[n_0] + \int d^3\mathbf{r} n_0(\mathbf{r}) v_{ext}(\mathbf{r}) + E_{II} \\ &= \left\langle \Psi_{0,\sigma} \middle| \hat{H} \middle| \Psi_{0,\sigma} \right\rangle \\ &= E[n_0], \end{aligned} \tag{2.26}$$

thus the Kohn-Sham ground state energy functional equality holds for $\Psi_{i\sigma} = \Psi_{0,\sigma}$, which are functionals of the density for the trial density, $n(\mathbf{r})$, and exact density, $n_0(\mathbf{r})$. Therefore, all properties of the energy functional, or any other observable that is a functional of the electron density, can be determined by functional variations of the many-body energy with respect to the electron density, otherwise Equation 2.26 would not yield anything desirable *Q.E.D.*[54]

The above Hohenberg-Kohn theorems might be generalized by considering the sets of all external potentials, $\mathcal{V}$, ground state wavefunctions, $\mathcal{G}$, and ground state densities, $\mathcal{N}$, Figure 2.3.[3] Since **HK.1** is true, then you can assert that a collection

of external potentials exist such that the set

$$\mathcal{V} = \{v_{ext} | v_{ext} \iff \exists |\Psi_0\rangle \wedge v_{ext}^{'} \neq v_{ext} + C\}, \tag{2.27}$$

where the set ground state wavefunctions is,

$$\mathcal{G} = \{|\Psi_0\rangle || \Psi_0\rangle \iff \mathcal{V}. \ni .|\Psi_0^{'}\rangle \neq e^{i\phi}|\Psi_0\rangle\}, \tag{2.28}$$

form a correspondence, or mapping, $A : \mathcal{V} \mapsto \mathcal{G}$, that is bijective between each set containing each collection of object, potentials and wavefunctions, Figure 2.3(a).[3] Moreover, the set of ground state densities is defined,

$$\mathcal{N} = \{n_0(r) | n_0(r) = \langle \Psi_0 | \hat{n}(r) | \Psi_0 \rangle, \forall |\Psi_0\rangle \in \mathcal{G}\}, \tag{2.29}$$

where $\hat{n}(r) = \sum_i \delta(\mathbf{r} - \mathbf{r}_i)$ is the particle (Fermion) operator. The correspondence between the ground state wavefunctions and electron densities, $B : \mathcal{G} \mapsto \mathcal{N}$, is bijective, since each ground state wavefunction, which is a solution to Equation 2.10, maps each wavefunction to a density, where the converse holds as well, Figure 2.3(a). This generalization holds for both degenerate and nondegenerate many-body solutions to the Schrödinger equation, Figure 2.3. However, for the case of degeneracy , seen as lighter circular regions in set $\mathcal{G}$ and $\mathcal{N}$ in Figure 2.3, the possibility of multiple wavefunctions and electron densities can occur. Nevertheless, as shown in Figure 2.3(b), the Hohenberg-Kohn theorems still apply. Because a particular set of wavefunctions ($\mathcal{G}_{v1}$) can give rise to a set of densities ($\mathcal{N}_{v1}$) each class always corresponds to an external potential within the set $\mathcal{V}$, or in this case $v_{ext,1}$, Figure 2.3(b).[3] However, in spite of the applicability of *v-representable* pure-state electron densities, this criterion is too stringent to be obeyed, and counterexamples exist that have shown

v-representability may not be proven sound. In fact, it is clear that within the degenerate interacting case described above that bijectivity of the mapping between each set (A & B) cannot hold. Hence, as we shall see below, the problem can be reformulated for "*N-representable*" pure-state electron density.[55,56]

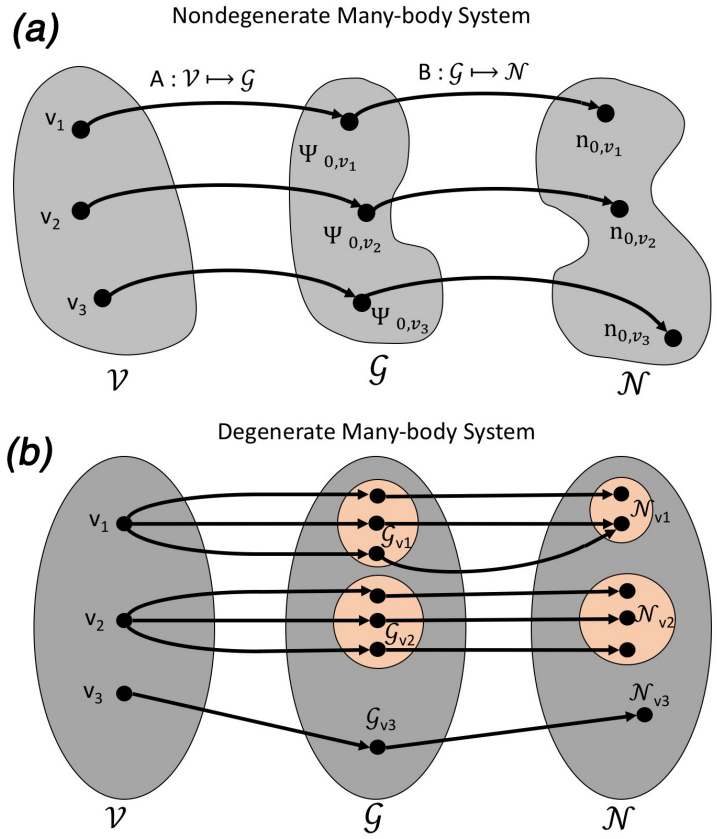

Figure 2.3. These diagrams show the subsequent formulation of DFT into bijective mappings between sets of external potentials, $\mathcal{V}$, ground state wavefunctions, $\mathcal{G}$, and ground state densities, $\mathcal{N}$. Here the mapping of A and B are one-to-one and onto (bijective) among the sets obeying the time-independent Schrödinger equation. (a) shows the conclusions of **HK.1** and **HK.2** for nondegenerate many-body systems; (b) shows the same situation as (a) but for degenerate many-body systems.[3]

The two theorems **HK.1** and **HK.2** codify DFT into an immensely powerful *ab initio* framework that enables predictions of correlated many-body systems using the simpler scalar function, the electron density; this avoids the more demanding

wavefunction based formalism discussed above allowing for the ability to observe chemically relevant phenomena of great importance. However, the Hohenberg-Kohn theorems do not specify what the form of $F_{HK}[n]$ should be, yet this required another significant realization provided by the Levy-Lieb constrained search approach that permitted DFT reach prominence and wide-spread usage into many disciplines of science.[40]

2.2.2 Levy-Lieb Constrained Search

The Levy-Lieb constrained search approach allowed for density functional theory to be formulated into a variational solution for the ground state of a given system.[55–59] Moreover, as we shall see, it becomes possible to use "N-representable" electron densities rather than the more stringent "v-representable" case originally presumed in the Hohenberg-Kohn theorems of the previous section.

In order to highlight the Levy-Lieb constrained search it is important emphasize that instead of searching over "v-representable" pure-state electron densities, instead the constrained search approach focuses on "N-representable" electron densities, that is, an electron density is obtained from some antisymmetric N-particle wavefunction.[55,56] Moreover, all electron densities are pure state N-representable if they obey $n(\mathbf{r}) \geq 0$, $\int d^3\mathbf{r} n(\mathbf{r}) = N$, and $\int d^3\mathbf{r} |\nabla \sqrt{n(\mathbf{r})}|^2 < \infty$.[59,60] These three constraints on the electron density insure that the density is positive definite, normalized, and finite. From these constraints on the electron density the Levy-Lieb constrained formulation proceeds with Equation 2.26 by requiring the Kohn-Sham energy to have a lower bound (infimum) or no variation over a set of antisymmetric wavefunctions

$\mathcal{G}$,

$$
\begin{aligned}
E_0[n] &= \inf_{|\Psi\rangle} \langle \Psi | \hat{H} | \Psi \rangle \\
&= \inf_{|\Psi\rangle} \langle \Psi | \hat{T}_e + E_{ee} + E_{ext} | \Psi \rangle \\
&= \inf_{n(\mathbf{r})} \Big[\inf_{|\Psi\rangle \in \mathcal{G}} \langle \Psi | \hat{T}_e + E_{ee} | \Psi \rangle + \int d^3\mathbf{r} n(r) v_{ext}(\mathbf{r}) \Big] \\
&= \inf_{n(r)} \Big[F[n] + \int d^3\mathbf{r} n(\mathbf{r}) v_{ext}(\mathbf{r}) \Big], \qquad (2.30)
\end{aligned}
$$

thus the constrained search is a minimization over all antisymmetric wavefunctions yielding $n(\mathbf{r})$, and a constrained search over electron densities.[55] Therefore, the Levy-Lieb constrained search establishes an apt definition for $F[n]$ as being a functional of the ground state electron density that is pure state N-representable, such that, the electron density minimizes the ground state energy for a given external potential (**HK.1**).[2,55,59] Furthermore, the constrained search approach establishes a variational procedure to the Kohn-Sham ground state energy functional that arrives at a minimum for the many-body Hamiltonian. Consequently, combined with the Kohn-Sham self-consistent field (SCF) scheme, the ground state properties of a given system can be understood with exchange-correlation effects included.[61]

The self-consistent scheme, Figure 2.4, originally formed by Kohn and Sham, follows the variational approach presented within the constrained search, Equation 2.30.[61] Here we present the canonical equations of motion of an *auxiliary* system based on the Kohn-Sham energy functional for the ground state of a given system. It was originally presumed that the Kohn-Sham energy functional was composed of noninteracting fermions, and only the exchange-correlation contained the interaction so important for accurate predictions.[61] We will determine the variational solution to $E_{KS}[n]$ (Equation 2.18) for an noninteracting N-representable pure state electron

density via a minimization over a grand-canonical functional, Ω_{KS},

$$\begin{aligned}
&\delta\Omega_{KS}[n] = \delta\Big[T_s[n] + E_{ext}[n] + U_H[n] + E_{XC}[n] - (\sum_{\sigma}\epsilon_{i\sigma}\int d^3\mathbf{r}n_\sigma(\mathbf{r}) - \delta_{ij}\delta_{\sigma\sigma'})\Big] = 0 \\
&\Rightarrow \frac{\delta E_{KS}}{\delta\Psi^*_{i\sigma}(\mathbf{r})} = \frac{\delta\hat{T}_s[n]}{\delta\Psi^*_{i\sigma}(\mathbf{r})} + \Big[\frac{\delta E_{ext}[n]}{\delta n(\mathbf{x})} + \frac{\delta U_H[n]}{\delta n(\mathbf{x})} + \frac{\delta E_{XC}[n]}{\delta n(\mathbf{x})}\Big]\frac{\delta n(\mathbf{x})}{\delta\Psi^*_{i\sigma}} - \epsilon_{i\sigma}\Psi_{i\sigma}(\mathbf{x}) = 0 \\
&\Rightarrow (\hat{H}_{KS} - \epsilon_{i\sigma})\Psi_{i\sigma}(\mathbf{x}) = 0 \\
&\therefore \hat{H}_{KS}\Psi_{i\sigma}(\mathbf{x}) = \epsilon_{i\sigma}\Psi_{i\sigma}(\mathbf{x}),
\end{aligned} \tag{2.31}$$

which is a single-particle Schrödinger equation for the Kohn-Sham equations of motion.[2,61] The Kohn-Sham Hamiltonian has the form,

$$\hat{H}_{KS} = -\frac{\hbar^2}{2m_e}\nabla^2 + V^\sigma_{KS}, \tag{2.32}$$

for the effective Kohn-Sham potential energy,

$$V^\sigma_{KS} = V_{ext}[n](\mathbf{r}) + V_H[n](\mathbf{r}) + V^\sigma_{XC}[n]. \tag{2.33}$$

Hence, the full expression has the form,

$$\Big(-\frac{\hbar^2}{2m_e}\nabla^2 + V_{ext}[n](\mathbf{r}) + V_H[n](\mathbf{r}) + V^\sigma_{XC}[n]\Big)\Psi_{i\sigma}(\mathbf{r}) = \epsilon_{i\sigma}\Psi_{i\sigma}(\mathbf{r}), \tag{2.34}$$

which is the canonical form of the Kohn-Sham equations.[61] The solution to Equation 2.34 requires an iterative self-consistent approach since the potential energy contains the electron density, which can be clearly seen by expanding Equation 2.33,

$$V^\sigma_{KS} = V_{ext}[n](\mathbf{r}) + \frac{e^2}{4\pi\epsilon_0}\sum_{\sigma'}\int d^3\mathbf{r}'\theta(\mu - \epsilon_{j\sigma'})\frac{n_{\sigma'}(\mathbf{x}')}{|\mathbf{r} - \mathbf{r}'|} + \frac{\delta E^\sigma_{XC}[n]}{\delta n(\mathbf{x})}, \tag{2.35}$$

where the external potential energy, Hartree energy, and exchange-correlation potential energy per particle each contain the electron density. Hence, the solution to

the canonical Kohn-Sham eigen-equation for the minimum ground state wavefunctions yields the ground state density, external potential energy, and the Kohn-Sham ground state energy for an N-correlated many-body system of N-fermions, Figure 2.4.

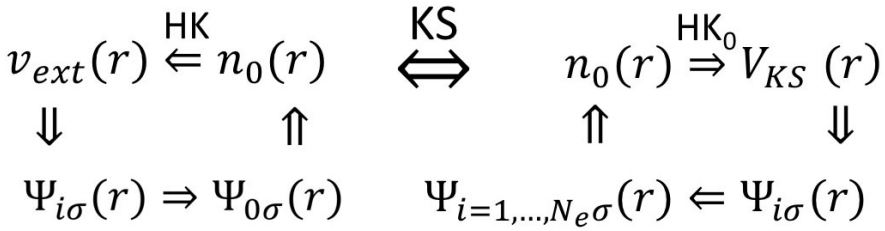

Figure 2.4. The Hohenberg-Kohn and Kohn-Sham schemes for solving the interacting and auxiliary systems. The left side represents the interacting portion provided by the existence theorems of the Hohenberg-Kohn theorems. The right side displays the Kohn-Sham variational scheme for the noninteracting system, where the solution of the ground state density, $n_0(r)$, is found by Levy-Lieb constrained search over all Kohn-Sham wavefunctions, $\Psi_{i=1,\ldots,N_e\sigma}(r)$, for the noninteracting N_e-electron system. Note the **H.K.** theorems can be applied to both cases.[2]

The above expressions define all the terms that enter into the Kohn-Sham equations (Equations 2.34-2.35) that permits the solution to the many-body problem, and defines what $F[n]$ should be within this construction. Hence, the universal functional ($F[n]$) is the stationary solution to the Kohn-Sham eigenvalue problem, and the functional derivative of the exchange-correlation energy , $E^{\sigma}_{XC}[n]$, yields the potential energy of exchange-correlation energy per particle that contains all additional quantum effects of the system as a result of the external potential experienced by the electrons. Therefore, the exchange-correlation potential energy per electron is the only unknown that is left, in fact, the correlation energy per particle, $E_C[n]$, is the only quantity that is unknown since exact exchange has been derived since the Hartree-Fock approximation, which predates DFT.[62–66] These critical terms are discussed in the proceeding section.

2.2.3 *Nature's Glue: Exchange-Correlation Energy*

As discussed in the preceding section the exchange-correlation energy per particle is the only unknown to the Kohn-Sham equations (Equation 2.35). In fact, most of DFT research is intensely focused on approximating this term ($E_{XC}[n]$), which is likely the source of great obfuscation among researchers around the field. In this section we discuss the essential "ingredients" to various approximations used throughout this document to provide some understanding to the encyclopedia of acronyms associated with various approximations in DFT, see Figure 2.1 in section 2.2 above.

Before covering various approximations to the exchange-correlation energy it is instructive to highlight why this term is so critical in the Kohn-Sham equation (Equation 2.34). This question can be explained by viewing the range of energies that that are accessible to the exchange and correlation energy functional. The correlation energy can fluctuate dramatically from $0.87 - 130eV(83.7 - 12,550kJmol^{-1})$, and the exchange energy can vary significantly as well to $0.87 - 1301eV(83.68 - 125,519.8kJmol^{-1})$![67] These energies are extraordinarily disparate, and leads to difficulties in describing electron densities in chemical environments where the density is diffuse or highly concentrated. In the intermittent regime (low-*here somewhere*-high density) the incessant fluctuation of electron density becomes a significant challenge to comprehend with exact analytical expressions (See Appendix B). This is dynamically driven by the motion of electrons within condensed phases, hence the screening of electrons (Thomas-Fermi screening, k_S), and, correspondingly, the kinetic energy (Fermi wavevector, k_F) of the electrons can fluctuate per unit volume time resulting from the interplay of these two physical effects. So, as discussed below, the exchange-correlation energy per particle can be considered to be *nature's glue* for chemical bonding, which is the bedrock upon all subsequent chemical/physical properties are based. Hence, the approximations to $E_{XC}[n]$ will have a critical impact on the predictions and computational ease for comparison to experimental observables.

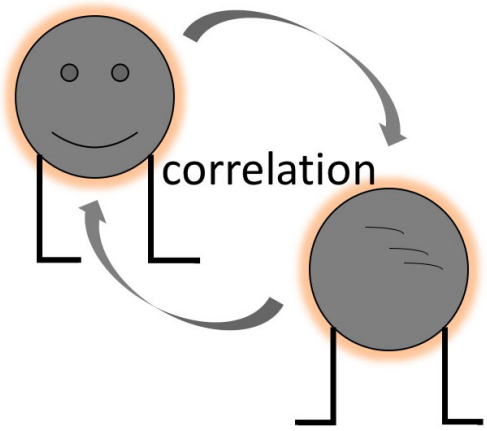

Figure 2.5. "Correlation dance".Correlation is the tendency of electrons to dynamically avoid one another resulting from their mutual Coulomb repulsion (Coulomb correlation). The avoidance of electrons leads to an alteration of their kinetic energy densities.

The construction of various approximations to the exchange correlation energy is central to forming reliable predictions with computational ease in DFT. The exchange-correlation energy can be understood by combining the Hohenberg-Kohn exact energy functional (Equation 2.25) with the Kohn-Sham noninteracting energy functional (Equation 2.31), which yields,

$$E_{XC}^{\sigma}[n] = (\hat{T}[n] - \hat{T}_s[n]) + (\langle \hat{V}_{ee} \rangle - U_H[n]). \tag{2.36}$$

This shows that the exchange-correlation hole (XC-hole) originates from the change in the interacting kinetic energy density and noninteracting Kohn-Sham kinetic energy density, and the electron-electron interaction with the removal of the Hartree energy.[2,67,68] Another way of writing Equation 2.36 is with respect to a parameter λ,

$$E_{XC}[n] = \frac{1}{2}\frac{e^2}{4\pi\epsilon_0}\int_0^1 d\lambda \int\int d^3\mathbf{r} d^3\mathbf{r}' \frac{n_\sigma(\mathbf{r}) n_{XC}^{\lambda}(\mathbf{r},\mathbf{r}')}{|\mathbf{r}-\mathbf{r}'|}, \tag{2.37}$$

here λ is a coupling constant that links the noninteracting system ($\lambda = 0$) to the fully interacting system ($\lambda = 1$).[69–71] See Appendix C for the derivation of this result. This second expression in Equation 2.37 is often known in the literature as the "Adiabatic Connection" expression for the exchange-correlation energy.[70–72] Therefore, this expression holds that the exchange-correlation hole, within the Kohn-Sham scheme, is the difference between the fully interacting (correlated) system and the *auxiliary* system, Figure 2.4.[2] Furthermore, the XC-hole is the only unknown in the Kohn-Sham equations, Equation 2.34, so any approximation for the XC-hole will have a significant impact on the quality of the predictions. The XC-hole originates from electron correlations, or to be more precise, from parallel spin fermions tendency to avoid each other in a system (Fermi correlation), see Figure 2.6. This is the fundamental Paul-Exclusion principle that gives all matter its structure. Hence the effect of two electron densities of equal quantum numbers being in proximity of each other results in the reduction of probability amplitude in the neighborhood of the second electron (Figure 2.6) creating a "hole" of dimished density around the second electron. Therefore, the density functional approximations to the exchange-correlation energy attempt to accuratly capture the XC-hole, but this is no trivial task.

In the original *ansatz* for the expansion of the exchange-correlation energy, Kohn-Sham introduced,

$$E_{XC}^{\sigma}[n] = \int d^3\mathbf{r}(\epsilon_{XC}^{LDA}[n](\mathbf{r})n(\mathbf{r}) + \epsilon_{XC}[n, |\nabla n|]|\nabla n|^2 + ...), \tag{2.38}$$

where the first term is the local density approximation, the second the generalized expansion approximation, and so on.[61,73,74] The first order term in Equation 2.38 can be written as,

$$E_{XC}^{LDA}[n] = \int d^3\mathbf{r}n(\mathbf{r})\epsilon_{XC}^{LDA}[n](\mathbf{r}), \tag{2.39}$$

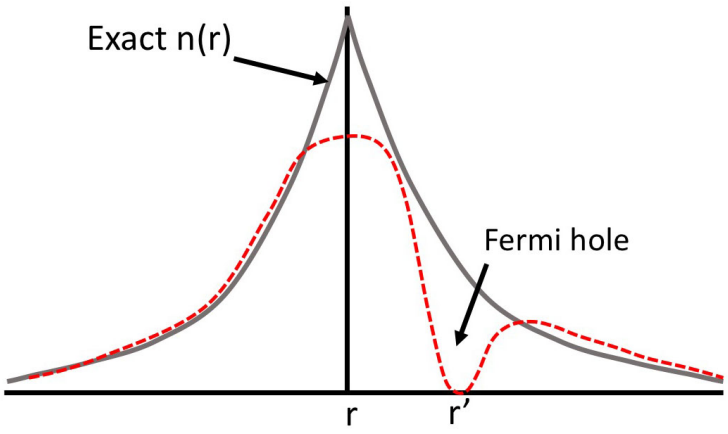

Figure 2.6. This diagram highlights the origins of the term of "XC-hole". The figure shows the exact ground state density (gray line) of an atom (say He), where an electron is placed at the origin, r, and another electron is placed at r', such that their spins are collinear (oriented up or down). The depletion of density (red dotted line) around r' shows the formation of a *hole* around the second electron. The hole can be understood to originate from the Pauli-Exclusion principle, and dubbed the Fermi hole for exchange energy contribution. The correlation hole has the same effect although smaller than the Fermi hole.

so that the exchange-correlation energy within LDA depends on the homogeneous densities (slow variations) of the electron liquid, and $\epsilon_{XC}^{LDA}[n](\mathbf{r})$ is the XC-energy per particle.[61,74] In LDA, the exchange-correlation hole is assumed to be equivalent to that of the uniform electron gas, i.e., $\epsilon_{XC}^{LDA}[n](\mathbf{r}) \approx \epsilon_{XC}^{unif}[n](\mathbf{r})$, which has exact known constraints for exchange and approximate correlation energies. The exchange energy for a uniform electron gas (UEG) was expressed by Dirac in 1930.[75] Dirac exchange was formulated for a plane wave basis originally, and takes the form,

$$\epsilon_{X}^{unif}[n](\mathbf{r}) = -C_X \int d^3\mathbf{r} n_\sigma(\mathbf{r})^{4/3}, \tag{2.40}$$

where $C_X = \frac{3}{4}(\frac{3}{\pi})^{1/3}$ is a constant. The correlation energy, however, has many numerous approximations each of which are derived from UEG, where the correlation is parameterized with Monte Carlo data for example, see Appendix B.[41,76–79] The LDA surprisingly has been found to be accurate for solids, in particular, because the above

expression obeys known exact constraints for the UEG. For example, the exchange and the correlation energy are nonpositive, $E_X < 0$ and $E_C \leq 0$, or the Lieb-Oxford bound $E_{XC} \geq -C_{LO} \int d^3\mathbf{r} n_\sigma(\mathbf{r})^{4/3}$ ($C_{LO} \leq 2.273$), and spin-scaling relations for the more general case of fermions are all obeyed.[40,80–83] Moreover, LDA has two important inverse length scales, namely, $\frac{|\nabla n|}{n} << k_F$ and $\frac{|\nabla n|}{n} << k_S$, where the density varies slowly over space. (here we have the Fermi-wavevector, $k_F = (3\pi^2 n(\mathbf{r}))^{1/3}$, and the Thomas-Fermi screening-wavevector, $k_S = \frac{2}{\pi^{1/2}}(3\pi^2 n(\mathbf{r}))^{1/6}$ (both are in atomic units))[40] The Fermi and Thomas-Fermi wavevectors originate from the kinetic energy of the electrons and the screening of electrons within a condensed phase, or molecule. In this case, densities that are more homogeneous tend to yield good results within LDA. In fact, using Equation 2.16 and the expression for the XC-hole, the XC-hole ($n_{XC}(\mathbf{r}, \mathbf{r}') = n_X(\mathbf{r}, \mathbf{r}') + n_C(\mathbf{r}, \mathbf{r}')$) obeys the following constraints, $n_X(\mathbf{r}, \mathbf{r}') < 0$, $\int d^3\mathbf{r} n_X(\mathbf{r}, \mathbf{r}') = -1$, and $\int d^3 r n_C(\mathbf{r}, \mathbf{r}') = 0$.[73,74,84] These constraints (positivity and sum rules) on the XC-hole follow from the constraints on the energies of each term above. However, in systems with dopants, or other matter that may violate the above constraints, LDA tends to poorly describe various empirical aspects of such systems, see Chapter 3-4, e.g., over delocalization.[71]

The second order case is the generalized expansion approximation, which was intended to include inhomogeneities that commonly occur in condensed matter systems.[73,74] The exchange-correlation energy per particle for the GEA has the following form,

$$E_{XC}^{GEA}[n] = \int d^3\mathbf{r} \epsilon_{XC}^{GEA}[n(\mathbf{r}), |\nabla n|] |\nabla n(\mathbf{r})|^2. \tag{2.41}$$

In the GEA, it was discovered that the exchange-correlation hole within this expansion becomes positive, yet in LDA the exchange and correlation are not positive for the UEG.[73,74,85] This lead to a *real-space cutoff* for the GEA by requiring the XC-hole to become effectively zero for low densities.[42–44,86] This established the generalized gradient approximation, the ansatz for the exchange-correlation energy per electron

is,

$$E_{XC}^{GGA}[n] = \int d^3\mathbf{r} n(\mathbf{r}) \epsilon_{XC}^{GGA}[n(\mathbf{r}), |\nabla n|], \tag{2.42}$$

where the expansion includes the real-space cutoff for the XC-hole.[73,74,87–90] This form for the second-order term in the expansion of the exchange-correlation energy allowed for the inclusion of further *ingredients* or constraints to improve upon LDA. The GGA of Equation 2.42 can be rewritten in the following form,

$$E_{XC}^{GGA}[n] = \int d^3\mathbf{r} \epsilon_X^{UEG}[n] F_{XC}(r_S(n), s(\mathbf{r})), \tag{2.43}$$

where the dimensionless density-gradient captures inhomogeneities, $s(\mathbf{r}) = \frac{|\nabla n|}{2k_F n(\mathbf{r})}$, and r_S is the Wigner-Seitz radius (Appendix B), which are both set as independent variables of an enhancement factor, F_{XC}, and $\epsilon_X^{UEG}[n]$ is Dirac exchange defined above.[73,74,87–90] This formal expression is the basis of the commonly used PBE GGA functional that has demonstrated exceptional predictive power, and it is employed throughout this dissertation (see Appendix A). Typically, PBE can achieve 0.5% error and 5% error in the exchange and correlation energies over a given system.[40] Moreover, bond lengths tend to be 1% too long effectively yielding correct structures, but have 30% (too low) errors in energy barriers.[40] This has been an improvement over LDA, which has 5% error in exchange energy, 100% error in correlation energy, 1% too short of bond lengths, and 100% too low energy barriers.[40] The improvement in the second rung of Jacob's ladder (Figure 2.1) results from the inclusion of higher order-gradient terms in the GGA not contained within LDA. The success of PBE can be attributed to the use of exact-constraints on the exchange-correlation functional, rather than using test sets for highly parameterized exchange-correlation functionals commonly known as semiempirical DFT. However, it should be noted that the advantage of semiempirical DFT is the expedience of an answer for a given chemical circumstance,

but does not describe why the formulation works. Nevertheless, the PBE formulation has formed the basis for higher order expansions of the exchange-correlation energy.

The next rung contains the meta-GGA. These approximations include the same ingredients as the lower order approximations seen for LDA and GGA, but include the kinetic energy of the electron density, $\tau_\sigma = -\frac{\hbar^2}{2m_e}\sum_{i\sigma}\theta(\mu-\epsilon_{i\sigma})|\nabla\Psi_{i\sigma}|^2$.[40] The orbital kinetic energy density for spin σ incorporated into the exchange-correlation energy per electron becomes,

$$E_{XC}^{MGGA}[n] = \int d^3\mathbf{r} n(\mathbf{r})\epsilon_{XC}^{MGGA}[n(\mathbf{r}), |\nabla n|, \tau_\sigma], \tag{2.44}$$

which includes a nonlocal τ_σ term to the exchange-correlation. In general, the MGGA improves overall predictions of GGA, but it heavily depends on the type of MGGA used, and in some cases, the MGGA can make worse predictions compared to LDA and GGA.[40] However, a new MGGA based on exact constraints (17 constraints in total) was recently released.[48,49] This formulation, dubbed strongly constrained and appropriately normed (SCAN), was shown to improve over several metrics for chemical systems with lower mean average errors (MAE).[48,49] It has been shown that for the G3-test (atomization energies of 223 molecules) $MAE(SCAN) = 0.25$ eV ($MAE(PBE) = 0.96$ eV), for the BH76-test set (76 reaction barriers) $MAE(SCAN) = 0.33$ eV ($MAE(PBE) = 0.40$ eV), for the S22 (22 molecular complexes bound by weak bonds) $MAE(SCAN) = 0.04$ eV ($MAE(PBE) = 0.12$ eV), and for the LC20-test set (20 solids lattice constants including metals, semiconductors, and insulators) $MAE(SCAN) = 0.0007$ eV ($MAE(PBE) = 0.0025$ eV).[48,49,91] These results are striking considering that chemical accuracy is around 0.05 eV, Figure 2.1. Moreover, the MGGA-SCAN includes short-range van der Waals interactions, which are neglected in semilocal GGAs and LDA.[49] However, a long range correction is needed to correctly describe the van der Waals interaction that is important in multilayer ultrathin films, see Chapter 4.[49,92–102] In fact, MGGA, such as with SCAN, it is

possible to obtain observations at the hybrid-level of approximation or even variational Monte-Carlo to the Kohn-Sham exchange-correlation energy.[48,49 49] However, LDA, GGA, and MGGA do not improve the overall bandgap commonly observed in semiconductors or insulators since they fail to capture the exact electron affinity (A) and ionization potential (I), which are the lowest unoccupied molecular orbital (LUMO) and highest occupied molecular orbital (HOMO), respectively.[71,103] The errors can range 30-50% in semilocal approximations.[103] The origin of the failure of the semilocal approximations is attributed to the derivative discontinuity originating from the removal or addition of an electron, hence, in the Kohn-Sham formalism the fundamental band gap has an additional term that alters the band gap prediction, $E_g = \epsilon_{CBM} - \epsilon_{VBM} + \Delta_{XC}$. The Δ_{XC} term originates from the derivative discontinuity in the exchange-correlation energy approximation.[103] However, the semilocal approximations discussed so far can be corrected with the inclusion of an admixture of non-local exact Fock exchange.[45–47,103] Exact exchange remedies the fundamental gap to near experimental measurements because within Hartree-Fock, Koopman's theorem is obeyed for the removal or addition of an electron so long as relaxation of the remaining electronic states does not occur.[103] Capturing the correct fundamental gap is critical for understanding the absorption process in ultrathin films, see Chapter 6.

As mentioned above, the hybrid rung of Jacob's ladder (Figure 2.1) includes an admixture of exact exchange (Fock exchange).[45,46,104] The hybrid level generally improves the overall accuracy for material observables, yet the computational cost scales poorly against lower runges of Jacob's ladder. This has made hybrid functionals for periodic systems prohibitive until recent years. The first pure hybrid functional was derived from PBE, which has the exchange-correlation approximation of the form,

$$E_{XC}^{PBE0}[n] = E_{XC}^{PBE} + a_0[E_{XX} - E_X^{PBE}], \tag{2.45}$$

where $a_0 = \frac{1}{4}$ was found to yield an optimum mixture of exact exchange, and E_{XX} is the exact exchange shown in Equation 2.15, where this hybrid approximation is known as PBE0.[104] In the case of PBE0, the inclusion of 75% PBE-exchange and 100% PBE-correlation is included at the semilocal approximation, which is accompanied with 25% exact exchange, Equation 2.45. This exchange-correlation approximation improves on the fundamental gap for semiconductors and insulators.[105] Another extension of the hybrid density functional approximation was developed within a screened hybrid approximation decomposing the exact exchange term into short-range and long-range exact exchange.[45,46,106] The screened hybrid construction for the exchange-correlation energy per electron has the following form,

$$E_{XC}^{HSE06}[n] = aE_X^{SR-HF}(\omega) + (1-a)E_X^{SR-PBE}(\omega) + E_X^{LR-PBE}(\omega) + E_C^{PBE}, \quad (2.46)$$

where the HSE06 functional is composed of a fraction of short-range PBE exchange, full long-range PBE exchange and correlation, while the exact exchange is partitioned into short-range exact exchange with screening parameter, $\omega = 0.2$, and $a = \frac{1}{4}$ similar to PBE0.[106] Here the screening parameter, ω, is chosen to optimize fundamental gap predictions over a large set of molecules and solids.[106] The MAE for band gaps with HSE06 was later estimated to be 21% or 0.26 eV, and 1.13 eV for PBE, which is a much better improvement over semilocal approximations.[107] The ability to accurately capture band edges is very critical to understanding optical response in ultrathin films, see Chapter 6 compared with band gaps in Chapter 5.

The structure of DFT, laid out above, forms a series of successive approximations that generally improve upon lower rungs of Jacob's ladder, Figure 2.1. However, one may wonder why density functional theory works at all, considering the density is the central quantity in all of the above approximations for the exchange-correlation potential. And the use of wavefunction based theories have demonstrated exceptional accuracy compared with DFT, albeit with an enormous computational cost. So why

focus on DFT and not on improving computational scaling of wavefunction based approaches? The reason for the success of DFT rest in what is being approximated and the contribution to the Hamiltonian. For example, if one were to examine the size of each term in the Kohn-Sham energy functional (Equation 2.17) for the neon atom. The exact kinetic energy for the neon atom is 128.94 Ha (Hartree), V_{ee} is 53.24 Ha, and V_{ext} is -311.12 Ha; the Kohn-Sham kinetic energy is 128.61 Ha, U 66.06 Ha, and E_{XC} is -12.98 Ha. From the numerics for the neon atom it is clear that the noninteracting kinetic energy is very close to the interacting kinetic energy ($\Delta T = 0.33$ Ha), while the E_{XC} contribution is very small relative to the other terms entering into the Kohn-Sham potential.[108] Furthermore, subtracting the Hartee energy and exchange-correlation energy from the exact electron-electron potential energy, V_{ee}, yields 0.16 eV, which is in very close agreement. Therefore, the success of DFT is centered on capturing the smallest contribution to the many-body system relative to other terms. However, without accurate approximations formed on rigorous underpinnings of exact constraints, predictions would not prove useful in any chemical context; therefore, in spite of the paucity of the contribution the exchange-correlation energy makes to the Kohn-Sham Hamiltonian, the $E_{XC}[n]$ term provides the requisite *glue* for the formation of corpuscular matter of all varieties. These density functional approximations have been used throughout this dissertation to make various predictions of ultrathin films for a range of properties significant for chemical characterization and application highlighted in the subsequent chapters.

2.2.4 Periodicity & Plane-Wave DFT

This dissertation is focused on the study of crystalline systems, in particular, the application of *ab initio* methods, highlighted in the previous section, to the study of ultrathin films and their chemical properties. We will define here how translational invariance is characterized and extend this to the Kohn-Sham formulation given in the preceding section.

Crystals are distinguished by their periodicity, where a single set of constituent elements (basis) can be repeated *ad infinitum* on a lattice generating a solid crystalline material.[2,109] The crystal is formed by defining three Bravais lattice vectors $\mathbf{a}_1$, $\mathbf{a}_2$, and $\mathbf{a}_3$, where the volume of the crystal lattice is $\Omega_{UC} = det(h)$ ($h = [\mathbf{a}_1, \mathbf{a}_2, \mathbf{a}_3]$ Bravais matrix). With the Bravais lattice vectors defined the primitive unit cell can be constructed, Figure 2.7(a). The primitive unit cell (PUC) contains the essential space group symmetry of the two-dimensional crystal such that no voids or gaps are formed as a result of selecting Bravais lattice vectors. Because perfect crystals are spatially invariant it is commonly preferred to employ periodic boundary conditions, e.g., $r_{PBC} = r - h[h^{-1}r]_{NINT}$, such that the spatial representation is *wrapped* back within the primitive unit cell with the nearest-integer function ($NINT$).[37] With the redundancy of forming the tessellation of the lattice; any crystal lattice can be constructed by a linear combination of integer multiples of each primitive lattice vector to form an infinite number of translational lattice vectors, i.e., $R_{n_1 n_2 n_3} = n_1\mathbf{a}_1 + n_2\mathbf{a}_2 + n_3\mathbf{a}_3$, which are repetitions of the PUC, Figure 2.7(a) For two-dimensional systems the third component can be neglected ($n_3 = 0$). Related to the Bravais lattice vectors of the crystal are the reciprocal lattice vectors, $\mathbf{b_i}, i \in \{1, 2, 3\}$, which are orthogonal to the Bravais lattice vectors,

$$\mathbf{b}_i \cdot \mathbf{a}_j = 2\pi\delta_{ij}. \tag{2.47}$$

The reciprocal lattice vectors have the form,

$$\mathbf{b}_i = \frac{2\pi}{\Omega_{UC}}\mathbf{a}_j \times \mathbf{a}_k, \tag{2.48}$$

where $\Omega_{UC} = \mathbf{a}_1 \cdot (\mathbf{a}_2 \times \mathbf{a}_3)$ is the volume of the PUC or conventional cell if expanded. The reciprocal lattice is shown in Figure 2.7(b)-(c), where the Wigner-Seitz volume (Figure 2.7(b)) is shown for graphene, or any hexagonally symmetric crystal. In addition to the reciprocal lattice vectors in reciprocal space, there exist translational

reciprocal lattice vectors, $\mathbf{G}$, in reciprocal space as well, i.e., $\mathbf{G_m} = \mathbf{G}_{m_1 m_2 m_3} = m_1\mathbf{b}_1 + m_2\mathbf{b}_2 + m_3\mathbf{b}_3$ or $\mathbf{G} = 2\pi(h^T)^{-1}g, \forall g \in \{i, j, k\} \in \mathbb{Z}^3$ ($[\mathbf{b}_1, \mathbf{b}_2, \mathbf{b}_3] = 2\pi(h^T)^{-1}$ following from Equation 2.47). This characterizes both real and reciprocal lattice spaces, which are inverse spaces. The consequences of translational invariance on the Kohn-Sham wavefunctions will now be discussed.

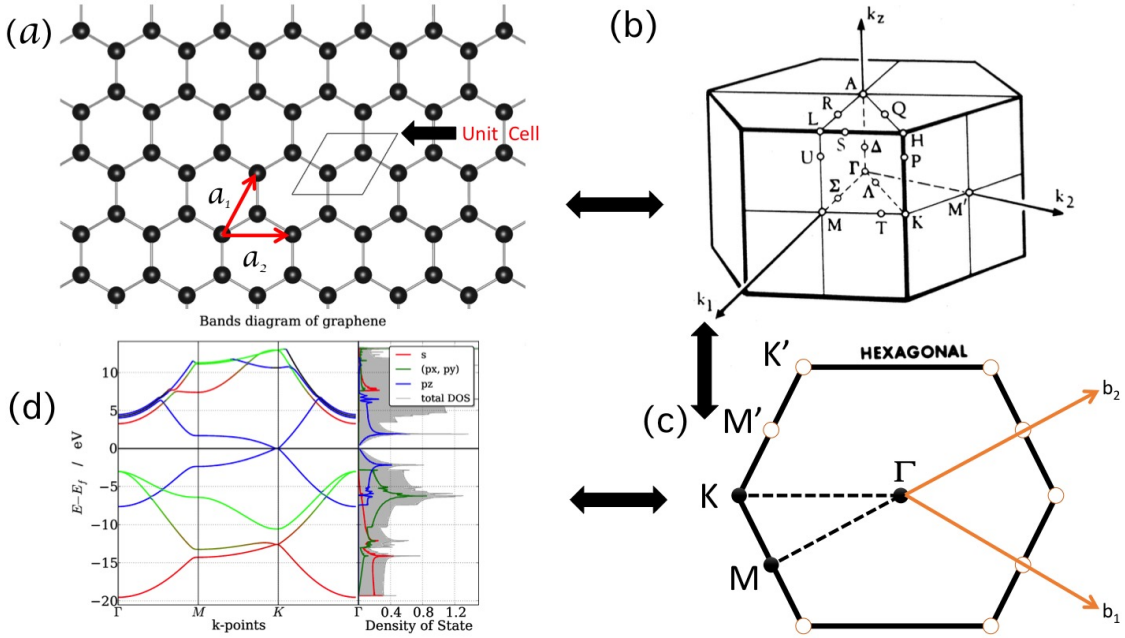

Figure 2.7. Crystal lattice representation and the reciprocal lattice representation displaying the path to band structures and density of states.(a) The real space lattice constructed from primitive lattice vectors $\mathbf{a}_1$ and $\mathbf{a}_2$, where the hexagonal unit cell shows a shift to the primitive lattice vectors. (b) The Wigner-Seitz cell formed around a single point generating the first-Brillouin zone for a hexagonal cell. Labels within the first-Brillouin zone mark high symmetry point in reciprocal space shown in the band structure. (c) Two-dimensional slice of the first-Brillouin zone in (b) showing high symmetry points K, M, and Γ (zone center) commonly integrated over to generate band structures for hexagonal cells (dotted line). (d) Resulting band structure and projected density-of-states for graphene.

Symmetries in quantum equations of motion are typically accompanied with *good* quantum numbers, which mark different discrete and allowed quantum states for a given atom, molecule, or solid. In the case of solids the crystal momentum (wavevector), $\mathbf{k} = \sum_i \frac{l_i}{N_i}\mathbf{b}_i (\forall(l_i \wedge N_i) \in \mathbb{Z}^3)$ & $i \in \{x, y, z\}$, labels allowed reciprocal

states of a crystal by Born-von Karman (periodic) boundary conditions. The periodic boundary conditions lead to the well known Bloch theorem for translationally invariant wavefunctions, which are expanded in a complete plane wave basis. Bloch's theorem states: *an electron in a periodic potential has eigenstates of the form,*

$$\Psi_{n\mathbf{k}}(\mathbf{r}) = e^{i\mathbf{k}\cdot\mathbf{r}} u_{n\mathbf{k}}(\mathbf{r}) \tag{2.49}$$

$$= \frac{1}{\sqrt{\Omega_{UC}}} \sum_{\mathbf{G}} c_{n\mathbf{k}}(\mathbf{G}) e^{i(\mathbf{k}+\mathbf{G})\cdot\mathbf{r}}, \tag{2.50}$$

where $u_{n\mathbf{k}}(\mathbf{r}) = \frac{1}{\sqrt{\Omega_{UC}}} \sum_{\mathbf{G}} c_{n\mathbf{k}}(\mathbf{G}) e^{i\mathbf{G}\cdot\mathbf{r}}$ *is a periodic function in the unit cell normalized with crystal volume,* Ω_{UC}*, and* $\mathbf{k}$ *chosen to be in the first-Brillouin zone.*[110,111] Bloch's theorem enforces translational invariance such that the translation operator, $\hat{\mathcal{T}}_{\mathbf{R}}$, acting on Equation 2.50, $\hat{\mathcal{T}}_{\mathbf{R}} \Psi_{n\mathbf{k}}(\mathbf{r}) = \Psi_{n\mathbf{k}}(\mathbf{r}+\mathbf{R})$. The effect this has on the Bloch wavefunction is, $\Psi_{n\mathbf{k}}(\mathbf{r}+\mathbf{R}) = \frac{1}{\sqrt{\Omega_{UC}}} \sum_{\mathbf{G}} c_{n\mathbf{k}}(\mathbf{G}) e^{i(\mathbf{k}+\mathbf{G})\cdot(\mathbf{r}+\mathbf{R})} = e^{i\mathbf{k}\cdot\mathbf{R}} \Psi_{n\mathbf{k}}(\mathbf{r})$, where it is required under PBC's that $e^{i\mathbf{G}\cdot\mathbf{R}} = 1(\forall\mathbf{R})$. Hence, $\hat{\mathcal{T}}_{\mathbf{R}} = e^{i\mathbf{k}\cdot\mathbf{R}}$. Moreover, $\hat{\mathcal{T}}_{\mathbf{R}}$ commutes with the electronic Hamiltonian, hence $\hat{\mathcal{T}}_{\mathbf{R}}$ is a simultaneous solution to the electronic Schrödinger equation.[111] Thus, it is clear that any periodic function can be expanded in a plane wave basis, which is the Fourier transform of the real-space function to a frequency space function. Or, in other words, in crystalline solids the crystal wavefunctions are modulated by a periodic function of the crystal.[109,112] Hence, the other terms that enter into the Kohn-Sham equations can be expressed in their Fourier expansions via Equation 2.50.

The Fourier expansion of the Kohn-Sham wavefunction serve as an excellent approach of representing crystal wavefunctions since the periodicity or translational

symmetry is embedded within the summation over reciprocal lattice translation vectors, Equation 2.50. In fact the electron density can be written as a Fourier transform,

$$n(\mathbf{r}) = \frac{1}{\Omega}\sum_{n}\int_{\Omega_{BZ}} f_{n\mathbf{k}} \sum_{\mathbf{G}\mathbf{G}'} c^{*}_{n\mathbf{k}}(\mathbf{G}')c_{n\mathbf{k}}(\mathbf{G})e^{i(\mathbf{k}+\mathbf{G})\cdot\mathbf{r}}d^3k \tag{2.51}$$

$$= \sum_{\mathbf{G}} n(\mathbf{G})e^{i\mathbf{G}\cdot\mathbf{r}}, \tag{2.52}$$

here the integration is over k-space of the first-Brillouin zone, and $f_{n\mathbf{k}}$ are the occupations for band index, n and wavevector, $\mathbf{k}$. The Kohn-Sham equations can be rewritten in a Fourier form as well by substituting Equation 2.50 into Equation 2.34 and projecting $\langle \mathbf{k} + \mathbf{G}_{\mathbf{m}'}|$ yields,

$$\Big(\frac{\hbar^2}{2m}|\mathbf{k}+\mathbf{G}_{\mathbf{m}}|^2\delta_{\mathbf{G}_{\mathbf{m}}\mathbf{G}_{\mathbf{m}'}} + V_{KS}(\mathbf{G}_{\mathbf{m}}-\mathbf{G}_{\mathbf{m}'})\Big)c_{n\mathbf{k}}(\mathbf{G}_{\mathbf{m}'}) = \epsilon_{n\mathbf{k}}c_{n\mathbf{k}}(\mathbf{G}_{\mathbf{m}}). \tag{2.53}$$

This is the well-known Fourier Schrödinger equation of the real-space representation of the Kohn-Sham equations of Equation 2.34.[2] In Equation 2.53 we demand that the plane-wave expansion be orthogonal over the unit cell volume, $\langle \mathbf{q}'|\mathbf{q}\rangle = \delta_{\mathbf{G}_{\mathbf{m}}\mathbf{G}_{\mathbf{m}'}}$ (here $m = (m_1, m_2, m_3) \in \mathbb{Z}^3$ given above for reciprocal lattice vectors). Moreover, the effective Kohn-Sham potential is Fourier expanded, $V_{KS}(\mathbf{G}_{\mathbf{m}} - \mathbf{G}_{\mathbf{m}'}) = \int_{\Omega} d^3\mathbf{r} V_{KS}(\mathbf{r})e^{i(\mathbf{G}_{\mathbf{m}'}-\mathbf{G}_{\mathbf{m}})\cdot\mathbf{r}}$, where the Kohn-Sham potential energy, $V_{KS}(\mathbf{r})$, is given in Equation 2.35. The solution to Equation 2.53 permits understanding of material properties and forms the basis of band theory reformulated in DFT. Hence, this expression forms the basis of all predictions made in subsequent chapters, allowing for the broad study of ultrathin films, see Chapters 3-7, Figure 2.7(d) and Figure 2.8. However, the use of plane-waves to describe highly oscillatory radial wavefunctions near the nucleus of an atom (core Bohr orbits) is prohibitively expensive. In order to circumvent this deleterious circumstance, decomposing an atom into core and valence

wavefunctions provides a suitable point to reduce the need of accounting for rapid oscillations in the wavefunctions near the nucleus of the atom. This inherent limitation in plane-wave basis sets was remedied with the use of the projector augmented wave method (PAW).[113]

2.2.5 Projector-Augmented Wave Method (PAW)

The intractability of employing plane-wave basis sets for the expansion of wavefunctions can be redressed by decomposing the atom into core and valence electrons.[113] The PAW method achieves this by realizing that within in an element inner Bohr orbits are well localized because, while in higher energy bound states of the atom, within a crystal, can become delocalized to form bands of states, Figure 2.8. This process of decomposing the atoms into core and valence electrons is commonly referred to as pseudization, and has proven effective in computing quantum properties in many different environments for a given pseudized element of the periodic table.[37] It is important to emphasize the PAW method originated after other approximations made in this spirit were established, such as, ultrasoft pseudopotentials, norm-conserving pseudopotentials, etc.[2,37]

The PAW method, as mentioned above, can be formed by finding an operator that pseudizes the all-electron (AE) wavefunction into core and valence moments or channels such that,

$$|\Psi_m\rangle = \mathfrak{T}|\tilde{\Psi}_m\rangle.^{113} \tag{2.54}$$

We employ a general composite indice $m = (n', l, m_l, \mathbf{k}, n, \sigma)$, which are defined throughout this chapter, $|\tilde{\Psi}_n\rangle$ is a pseudowavefunction for valence states, and $\mathfrak{T}$ is an unknown operator that connects the all-electron wavefunction to the pseudized wavefunction.[2,37,113] It is important to note that the operation of Equation 2.54 is tantamount to transforming between all-electron and pseudized spaces similar to transforming from Heizenberg and Schrödinger pictures in quantum mechanics.[113]

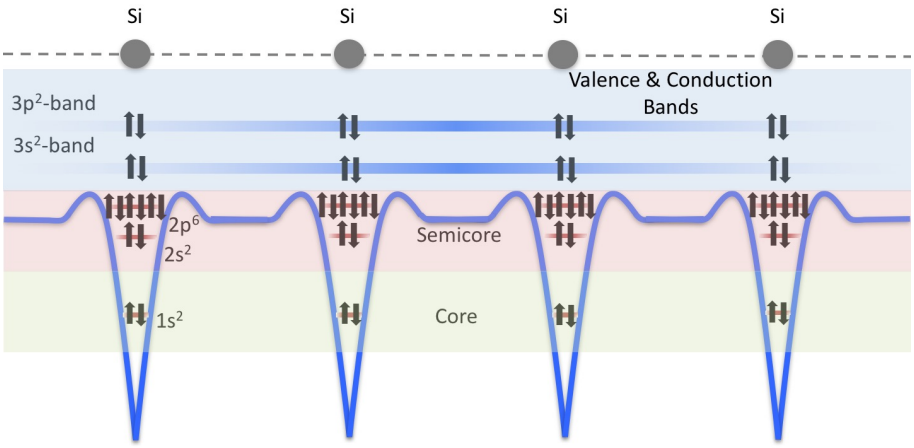

Figure 2.8. Cartoon of the periodic potential resulting from the crystal translational symmetry of silicon atoms. The arrangement of nuclei into a repeating pattern results in the formation of core, semicore, and valence states. The extent of localization of core and semicore states ensures that their interaction is weak, and the importance of their inclusion into the pseudopotential is less relevant. The envelope (valence) states can couple across many atoms leading to the formation of bands as a function of crystallographic translational symmetry. Plane wave basis set is an appropriate basis to expand wavefunctions within crystals.

The transformation can be constructed by setting a cutoff radius for an atom, r_c^a, for those Bohr orbits or atomic quantum states that fall within this distance, Figure 2.8 and Figure 2.9. However, it is critical that the functions within the augmentation spheres, pseudo-onsite (auxiliary) partial waves, $|\tilde{\phi}_m^a\rangle$, and all-electron onsite partial-waves, $|\phi_m^a\rangle$, be *smoothly* mapped onto the all-electron wavefunctions to ensure accurate characterization of the envelope states, which are relevant to chemical bonding and material properties.[37] The onsite wavefunctions and $\mathfrak{T}$ are objects within the augmentation spheres of the atoms, and contain the more rapid terms in the all-electron wavefunctions.[2,37,113] The $\mathfrak{T}$ is an atom-centered transformation which is written in the form,

$$\mathfrak{T} = 1 + \sum_a \mathfrak{T}^a, \tag{2.55}$$

which transforms the all-electron wavefunction within r_c^a such that the augmentation spheres among elements do not overlap.[113] The augmentation spheres are expanded in terms of the auxiliary partial waves and onsite partial waves, $|\phi_m^a\rangle = (1+\mathfrak{T}^a)|\tilde{\phi}_m^a\rangle$, such that, $\mathfrak{T}^a|\tilde{\phi}_m^a\rangle = |\phi_m^a\rangle - |\tilde{\phi}_m^a\rangle$ for all m and a. Since $\mathfrak{T}^a$ does not operate outside the cutoff radius, then for $r > r_c^a$ $|\phi_m^a\rangle = |\tilde{\phi}_m^a\rangle$, which will insure that pseudo onsite partial waves smoothly map onto the all-electron partial waves.[113] The smooth pseudo-onsite partial waves form a complete set within the augmentation spheres, hence the pseudo wavefunctions can be expanded with them as a basis,

$$|\tilde{\Psi}_m\rangle = \sum_i P_{mi}^a |\tilde{\phi}_i^a\rangle, \tag{2.56}$$

where the P_{mi}^a are undetermined functions to be defined below, and the expansion is within the cutoff radius. Because $|\phi_m^a\rangle = \mathfrak{T}^a|\tilde{\phi}_m^a\rangle$, then within the augmentation spheres,

$$\begin{aligned} |\Psi_m\rangle &= \mathfrak{T}|\tilde{\Psi}_m\rangle \\ &= \sum_i P_{mi}^a |\phi_i^a\rangle. \end{aligned} \tag{2.57}$$

Since $\mathfrak{T}$ is a linear operator, then P_{mi}^a is a linear function of $|\tilde{\Psi}_m\rangle$, hence

$$\begin{aligned} P_{mi}^a &= \langle \tilde{p}_i^a | \Psi_m \rangle \\ &= \int d^3\mathbf{r} \tilde{p}_i^a(\mathbf{r} - \mathbf{R}^{\mathbf{a}}) \tilde{\Psi}_m(\mathbf{r}), \end{aligned} \tag{2.58}$$

which are fixed functions within the augmentation spheres commonly referred to as projector functions.[113] The projector functions form a complete set within the augmentation spheres, hence $\sum_i |\tilde{\phi}_i^a\rangle\langle\tilde{p}_i^a| = 1$. Furthermore, the projector functions must be orthogonal within each augmentation sphere, $\langle \tilde{p}_i^a | \tilde{\phi}_j^a \rangle = \delta_{ij}$.[113] Using the results thus far the onsite transformation operator can be written, $\mathfrak{T}^a = \sum_i |\tilde{\phi}_i^a\rangle\langle\tilde{p}_i^a| =$

$\sum_i(|\phi_i^a\rangle - |\tilde{\phi}_i^a\rangle)\langle\tilde{p}_i^a|$. Therefore, the transformation operator has the complete form, $\mathfrak{T} = 1 + \sum_a \sum_i(|\phi_i^a\rangle - |\tilde{\phi}_i^a\rangle)\langle\tilde{p}_i^a|$.[113] Introducing the transformation operator to Equation 2.54 yields the needed transformation between the all-electron wavefunction to a pseudized wavefunction for the valence electrons,

$$|\Psi_m\rangle = |\tilde{\Psi}_m\rangle + \sum_a \sum_i (|\phi_i^a\rangle - |\tilde{\phi}_i^a\rangle)\langle\tilde{p}_i^a|\tilde{\Psi}_m\rangle. \tag{2.59}$$

This expression rewrites the all-electron wavefunction into a form that separates the core electron wavefunctions and highly oscillatory terms within the augmentation spheres from the smooth portions of valence electrons that are typically many Bohr radii away from the nucleus of an element. Thus, to carryout the transformation we need three terms: the onsite partial waves, the smooth pseudo partial waves, and the smooth projector functions. Furthermore, it is important to note that the pseudo-wavefunctions are expanded in a plane wave basis which use a plane wave grid (Equation 2.48), whereas the onsite terms or quantities defined within the augmentation spheres are determined on radial grids. Because of this algorithmic separation between these quantities the pair-wise interactions will have to be compensated to enable a separation of each quantity in the final expressions, for instance the Hartree energy.[114] This transformation of the all-electron wavefunctions into pseudized wavefunctions must be applied to all subsequent operators to generate pseudo-operators within in PAW.

The linear Hermitian operators or observables computed within the PAW method must be pseudized applying Equation 2.59 to the general expectation operator of local operators which yield (after manipulations),

$$\langle\mathcal{O}\rangle = \sum_m^{val} f_m \langle\tilde{\Psi}_m|\mathcal{O}|\tilde{\Psi}_m\rangle + \sum_a \sum_{ij} \left(\langle\phi_i^a|\mathcal{O}|\phi_j^a\rangle - \langle\tilde{\phi}_i^a|\mathcal{O}|\tilde{\phi}_j^a\rangle\right)\rho_{ij}^a + \sum_a \sum_\alpha^{core} \langle\phi_\alpha^{a,core}|\mathcal{O}|\phi_\alpha^{a,core}\rangle, \tag{2.60}$$

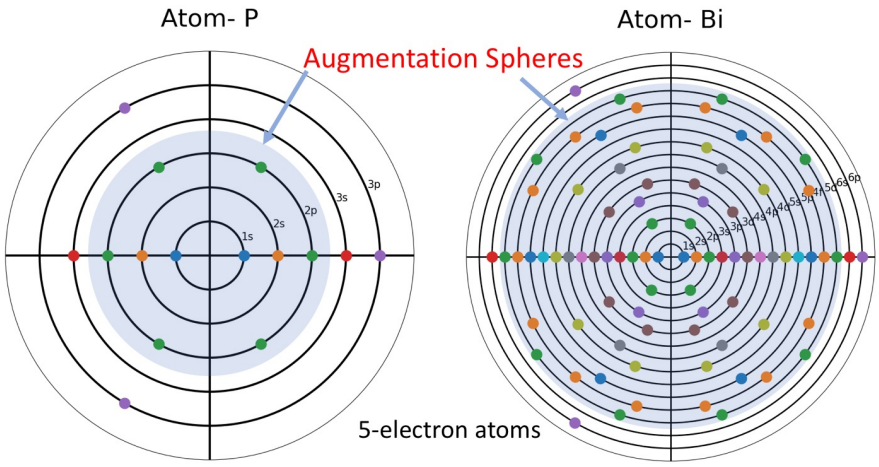

Figure 2.9. Pseudized atoms of (a) phosphorus and (b) bismuth. The lighter blues highlights the augmentation regions of each element to be frozen and subsequently subtracted from the all-electron wavefunction. Both elements account for five electrons to be computed in the Kohn-Sham equations.

where the $\rho^a_{ij} = \sum_m f_m \langle \tilde{\Psi}_m | \tilde{p}^a_i \rangle \langle \tilde{p}^a_j | \tilde{\Psi}_m \rangle$ is a one-center density matrix, and we have added the frozen core electrons that are always present. Such general operators can be applied to reveal the PAW or simply pseudo operators that are solved self-consistently within DFT. For instance, the pseudo-density becomes,

$$n(\mathbf{r}) = \sum_m^{val} |\tilde{\Psi}_m(\mathbf{r})|^2 + \sum_a \sum_{ij} \left(\phi^a_i(\mathbf{r}) \phi^a_j(\mathbf{r}) - \tilde{\phi}^a_i(\mathbf{r}) \tilde{\phi}^a_j(\mathbf{r}) \right) \rho^a_{ij} + \sum_a \sum_\alpha^{core} |\phi^{a,core}_\alpha|^2 \tag{2.61}$$

$$= \tilde{n}(\mathbf{r}) + \sum_a (n^a(\mathbf{r}) - \tilde{n}^a(\mathbf{r})), \tag{2.62}$$

which shows that three terms contribute to the PAW-electron density: the pseudo-density, the onsite all-electron partial density, and the onsite pseudo-partial density. In fact, as we shall see, all operators reduce to this pattern shown for the pseudized electron density, Equation 2.61. Therefore, the noninteracting Kohn-Sham kinetic

energy has the following form, using Equation 2.60,

$$T_S[n] = \sum_m^{val} f_m \langle \tilde{\Psi}_m | - \frac{\hbar^2}{2m_e}\nabla^2 | \tilde{\Psi}_m \rangle$$
$$+ \sum_a \sum_{ij} \Big(\langle \phi_i^a | - \frac{\hbar^2}{2m_e}\nabla^2 | \phi_j^a \rangle - \langle \tilde{\phi}_i^a | - \frac{\hbar^2}{2m_e}\nabla^2 | \tilde{\phi}_j^a \rangle \Big) \rho_{ij}^a + \sum_a \sum_\alpha^{core} \langle \phi_\alpha^{a,core} | - \frac{\hbar^2}{2m_e}\nabla^2 | \phi_\alpha^{a,core} \rangle \tag{2.63}$$

$$= T_S[\tilde{n}] + T_S[n^a] - T_S[\tilde{n}^a], \tag{2.64}$$

which is expected.[113,114] Furthermore, the exchange-correlation energy per particle bears a similar resemblance,

$$E_{XC}[n] = E_{XC}[\tilde{n}] + E_{XC}[n^a] - E_{XC}[\tilde{n}^a], \tag{2.65}$$

where the pseudized exchange-correlation energy obeys Equation 2.60, and varies depending on the level of approximation, i.e., LDA, GGA, etc. In the case of the Hartree energy care must be taken in pseudizing this term in the electronic Hamiltonian. In the case of the Hartree energy, this term is nonlocal and introducing Equation 2.61 into Equation 2.16 ($U_H[n]$),

$$U_H[n] = \frac{1}{2}(n)(n) \tag{2.66}$$
$$= \frac{1}{2}(\tilde{n})(\tilde{n}) + (n^a - \tilde{n}^a)(\tilde{n}) + \frac{1}{2}(n^a - \tilde{n}^a)(n^a - \tilde{n}^a), \tag{2.67}$$

where the first and third terms are expanded on a plane wave grid and radial grid, respectively. Here the shorthand $(a)(b) = \int d^3\mathbf{r} d^3\mathbf{r}' \frac{a(\mathbf{r})b(\mathbf{r}')}{|\mathbf{r}-\mathbf{r}'|}$ is used. However, the second term contains mixed terms that are expanded on two distinctly different numerical grids. This circumstance is assumed to be avoided by replacing $\tilde{n}$ with $\tilde{n}^a$, where the pseudo charge density is approximated with its onsite pseudo-charge density.[114] From this assumption, which relies on the projector functions to form a complete

basis within the augmentation spheres, the Hartree energy decomposes into,

$$U_H[n] = \frac{1}{2}(\tilde{n})(\tilde{n}) + \frac{1}{2}(n^a)(n^a) - \frac{1}{2}(\tilde{n}^a)(\tilde{n}^a), \tag{2.68}$$

which is the needed decomposition obeying Equation 2.60.[114] This form of $U_H[n]$ is referred to as the Kresse-Joubert approximation to the Hartree energy, however it is the same as that used by Blöchl.[113,114] In order to derive the pseudized Hamiltonian, $\tilde{H}$, it is necessary to include the more baroque expressions that have been obscured until now, for simplicity.

The pseudized Hamiltonian can be determined by variation over the pseudized density matrices, $\tilde{\rho} = \sum_m |\tilde{\Psi}_m\rangle\langle\tilde{\Psi}_m|$,

$$\frac{\partial E}{\partial \tilde{\rho}} = \hat{H}. \tag{2.69}$$

The density matrix enters into the above expressions for the one-center density matrices, ρ^a_{ij}, all-electron onsite charge density, pseudo-onsite charge density, and the compensation charge. The compensation charge, $\hat{n}$, is included into each term to ensure that $\tilde{n}^a + \hat{n}$ has the same multipole moments as the all-electron charge density, n^a inside the augmentation region.[114] The compensation charge is defined to be a sum of one center terms, $\hat{n} = \sum_{ij}\sum_L \rho^a_{ij}\hat{Q}^L_{ij}(\mathbf{r})$, where $\hat{Q}^L_{ij}(\mathbf{r}) = q^L_{ij} g_l(|\mathbf{r}-\mathbf{R}|)Y_L(\mathbf{r}-\mathbf{R})$. Here $L = (l, m)$ is the angular momentum indices and $g_l(|\mathbf{r}-\mathbf{R}|)$ are site-dependent compensation functions expanded in spherical Bessel functions that ensure agreement within the augmentation spheres between the all-electron and pseudo-charge densities.[114] In this form, Kresse et al., gaurantees smooth mapping between the augmentation spheres and the (pseudized) valence wavefunctions.[114] It is now possible to determine the pseudo-Kohn-Sham ground state energy, pseudized Hamiltonian, and eigenvalue equation beginning with Equation 2.69.

The total energy is split into three terms, as expected, $E = \tilde{E} + E^a - \tilde{E}^a$, where the first is the pseudo-energy,

$$\tilde{E} = \sum_m f_m \langle \tilde{\Psi}_m | - \frac{\hbar^2}{2m_e} \nabla^2 | \tilde{\Psi}_m \rangle + E_H[\tilde{n} + \hat{n}] + \int d^3\mathbf{r} v_H[\tilde{n}_{Zc}][\tilde{n}(\mathbf{r}) + \hat{n}(\mathbf{r})] + U(\mathbf{R}, Z_{ion}), \tag{2.70}$$

which contains the frozen core all-electron charge density and point charge density of the nuclei, $n_{Zc} = n_c + n_Z$, respectively.[114] Here $U(\mathbf{R}, Z_{ion})$ is the nuclear-nuclear energy, or $\mathcal{V}_{II}$ for a given atomic number Z_{ion}. The second term is the onsite all electron energy,

$$E^a = \sum_{ij} \rho^a_{ij} \langle \phi^a_i | - \frac{\hbar}{2m_e} \nabla^2 | \phi^a_j \rangle + E_H[n^a] + \int d^3\mathbf{r} v_H[n_{Zc}] n^a(\mathbf{r}) + E_{XC}[n^a + n_c], \tag{2.71}$$

and the final term is the pseudo-onsite energy,

$$\tilde{E}^a = \sum_{ij} \rho^a_{ij} \langle \tilde{\phi}^a_i | - \frac{\hbar}{2m_e} \nabla^2 | \tilde{\phi}^a_j \rangle + E_H[\tilde{n}^a + \hat{n}] + \int d^3\mathbf{r} v_H[\tilde{n}_{Zc}][\tilde{n}^a(\mathbf{r}) + \hat{n}(\mathbf{r})] + E_{XC}[\tilde{n}^a + \hat{n}], \tag{2.72}$$

which completes the total pseudized energy.[114] In order to determine the pseudized Hamiltonian we employ Equation 2.69 and treat each Equation (2.70)-(2.72) separately which has the formal general expression,

$$\frac{dE}{d\tilde{\rho}} = \frac{\partial E}{\partial \tilde{\rho}} + \int d^3\mathbf{r} \frac{\delta E}{\delta \tilde{n}(\mathbf{r})} \frac{\partial \tilde{n}(\mathbf{r})}{\partial \tilde{\rho}} + \sum_{ij} \frac{\partial E}{\partial \rho_{ij}} \frac{\rho_{ij}}{\partial \tilde{\rho}}.^{114} \tag{2.73}$$

The total derivative of the ground state energy must be applied to all contributions to the total energy above, which yields the pseudo-Hamiltonian that is solved in subsequent chapters. Applying Equation 2.73 to Equation 2.70 yields,

$$\frac{\partial \tilde{E}}{\partial \tilde{\rho}} = -\frac{\hbar}{2m_e} \nabla^2 + \tilde{v}_{eff}(\mathbf{r}) + \sum_L \int d^3\mathbf{r} \tilde{v}_{eff}(\mathbf{r}) \hat{Q}^L_{ij}(\mathbf{r}).^{114} \tag{2.74}$$

Continuing to the subsequent contributions only the one-center density matrices have a dependence on the pseudo-density matrices and the compensation charges, thus,

$$D^a_{ij} = \frac{\partial E^a}{\partial \tilde{\rho}} = \langle \phi^a_i | - \frac{\hbar}{2m_e}\nabla^2 + v^a_{eff}(\mathbf{r}) | \phi^a_j \rangle, \tag{2.75}$$

and the pseudo-onsite energy takes the form,

$$\tilde{D}^a_{ij} = \frac{\partial \tilde{E}^a}{\partial \tilde{\rho}} = \langle \tilde{\phi}^a_i | - \frac{\hbar}{2m_e}\nabla^2 + v_{eff}(\mathbf{r}) | \tilde{\phi}^a_j \rangle + \sum_L \int d^3\mathbf{r} \tilde{v}^a_{eff}(\mathbf{r}) \hat{Q}^L_{ij}(\mathbf{r}).^{114} \tag{2.76}$$

Combining Equations (2.74)-(2.76) results in the pseudized Hamiltonian,

$$\hat{H} = -\frac{\hbar^2}{2m_e}\nabla^2 + \tilde{v}_{eff}(\mathbf{r}) + \sum_{ij} |\tilde{p}^a_i\rangle (\hat{D}_{ij} + D^a_{ij} - \tilde{D}^a_{ij}) \langle \tilde{p}^a_j |, \tag{2.77}$$

which has an elegant form.[114] The $\hat{D}_{ij}$ term is an interaction between the compensation charge accompanied with an electron with the effective one-electron potential energy, while the last two terms D^a_{ij} and $\tilde{D}^a_{ij}$ are onsite terms that contain rapid variations not present in the pseudo-effective potential, $\tilde{v}_{eff}(\mathbf{r})$, and pseudo-wavefunction, $|\tilde{\Psi}_m\rangle$.[114] This Hamiltonian is solved within the eigenvalue expression,

$$\mathfrak{T}^\dagger \hat{H} \mathfrak{T} |\tilde{\Psi}_m\rangle = \epsilon_m \mathfrak{T}^\dagger \mathfrak{T} |\tilde{\Psi}_m\rangle, \tag{2.78}$$

which is the well-known eigen-equation for electronic structure theory.[113] The left side contains the pseudized Hamiltonian which is a similarity transform from all-electron space to pseudo-space for a given element, and the term, $\mathfrak{T}^\dagger\mathfrak{T}$, is the overlap operator, $\tilde{S} = \mathfrak{T}^\dagger\mathfrak{T} = 1 + \sum_{ij} |\tilde{p}^a_j\rangle (\langle \phi^a_i | \phi^a_j \rangle - \langle \tilde{\phi}^a_i | \tilde{\phi}^a_j \rangle) \langle \tilde{p}^a_j |$.[113,114] Hence, the general pseudo-eigenvalue equation takes the form, $\tilde{H}|\tilde{\Psi}_m\rangle = \epsilon_m \tilde{S} |\tilde{\Psi}_m\rangle$. This form of the pseudo-eigenvalue effective Schrödinger equation resembles the original form of the expression, Equation 2.34. The final form of the PAW eigen-equation is the basis

of predictions made herein; furthermore, this formulation is computationally fast and remedies the shortcomings of employing a plane-wave basis that is needed for crystalline structures, such as ultrathin films, by reducing the explicit inclusion of all Bohr orbits (lower core-electrons) to just the valence states involved in chemical activity, Figure 2.8 and Figure 2.9.

2.3 Excited-State Density Functional Theory

Density functional theory can be extended to include temporal phenomena such as Born-Oppenheimer dynamics, or excited state transitions within the PAW framework. Excited state phenomena provide salient spectroscopic signatures of a given material, or fingerprint for characterizing the optical response of a crystalline material. In the study of ultrathin films an interesting physical scenario arises, where one crystallographic direction is significantly smaller, which is the thickness of an atom in the most extreme, i.e., graphene. The optical response of a material when exposed to light is shown in Figure 2.10. In the first panel, an insulator with band gap energy separates occupied and unoccupied states within the crystal. Typically, in this work especially, the Fermi energy, ϵ_F, is taken to be zero (dotted green line Figure 2.10). In order to induce a transition across the energy gap it is necessary to provide a photon equivalent or greater than the bandgap. The second panel displays the photoexcitation event leading to the excitation of a single electron into the conduction states (unoccupied), or absorption. The third panel displays what can commonly occur in crystalline systems, which is the formation of a bound electron-hole pair or exciton. Depending on the chemical bonding of the crystal, the type of exciton can be localized (Frenkel) or delocalized (Wannier-Mott).[2,115] Moreover, the final panel shows the relaxation back to the valence states recombining radiatively (or nonradiatively) with the hole which forms after photoabsorption, Figure 2.10. Therefore, the type of excitations we will capture, see Chapter 6, are neutral excitations involving exciton generation. This type of optical response of a crystalline system

can be described within linear response theory, which is elaborated below within time-dependent density functional theory (TDDFT). In this section we develop some critical components to the understanding of the optical response of crystalline systems such as ultrathin films. And we extend notions of TDDFT to the computing of the intrinsic optical response of ultrathin films such as the dielectric response. As we shall see, the dielectric response characterizes the interaction of electric fields within matter.

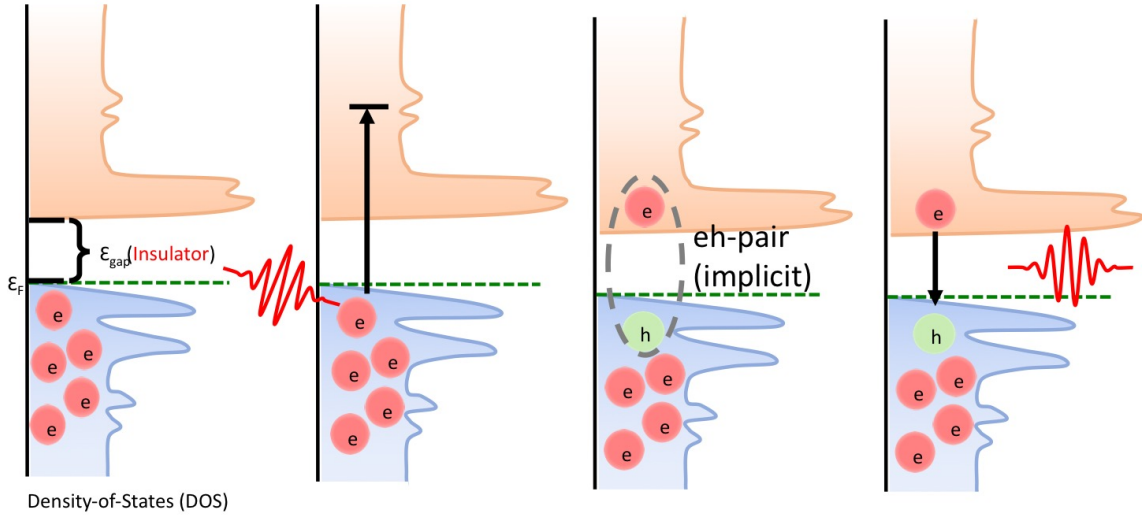

Figure 2.10. Excitation within a crystalline system (insulating), such as a semiconducting ultrathin film. (left-to-right) The excitation process occurs via photon source and absorption from valence band electrons, where if the photon energy is in excess of the bandgap, the formation of conduction band electrons and a hole (single excitation) can occur (exciton = eh-pair), and finally radiative (or nonradiative) relaxation back to the valence band annihilating the electron-hole pair. Note that the eh-pair within TDDFT is implicitly constructed, where only excited state and ground state wavefunctions are mixed within the formalism.

2.3.1 *Time-dependent DFT*

In TDDFT, just as in DFT, we map the temporal wavefunction onto an effective potential with,

$$i\hbar\frac{\partial\Psi(\mathbf{r},t)}{\partial t} = \hat{H}\Psi(\mathbf{r},t), \tag{2.79}$$

which is the time-dependent Schrödinger equation.[2] The TDDFT formulation was highlighted by the Runge-Gross theorems (1984), which, like in static DFT, a bijective mapping exists between the time-dependent density $n(\mathbf{r},t)$ and the time-dependent external potential $v_{ext}(\mathbf{r},t)$.[116] The time-dependent Kohn-Sham expression of Equation 2.79 has the following form,

$$i\hbar\frac{\partial\Psi_m(\mathbf{r},t)}{\partial t} = \Big[-\frac{\hbar^2}{2m_e}\nabla^2 + v_{eff}[n](\mathbf{r},t)\Big]\Psi_m(\mathbf{r},t), \tag{2.80}$$

where the effective Kohn-Sham potential energy is the well-known $v_{eff}[n](\mathbf{r},t) = v_{ext}(\mathbf{r},t) + v_H[n](\mathbf{r},t) + v_{XC}[n](\mathbf{r},t)$. The first term is the external potential energy between electrons and nuclei, the second term is the time-dependent Hartree potential, $v_H[n](\mathbf{r},t) = \frac{e^2}{4\pi\epsilon_0}\int d^3\mathbf{r}'\frac{n(\mathbf{r}',t)}{|\mathbf{r}-\mathbf{r}'|}$, and the exchange-correlation energy discussed above. With this expression we can formulate the linear response of a system to an external perturbation.

Linear response is appropriate for external fields whose field strength does not exceed the internal electric field of the nuclei, common in spectroscopy, which permits a perturbative treatment of the induced density. In linear response theory, the optical susceptibility, $\chi(\mathbf{r},\mathbf{r}',t-t')$, is critical in the description of the induced density, $\delta n(\mathbf{r},t)$, if the external potential changes at $\delta v_{ext}(\mathbf{r}',t')$,

$$\delta n(\mathbf{r},t) = \int dt' \int d^3\mathbf{r}'\chi(\mathbf{r},\mathbf{r}',t-t')\delta v_{ext}(\mathbf{r}',t'), \tag{2.81}$$

where the optical susceptibility is $\chi(\mathbf{r},\mathbf{r}',t-t') = \delta n(\mathbf{r},t)/\delta v_{ext}(\mathbf{r}',t')$.[2,117,118] However, we will establish a link between the exact case (Equation 2.81) with the Kohn-Sham formalism. In this case, we expect the Kohn-Sham response function, $\chi_{KS}(\mathbf{r},\mathbf{r}',t-t')$, to have the same formulation,

$$\delta n(\mathbf{r},t) = \int dt' \int d^3\mathbf{r}' \chi_{KS}(\mathbf{r},\mathbf{r}',t-t')\delta v_{eff}(\mathbf{r}',t'), \tag{2.82}$$

where, in a similar fashion, the Kohn-Sham optical susceptibility $\chi_{KS}(\mathbf{r},\mathbf{r}',t-t') = \delta n(\mathbf{r},t)/\delta v_{eff}(\mathbf{r}',t')$. In the case of the exchange-correlation energy per particle within linear response,

$$v_{XC}[n+\delta n](\mathbf{r},t) = v_{XC}[n](\mathbf{r},t) + \int d^3\mathbf{r} f_{XC}[n](\mathbf{r},\mathbf{r}',t-t')\delta n(\mathbf{r}',t'), \tag{2.83}$$

where the exchange-correlation kernel is defined as $f_{XC}(\mathbf{r},\mathbf{r}',t-t') = \delta v_{XC}(\mathbf{r},t)/\delta n(\mathbf{r}',t')$, which is evaluated for the ground-state density, $n(\mathbf{r})$. In order to link Equation 2.81 and Equation 2.82, we recognize that the density response is the same in both expressions, hence,

$$\begin{aligned}\int dt' \int d^3\mathbf{r}' \chi(\mathbf{r},\mathbf{r}',t-t')\delta v_{ext}(\mathbf{r}',t') \\ = \int dt' \int d^3\mathbf{r}' \chi_{KS}(\mathbf{r},\mathbf{r}',t-t')\delta v_{ext}(\mathbf{r}',t') + \delta v_H[n]\mathbf{r}',t' + \delta v_{XC}[n](\mathbf{r}',t'),\end{aligned} \tag{2.84}$$

where this expression can be expanded for each potential energy using the functional derivatives of the optical susceptibilities mentioned above,

$$\delta v_H[n](\mathbf{r}',t') = \int\int dt_1 dt_2 \int\int d^3\mathbf{r}_1 d^3\mathbf{r}_2 \frac{\delta v_H[n](\mathbf{r}',t')}{\delta n(\mathbf{r_1},t_1)} \frac{\delta n(\mathbf{r}_1,t_1)}{\delta v_{ext}(\mathbf{r}_2,t_2)} \delta v_{ext}(\mathbf{r}_2,t_2)$$
$$= \int\int dt_1 dt_2 \int\int d^3\mathbf{r}_1 d^3\mathbf{r}_2 \frac{e^2}{4\pi\epsilon_0} \frac{1}{|\mathbf{r}_1 - \mathbf{r}'|} \chi(\mathbf{r}_1,\mathbf{r}_2,t_1-t_2)\delta v_{ext}(\mathbf{r}_2,t_2), \quad (2.85)$$
$$\delta v_{XC}[n](\mathbf{r}',t') = \int\int dt_1 dt_2 \int\int d^3\mathbf{r}_1 d^3\mathbf{r}_2 \frac{\delta v_{XC}[n](\mathbf{r}',t')}{\delta n(\mathbf{r_1},t_1)} \frac{\delta n(\mathbf{r}_1,t_1)}{\delta v_{ext}(\mathbf{r}_2,t_2)} \delta v_{ext}(\mathbf{r}_2,t_2)$$
$$= \int\int dt_1 dt_2 \int\int d^3\mathbf{r}_1 d^3\mathbf{r}_2 f_{XC}(\mathbf{r},\mathbf{r}',t'-t)\chi(\mathbf{r}_1,\mathbf{r}_2,t_1-t_2)\delta v_{ext}(\mathbf{r}_2,t_2), \quad (2.86)$$

and rewriting these expressions into frequency space yields the optical susceptibility,

$$\chi(\mathbf{r},\mathbf{r}',\omega) = \chi_{KS}(\mathbf{r},\mathbf{r}',\omega)$$
$$+ \int\int d^3\mathbf{r}_1 d^3\mathbf{r}_2 \chi_{KS}(\mathbf{r},\mathbf{r}_1,\omega)\Big(\frac{e^2}{4\pi\epsilon_0}\frac{1}{|\mathbf{r}_1-\mathbf{r}_2|} + f_{XC}[n](\mathbf{r}_1,\mathbf{r}_2,\omega)\Big)\chi(\mathbf{r}_2,\mathbf{r}',\omega). \quad (2.87)$$

This expression for the optical susceptibility is a Dyson equation. In this expression, the optical susceptibility is evaluated by determining the Kohn-Sham optical susceptibility with some approximated exchange-correlation functional. It is common to write Equation 2.88 in a more compact form, $\chi = \chi_{KS} + \chi_{KS}K(\mathbf{r}_1,\mathbf{r}_2)\chi$, where $K(\mathbf{r}_1,\mathbf{r}_2) = \frac{e^2}{4\pi\epsilon_0}\frac{1}{|\mathbf{r}_1-\mathbf{r}_2|} + f_{XC}[n](\mathbf{r}_1,\mathbf{r}_2,\omega)$. For the case of $f_{XC} = 0$, we have the well known random-phase approximation (RPA) or Hartree approximation since no effects of exchange and correlation enter into the Dyson equation (Equation 2.88). However, we must show what the Kohn-Sham optical response function is based on time-dependent perturbation theory.

In order to determine the Kohn-Sham response function we can introduce a time-dependent perturbation , $\delta H(t)$, into the time-dependent Kohn-Sham equation, Equation 2.80,

$$i\hbar\frac{\partial\Psi_m(\mathbf{r},t)}{\partial t} = [\hat{H}_0 + \delta H(t)]\Psi_m(\mathbf{r},t). \quad (2.88)$$

The time-dependent perturbation can be written $\delta H(t) = e^{\eta t} \sum_{i=1}^{N} \delta v(\mathbf{r_i}, t)$, where the exponential ensures an adiabatic switching on of the external perturbation, and $0 < \eta << 1$.[118,119] The frequency space formulation of the time-dependent perturbation can be written in the form,

$$\delta H(t) = \int d^3\mathbf{r} \int \frac{d\omega}{2\pi} e^{-i\breve{\omega}t} \delta v(\mathbf{r}, \omega) \hat{n}(\mathbf{r}), \tag{2.89}$$

where $\breve{\omega} = \hbar\omega + i\eta$, and $\hat{n}(\mathbf{r}) = \sum_{i=1}^{N} \delta(\mathbf{r} - \mathbf{r_i})$ is the density operator.[118,119] Within first-order time-dependent perturbation theory the wavefunction can be written in the form,

$$|\Psi(t)\rangle = e^{-iE_0 t}|\Psi_0\rangle + \sum_{j\neq 0} a_j(t) e^{-iE_j t}|\Psi_j^0\rangle. \tag{2.90}$$

The first term is the principle solution to the unperturbed case, while the second term contains the perturbation on the ground-state wavefunction. The time-dependent coefficients admix excited state contributions to the unperturbed wavefunction and have the following form,

$$\begin{aligned} a_j(t) &= -i \int_{-\infty}^{t} dt' e^{i\breve{\omega}_{0j}t'} \langle \Psi_j^0 | \delta H(t') | \Psi_0 \rangle \\ &= -i \int d^3\mathbf{r}' \int \frac{d\omega}{2\pi} \int_{-\infty}^{t} dt' e^{-i(\omega_{0j} - \breve{\omega})t'} \delta v(\mathbf{r}', \omega) \langle \Psi_j^0 | \hat{n}(\mathbf{r}) | \Psi_0 \rangle \\ &= -\int d^3\mathbf{r}' \int \frac{d\omega}{2\pi} \delta v(\mathbf{r}', \omega) \langle \Psi_j^0 | \hat{n} | \Psi_0 \rangle \frac{e^{i(\omega_{0j} - \breve{\omega})t}}{\omega_{0j} - \breve{\omega}}, \end{aligned} \tag{2.91}$$

where $\omega_{0j} = E_j - E_0$ is the energy difference from the excited state-j and ground state. The induced density is given by the change in the perturbed expectation of the density operator and the ground-state expectation density operator,

$$\delta n(\mathbf{r}, t) = n_{ind}(\mathbf{r}, t) = \langle \Psi(t) | \hat{n} | \Psi(t) \rangle - \langle \Psi_0(t) | \hat{n} | \Psi_0(t) \rangle, \tag{2.92}$$

which when expanded,

$$n_{ind}(\mathbf{r},t) = \sum_{j\neq 0}[a_j(t)\langle\Psi_0|\hat{n}|\Psi_j^0\rangle e^{-i\omega_{0j}t} + a_j^*(t)\langle\Psi_j^0|\hat{n}|\Psi_0\rangle e^{i\omega_{0j}t}]$$
$$= -\int d^3\mathbf{r}' \int \frac{d\omega}{2\pi}\delta v(\mathbf{r},\omega)e^{-i\breve{\omega}t}\sum_{j\neq 0}\Big[\frac{\langle\Psi_j^0|\hat{n}(\mathbf{r}')|\Psi_0\rangle\langle\Psi_0|\hat{n}(\mathbf{r})|\Psi_j^0\rangle}{\omega_{0j}-\breve{\omega}}$$
$$+\frac{\langle\Psi^0|\hat{n}(\mathbf{r}')|\Psi_j^0\rangle\langle\Psi_j^0|\hat{n}(\mathbf{r})|\Psi_0\rangle}{\omega_{0j}+\breve{\omega}}\Big]. \quad (2.93)$$

In frequency space Equation 2.93 becomes,

$$n_{ind}(\mathbf{r},\omega) = -\int d^3\mathbf{r}' e^{-i\breve{\omega}t}\sum_{j\neq 0}\Big[\frac{\langle\Psi_j^0|\hat{n}(\mathbf{r}')|\Psi_0\rangle\langle\Psi_0|\hat{n}(\mathbf{r})|\Psi_j^0\rangle}{\omega_{0j}-\breve{\omega}}$$
$$+\frac{\langle\Psi^0|\hat{n}(\mathbf{r}')|\Psi_j^0\rangle\langle\Psi_j^0|\hat{n}(\mathbf{r})|\Psi_0\rangle}{\omega_{0j}+\breve{\omega}}\Big]\delta v(\mathbf{r},\omega). \quad (2.94)$$

From Equation 2.94, the frequency space induced density can be related to the optical susceptibility by using the the functional derivative of the induced density relative to the change in the potential,

$$\chi(\mathbf{r},\mathbf{r}',\omega) = \frac{\delta n(\mathbf{r},\omega)}{\delta v(\mathbf{r}',\omega)} = -\sum_{j\neq 0}\Big[\frac{\langle\Psi_j^0|\hat{n}(\mathbf{r}')|\Psi_0\rangle\langle\Psi_0|\hat{n}(\mathbf{r})|\Psi_j^0\rangle}{\omega_{0j}-\breve{\omega}}$$
$$+\frac{\langle\Psi^0|\hat{n}(\mathbf{r}')|\Psi_j^0\rangle\langle\Psi_j^0|\hat{n}(\mathbf{r})|\Psi_0\rangle}{\omega_{0j}+\breve{\omega}}\Big]. \quad (2.95)$$

With this general expression we can determine the Kohn-Sham optical susceptibility, but we define the ground ($|\Psi_0\rangle$) and excited state ($|\Psi_j^0\rangle$) wavefunctions to rewrite the numerators of Equation 2.95. The ground state fermion wavefunction must be a product of antisymmetric spin-orbitals or a Slater determinant. If we write the ground state wavefunction in this form, then,

$$\Psi_0(\mathbf{r}_1,...,r_{N/2}) = \psi_1(\mathbf{r}_1)\psi_2(\mathbf{r}_2)...\psi_n(\mathbf{r}_i)...\psi_{N/2}(\mathbf{r}_{N/2}), \quad (2.96)$$

where the wavefunctions $\psi_1(\mathbf{r}_1), ..., \psi_{N/2}(\mathbf{r}_{N/2})$ are the lowest filled states forming the ground-state solution to the static Kohn-Sham equations. For single excitations, the excited state wavefunction can be formed creating an electron in a higher energy state and destroying an electron in the ground state,

$$\Psi_j^0(\mathbf{r}_1, ..., r_{N/2}) = \psi_1(\mathbf{r}_1)\psi_2(\mathbf{r}_2)...\psi_m(\mathbf{r}_i)...\psi_{N/2}(\mathbf{r}_{N/2}), \tag{2.97}$$

where the mth-electron is greater than the highest ground state wavefunction. The matrix elements of the numerator can be understood by expanding the electron particle number, $\hat{n}$, and using the shifting property of Dirac delta functions, i.e., $\langle\psi_1(\mathbf{r}_1)\psi_2(\mathbf{r}_2)...\psi_n(\mathbf{r}_i)...\psi_{N/2}(\mathbf{r}_{N/2})|\delta(\mathbf{r}-\mathbf{r}_k)|\psi_1(\mathbf{r}_1)\psi_2(\mathbf{r}_2)...\psi_n(\mathbf{r}_i)...\psi_{N/2}(\mathbf{r}_{N/2})\rangle$, and summing over k, reduces to $\psi_n^*(\mathbf{r})\psi_m(\mathbf{r})$, which is just a product of the one-particle ground state wavefunction and one-particle excited state wavefunction. This allows for the independent density-density response function to be written in the form,

$$\chi_{KS}(\mathbf{r}, \mathbf{r}', \omega) = -\sum_n \sum_m 2f_n(1-f_m)\Big(\frac{\psi_m^*(\mathbf{r}')\psi_n(\mathbf{r}')\psi_n^*(\mathbf{r})\psi_m(\mathbf{r})}{\epsilon_m - \epsilon_n - \breve{\omega}} + \frac{\psi_n^*(\mathbf{r}')\psi_m(\mathbf{r}')\psi_m^*(\mathbf{r})\psi_n(\mathbf{r})}{\epsilon_m - \epsilon_n + \breve{\omega}}\Big). \tag{2.98}$$

The summation over occupied and unoccupied states is accompanied with the occupancies f_n and $1 - f_m$, respectively. For fermion states the occupation, f_n, can be 0 and 1. In order to rewrite Equation 2.98 into form the reflects the periodicity of the crystal lattice we must Fourier transform the Kohn-Sham optical response function, $\chi_{KS}(\mathbf{q}, \mathbf{q}', \omega)$. By Bloch's theorem $\chi_{KS}(\mathbf{q}, \mathbf{q}', \omega)$ is nonzero if $\mathbf{q}$ and $\mathbf{q}'$ differ by a reciprocal lattice vector $\mathbf{G}$ such that $\mathbf{q}$ (propagation direction of light) is in the first Brillouin zone. Hence, $\mathbf{q} \to \mathbf{q} + \mathbf{G}$ and $\mathbf{q}' \to \mathbf{q}' + \mathbf{G}$; furthermore, sum over states includes the allowed crystal momentum, $\mathbf{k}$, such that $n \to n\mathbf{k}$ and $m \to m\mathbf{k}$ for all $\mathbf{k}$ within the first Brillouin zone. Finally, the Kohn-Sham optical susceptibility with

the Fourier representation is given by,

$$\chi^{KS}_{\mathbf{G}\mathbf{G}'}(\mathbf{q},\omega) = -\frac{1}{\Omega}\sum_{n\mathbf{k}}\sum_{m\mathbf{k}'} 2f_{n\mathbf{k}}(1-f_{m\mathbf{k}'})$$
$$\Big(\frac{\langle\psi_{m\mathbf{k}'}|e^{i(\mathbf{q}+\mathbf{G})\mathbf{r}}|\psi_{n\mathbf{k}}\rangle\langle\psi_{n\mathbf{k}}|e^{-i(\mathbf{q}+\mathbf{G}')\mathbf{r}'}|\psi_{m\mathbf{k}'}\rangle}{\epsilon_{m\mathbf{k}'}-\epsilon_{n\mathbf{k}}-\breve{\omega}} + \frac{\langle\psi_{m\mathbf{k}'}|e^{i(\mathbf{q}+\mathbf{G})\mathbf{r}}|\psi_{n\mathbf{k}}\rangle\langle\psi_{n\mathbf{k}}|e^{-i(\mathbf{q}+\mathbf{G}')\mathbf{r}'}|\psi_{m\mathbf{k}'}\rangle}{\epsilon_{m\mathbf{k}'}-\epsilon_{n\mathbf{k}}+\breve{\omega}}\Big)$$
$$= -\frac{1}{\Omega}\sum_{vc\mathbf{k}} 2f_{v\mathbf{k}}(1-f_{c\mathbf{k}+\mathbf{G}})\Big(\frac{\rho_{vc\mathbf{k}}(\mathbf{q}+\mathbf{G})\rho^*_{vc\mathbf{k}}(\mathbf{q}+\mathbf{G}')}{\epsilon_{c\mathbf{k}+\mathbf{G}}-\epsilon_{v\mathbf{k}}-\breve{\omega}} + \frac{\rho_{vc\mathbf{k}}(\mathbf{q}+\mathbf{G})\rho^*_{vc\mathbf{k}}(\mathbf{q}+\mathbf{G}')}{\epsilon_{c\mathbf{k}+\mathbf{G}'}-\epsilon_{v\mathbf{k}}+\breve{\omega}}\Big). \tag{2.99}$$

Note we have made the notational change from $n \mapsto v$ and $m \mapsto c$ for momentum transfer $\mathbf{q} \mapsto \mathbf{k}+\mathbf{G} \in BZ$ on the last line. And the $\rho_{vc\mathbf{k}}(\mathbf{q}+\mathbf{G}) = \int d^3r$ $\psi^*_{v\mathbf{k}}(r)e^{i(\mathbf{q}+\mathbf{G})r}\psi_{c\mathbf{k}+\mathbf{G}}(r)$.[120,121] This expression contains the momentum space representation of the independent particle optical susceptibility within the Kohn-Sham formalism.[118,122,123] Introducing Equation 2.99 into the Dyson expansion of the optical susceptibility yields the full optical susceptibility of the density response (Equation 2.87). The optical susceptibility will play a critical role in computing the dielectric response of an ultrathin film, see Chapter 6.

2.3.2 Dielectric Response

Optical properties of solids provide needed spectroscopic signatures of the band structure of the material. But optical properties can provide additional insight into impurity levels, lattice vibrations, localized defects, excitons, and magnon excitations.[124] Typically, the dielectric response can be determined from ellipsometric spectroscopy, and can be separated into two contributions: real and imaginary frequency-dependent dielectric functions.[125] The imaginary dielectric response is the key physical observable that is often used to characterize the band structure. Moreover, the frequency-dependent complex dielectric function can be used to relate to other observables, such as the absorption coefficient, enabling their computation, see Chapter 6.

The propagation of electromagnetic waves has long since been characterized by Maxwell's equations.[126] In the following, we will work in Fourier space unless otherwise stated. And we assume that the electric field is irrotational, i.e.,$rot\mathbf{E} = 0$, such that the electric field depends on the gradient of a scalar potential, $\mathbf{E} = \nabla\phi$.[126,127] In the electronic response of a material to an external perturbation the density can be rewritten to include external and internal contributions, $n_{tot} = n_{ext} + n_{int}$.[2] Consequently, all of the electrodynamic equations can be partitioned this way, where the external contributions vanish within the material.[2] The displacement field is related to the dielectric response of a material (Fourier representation), via, $\mathbf{D}(\mathbf{q},\omega) = \sum_\beta \epsilon_{\alpha\beta}(\mathbf{q},\omega)\mathbf{E}_\beta(\mathbf{q},\omega)$.[127] Here the 3x3 tensor ϵ is the frequency dependent dielectric function. Employing the Maxwell relations $\nabla\cdot\mathbf{D} = 4\pi e n_{ext}(\mathbf{r},t)$, and for the electric field $\nabla\cdot\mathbf{E} = 4\pi e n_{tot}(\mathbf{r},t)$, where the real-space representation is used we can formulate the frequency-dependent dielectric function.[2,127] Fourier transforming the real-space representations of the displacement field and electric field and solving for the dielectric function yields, $\epsilon_{\mathbf{GG'}}(\mathbf{q},\omega) = n_{ext}(\mathbf{q},\omega)/n_{tot}(\mathbf{q},\omega)$.[127] This expression for the dielectric function can be rewritten with the aid of Poisson's equation, we find,

$$\epsilon_{\mathbf{GG'}}(\mathbf{q},\omega) = \frac{\delta V_{ext}(\mathbf{q},\omega)}{\delta V_{tot}(\mathbf{q},\omega)}, \tag{2.100}$$

where a variation is applied to the numerator and denominator for the Poisson equation ($q^2\delta V = 4\pi e\delta n$). With Equation 2.100, we can expand the external potential ($V_{ext} = V_{tot} - V_H$) and use the chain-rule for the Fourier Hartree potential with respect to the total, i.e., $\epsilon_{\mathbf{GG'}}(\mathbf{q},\omega) = 1 - \frac{\delta V_H}{\delta n}\frac{\delta n}{\delta V_{tot}}$, which reduces to the following expression for the macroscopic frequency dependent dielectric function,

$$\epsilon_{\mathbf{GG'}}(\mathbf{q},\omega) = \delta_{\mathbf{GG'}} - \nu_C P_{\mathbf{GG'}}(\mathbf{q},\omega), \tag{2.101}$$

where $\nu_C = \frac{4\pi e^2}{|\mathbf{q}+\mathbf{G}||\mathbf{q}+\mathbf{G}'|}$ is the Fourier Coulomb kernel and $P_{\mathbf{G}\mathbf{G}'}(\mathbf{q},\omega) = \delta n/\delta V_{tot}$ is the polarization response or irreducible polarizability of the electrons.[2,118] Here we applied $\mathbf{q} \rightarrow \mathbf{q}+\mathbf{G}$ as above for the independent Kohn-Sham susceptibility. Moreover, it can be shown that the irreducible polarizability is related to the Kohn-Sham optical susceptibility with the following Dyson like equation,

$$P_{\mathbf{G}\mathbf{G}'}(\mathbf{q},\omega) = \chi^{KS}_{\mathbf{G}\mathbf{G}'}(\mathbf{q},\omega) + \sum_{\mathbf{G_1}\mathbf{G_2}} \chi_{\mathbf{G}\mathbf{G_1}}(\mathbf{q},\omega) f_{XC,\mathbf{G_1}\mathbf{G_2}}(\mathbf{q},\omega) P_{\mathbf{G_2}\mathbf{G}'}(\mathbf{q},\omega).^{118,128} \tag{2.102}$$

This form of the irreducible polarizability contains additional contributions from the exchange-correlation kernel, f_{XC}. The inclusion of the last term goes beyond RPA; however, the exchange-correlation kernel is zero, hence,

$$\epsilon^{RPA}_{\mathbf{G}\mathbf{G}'}(\mathbf{q},\omega) = \delta_{\mathbf{G}\mathbf{G}'} - \nu_C \chi^{KS}_{\mathbf{G}\mathbf{G}'}(\mathbf{q},\omega), \tag{2.103}$$

where it is clear that the irreducible polarizability is equivalent to the Kohn-Sham optical susceptibility of Equation 2.99.[118,121] From Equation 2.103 the dielectric response can be determined in terms of interband transitions within crystalline systems, which permits the computation of absorption spectra, Chapter 6. The macroscopic dielectric function (Equation 2.103) can be approximated from the head of the microscopic dielectric function in the optical limit or long wavelength limit ($\mathbf{q} \rightarrow 0$), $\epsilon(\mathbf{q},\omega) \sim \lim_{\mathbf{q}\rightarrow 0} \epsilon_{00}(\mathbf{q},\omega) = 1 - \lim_{\mathbf{q}\rightarrow 0} \frac{4\pi e^2}{q^2} \chi^{KS}_{00}(\mathbf{q},\omega).^{118,121}$ With this approximation and using the complex dielectric function ($\epsilon = \epsilon^{(1)} + \epsilon^{(2)}$), where the imaginary term characterizes the absorption or attenuation of light, $\epsilon^{(2)}(\omega)$, can be determined for a given material.[118,121] With the independent Kohn-Sham response function of Equation 2.99 and the various approximations made to the macroscopic dielectric function, the frequency dependent complex dielectric function can be written in the following form with the aid of the Sokchatsky-Weierstrass theorem ($\lim_{\gamma\rightarrow 0^+} \int_{-\infty}^{\infty} dx \frac{f(x)}{x+i\gamma} =$

$\mathbb{P}(\frac{1}{x}) \pm i\pi\delta(x)$ keeping the Dirac term for the complex dielectric function),

$$\epsilon^{(2)}_{\alpha\beta}(\mathbf{q},\omega) = \frac{4\pi e^2}{\Omega_{UC}} \lim_{\mathbf{q}\to 0} \frac{1}{q^2} \sum_{cv\mathbf{k}} 2w_{\mathbf{k}} \langle u_{c\mathbf{k}+\mathbf{e}_\alpha\mathbf{q}} | u_{v\mathbf{k}} \rangle \langle u_{c\mathbf{k}+\mathbf{e}_\beta\mathbf{q}} | u_{v\mathbf{k}} \rangle$$
$$[\delta(\epsilon_{c\mathbf{k}} - \epsilon_{v\mathbf{k}} - \hbar\omega) - \delta(\epsilon_{c\mathbf{k}} - \epsilon_{v\mathbf{k}} + \hbar\omega)], \quad (2.104)$$

where we have included the tensor dependence, e.g., $\epsilon^{(2)}_{\alpha\beta}(\mathbf{q},\omega) = \hat{\mathbf{q}}_\alpha \cdot \epsilon^{(2)}(\mathbf{q},\omega) \cdot \hat{\mathbf{q}}_\beta$, of the complex dielectric function because of spatial correlations associated with the direction of propagation of light, $\mathbf{q} = \hat{\mathbf{q}}/|\mathbf{q}|$, and the weight of each symmetrized crystal wavevector, $w_{\mathbf{k}}$.[118,121] The two $\delta(x)$ functions in Equation 2.104 represent the absorption ($-\hbar\omega$) and emission ($\hbar\omega$) of light. The complex dielectric function of Equation 2.104 has some interesting properties. First, the inclusion of the Dirac delta function enforces a selection rule for translationally invariant systems wherefore the crystal momentum, $\mathbf{k}$, must be equivalent between conduction (c index) and valence (v index) band transitions, hence, $\mathbf{k}_c \sim \mathbf{k}_v$ for allowed vertical interband transitions. Second, the transition probability is given by the cell-periodic functions, $|u_{n\mathbf{k}}\rangle$, originally shown in Equation 2.50, and contribute nonzero values for a given photon frequency, where wavevector conservation is obeyed. Finally, since no explicit dependence on reciprocal lattice vectors is present, the complex dielectric function (Equation 2.104) does not include local field effects provided by the underlying crystal structure.[2,118,121] Nevertheless, Equation 2.104 is valid within the linear response regime for weak electric fields that do not vary on the order of a lattice constant. This form of the dielectric function can be improved with higher level inputs such as electron-hole wavefunction expansions for the case of neutral excitons, or many-body perturbation expansion of the exchange-correlation functional.[128]

CHAPTER THREE

Periodic Trends of Pnictogen Substitution into a Graphene Monovacancy: A First-Principles Investigation

This chapter published as: Paul A. Brown; Chengyong Xu; and Kevin L. Shuford
Chem. Mater. **2014** 26, 19, 5735-5744

3.1 Abstract

We present a theoretical investigation on the electronic properties and formation energetics of pnictogen substitution into a graphene monovacancy. Our work elucidates the fundamental interactions that occur between the dopant and graphene, which ultimately dictate the observed behavior of the material. We find a linear trend for the energy of formation proceeding down group 15 of the periodic table. Further, we observe the formation of a protrusion at the monovacancy site, which is particularly conspicuous for larger pnictogens. This blistering can be attributed to charge transfer between the substituted heteroatom and the bordering carbon atoms of the monovacancy. Reorganization of the defect site of graphene becomes more pronounced for the latter pnictogens antimony and bismuth. An interaction regime emerges among this group, whereby nitrogen and phosphorus chemisorb strongly to the vacancy site, arsenic weakly chemisorbs, while antimony and bismuth physisorb to the surface. These interactions introduce moderate band gaps and yield impurity states near the Fermi energy, similar to a doped semiconductor material. Moreover, the extent of chemical bonding and planarity notably alters the band structure and the accessibility of low lying energy states, which are important for charge transport and reactivity. This work suggests the possibility of tailoring graphene surfaces for electronic devices or chemical transformations of interest *via* the appropriate choice of pnictogen dopant.

3.2 Introduction

Graphene has emerged as one of the most promising materials of the 21st century.[6,7,129] The two dimensional bipartite lattice of graphene exhibits unique electronic properties, which makes graphene an interesting material to study.[129] Graphene's properties like superlative structural rigidity, high surface area, high extrinsic mobility, long mean free path, high thermal and electrical conductivity,[129] etc. make it an excellent material for new age electronic devices and as a scaffold for novel nanoassemblies.[130,131]

Current research on graphene has focused on tailoring its electronic properties by doping heteroatoms or forming vacancies directly into the lattice structure.[132–138] Heteroatoms may be deposited *via* chemical vapor deposition onto graphene sheets at various concentrations.[139,140] Vacancies can be formed during fabrication or by ion irradiation of mechanically exfoliated graphene sheets.[141–143] Clever methods for structurally manipulating graphene's charge carriers by introducing (n-type) or abstracting (p-type) electrons from graphene could permit graphene based electronic devices with various modalities.[144] In particular, atomic nitrogen and gold have been suggested as excellent candidates in achieving this for future graphitic devices, since molecular absorbates may be too entropically unstable or reactive for such applications.[145] With the improvement of microscopic technologies, such as transmission electron microscopy,[146–148] scanning tunneling microscopy,[132,149,150] and aberration-corrected transmission electron microscopy,[151] atomic resolution of such defects can be observed at the atomistic scale.

Prior studies of graphene have examined nitrogen and phosphorus lattice substitutions;[152–161] however, research concerning latter pnictogens is rather sparse.[162–164] These carbon alloys might have potentially prominent chemical and electronic utility in many diverse areas. The rich electronic properties of these elements could vary wildly proceeding down the group as metallic character increases. Thus, it may be

possible to influence the concentration of charge carriers by simply controlling the composition or type of substituent within the graphene defect site.

In this research, we systematically focus on the the entire pnictogen series with first principles density functional theory (DFT).[54,61] We focus on the simplest (*lex parsimoniae*) interaction between heteroatoms and a single graphene monovacancy. In particular, we substitute all pnictogens into a monovacancy to delineate fundamental trends associated with atomic doping of free standing graphene. We find that stability decreases down the group as formation energies rise. Moreover, the sorption characteristics and electronic properties of the system change as the pnictogen size increases. In particular, impurity states form near the Fermi energy generating magnetic ground states and local charging, which subsequently diminishes going down the series. The local magnetic order will be presented in a separate account.

The remainder of this article is outlined as follows. The equations applied to determine the energy of formation and charge density differences are discussed in the computational methods section. In the results and discussion section, we present the stability associated with each pnictogen within the monovacancy and charge density difference maps highlighting primary interactions between the graphene sheet and pnictogen. We include the atomic projected density of states of each pnictogen atom to illustrate the strength of interaction with the graphene monovacancy. We also present the electronic band structures with selected bands decomposed to show the perturbing effects of each pnictogen on the graphene monovacancy. We conclude by summarizing the emergent trends upon substitution into a graphene monovacancy.

3.3 Computational Methods

DFT calculations were conducted with the software package VASP, where the core-valence interaction was treated within projector augmented wave method.[113,165] The exchange-correlation was treated at the generalize gradient approximation (GGA) level of theory; the Perdew-Burke-Ernzerhof (PBE) functional was utilized.[85] Spin

polarization was accounted for in all cases where the pnictogen substituent was positioned out of the plane of graphene. A 5 x 5 supercell was constructed with 12 Å of vacuum space to minimize interactions between images. Note, the supercell approximation is chosen for computational ease for delinating relative trends associated with pnictogen substitution, though larger supercells will converge to smaller differences in computed values due to lesser image interaction and lower dopant concentrations. The lattice constant was set to 2.46 Å to match the experimentally determined value. The kinetic energy cutoff was set to 520 eV for all cases studied herein. All structures were relaxed on a 12 x 12 x 1 gamma point grid, followed by linear combination of charge density on 20 x 20 x 1 gamma point grid to optimize bonding interactions. All energies of formation were determined from the tetrahedron method plus Blöchl corrections.[166] The projected density of states each system was simulated on the same dense k-point grid with smearing temperature set to $\sigma = 0.01$ (N, P, As) and $\sigma = 0.1$ (Bi, Sb), respectively, where Gaussian smearing was applied to the former and Methfessel-Paxton smearing[167] for the latter. Geometry optimization was performed on all structures to minimize the Hellmann-Feynman forces with a tolerance of 0.001 eV/Å. The final, relaxed heteroatom-graphene structures were permitted to explore all three degrees of freedom, with the pnictogens initially placed above the graphene sheet monovacancy.

In order to compute the energy of formation E_f of substituted graphene, we first determined the chemical potentials of carbon, μ_C, and pnictogens, μ_{PN}. We define the energy of formation to be

$$E_f = E_s - n_C\mu_C - n_{PN}\mu_{PN}, \tag{3.1}$$

where E_S is the total energy of the substituted graphene monovacancy, n_C is the number of carbon atoms, and n_{PN} is the number of pnictogens substituted, which is unity in this study. Note, the chemical potentials of each pnictogen, μ_{PN}, were

determined from their respective reference states from first principles calculation. The reference states of each pnictogen are taken as follows: gaseous nitrogen, white phosphorus, arsenic grey, orthorhombic antimony, and, finally, trigonal rhombohedral bismuth. To explore the influence of the charge transferred between the defective graphene sheet and heteroatoms, we determined the density difference as

$$\Delta\rho = \rho_{SG} - \rho_{MV} - \rho_S \tag{3.2}$$

where ρ_{SG} is the total charge density of the graphene-heteroatom system, ρ_{MV} is the total charge density of the defect monolayer graphene, and ρ_S is the total charge density of the substituent heteroatom. Note, the substituent atomic charge density is placed within identical supercells at the optimized locations within the supercell. The charge difference topologies presented display the absolute value of $\Delta\rho$, and therefore highlight the strongest interactions between the heteroatom and graphene carbons, after subtraction of the monovacancy total charge density and dopant total charge density. These plots display the magnitude of charge density that has been shifted between spatial locations. The numerical and topological data are presented in the results and discussion below.

3.4 Results & Discussion

Pnictogen Configurations & Charge Transfer. The geometry optimized structures were computed at the GGA level of theory treating the exchange-correlation with the PBE functional. The original, pristine graphene C-C bond lengths resulting from our approach were found to be 1.42 Å. This is consistent with experimental assessment of graphene carbon-carbon bond lengths.[6,7,129] The lattice constant was set to be 2.42 Å to ensure accuracy of these calculations. In the case of the monovacancy defect, we observe an interesting reorganization of the vacancy, 3.1. The initial structure, 3.1a, begins with D_{3h} symmetry. Upon relaxation, C_2 and C_3 deform the

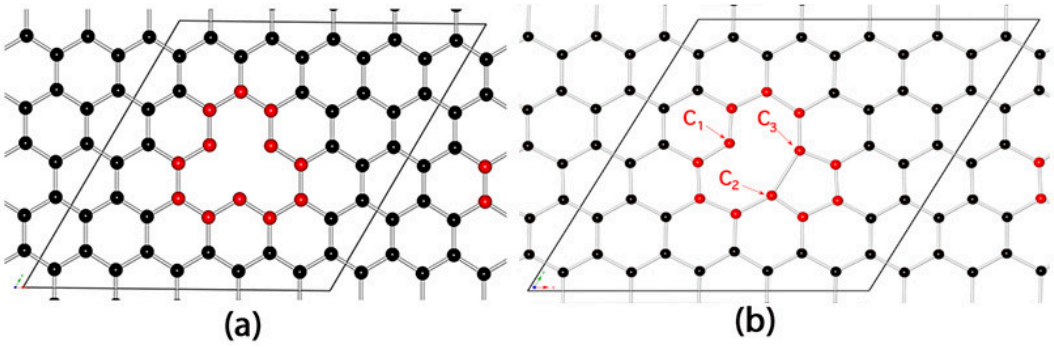

Figure 3.1. Geometry optimized structures of the monovacancy. Panel (a) contains the monovacancy with bordering carbon atoms highlighted in red. Panel (b) displays the structure following relaxation. Note the symmetry has been reduced.

monovacancy by shortening the distance between each other from 2.46 Å to 2.03 Å. This is the noticeable Yahn-Teller (YT) distortion of the monovacancy, where the symmetry has been reduced to C_s. Moreover, the energy of formation computed from 3.1 is 7.66 eV, which is consistent with other studies.[151]

The results of the relaxed structures with pnictogens interacting with the monovacancy are presented in 3.1. Each pnictogen was placed above the monovacancy and fully relaxed to reach self-consistency. The optimized structures are shown in 3.2. Nitrogen substituted graphene prefers to sit in the plane of graphene. This is because of its small atomic radius, smaller than carbon. The pnictogen-carbon bond lengths were found to be 1.40 Å, approximately 0.02 Å smaller than carbon-carbon bond lengths. Within the plane of graphene, nitrogen adopts full sp^2 character having bond angles of approximately 120° making it configurationally trigonal planar. The bond lengths of neighboring carbons were found to be shorten slightly to 1.41 Å, suggesting charge transfer between the nitrogen and nearest neighbor carbons. Analysis of the nitrogen substituted defect graphene via 3.2 shows 1.06 units of charge is transferred to the graphene sheet (3.1). 3.3a clearly shows the local nature of the charge distribution around nitrogen and the nearest neighbor carbons. However,

Pnictogen	d(PN-C), Å	d(C-C), Å	Bond Angle (°)	OOP, Å	CT (e)
N	1.40	1.47-1.426	120	-	1.06
P	1.76	1.44-1.44	99.7	1.54	2.39
As	1.90	1.41-1.44	92.6	1.88	1.07
Sb	2.10	1.40-1.45	83.9	2.31	2.02
Bi	2.20	1.40-1.45	79.9	2.48	1.99

Table 3.1. Geometric parameters of substituted graphene structures. Distances between the pnictogen and graphene are given as d(PN-C). The range of carbon-carbon bonds within the entire supercell is d(C-C), followed by the angle measured between the nearest neighbor atoms and heteroatom. The out-of-plane (OOP) distance is measured vertically from the lowest in-plane carbon atoms in the unit cell to the heteroatom. The magnitude of charge transferred between the pnictogen and graphene is presented as CT.

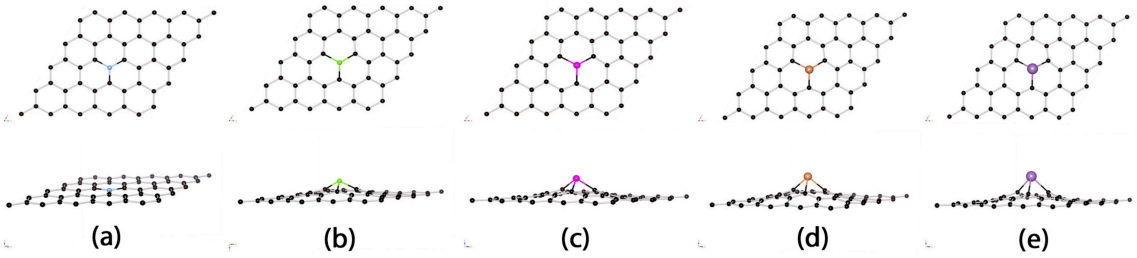

Figure 3.2. Top and side views of optimized pnictogen-graphene monovacancy systems: (a) nitrogen (blue), (b) phosphorus (green), (c) arsenic (violet), (d) antimony (orange), (e) bismuth (purple).

beyond this structural detail, little reorganization is observed near the monovacancy. The latter pnictogens adopt a different configuration due to steric frustration.

Phosphorus is larger in comparison to carbon and nitrogen, so it adopts a quasi-trigonal pyramidal type configuration when interacting with the monovacancy graphene. In-plane phosphorus is possible, but less stable than the out of plane phosphorus configuration. The difference in energy between in-plane and out-of-plane phosphorus doped graphene is 2.1 eV. The equilibrium bond length was found to be 1.76 Å, in agreement with other reports.[160,161] The monovacancy with phosphorus juxtaposed above leads to the puckering of the defect site, where phosphorus sits 1.54 Å out of the plane (3.2b and 3.1). This is primarily driven by the dangling states of

C_1, C_2, and C_3. Because the monovacancy forms a protuberance around the vacancy, the bond lengths vary dramatically within the entire graphene sheet, as shown in 3.1. Those carbon atoms within the monovacancy obtain the shortest bond lengths of 1.404 Å, which is counterposed by the longest bond lengths of 1.441 Å. This extreme reorganization is driven by the charge transferred between the phosphorus and graphene sheet, in particular near the monovacancy. Analysis of the amount of charge transferred was found to be 2.39 for phosphorus. The difference in charge transferred between phosphorus and the graphene sheet can be attributed to differences in electron affinity. In the case of phosphorus, lots of charge is transferred to the nearest neighbors (making these atoms partially negative overall) and additionally some to the monovacancy site itself (see 3.3b). The addition of charge localized within the monovacancy saturates the bordering carbon-carbon bonds forcing rehybridization. Consequently, a protuberance forms around the phosphorus substituent breaking the two dimensional symmetry of the graphene lattice.

Arsenic, similar to phosphorus, initiates structural reorganization of the monovacancy. The arsenic-carbon equilibrium bond length was found to be 1.90 Å, an increase. Arsenic forms smaller bond angles, which is consistent with longer bonds (3.1). However, the deformation of the monovacancy grows larger, leading to large variations in bond lengths between carbon atoms within the graphene sheet. Nevertheless, the above-plane equilibrium position of arsenic drives reorganization of the entire monovacancy, where the arsenic atom rests 1.88 Å above the graphene. Similar to the nitrogen case, little charge is transferred between arsenic and graphene; however, the charge is distributed in a manner similar to phosphorus (see 3.3). We find that the d-manifold remains in its singlet state; most of the charge donated originates from the 4s and 4p electrons, which contribute 1.07 electrons to the monovacancy. Thus, the primary interaction between the arsenic and defect graphene is to weakly

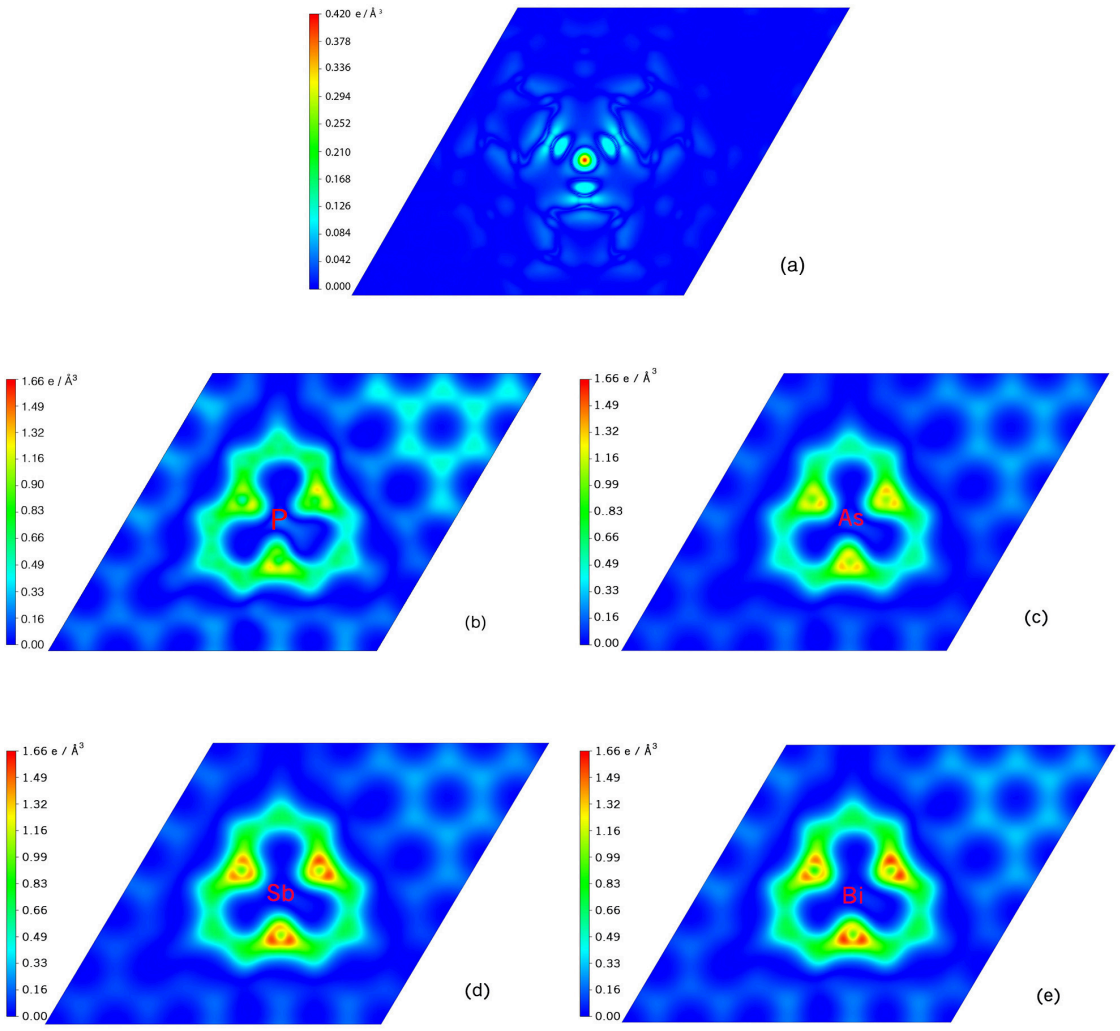

Figure 3.3. Absolute value of charge density differences for various atomic substituents and a graphene monovacancy: (a) nitrogen (b) phosphorus (c) arsenic (d) antimony (e) bismuth. Only nearest neighbors interact strongly with the nitrogen dopant, while latter pnictogens show charge delocalization over the entire monovacancy. Contour plots taken in the plane of graphene for nitrogen and $\sim$0.8 Å above the sheet for all others, corresponding to the location of C_1, C_2, and C_3.

chemisorb to the monovacancy, as some charge is transferred to nearest neighbor carbons C_1, C_2, and C_3 and diffused over the entire monovacancy. Consequently, the dangling states of these nearest neighbor carbons become partially coupled to arsenic driving them out of the plane, leading to the puckering seen in 3.2.

For the remaining pnictogens, many of the trends described above continue. The larger atomic radius of antimony leads to longer bonds and shorter bond angles, 3.1. The equilibrium distance of antimony and the graphene defect was found to be 2.10 Å, in good agreement with previous work.[162] Moreover, the carbon-carbon bonds fluctuate between 1.40 Å at their shortest to 1.452 Å at their longest within the monovacancy. Bismuth has the longest pnictogen-carbon distance[163] at 2.20 Å and the smallest angle, which deforms the carbon-carbon bond distances like the antimony system. The OOP distance of bismuth is 0.17 Å longer than antimony (3.1). Similar amounts of charge are transferred to the carbon lattice in both cases, and the diffuse nature of the charge redistribution mimics the phosphorus system (3.3). Both antimony and bismuth form weak interactions in contrast with earlier pnictogens like nitrogen and phosphorus. The energetics of all pnictogen substitutions will be discussed in the next subsection.

In general, the underlying driving force for the formation of these protrusions can be attributed to rehybridization of p_z states of vacancy carbon atoms, which further stabilizes the pnictogen-graphene system. This enables the formation of charge localization around the monovacancy, where the addition of charge between the pnictogen and graphene further distorts the monovacancy. Moreover, because the atomic radii increase going down the series, the charge is spread out over a larger region above the vacancy with respect to the carbon atoms C_1, C_2, and C_3, which further exacerbates the puckering of the monovacancy.

Energetics of Formation. The structural behavior discussed in the last section is reflected in the energetics of each pnictogen system. In particular, we focus

Table 3.2. Energies of formation, E_f, for each pnictogen-defect graphene system. Notice the energy steadily rises yet even the least stable substituent lowers the energy of the monovacancy (MV).

Pnictogen	N	P	As	Sb	Bi	MV
E_f	0.86	2.94	4.05	5.38	6.14	7.65

on the energy of formation of each congener, as defined in 3.1 (see Methods). As shown in 3.2, nitrogen forms the most stable configuration among all the pnictogens, with the lowest formation energy of 0.863 eV. This is to be expected because nitrogen is the smallest congener and can be substituted directly into the planar graphene lattice. Thus, little reconstruction is necessary, permitting the surrounding carbon atoms to retain their equilibrium distances. However, little resemblance can be drawn below nitrogen in group 15. The formation energy of the phosphorus dopant was found to be 2.946 eV. Beyond phosphorus, the formation energy steadily rises, almost linearly (3.2). As surface reconstruction and the formation of protrusions driven by charge localization rises, so too does the formation energy. Therefore, the stability of the latter pnictogens lowers leading to more weakly bound system.

Within the series, nitrogen and phosphorus chemisorb to the graphene monovacancy, while for the d-manifold pnictogens, arsenic tends to weakly chemisorb, and antimony and bismuth physisorb to the monovacancy. This assertion is further supported by the projected density of states (PDOS) of the pnictogen, which shows the nature and extent of interaction between the heteroatom and monovacancy, 3.4. Nitrogen substituent interacts most strongly through sp^2 hybridization via in-plane bonding with monolayer graphene. Thus, nitrogen's p_x and p_y states are broadly dispersed as shown in 3.4a. Such a broad distribution of states can be attributed to strong interactions with the graphene sheet. Moreover, the p_z electrons are also widely dispersed and sufficiently incorporated into the network to contribute to impurity states residing near the Fermi energy, which are seen as sharp peaks (3.4a). Hence, nitrogen strongly chemisorbs to the monovacancy defect site. Similar state

dispersion can be observed with the phosphorus substituent (3.4b); however, the p-electrons of phosphorus interact more strongly with the monovacancy leading to a slightly broader distribution of electrons from phosphorus. Again, an impurity state arising from the p_z electrons of phosphorus forms at the Fermi energy (3.4b). Arsenic displays many sharp bands indicating that this substituent interacts more weakly with the monovacancy and mixes less. Note its contribution to impurity states at the Fermi energy also decreases notably (3.4c). Antimony (3.4d) and bismuth (3.4e) continue this trend of localization of atomic states and decreasing contribution to the impurity band at the Fermi level, suggesting far less state mixing with the graphene monolayer and more of a physisorption-like interaction with the sheet.

Thus, our calculations suggest that stability falls as one proceeds down group 15. The increase in formation energy is accompanied by larger OOP distances and more planar deformation. The structural properties coupled to charge transfer characteristics suggest a crossover in sorption characteristics, where early pnictogens chemisorb while latter pnictogens physisorb. The PDOS supports this interpretation. Even with notable sheet deformation, it is clear that vacancies can accommodate the larger pnictogens bismuth and antimony, potentially extending functionality. As we shall see, this has important consequences influencing the band structures of each pnictogen-defect graphene system presented in the following section. Note, we tested the extent that nonlocal dispersion interactions affected the results via the Tkatchenko-Scheffler scheme.[168] We found little influence of the structural equilibria and energetics of formation.

Pnictogen Electronic Band Structure. We now examine the electronic band structure of each pnictogen-substituted, monovacancy system. In 3.5, we show the band structure and the partial band decomposition for the monovacancy defect site. As observed in other studies of this defect state, two resonance bands form near the Fermi energy, which can be attributed to dangling states from C_1, C_2, and

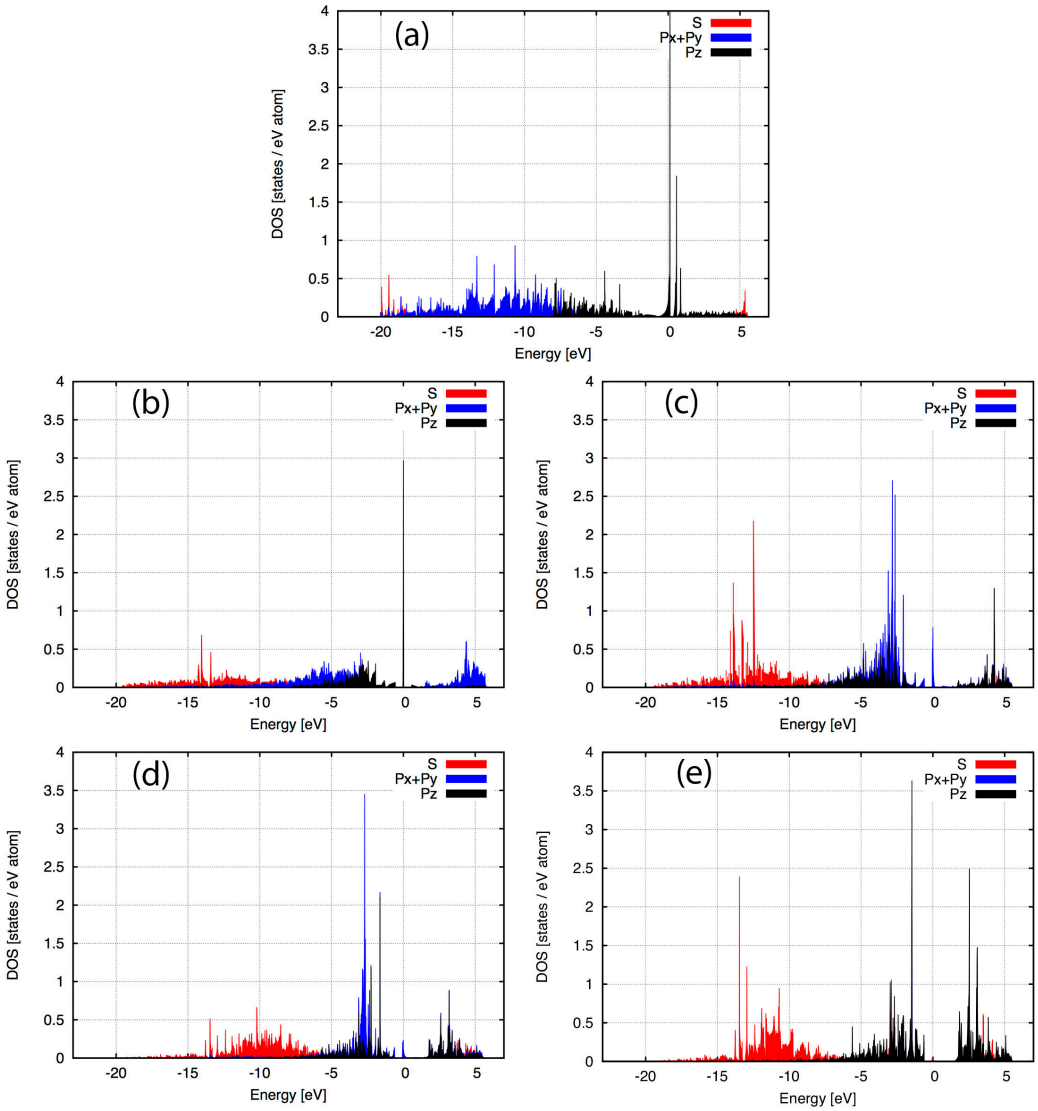

Figure 3.4. Projected density of states of each pnictogen atom upon interacting with monovacancy graphene: (a) nitrogen, (b) phosphorus, (c) arsenic, (d) antimony, and (e) bismuth. A broader PDOS distribution suggests more mixing with the graphene monovacancy.

C_3.[150,169] Dispersion within these bands is marked by Coulombic repulsion between each carbon atom within the monovacancy. Partial band decomposition of resonance bands at the Fermi energy reveal that C_1, C_2, and C_3 primarily form these bands, and remain localized near or around the monovacancy. Consequently, the single vacancy has a noticeable magnetic moment of 0.9 μ_B following Lieb's theorem for bipartite lattice discussed elsewhere.[170–176] The magnetic ground state forms from unquenched dangling sp^2 state of C_1 leading to anisotropic charge distribution of the monovacancy, 3.5c. The second resonance state forms from partially quenched YT-carbons C_2 and C_3 as shown in 3.5d. It is interesting to note that for both resonance states most of the charge can be found on a sublattice of graphene, which clearly results from the importance of forming a defect state on a bipartite lattice.[176] Moreover, the symmetry of the canonical bands of π and π^* of pristine graphene is destroyed, breaking the linear dispersion in these bands at K and K', 3.5b (blue dot) and 3.5e (red dot). Consequently, the π^* bands are pushed further into the conduction bands, while the π states are lowered into the valence bands. This stabilizes the defect state allowing for the formation of a localized magnetic ground state lowering the Coulombic repulsion between carbon atoms within the monovacancy.

As mentioned in the introduction, nitrogen substitution has been studied previously.[152–158] For validation of our computational approach, we report the electronic band structure and the partial band decomposition of states near the Fermi energy. These states are critical to the performance of electronic devices or chemical reactivity. The nitrogen substituent, due to its small size, can be directly inserted into the lattice of graphene. From 3.6a we notice the neutrality point (where the π and π^* bands intersect at the Fermi level) has shifted down from the original point in pristine graphene. Note the gap between the valence bands and conduction bands is highlighted light blue. Because nitrogen has an additional electron that can be donated to the graphene lattice, the π^* band shifts down into the valence bands (blue

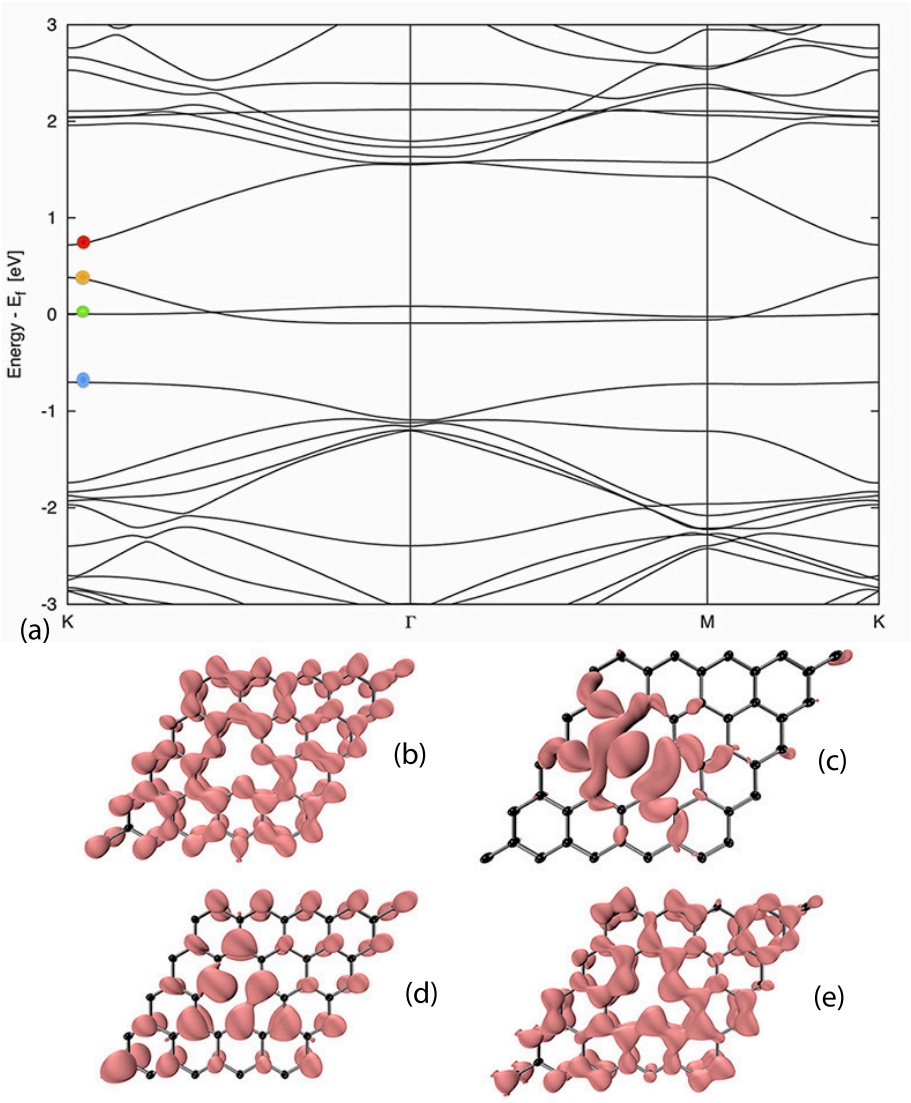

Figure 3.5. Monovacancy band structure (a) and band decomposed charge densities of relevant bands near the Fermi energy (b-e). Panels b and e are the π and π^* bands of graphene (blue and red dot, respectively). Panels c and d are impurity states (green and yellow dots respectively). Panel c is composed of primarily C_1 density. Panel d is a mixed band composed of C_2 and C_3 mostly, but it crosses with c mixing in C_1 states. Both c and d comprise the dangling states forming near the Fermi energy. All charge densities are set at 0.01 e/Å^3.

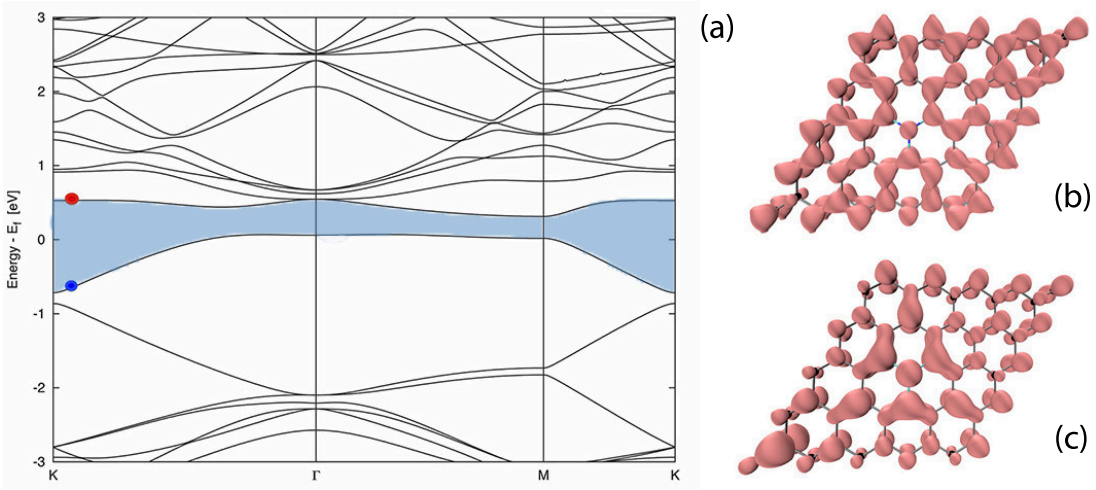

Figure 3.6. Singly substituted nitrogen band structure and band decomposed charge densities of relevant bands near the Fermi energy. (a) Band structure. (b) Charge density of the highest occupied band (blue dot) (c) Impurity band introduced by nitrogen substituent (red dot). All charge densities are set at 0.01 e/Å^3.

dot). Shifting these states of graphene into the valence bands is emblematic of n-type doping, where the additional electron provided from nitrogen is shuttled into the graphene sheet. The states corresponding to this band are shown in 3.6b. Clearly, the p_z states of the graphene lattice dominate, though the p_z orbital can also be seen on the nitrogen substituent (3.6b). Moreover, nitrogen introduces an impurity band (3.6c, red dot) in the band structure of single defect graphene. This impurity state near the Fermi energy resembles reports for antibonding STM images of this defect state.[160] These states could serve as potential sites of reactivity to anchor various nanoassemblies or induce impurity scattering within an electronic device.

The phosphorus substituent is not only structurally and energetically different, its electronic signatures differ substantially from that of the nitrogen case, 3.7. A resonance state forms at the Fermi energy arising from both the phosphorus dopant and also its nearest neighbors C_1, C_2 and C_3. The band decomposition is shown in 3.7c (yellow dot). Because of the presence of the impurity state at the Fermi energy, the graphene π and π^* bands lose their symmetry and shift downward into

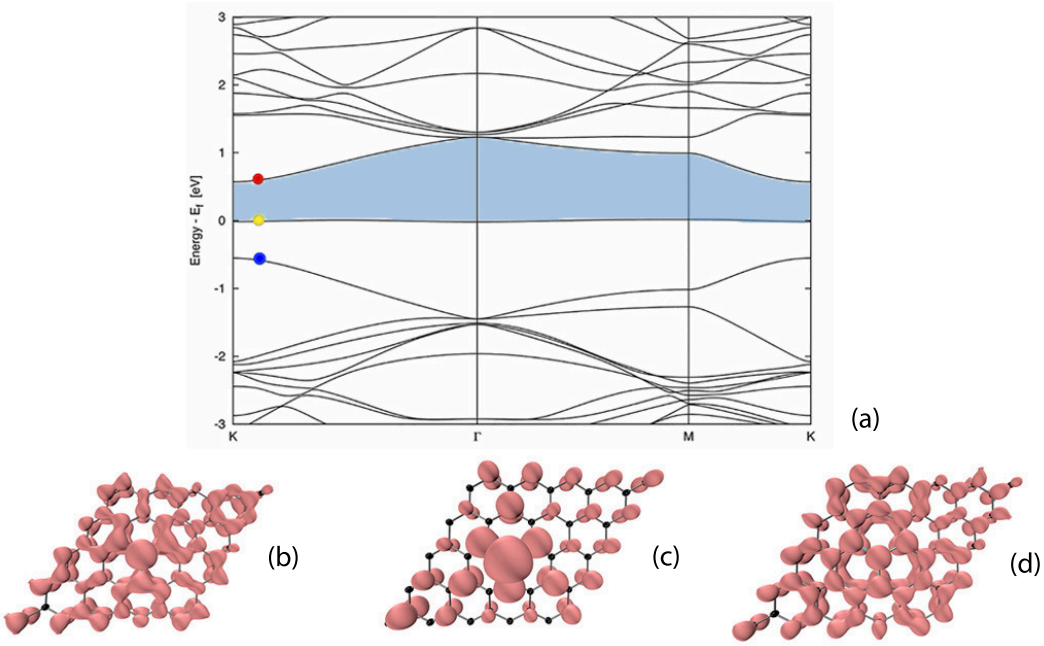

Figure 3.7. Singly substituted phosphorus band structure and band decomposed charge densities of relevant bands near the Fermi energy. (a) Band structure. (b) Charge density of π states of graphene (blue dot). (c) Impurity band attributed to phosphorus and the nearest neighbor carbon atoms (yellow dot). (d) Charge density of π^* states of graphene (red dot). All charge densities are set at 0.01 e/Å^3.

the valence bands and upward into the conduction bands, respectively. A pronounced charge density can be found centered on the phosphorus and its nearest neighbors (3.7b-d). Consequently, this site could serve as a reactive hot spot for catalyst.[177] Furthermore, the presence of a populated impurity band transforms graphene into a moderate band gap semiconductor with an energy gap of approximately 0.55 eV. The itinerant electrons confined within this narrow band could alter the transport properties of pristine graphene.[164,178]

We now turn to the latter pnictogens – arsenic, antimony, and bismuth. These elements differ only in their size, electron affinity, and electronegativity; however, they are the same in terms of their envelope states. For these elements, we have included the d-manifold for completeness. The arsenic band structure is similar to that of phosphorus, but the impurity state contains some dispersion arising from inter-vacancy

interactions or renormalization of p_z for nearest neighbor carbons, 3.8a (yellow dot). Recall that the protrusion is growing ever larger, induced by charge transfer into the monovacancy. Therefore, blistering of the graphene vacancy shortens the distance between p_z states within the monovacancy, since the curvature of the sheet positions p_z states such that they achieve greater overlap. Moreover, breaking the symmetry of the graphene monovacancy induces a irrecoverable change in the symmetry at the neutrality point, located at zero in the band structure plots, which causes the π (blue dot) and π^* (red dot) bands to deviate from the Fermi energy, 3.8a. Arsenic has an appreciable amount of charge localized onto itself, largely originating from the nearest neighbor carbon atoms (3.8b). Additionally, the charge is redistributed less uniformly onto the sublattice of graphene in comparison to the phosphorus substituent (see 3.7c). Unlike phosphorus, arsenic localizes no excited state density from the π^* band, suggesting this pnictogen contributes little to the lowest unoccupied states, 3.8d (red dot). The addition of arsenic into the monovacancy opens up an energy gap of 0.49 eV. Thus, atomic substitution of this particular pnictogen again yields a semiconductor-like structure. However, in this case, the weaker interactions lead to a partially unoccupied impurity band, more reminiscent of a hole doped material or electrophile.

Antimony, similar to arsenic, possesses an impurity band at the Fermi energy that is formed primarily from nearest neighbor carbon atoms C_1, C_2 and C_3, with some additional contributions from the graphene sublattice (3.9c). Even so, some density is localized on antimony in the impurity state; however, antimony's contribution to the π and π^* bands is diminished greatly (3.9b and d). Thus, antimony forms weak interactions with the monovacancy but still lowers the energy of the entire monovacancy. Like arsenic, antimony forms a semiconducting material with a band gap of 0.45 eV and has a partially unoccupied impurity band that can abstract electrons. It has been reported that doping antimony onto pristine graphene can lead

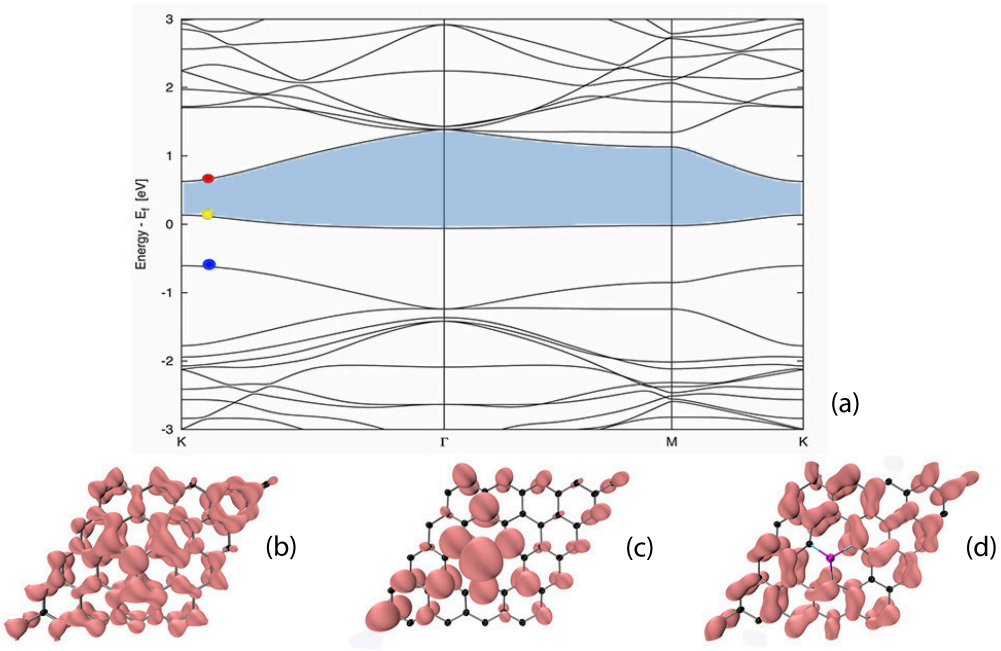

Figure 3.8. Singly substituted arsenic band structure and band decomposed charge densities of relevant bands near the Fermi energy. (a) Band structure. (b) Charge density of π bands of graphene (blue dot). (c) Impurity band attributed to arsenic and nearest neighbor atoms (yellow dot). (d) Charge density of π^* band of graphene (red dot). All charge densities are set to 0.01 e/Å^3.

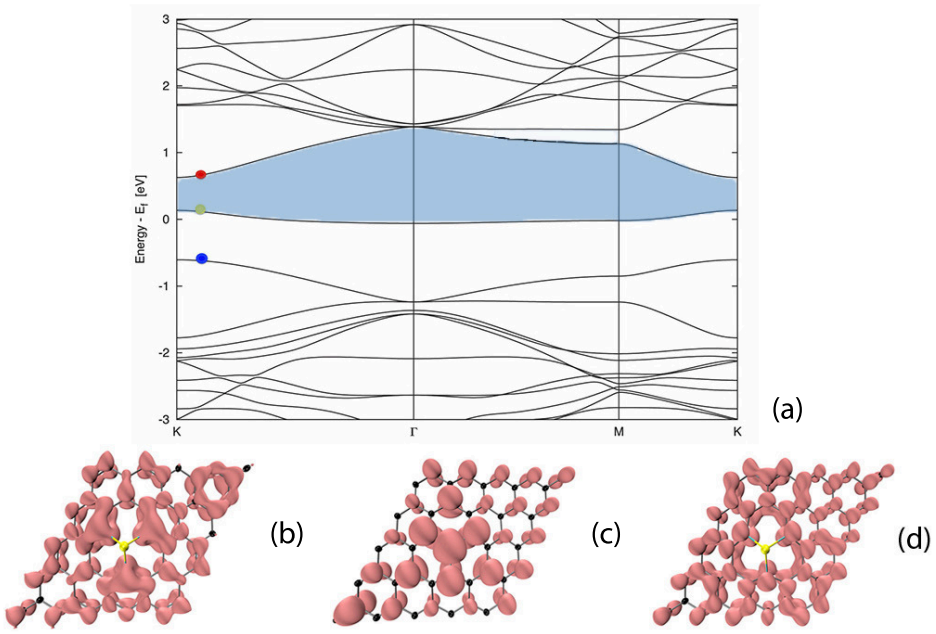

Figure 3.9. Singly substituted antimony band structure and band decomposed charge densities of relevant bands near the Fermi energy. (a) Band structure. (b) Charge density of π bands of graphene (blue dot). (c) Impurity band attributed to antimony and mostly nearest neighbor carbon atoms (yellow dot). (d) Charge density of π^* bands of graphene (red dot). All charge densities are set to 0.01 e/Å^3.

to the diminution of electrons in graphene, thus generating an upward shift in the Dirac point of the experimental band structure.[145] We observe a similar shift here.

Bismuth mirrors much of antimony's electronic complexity. However, minute changes in the resonant state at the Fermi energy can be observed, where dispersion at the K-points can be seen, (3.10a, yellow dot). The majority of the charge is found on the nearest neighbor carbon atoms and distributed over the monovacancy sublattice (3.10c). In contradistinction with the other pnictogens, bismuth contributes essentially nothing to the resonant states observed at the Fermi energy. Moreover, partial charge decomposition of all states near the Fermi energy show no build up of density on bismuth (3.10b-d). Overlap between nearest neighbors has reached a maximum for bismuth substitution, driven by its larger radius smeared over a greater

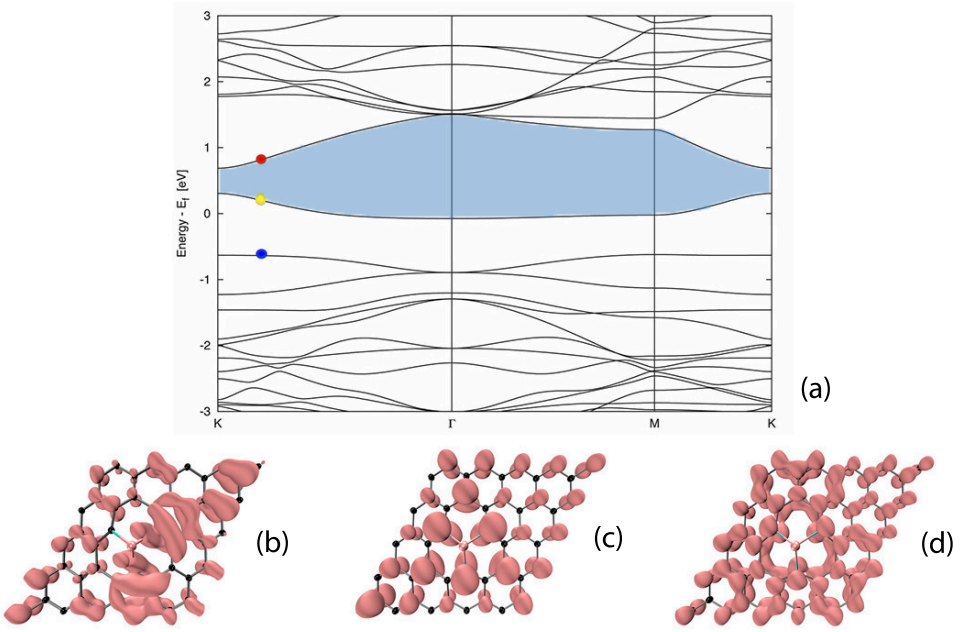

Figure 3.10. Singly substituted bismuth band structure and band decomposed charge densities of relevant bands near the Fermi energy. (a) Band structure. (b) Charge density of π bands of graphene monovacancy (blue dot). (c) Impurity state arising from C_1, C_2, and C_3 nearest neighbor carbon atoms (yellow dot). (d) Charge density of π^* bands of the graphene (red dot). All charge densities are set to 0.01 e/Å^3.

volume compared to its higher members of group 15. Consequently, bismuth stabilizes the monovacancy the least. Again we find that interactions between this congener and the monovacancy generate a band gap of approximately 0.45 eV and a partially unoccupied impurity band, which may display interesting transport properties or unique chemical reactivity.

3.5 Conclusions

We have investigated the unit substitution of pnictogens within a single vacancy site formed from pristine graphene. We have found noticeable trends associated with each pnictogen substituent. In particular, we have observed a regime of interaction, whereby nitrogen and phosphorus chemisorb to the monovacancy, arsenic has a tendency to weakly chemisorb, and both antimony and bismuth physisorb to the vacancy. This trend can be attributed to the influence of charge transferred and the

renormalization of the states within the monovacancy. Consequently, reorganization of the monovacancy ensues altering the bond lengths and bond angles. Thus, the energy of formation rises going down group 15. Moreover, each pnictogen transforms the zero band gap semi-metallic nature of pristine graphene into a moderate band gap semiconductor, whose electronic properties are dependent upon the extent of interaction between the dopant and surface. The ability to tune the exceptional electronic properties of graphene is of paramount importance for the design of material devices possessing wide application in both graphitic-electronic devices and chemical catalyst. Because of the paucity of electrons in graphene, the ability to alter its properties by simple atomic substitution is indeed an advantage, which could find many areas of application far afield.

CHAPTER FOUR

Electronic Properties of Halogen-Adsorbed Graphene

This chapter published as: Chengyong Xu; Paul A. Brown; and Kevin L. Shuford *J. Phys. Chem. C*, **2015**, 119, 30, 17271-17277

4.1 Abstract

We have investigated the electronic properties of 1-, 2-, and 3-layer graphene upon surface adsorption of halogen molecules by means of density functional calculations. The most stable adsorption site is parallel to the graphene surface with the diatomic atoms centered over adjacent carbon rings. Bader analysis shows a large charge transfer between F_2 and graphene, which significantly extends the fluorine bond length, while only small amounts of charge are transferred to Cl_2, Br_2, and I_2. Adsorbed halogens alter the electronic properties of graphene by pushing the Fermi level down and bringing forth an accessible impurity band that can be utilized to alter the material properties. Moreover, molecule-surface interactions introduce a bandgap at the K-point between 3 and 330 meV, depending upon the particular graphene-halogen system. When adsorbed on 1-layer graphene, halogen molecules typically open a small bandgap; however, they induce a notably larger bandgap on the 2-layer AB-stacked and 3-layer ABC-stacked graphene. This work suggests an effective way to tune the electronic properties of two-dimensional graphene by adsorption of halogen molecules.

4.2 Introduction

Graphene, first isolated by Novoselov and Geim in 2004,[6] is a two-dimensional crystal composed of atomic layers of carbon arranged in a lattice of hexagon rings. Since its mechanical exfoliation, graphenes unique properties[7,7,179,180] - such as long spin relaxation time and length, high mobility, and high thermal conductivity have

gained significant attention in condensed matter physics, chemistry, nanotechnology, and materials science.[8] Graphene has found various applications by acting as a platform for anchoring or supporting catalyst, solar fuel, solar cells, and battery devices.[181] In graphene, two equivalent carbon atoms in a primitive unit cell sp^2 hybridize, while the remaining p_z orbital forms π-bonds. From a tight-binding analysis of graphene, the interaction of p_z orbitals yields π and π^* bands in the band structure, which cross each other at the K-points in the first Brillioun zone. Moreover, graphene forms a bipartite lattice, where it is possible to distinguish the two-atom basis into two groups of carbons, α-carbons and β-carbons, that form an intralayer sublattice.[6] Due to its remarkable mechanical and electronic properties, the incorporation of graphene into practical devices,[182,183] such as field-effect transistors,[184,185] is an active area of research.

Graphenes exceptional electronic properties can be traced to the canonical dispersion at K-K' within its band structure, which gives rise to chiral Dirac fermions that can only be described by the Dirac equation.[7] In general, the zero bandgap condition of graphene holds for 1-layer and multilayer bernal and rhombohedral families;[186] however, graphene based devices, such as field-effect transistors, often demand a non-zero bandgap to function.[187] Therefore, creating a bandgap in graphene and controlling its magnitude is an important technological advance. While spin-orbit and electron-phonon coupling at the K-point makes this challenging, an effective way to introduce a bandgap is by disturbing the electron distribution. Several means have been proposed such as chemical physical adsorption,[187] chemical modification,[188,189] electric field tuning,[190–192] dimensional restriction,[193,194] and substrate-based deposition.[195,196] Among these, molecular adsorption is attractive because it preserves the planar hexagonal rings, and electrons undergo less impurity scattering. Various molecular species have been introduced onto graphene, ranging from small molecules (H_2O,[197,198] CO_2,[199] NO_2,[200] NH_3,[198,200] halogens[201]) to more complex

organic molecules (e.g. N-methylpyrrolidone,[202] phthalocyanines,[203] TCNQ[204,205]). Note this is different from atomic doping into the graphene lattice, which changes the electronic structure and density of states (DOS) greatly.[206–208] Molecular adsorbates introduce an impurity band near the Fermi level, but the effect on the overall band structure is less drastic (barring a Fermi level shift and introduction of a bandgap, as will be discussed below). Moreover, atomic dopants in graphene have been shown to decrease mobility because of impurity scattering arising from significant structural reorganization.[209,210] Halogen molecules, however, outperform other dopants like ammonia in the sense that the detrimental effects on mobility are less pronounced.[211]

In this work, we focus on several different layered graphene structures (1-, 2-, and 3-layer) adsorbed with halogen molecules (X_2, X = F, Cl, Br, and I). The interaction between the molecules and the graphene layer is nonlocal, as they are not covalently bonded. As a result, van der Waals (vdW) interactions need to be included to accurately model dispersion interactions. After determining the most energetically stable adsorption sites, we investigate the electronic properties of the graphene-halogen systems. In particular, the bandgap opening effect and the ability to tune the magnitude of bandgap opening via halogen selection and number of graphene layers will be presented and discussed. Finally, conclusions and perspectives will be presented in the last section.

4.3 Computational Methods

Model structures. A halogen molecule may take a parallel or perpendicular orientation with respect to a graphene layer as illustrated in Fig. 1. We have investigated four parallel (Fig. 1 A-D) and three perpendicular (Fig. 1 E-G) sites according to high-symmetry configurations. Here we only consider the adsorption of halogen molecules on one side of graphene to focus specifically on the effects induced by layering graphene sheets in various ways. Periodic supercells were constructed from hexagonal 4x4 unit cells, containing 32, 64, and 96 carbon atoms for 1-, 2-, and

3-layer graphene, respectively. The lattice constant a is taken to be 9.84 Å, four times that of the experimental value (2.46 Å) of the primitive unit cell at low temperature.[4] Lattice constant c is chosen so that periodic images are separated by approximately 15 Å of vacuum. Such a separation is large enough to eliminate interactions between the periodic images in directions normal to the surface. In 2-layer graphene, layers can form into AA or AB stacking. However, AA is higher in energy than AB stacking by approximately 1040 meV per atom.[212] Therefore, we only consider AB stacking in 2-layer graphene, and in 3-layer graphene, ABA or ABC stacking are considered. We denote X_2G1, X_2G2, X_2G3_{ABA} and X_2G3_{ABC} (X = F, Cl, Br, and I) to be the X_2 diatom adsorbed on 1-layer, 2-layer-AB stacking, 3-layer-ABA stacking (bernal), and 3-layer-ABC stacking (rhombohedral) graphene, respectively (see Fig. 1).

Computational approach. Using density functional theory (DFT), the energies and electronic properties of halogen-graphene systems have been calculated with a plane wave basis and projector augmented-wave (PAW) pseudopotentials for the interaction between the electrons and ions[113,114] as implemented in VASP[114,165] package. Molecules adsorbed to a surface are weakly bound, so it is important to consider dispersion interactions using a vdW correction. Several schemes based on semi-empirical dispersion potentials have been suggested, such as DFT-D/DFT-D2 (Dispersion correction),[92,213] vdW-DF,[214,215] and the Tkatchenko-Scheffler (TS) method.[95,97] We tested different vdW schemes as well as non-vdW methods on 2-layer graphene to determine the best one for our systems (results presented below). We found the combination of TS-GGA (PBE functional) predicts the inter-layer distance closest to experimental value; therefore, this scheme of vdW interaction and exchange correlation functional were used for the energy and electronic calculations. The geometry was optimized until the force on each atom is no more than 0.005 eV/Å. A Monkhorst-Pack[216] k-point mesh of 5x5x1 and 19x19x1 were used for geometric relaxation and density of states for all structures, respectively. The band structures

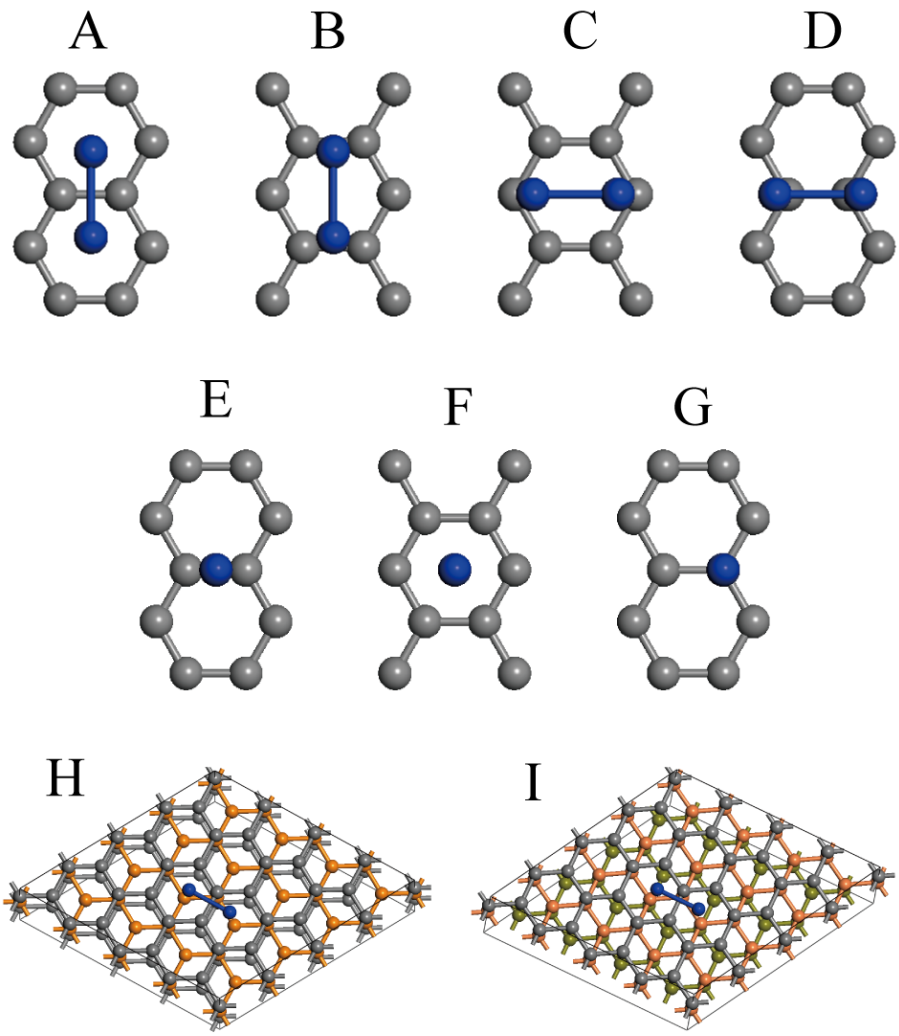

Figure 4.1. Different adsorption sites available for halogen molecules on monolayer graphene (A-G). Gray and blue balls represent carbon and halogen atoms, respectively. Sites A-D are denoted as parallel orientations while sites E-G are perpendicular. H (I) shows the adsorption of molecule on 3-layer ABA (ABC) graphene. 2-layer-AB stacking is analogous to H (or I) without the bottom graphene layer present.

Table 4.1. Table 1. Inter-layer distance (d) of 2-layer graphene under different vdW schemes and the difference (Δd) between the calculated and the experimental inter-layer distance of 3.340 Å.[4] Positive (negative) Δd means the calculated d is larger (smaller) than the experimental value.

		vdW-GGA	vdW-DF		vdW-LDA	non-vdW	
	TS	DFT-D2		TS	DFT-D2	LDA	GGA
d (Å)	3.350,	3.204,	3.312	3.162	2.995	3.302	4.052
Δd (Å)	0.010,	-0.136,	-0.028	-0.178	-0.345	-0.038	0.712

were computed over the high symmetry points of the first Brillouin zone of graphene. The cutoff energy for the plane wave basis was 500 eV.

4.4 Results and Discussion

We tested different vdW schemes for suitability by investigating a model system consisting of 2-layer graphene. The inter-layer distance was computed with and without a vdW correction using both the GGA and LDA functionals. The results are displayed in Table 1. Using GGA-TS, the layer distance of 2-layer graphene was calculated to be 3.350 Å, in agreement with experimental value of 3.340 Å.[4] Moreover, the layer separation of 3-layer ABA and ABC graphene was computed and found to be approximately 3.350 Å, showing the universal validity of TS-GGA for graphene structures. The vdW-DF (using LDA correlation and GGA-PBE exchange functionals) also predicted an accurate layer distance (3.312 Å). GGA-DFT-D2 underestimated the layer distance by 0.136 Å within a 4.1 % error, even worse than non-vdW-LDA. Serendipitously, the LDA functional without vdW predicts a distance in good agreement with experiment (3.302 Å, 1.1 % error). This small error with LDA is due to two competing errors. There is a local density interaction error and long-ranged dispersion is ignored, the combination of which cancels each other fortuitously.[217] Using non-vdW (PBE) corrects one error by considering non-local electron interaction but leaves the other error intact,[218] yielding a larger layer distance of graphene (4.052 Å). On the contrary, vdW-LDA only corrected for vdW interactions and made no

alteration to the electron interaction error, resulting in the underestimation of layer distance between graphene polymorphs (3.00-3.16 Å). Considering the better agreement with experiment on 2-layer graphene, GGA-TS was chosen as the best approach for calculations on our layered graphene systems.

We then introduced halogens into the model system to further validate the approach. In general, surface interactions brought little change to the molecular bond lengths. Upon adding adsorbed halogens onto graphene, the GGA-TS approach predicts molecular bond lengths within 0.01-0.04 Å of experimental values of isolated molecules[5] except for fluorine. As for F_2, the bond length is found to be ∼0.245 Å (17 %) larger (it varies slightly with system) than isolated F_2 at the same level of theory. The notable bond length extension for F_2 on graphene suggests a sizeable charge redistribution, which is not present in the other halogens. We performed Bader analysis[219] to quantify charge transfer between the halogen molecules and graphene for adsorption site A. The results in Table 2 explain the sizable elongation of the F_2 bond length compared with Cl_2, Br_2, and I_2. All the halogen molecules act as electron acceptors. F_2 obtains 0.432-0.450 electrons from the graphene layer, which elongates the bond length of F_2 up to 0.246 Å. However, the charges accepted by Cl_2, Br_2, and I_2 are quite small, only marginally extending their bond lengths. Similar charge transfer from graphene to Br_2 was calculated by Yaya et al. (0.084 electron) using LDA[220] and Chen et al. (0.09 electron) using GGA[221] confirming the approach selected for this study is adequately describing the halogen-graphene systems, including their intimate interactions like charge transfer in the case of fluorine.

Adsorption of molecules on graphene. We calculated the binding energies, Ebind, of halogen molecules adsorbed on graphene by the usual definition:

$$E_{bind} = E_{system} - E_{graphene} - E_{molecule} \tag{4.1}$$

Table 4.2. Charge transfer (CT in units of e) between the halogen molecules and graphene, and the bond length elongation (BL in units of Å) in parentheses for adsorption site A. Elongation is relative to experimental measurements of isolated molecules.[5]

X_2		X_2G1	X_2G2	X_2G3_{ABA}	X_2G3_{ABC}
F_2	CT (e)	0.432	0.444	0.450	0.449
	BL (Å)	0.243	0.245	0.245	0.246
Cl_2	CT (e)	0.016	0.014	0.015	0.015
	BL (Å)	0.005	0.005	0.005	0.006
Br_2	CT (e)	0.065	0.073	0.074	0.081
	BL (Å)	0.042	0.050	0.049	0.054
I_2	CT (e)	0.010	0.027	0.030	0.049
	BL (Å)	0.020	0.025	0.025	0.028

[a]Elongation is relative to experimental measurements of isolated molecules.[5]

where E_{system}, $E_{graphene}$, and $E_{molecule}$ are total energies of the relaxed graphene-halogen system, pristine graphene, and halogen molecules, respectively. Table 3 shows the binding energy and equilibrium graphene-molecule distance for the various binding sites considered (see Fig. 1). For F_2 on 1-layer graphene, the binding energy of site A is slightly less (4 meV) than site G but nearly the same. For Cl_2, Br_2, and I_2, the binding energies of parallel configurations (A-D) are generally much larger than the perpendicular configurations (E-G). Adsorption site B is the least stable of the parallel orientations, while adsorption site A is found to be the most stable. Site A is typically about 20 meV more stable than the other parallel orientations, which all have similar binding energies within a range of 3-13 meV per unit cell. The perpendicular configurations are notably less stable than site A in all cases except for F_2, where site G is comparable. However, upon considering F_2 on 2- and 3-layer graphene, the binding energies of site A are 17-30 meV per unit cell more than on site G (See Table S1 in the Supplementary Information). Analogous results are found for all of the halogens. Given the comparable binding energies of fluorine at sites A and G for single layer graphene, and the universal agreement that site A is most stable for

Table 4.3. Binding energy (meV) and equilibrium molecule-layer distance in parentheses (Å) for single layer graphene-halogen systems at different adsorption sites shown in Fig. 1. For perpendicular orientations, the distance corresponds to the nearest halogen atom.

X_2		A	B	C	D	E	F	G
F_2	(meV)	482	464	464	461	449	364	486
	(Å)	2.919	2.968	2.966	2.971	2.405	2.826	2.278
Cl_2	(meV)	241	219	221	223	203	175	207
	(Å)	3.477	3.566	3.548	3.554	3.107	3.317	3.071
Br_2	(meV)	281	259	263	267	247	204	255
	(Å)	3.601	3.671	3.655	3.641	3.147	3.410	3.104
I_2	(meV)	367	350	355	363	295	261	300
	(Å)	3.744	3.771	3.761	3.748	3.344	3.521	3.309

[a]For perpendicular orientations, the distance corresponds to the nearest halogen atom.

multilayer graphene-halogen systems, all of the following calculations will be based on halogen adsorption at site A.

Our assertion that parallel adsorption site A is the most stable is consistent with the work of Rudenko et al.[222] They incorporated dispersion using the vdW-DF scheme to perform energy calculations on halogen-graphene (1-layer) systems. However, instead of carrying out a geometry relaxation for each configuration, they kept the molecular orientation and bond length fixed, and determined the distance of the molecules from the graphene plane by searching for the minimum energy configuration. Using this procedure, they also found that the parallel adsorption site A was most stable. However, since in our calculations the system is relaxed geometrically, we find the molecule-graphene separation distance is smaller than distance they reported by 0.11, 0.14, and 0.06 Å for Cl_2, Br_2, and I_2 respectively.

The same stable site A for Cl_2 was also confirmed by a previous calculation of Ijiäs et al.[223] Their binding energy was 2 - 3 times larger and their distance between Cl_2 and graphene layer was 0.3 - 0.4 Å less than our results. However, the perpendicular adsorption site G was calculated to be most energetically stable for Cl_2 by Liu et al.[224] This may be attributed to the use of GGA functional but without including van

der Waals interaction. The Cl_2-graphene distance at site A was 0.28 Å larger than ours, in the absence of dispersion. In another investigation on Br_2 adsorbed on monolayer graphene, LDA was used to study the energetics and electronic properties.[225] Contrary to our vdW-TS calculation, they found that the perpendicular binding site G (Br_2 residing exactly above a carbon atom) was energetically the most stable. This is contrary to our findings, as there are several parallel site configurations with larger binding energies. In particular, we find parallel site A to be 26 meV per unit cell more stable than perpendicular site G. Indeed, their calculation shows that the binding energy of three perpendicular sites are all larger than or equivalent to those of their parallel sites. The difference in predicted conformation likely originates from their approach of using LDA without including dispersion corrections, which neglects London forces that can affect geometries of surface complexes. Given the various reports in the literature, the question of preferred halogen binding orientation on graphene still exists, especially on multilayer structures. Below we address this specifically, including vdW corrections, for all of the halogens on various graphene polymorphs.

Halogen adsorption on multilayer graphene. Here we present the binding properties of halogen molecules on multilayer graphene structures. Only binding site A is considered, as this configuration was found to be the most stable (see Table S1 and preceding discussion). Table 4 displays the binding energies and equilibrium distances between halogen molecules and the nearest layer in 1-, 2-, and 3-layer graphene. The binding energies of X_2G1 are notably smaller than those of X_2G2, X_2G3_{ABA}, and X_2G3_{ABC} for all four halogen molecules. Generally, the binding energy increases with molecular polarizability and upon increasing the layers of graphene (F_2 displays slightly different behavior as described above). The largest increase occurs going from 1 to 2-layer graphene, where the binding energy increases approximately 6 % - 16 %. After this only minimal stability gains are achieved by adding an additional carbon layer. Note that for a specific molecule, the adsorption distances are almost

Table 4.4. Binding energies (meV) and equilibrium distances (Å) between halogen molecules and the nearest graphene layer in multilayer structures. Molecular adsorption is at site A.

X_2		A	B	C	D
F_2	(meV)	482	521	504	526
	(Å)	2.919	2.925	2.918	2.926
Cl_2	(meV)	241	277	284	289
	(Å)	3.477	3.481	3.471	3.465
Br_2	(meV)	281	326	334	339
	(Å)	3.601	3.606	3.593	3.594
I_2	(meV)	367	422	432	437
	(Å)	3.744	3.737	3.735	3.730

identical regardless of the number of layers, suggesting the strongest interactions between the molecule and graphene occur largely between the molecule and the nearest layer.

Electronic properties. The electronic properties of the halogen-graphene systems have been calculated using the same level of DFT described above. The molecular orientation was chosen to be parallel to the graphene sheets at adsorption site A. Fig. 2 shows a set of band structures for F_2 adsorbed on 1-, 2-, and 3-layer graphene, which is representative of the entire halogen series studied here. The Fermi level of the bands is pushed down below the valence band maximum (VBM) because of electron depletion from the graphene -band. The primary feature to note is the energy gap that opens up at the K-point resulting from the molecular adsorption. The bandgap data at the K-point for all the halogen-graphene systems are collected in Table 5. The magnitude of the energy gap varies considerably with the layers of graphene included and the halogen adsorbed. For single layer graphene, F_2, Br_2, and I_2 open a negligible bandgap of 3-8 meV while Cl_2 opens a gap of 75 meV. When adsorbed on 2-layer graphene, they generate much larger gaps except for Cl_2 with a decrease to 67 meV. However, F_2, Br_2, and I_2 show dramatic increases to 227, 56, and 35 meV, respectively. For 3-layer graphene, ABA and ABC graphene yield different

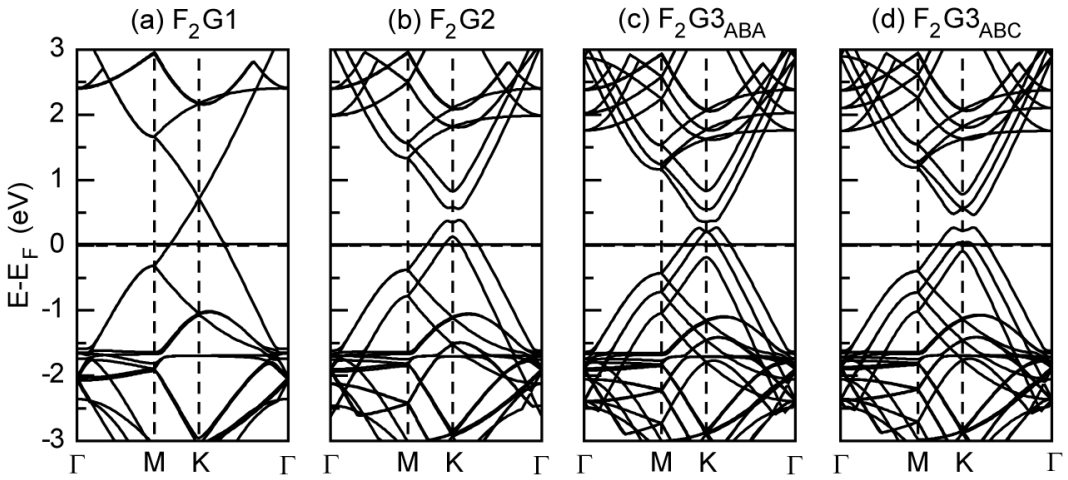

Figure 4.2. Band structure of F_2 adsorbed on (a) 1-layer, (b) 2-layer, (c) 3-layer ABA, and (d) 3-layer ABC stacking graphene. The dotted line indicates the Fermi level.

Table 4.5. Bandgap (meV) of halogen-graphene systems at the K-point in the first Brillouin zone. Molecular adsorption is at site A.

E_{gap} (meV)	X_2G1	X_2G2	X_2G3_{ABA}	X_2G3_{ABC}
F_2	3	227	150	330
Cl_2	75	67	12	78
Br_2	8	56	45	98
I_2	8	35	28	76

trends. The bandgaps induced in ABA stacking show a decrease from the 2-layer case for all halogens by 20-82 %. Conversely, ABC stacking yields an increase from 2-layer graphene of 45 %, 16 %, 75 %, and 117 % for F_2, Cl_2, Br_2, and I_2, respectively. For F_2, the X_2G3_{ABC} structure produces the largest bandgaps at the K-point of 330 meV. For Cl_2, Br_2 and I_2, their X_2G3_{ABC} structures produce band gaps in the range 76-98 meV. The larger energy gaps for F_2 compared Cl_2, Br_2, and I_2 (as well as other dissimilar trends reported) likely originate from the sizeable charge transfer found for these halogen systems.

Further insight into the band gap trends of the various layered systems can be gleaned from symmetry considerations. The symmetry group of monolayer (D_{6h})

and trilayer ABA (D_{3h}) graphene has a horizontal mirror symmetry, which protects the splitting of π and π^* bands even with the existence of an external electric field.[212] Halogen molecules function similarly to an electric field by inducing charge polarization. Therefore, the π and π^* bands are hardly split by halogen molecular adsorption, leading to small gaps in X_2G1 and X_2G3_{ABA} systems. However, the symmetry group of 2-layer and 3-layer ABC graphene are both (D_{3d}) and lack a horizontal mirror symmetry. Thus, the splitting of the π and π^* bands can be modulated to a larger degree by the redistribution of charges[212] brought by halogen molecular adsorption, resulting in larger bandgaps.

More generally, the origin of the bandgap and system properties can be understood by considering the effect adsorbed halogens have on the electronic properties of graphene. In pure graphene, it is well known that the valence and conduction bands intersect at the Fermi level and are linearly dispersed at the K-point, leading to zero mass electrons.[187] With halogen molecules adsorbed on graphene, the π and π^* bands are disturbed around the Dirac point and a bandgap emerges as shown in Fig. 2. Additionally, we find the Fermi level is pushed down in energy with respect to the VBM because of charge transfer between graphene layer and the molecule.[36,226] Such a shift is indicative of electrons transferring from graphene (donor) to the molecules (acceptor), p-doping the substrate. As more layers of graphene are included, the depression of the Fermi level is less due to stabilization provided by additional lattice sites capable of redistributing charge to hedge carrier depletion from molecular adsorption (Fig. 2ad). Lastly, the interaction with the molecule produces a flat impurity band that resides just above the Fermi level and below the VBM. This impurity band is very clearly visible in the density of states (DOS) as a peak just above the Fermi level (Fig. 3). Compared with pure graphene, the DOS of a graphene-halogen system is no longer linear near the Fermi level, or precisely zero at the Fermi level where valence and conduction bands normally meet. The destruction of the canonical dispersion of

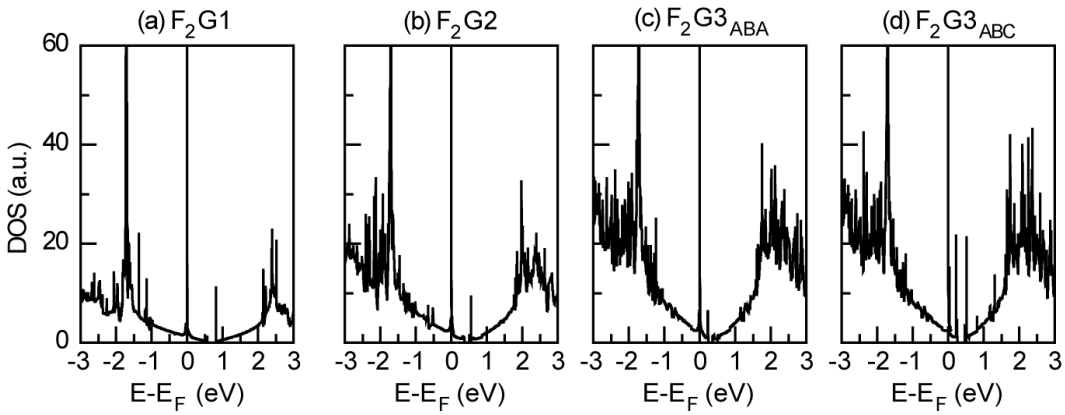

Figure 4.3. DOS of F_2 adsorbed on (a) 1-layer, (b) 2-layer graphene, (c) 3-layer ABA, and (d) 3-layer ABC stacking graphene. Note the states corresponding to the impurity band just above the Fermi level.

pristine graphene upon the introduction of halogen gas can be attributed to breaking the symmetry of graphene.[186] As a conseqence, the linear dispersion of the valence band and conduction band electrons is destroyed, causing band splitting. This opens up a bandgap at high symmetry K-points in the first Brillouin zone. Moreover, because the underlying symmetry of each graphene polymorphism changes throughout the halogen substitutions, the bandgaps vary as well. In particular, these systems possess characteristics reminiscent of both a semiconductor (small to moderate bandgap) as well as a metal (nonzero DOS at the Fermi level), the behaviors of which could each be displayed under certain conditions. For example, one could imagine tuning the system properties by adjusting the concentration of adsorbed species or meticulously selecting a particular polymorph. Indeed, it has been found experimentally that the in-plane conductance of graphene increases with the concentration of Br_2 surface adsorption.[227] Similar conductivity gains have been reported for I_2 doping and graphene adsorbed with NH_3.[200,201] This suggests that the unfilled impurity band is accessible to carriers near the Fermi energy, confirming some quasi-metallic character as alluded to above.

4.5 Conclusion

We have investigated the behavior of a system containing halogen molecules adsorbed on graphene layers. Taking van der Waals interactions into consideration, the most stable adsorption site of halogen molecules is typically parallel to the graphene surface, with the diatomic atoms centered over two adjacent carbon rings. The molecule-surface interaction, charge transfer, and symmetry breaking introduce a band gap into the band structure, whose magnitude depends on the halogen species and the number of layers of graphene. The electronic properties are further altered by a shift down in the Fermi level and the introduction of an impurity band just above the Fermi level but below the valence band maximum. These results suggest that the interaction of halogen species and graphene can be used as a mechanism to adjust the optical, electronic, and transport properties of these systems, potentially towards application as a practical device.

4.6 Supplemental Information

Table 4.6. Binding energy (meV) for halogens on different adsorption sites (A-G) of 1-, 2-, and 3-layer graphene.

X_2-Graphene	A	B	C	D	E	F	G
F_2G1	482	464	464	461	449	364	486
F_2G2	512	499	495	491	469	388	487
F_2G3_{ABA}	504	486	486	487	464	381	487
F_2G3_{ABC}	526	507	507	505	479	399	496
Cl_2G1	241	219	221	223	203	175	207
Cl_2G2	277	254	256	258	231	200	238
Cl_2G3_{ABA}	284	258	260	262	235	203	238
Cl_2G3_{ABC}	289	259	260	262	236	203	238
Br_2G1	281	259	263	267	247	204	255
Br_2G2	326	302	305	311	287	234	286
Br_2G3_{ABA}	334	309	313	316	288	239	295
Br_2G3_{ABC}	339	311	315	320	286	238	291
I_2G1	367	350	355	363	295	261	300
I_2G2	422	405	410	418	334	299	340
I_2G3_{ABA}	432	413	417	426	339	305	347
I_2G3_{ABC}	437	414	415	426	339	304	347

CHAPTER FIVE

Archimedean (4,8)-Tessellation of Haeckelite Ultrathin Nanosheets Composed of Boron and Aluminum-Group V Binary Materials

This chapter published as: Paul A. Brown and Kevin L. Shuford *Nanoscale*, **2016**, 8, 19287-19301

5.1 Abstract

A compendium of unique haeckelite boron and aluminum-group V binary materials have been assessed for their fundamental thermodynamic and ground state electronic properties within density functional theory. We explore their thermodynamic stability relative to new bulk haeckelite crystal structures and find a number of stable polymorphs of planar and buckled ultrathin nanosheets. The bulk boron and aluminum haeckelite crystals display semiconducting and metallic behavior. From the dispersion curves, we predict the formation of both indirect and direct bandgap crystals. We also discover the existence of a five-coordinate aluminum antimonide crystal hitherto never before observed. Moreover, it is found that a number of the Archimedean four and eight membered ring tessellation planar nanosheets could form should synthesis be attempted. It is predicted that these nanosheets can attain two configurations - planar and buckled. From this work we find that combinations of elements such as boron and nitrogen or phosphorus, and aluminum and nitrogen will likely become true single-atom thick nanosheets. These materials show intrinsic indirect bandgap character, which spans the ultraviolet, visible, and infrared spectrum. In the boron series of these materials, the planar structures show double extrema in the bandstructures with van Hove singularities in the projected density of states at the Fermi energy suggesting strong light-matter interactions. The aluminum series we observe strong charge transfer and larger indirect bandgap nanosheets. This

study serves as a starting point for a new class of inorganic bulk and ultrathin film materials, which can have many varied applications in nanotechnology.

5.2 Introduction

Ultrathin two-dimensional materials have emerged as a versatile component to fundamental research involving cross-fertilization of disciplines for their characterization. Since the isolation of graphene in 2004,[6,129,228] many new two-dimensional thin films have emerged like transition metal dichalcogenides,[229,230] black phosphorus,[229,230] mica,[229] MXenes,[229,230] covalent organic frameworks,[229,230] III-V materials,[194,231–238] etc., where these materials possess exceptional electronic, mechanical, and optical properties. Much of the impetus for research into these materials can be traced to their two-dimensional confinement with weak interlayer interactions, high mechanical flexibility, expansive active surface area, and optical transparency.[229,230] Consequently, two-dimensional ultrathin films have found new roles in many diverse areas as support and active components to emerging nanotechnologies like biomedicine,[221,230] energy storage and conversion,[12] electronics/optoelectronics,[6,10,142,143,239] and catalysis.[238,240] However, the most studied ultrathin films possess hexagonal symmetry like graphene, or transition metal dichalcogenides and boron nitride.[229]

Among the many emerging ultrathin films the III-V class exhibit many useful properties and structural polymorphisms. Such combinations of elements have varied applications for light-emitting diodes,[241,242] lasers,[243–245] and solar photovoltaics.[246,247] Recent research on two-dimensional thin films involving combinations of III-V elements have been extensively covered for hexagonal structures.[194,231,232,234–238] It was predicted that the possibility of forming honeycomb structures of combinations of III-V elements could be achieved with these metastable materials. Moreover, Singh et al., predicts that isoelectronic III-V ultrathin films could form with formation energies in the range of 0.1-1 eV/atom relative to bulk. And, Zhuang et al., predicted that these isostructural nanosheets possess a range of material properties from semiconducting

to metallic.[231,232] Incidentally, around that time hexagonal AlN was synthesized by molecular beam epitaxy, where STM measurements realized the formation of h-AlN on Au(111) surface.[248] Moreover, h-GaN was synthesized using a novel technique of graphene encapsulation to form both monolayer and bilayer nanosheets of both planar and buckled configurations.[249]

Recently it was predicted that a haeckelite configuration of GaN nanosheet and nanotubes possess competitive electronic properties to existing two-dimensional ultrathin films.[250] Haeckelite structures can be composed of polynuclear rings of four, five, six, seven, and eight members.[250–252] It was reported that haeckelite GaN possesses an indirect band gap of approximately 1.60 eV, and could be chemically modified to become a direct bandgap with values ranging from 1.54-3.45 eV predicted from semilocal exchange-correlation density functional theory.[250] Moreover, because of its low cohesive energy, this Archimedean (These are semiregular tessellations of regular polygons repeated periodically with the regular polygons forming along their vertice.) motif exhibits thermodynamic stability, which suggest potential few-layer nanosheet formation from possible exfoliation of the bulk (4,8)-GaN crystal.[250] Two-dimensional ultrathin films of this type will require novel synthetic strategies such as on-surface polymerization, where large varities of two-dimensional monomeric units form from covalent coupling to generate low-dimensional configurations with varying ploymorphisms and ring structures.[253–256]

We extend this haeckelite (4,8)-configuration to both boron and aluminum nanosheets. This article explores the ground state electronic properties of novel haeckelite structures composed of group-III and group-V elements with density functional theory.[54,61] In particular, we consider boron and aluminum combinations of pnictogens, which taken within their respective entirety are referred to as the boron and aluminum series. Furthermore, we explore the thermodynamic stability of these boron and aluminum haeckelite structures by determining their formation energy relative

to bulk, cohesive energy of each nanosheet, and ground state electronic properties. We find two configurational structures composed of in-plane and buckled thin films with reasonable stability. Moreover, we observe the formation of indirect bandgaps in these nanosheets spanning the infrared, visible, and ultraviolet suggesting possible use in light-driven nanotechnologies. Our discussion begins with the boron series and proceeds to the aluminum series where we cover the structural, thermodynamic, and electronic structure of each combination of the haeckelite series presented below. Finally, we conclude with possible candidates for experimental synthesis based on the key factors discussed in the preceding sections.

5.3 Computational Method

5.3.1 Computational Details

All ground state predictions herein are obtained within semilocal density functional theory employing the Perdew-Burke-Ernzerhof (PBE) exchange correlation approximation.[85] We use the Vienna ab-initio simulation package (VASP),[114] where the core-valence interaction is approximated within the projector augmented wave (PAW) method.[113] The ns^2mp^3 and ns^2mp^1 atomic configurations are used for the pnictogen and boron/aluminum elements core-valence pseudopotentials within the PAW method. The plane wave expansion was converged to 600 eV with a reciprocal space sampling of 42 x 42 x 1 gamma-centered and 12 x 12 x 12 Monkhorst- Pack[216] grids for haeckelite nanosheets and bulk crystals respectively. We also introduce a vacuum space of 12 Å and 18 Å for the nanosheet crystals of planar and buckled geometries respectively. The smearing width was set to 0.03 with finite temperature Gaussian smearing,[165] which has been applied to all band structures. For all crystal structures the forces are converged well below 1 meV/Å with external pressure less than 0.01 GPa. Moreover, the ground state energetics were converged to less than 1 meV. The resulting optimized ground state structures are presented in later sections.

The projected density of states (PDOS) was tabulated with the tetrahedron method plus Blöchl corrections.[166] Furthermore, all energetic tabulations made herein were computed from this approach.

5.3.2 Thermodynamic Stability

The thermodynamic stability is assessed by comparison to bulk crystal structures. In order to ascertain the thermodynamic stability of each nanosheet, we determine the formation energy of each combination using

$$E_f = \frac{1}{\mathcal{N}}[E_{ns} - (n_C\mu_C + n_{PN}\mu_{PN})] \tag{5.1}$$

where E_{ns} is the total energy of haeckelite nanosheet, μ_C is the chemical potential of boron or aluminum cation and μ_{PN} is the chemical potential of the pnictogen, $\mathcal{N}$, n_C, and n_{PN} are the total number of atoms in the unit cell, total number of boron or aluminum atoms, and total number of pnictogen atoms per unit cell, respectively. The chemical potentials of boron and aluminum are taken from bulk rhombohedral boron and FCC aluminum, where the latter is a naturally occurring reference state. It is important to mention that the homogeneous formation of elemental boron does not occur in nature. Thus, for continuity of our computations of formation energies containing boron, we've selected a homogeneous synthetic polymorph of boron. For the pnictogens we have extracted their chemical potentials from their respective reference states of formation (gaseous nitrogen, white phosphorus, arsenic grey, and orthorhombic antimony). Hence, the change in formation energy to form an ultrathin haeckelite nanosheet is obtained in this work by the expression

$$\Delta E_f = E_f^{2D} - E_f^{3D} \tag{5.2}$$

where E_f^{2D} and E_f^{3D} are the formation energies determined by Eqn. 5.1. Moreover, to get a sense of the depth of the potential energy of coalescence of elements forming each haeckelite nanosheet, we define the cohesive energy as

$$E_{coh} = \frac{1}{\mathcal{N}}[E_{ns} - (n_C E_C + n_{PN} E_{PN})] \tag{5.3}$$

where E_C is the total energy of the spin polarized boron or aluminum atom, and E_{PN} is the total energy of spin polarized pnictogen atom with respect to the number of atoms per unit cell. These quantities are tabulated and presented in the forthcoming sections.

5.4 Results and Discussion

5.4.1 Boron Series

5.4.1.1 Bulk Boron Pnictogen Crystals.

In this section we delineate the fundamental ground state and structural properties of the boron series of bulk haeckelite structures. We have formed each lattice following a similar construction as that reported elsewhere,[250] and the optimized crystal structures are displayed in Fig. 5.1 using the computational method above. We employ the shorthand H-B_8PN_8 to designate haeckelite structures with unit cell stoichiometry as subscripts in this work. As shown in Fig. 5.1, all boron pnictogen combinations form a body-centered tetragonal lattice, whose coordination yields tetrahedra around both boron and pnictogen elements with I4cm (C_{4v}^{10}) symmetry.[257] These crystals display gradual bond lengthening with increasing atomic number, and Bader analysis shows charge transfer is predominantly from boron to pnictogen elements (Table 5.1).[258,259] However, bulk H-B_8Sb_8 shows a dramatic reversal of charge transfer to the boron atom, -0.49 e/at., whereas lower atomic number congeners

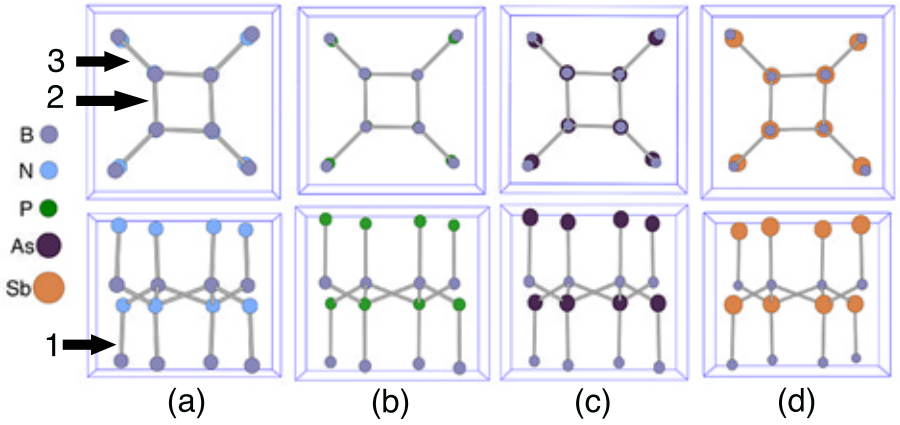

Figure 5.1. Top and side view of bulk haeckelite structures of the boron series. (a) H-B_8N_8, (b) H-B_8P_8, (c) H-B_8As_8, and (d) H-B_8Sb_8. 1-3 indicate bond labels for crystallographic directions: 1 c-axis, 2 ab-plane, and 3 diagonal. An expanded unit cell of H-B_8N_8 is shown as a representative model for bulk crystals of this type, Fig. S2.

display an opposite charge transfer effect. Incidentally, the cohesive energies rise implying a lower stability in these latter bulk haeckelite crystals, where the most stable H-B_8N_8 has a value of -5.319 eV/at. Coupled with these physical attributes, the formation energies also rise following a similar pattern of decreasing stability with increasing atomic number, with H-B_8N_8 obtaining the lowest formation energy, -0.998 eV/at., relative to standard state compounds. And H-B_8P_8 shows a stable energy of formation, -0.316 eV/at., while H-B_8As_8 and H-B_8Sb_8 show unstable formation energies relative to their standard states. Hence, stability in these crystalline structures proceeds as H-B_8N_8 > H-B_8P_8 > H-B_8As_8 > H-B_8Sb_8.

The formation of each combination of boron paired with a pnictogen yields a series of semiconducting crystals, whose bandgaps vary across the UV to IR, Table 5.1. However, only H-B_8N_8 has a direct bandgap at the Γ point (Fig. 5.2) , whereas H-B_8P_8 onwards possess an indirect bandgap where the conduction band edge is highlighted with a red dot along the Z-P high symmetry direction. From the PDOS, we see a notable presence of p-manifold of states contributed from the lower atomic number pnictogens, Fig. 5.3a, yet this contribution diminishes to higher

Table 5.1. Bulk boron haeckelite pnictogen crystals. For each material we show the boron-pnictogen bond length $d(B-PN)$ [Å] enumerated 1 - 3 for the c-axes, ab-plane, and diagonal bonds respectively, bandgap energy E_g [eV], charge transfer from boron to the pnictogen Δq [e/at.], cohesive energy E_{Coh} [eV/at.], and the formation energy E_f [eV/at.].

Material	$d(B-PN)$	E_g	Δq	E_{Coh}	E_f
H-B_8N_8	1.561, 1.612, 1.511	4.809	2.12	-5.319	-0.998
H-B_8P_8	1.981, 1.989, 1.938	1.200	0.41	-5.194	-0.316
H-B_8As_8	2.095, 2.110, 2.054	1.178	0.05	-4.538	0.159
H-B_8Sb_8	2.297, 2.315, 2.255	0.890	-0.49	-4.028	0.534

atomic number pnictogens, Fig. 5.3d. This can be attributed to the charge transfer previously discussed to which less charge is captured by the pnictogen elements as one proceeds to higher atomic number (Table 5.1). Moreover, a reversal occurs with H-B_8Sb_8, thus boron quantal states contribute to a greater extent near the Fermi energy. This suggests that the overall chemical bonding within these bulk crystals begins polar bonding with H-B_8N_8/H-B_8P_8 , covalent bonding H-B_8As_8, and polar-covalent bonding for H-B_8Sb_8. The ground state electronic structure indicates a weakening of the overall bonding as the splitting of valence and conduction bands lessens, hence the bandgap lowers, as shown in Fig 5.2. It is interesting to note that there is a sudden drop in bandgap going from H-B_8N_8 to H-B_8P_8, where H-B_8N_8 exhibits insulating character while H-B_8P_8 forms an optical semiconductor with a bandgap difference of 3.609 eV. This conspicuous lowering of the band edges can be understood from the charge transfer between boron and pnictogen elements. Furthermore, this disparity emerges from atomic (Pauli) electronegativities of the elements themselves, which underscores the trends discussed here. Thus, the greater the difference in electronegativity between boron and pnictogen atoms results in shorter bond lengths, and greater electrostatic stabilization between ions. Indeed, this is apparent from the ground state charge density of each crystal displayed in Fig. 5.4. We see regions of the bulk crystal with larger concentrations of charge (red) versus deprivation of charge (blue). For H-B_8N_8 there is immoderate localization around nitrogen

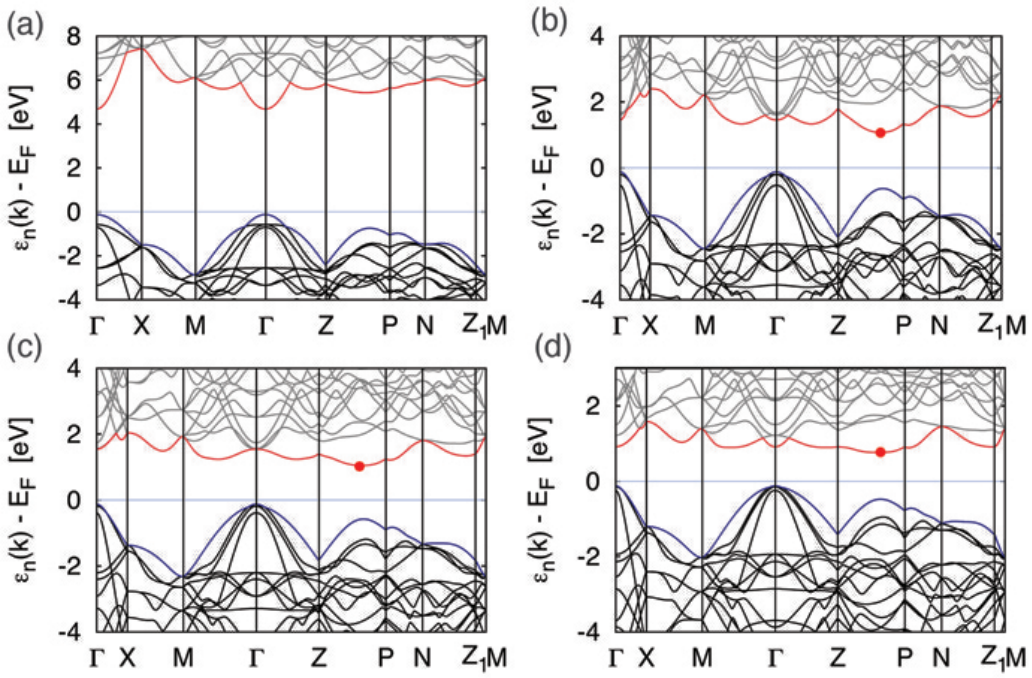

Figure 5.2. Dispersion curves of bulk boron haeckelite structures. (a) H-B_8N_8, (b) H-B_8P_8, (c) H-B_8As_8, and (d) H-B_8Sb_8. The red dot indicates the conduction band extrema for indirect bandgap materials.

centers, whereas proceeding down pnictogen congeners to antimony there is greater delocalization of charge. Transitioning to H-B_8P_8, we can see that the strong localization of charge around the pnictogen has lessened. This is evidenced by lesser charge transfer, Table 5.1. For H-B_8As_8 (Fig. 5.4c), we predict lesser polarization of charge density around the pnictogen centers as high density regions become more covalent in this bulk haeckelite material. Hence proceeding down group-V, the elemental properties like electronegativity weaken. Consequently, the binding of electrons around the pnictogen centers decreases, lowering the bandgap. However, once we reach H-B_8Sb_8 the reversal in charge transfer can be clearly seen in Fig. 5.4d, where the charge is redistributed onto the boron centers. This preserves the bandgap trend, hence this material remains semiconducting. These bulk haeckelite crystals will serve as a starting point for the formation of the ultrathin nanosheets of the boron series.

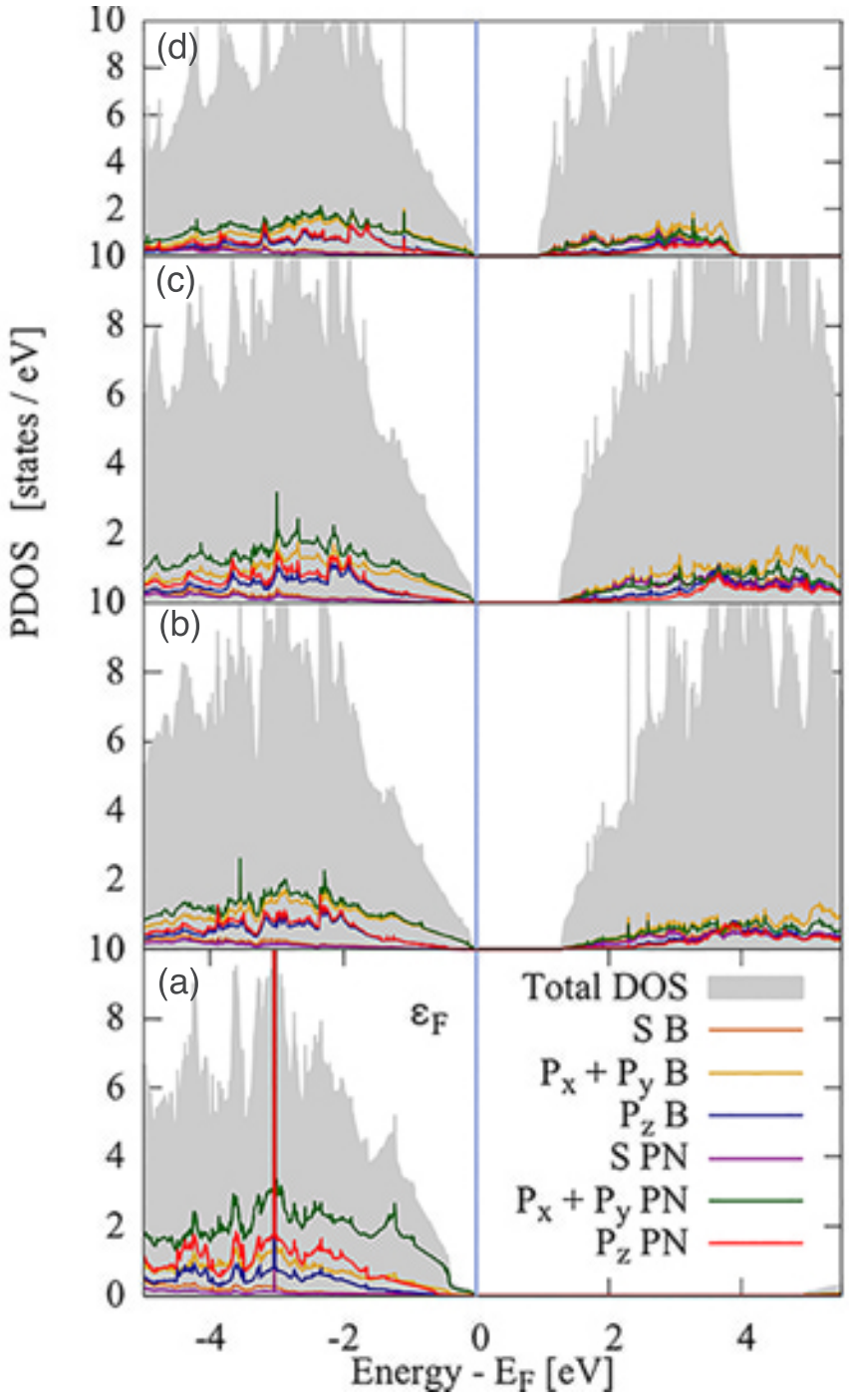

Figure 5.3. Projected density of states of bulk boron haeckelite structures. (a) H-B_8N_8, (b) H-B_8P_8, (c) H-B_8As_8, and (d) H-B_8Sb_8. The blue vertical line indicates the Fermi energy, ϵ_F.

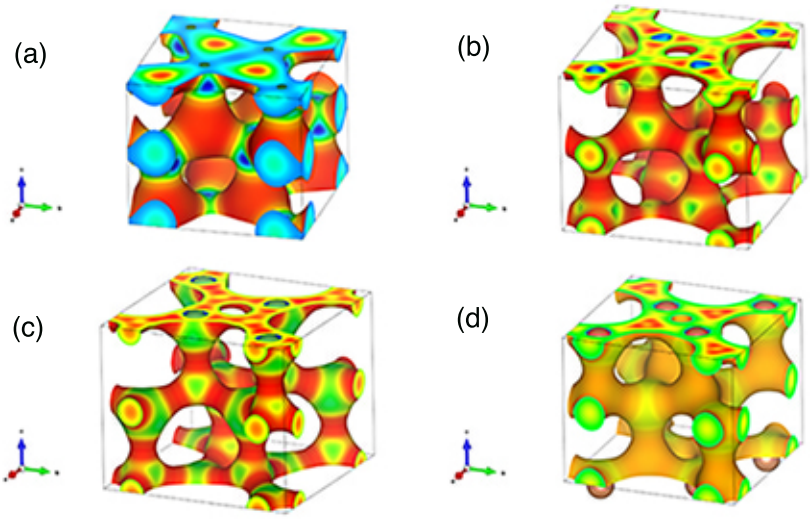

Figure 5.4. Isosurfaces of bulk haeckelite boron pnictogen crystals. (a) H-B_8N_8, (b) H-B_8P_8, (c) H-B_8As_8, and (d) H-B_8Sb_8. The charge density is projected onto the local potential to render the color map. Here red regions depict greater amounts of charge (e) per unit volume (Å^3).

5.4.1.2 Haeckelite Boron Nanosheets.

We begin our discussion of boron haeckelite ultrathin nanosheets with the structural and thermodynamic results shown in Fig. 5.5 and Table 5.2. From optimization within density functional theory, we find that H-B_4N_4 and H-B_4P_4 haeckelite nanosheets remain true two-dimensional crystalline lattices with space group symmetry P4/mbm (D^5_{4h}). For H-B_4N_4 we predict the shortest bond lengths forming a sp^2 hybridized haeckelite network of alternating bond lengths of 1.405 Å and 1.478 Å. Moreover, H-B_4P_4 also obtains similar sp^2 hybridization of 1.818 Å and 1.890 Å (Table 5.2). For these two cases, the longer bond is found to form in the smaller square ring, whereas the shorter bond forms a portion of the eight membered ring, Fig 5.5. Because of the strong electronegativity differences among these pnictogens (N,P) the cohesive energies per atom are quite stable; H-B_4N_4 is -6.778 eV/at. and H-B_4P_4 is -4.710 eV/at. Moreover, the formation energy change to create the two-dimensional films are small to moderate (Table 5.2). It is important to note that *h*-BN has a reported cohesive energy of approximately -7.1 eV/at.,[231] which we have found as

well applying the computational setup reported above. For H-B_4N_4 we find the formation energy, tabulated from Eqn. 5.2, to be 0.050 eV/at., and it increases to 0.482 eV/at. for the H-B_4P_4 nanosheet. This increase in the thermodynamic figures-of-merit can be attributed to the amount of charge transfer between boron and nitrogen or phosphorus. Here we see for H-B_4N_4 the greatest exchange of electrons at 2.20 e/at., whereas its ultrathin counterpart H-B_4P_4 obtains lesser charge transfer at 0.68 e/at. (Table 5.2). The chemical ramification of proceeding from nitrogen to phosphorus leads to the elemental reduction in electronegativity and an increase in ionic radius. Similar to bulk haeckelite boron crystals, the electrostatic interaction weakens in keeping with the elemental properties of the two congeners. Consequently, the strength of attraction between boron and phosphorus weakens making the change in formation energy larger, and thus a discernible decrease in charge transfer. Hence, the potential energy of attraction lowers as well, which increases the bond lengths in H-B_4P_4. This behavior extends to higher atomic number ultrathin films of H-B_4As_4 and H-B_4Sb_4, Table 5.2.

Table 5.2. Boron haeckelite pnictide nanosheets. The 'B' subscript under the material heading indicates buckled cases. For each material we show the boron-pnictogen bond length $d(B-PN)$ [Å], bandgap energy E_g [eV], charge transfer from boron to pnictogen Δ q [e/at.], cohesive energy E_{Coh} [eV/at.], and the change in formation energy to form the nanosheet relative to bulk ΔE_f [eV/at.].

Material	$d(B-PN)$	E_g	Δq	E_{Coh}	ΔE_f
H-B_4N_4	1.405, 1.478	4.077 (4.081)	2.20	-6.778	0.050
H-B_4P_4	1.818, 1.890	0.790 (0.791)	0.68	-4.710	0.482
H-B_4As_4	1.916, 1.999	0.703 (0.702)	0.23	-3.962	0.800
H_B-B_4As_4	2.031, 2.014	1.032	0.05	-4.163	0.372
H-B_4Sb_4	2.115, 2.204	0.361 (0.361)	-0.36	-3.252	1.886
H_B-B_4Sb_4	2.167, 2.343	Metallic	-0.41	-3.659	0.369

As shown in Fig. 5.5, the H-B_4As_4 and H-B_4Sb_4 nanosheets can form two possible configurations – planar (D^5_{4h}) and buckled ultrathin crystals. The buckled

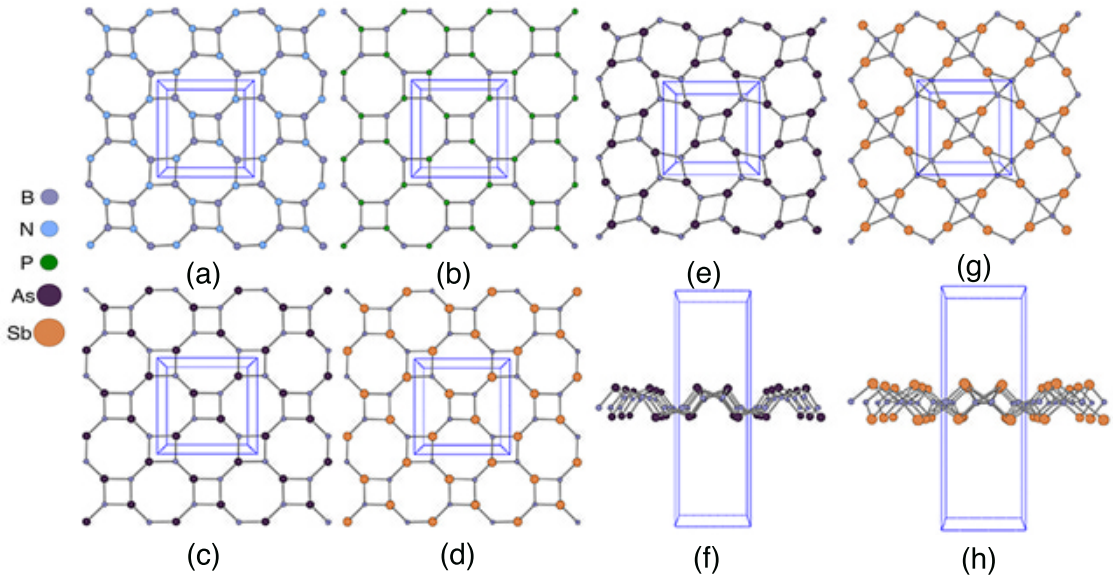

Figure 5.5. Planar (4,8)-tessellation of boron pnictide nanosheets and buckled structures. (a) H-B_4N_4, (b) H-B_4P_4, (c) H-B_4As_4, (d) H-B_4Sb_4, (e) & (f) H_B-B_4As_4, and (g) & (h) H_B-B_4Sb_4. Note that H_B-B_4Sb_4 forms a boron-boron bond connecting the vertices of the tetragonal ring.

ultrathin films, Fig. 5.5e- 5.5h, form corrugations arising from the formation of trigonal pyramidal geometry around both arsenic and antimony, while boron adopts a quasi-trigonal planar geometry within these nanosheets, whose symmetry becomes P-421m (D^3_{2d}). This lowering of symmetry in the buckled H_B-B_4As_4 and H_B-B_4Sb_4 decreases the overall energy of the nanosheet, hence the cohesive energy per atom for H-B_4As_4 is -3.962 eV/at. and H_B-B_4As_4 is -4.163 eV/at. We find H-B_4Sb_4 to be -3.252 eV/at. and H_B-B_4Sb_4 is -3.659 eV/at. The lowering of the cohesive energy can be understood as mitigating increasing ring strain of the square ring while accommodating the larger pnictogen congeners arsenic and antimony. In the buckled H_B-B_4As_4 (Figs. 5.5e & 5.5f), we observe bond lengths of 2.031 Å and 2.014 Å, Table 5.2. Moreover, the bonding in H_B-B_4As_4 suggests the formation of a sp^3 bonding network, whereas H-B_4As_4 nanosheet forms an sp^2 network with the unsaturated 1.916 Å and saturated bond of 1.999 Å, where, like H-B_4N_4 and H-B_4P_4, the unsaturated bond forms a portion of the eight-membered ring and the longer bond

forms the square ring (Table 5.2). A similar pattern occurs for the ultrathin film H-B_4Sb_4; however, for the H_B-B_4Sb_4 structure, an unusual bonding network forms, as shown in Figs. 5.5g & 5.5h. Surprisingly, upon buckling around the tetragonal rings, H_B-B_4Sb_4 forms a boron-boron bond. The bond length is found to be 1.631 Å. This distance suggests that the nature of the bond is unsaturated. Hence, when buckling H-B_4Sb_4 occurs around the square ring, the charge redistributes among the boron atoms and increases the amount of charge transfer rising from -0.36 e/at. to -0.41 e/at. Because of the apparent lowering of the cohesive energy for these cases, the overall change in the energy of formation of the two-dimensional haeckelite nanosheet lowers dramatically, Table 5.2. For H-B_4As_4 and H_B-B_4As_4, the formation energy lowers by 0.428 eV/at. Furthermore, as mentioned above, the preference of bonding network transforms from sp^2 to sp^3. Likewise, the H-B_4Sb_4 and H_B-B_4Sb_4 formation energy change lowers significantly by 1.517 eV/at. The large difference in the change in formation energy proceeding from 3D to 2D between these two materials can be understood to derive from the need to allow antimony to form a distorted trigonal pyramidal geometry. However, because of the competing differences in electronegativity, the loss of charge increases in this structural configuration. Together these two effects permit the unexpected formation of the boron-boron bond to form to which H_B-B_4Sb_4 seemingly enhances its stability. The ground electronic properties and charge density presented below will underscore the thermodynamics discussed here.

We now turn to the ground state electronic properties of boron haeckelite nanosheets shown in Figs. 5.6 & 5.7. In all planar cases, Fig. 5.6a- 5.6d, we observe the formation of intrinsic indirect bandgap semiconductors, whose gap energies span across the ultraviolet to the infrared. Interestingly, we observe a pair of bandgap extrema in these planar haeckelite crystals, where the band edges form along Γ-X and M-Γ high symmetry lines (Fig. 5.6a - 5.6d). The largest bandgap recorded occurs for H-B_4N_4 at 4.077 eV. Moreover, the projected density of states for the

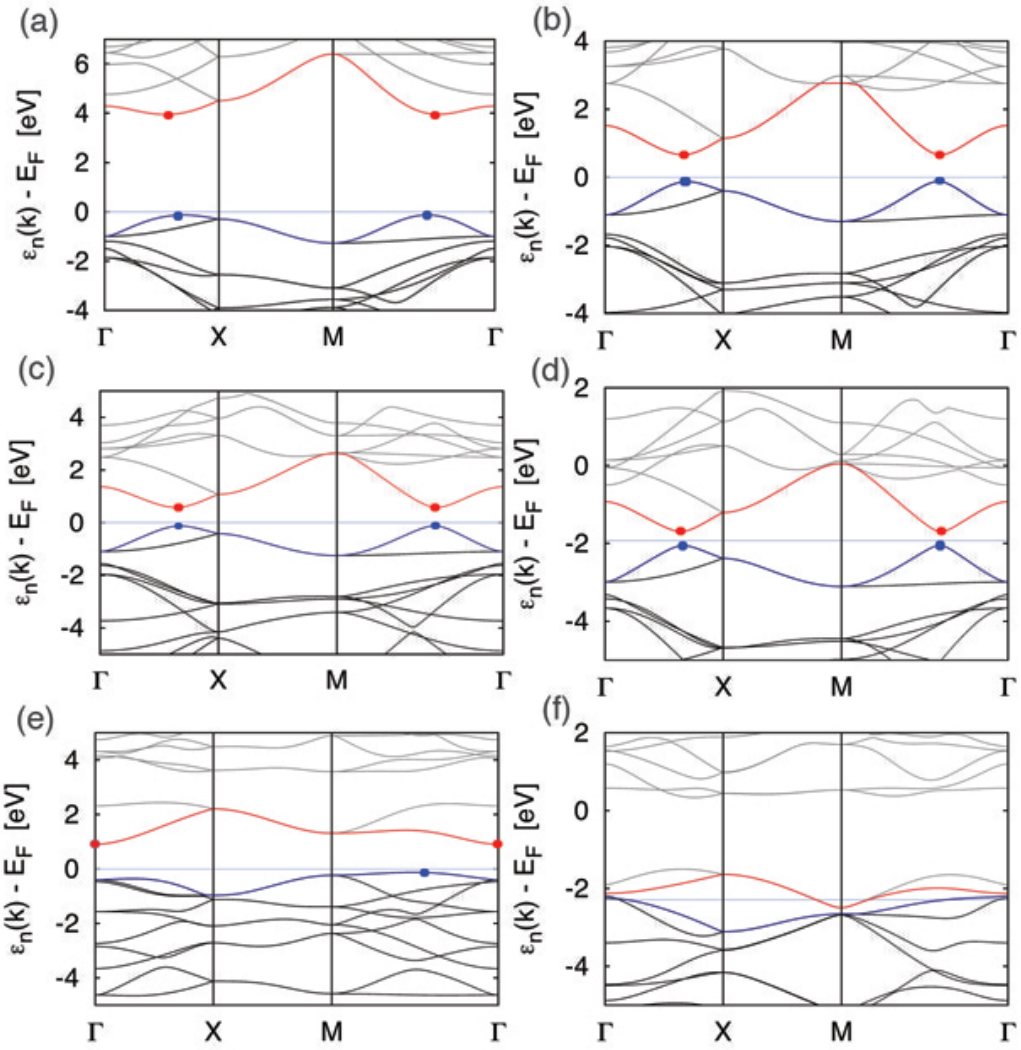

Figure 5.6. Dispersion curves of boron pnictide nanosheets. (a) H-B_4N_4, (b) H-B_4P_4, (c) H-B_4As_4, (d) H-B_4Sb_4, (e) H_B-B_4As_4, and (f) H_B-B_4Sb_4. The band extrema are indicated with blue (valence band maximum) and red (conduction band minimum) dots. The highlighted red band and blue band mark frontier states as a function of crystal wavevector, **k**. The horizontal blue line denotes the Fermi energy.

planar H-B_4N_4 possesses distinct van Hove singularities at the band edges, which arise from the p_z states of nitrogen in the valence band and boron in the conduction band, Fig. 5.7a. In the case of H-B_4P_4 we observe bandgap contraction to 0.790 eV. Further, we see in the PDOS of this material the same arrangement of quantal states near the Fermi energy as that of H-B_4N_4, Fig. 5.7b. The bandgap energies decrease subsequently with increasing atomic number of larger mass congeners for the planar cases (Table 5.2). For H-B_4As_4 and H-B_4Sb_4, the bandgap contraction continues to 0.703 eV and 0.361 eV, respectively. Furthermore, the PDOS depicts similar juxtaposition of quantum states, which follows closely the electronic trends of lighter pnictogen congeners. Hence, we see similar van Hove singularities at the band edges reminiscent of two-dimensional character for all of these planar haeckelite structures. Consequently, these critical points often show up in optical spectra as strong absorption peaks at the gap energy. Moreover, this doubling of band extrema suggest the possibility of interesting light-matter interactions should these materials be synthesized later in planar form.

We observe a departure of the bandgap trend seen in the planar boron haeckelite materials for the buckled configuration. For buckled H_B-B_4As_4 (Fig. 5.6e), the bandgap increases to 1.032 eV. Furthermore, the paired extrema in the planar H-B_4As_4, Fig. 5.6c, is eliminated and a band extremum forms instead only along M-Γ. Because of the formation of the trigonal pyramidal geometry in H_B-B_4As_4, we observe additional mixing in the p_x and p_y manifold of states among boron and arsenic valence electrons. This additional mixing of p-states leads to the formation of antibonding states around 1.5 eV above the Fermi energy, Fig. 5.7e. For H_B-B_4Sb_4 we predict the formation of a metal in the buckled configuration, Fig. 5.6f. Thus, H-B_4Sb_4 may form two phases upon deformation of the ultrathin crystal lattice. Within density functional theory we observe the formation of additional bands near the Fermi energy, Fig. 5.6f. These bands can be attributed to the formation of the boron-boron bond

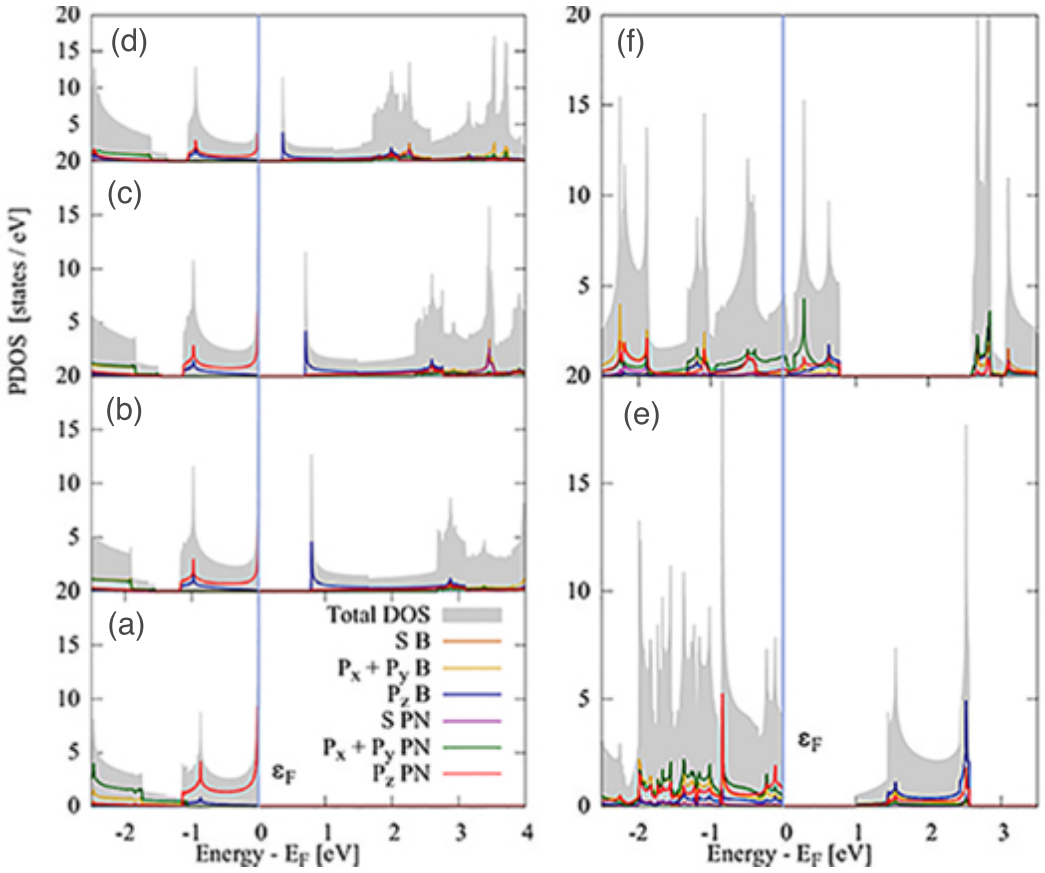

Figure 5.7. Projected density of states of boron pnictide nanosheets. (a) H-B_4N_4, (b) H-B_4P_4, (c) H-B_4As_4, (d) H-B_4Sb_4, (e) H_b-B_4As_4, and (f) H_B-B_4Sb_4. The Fermi energy is displayed as the blue vertical line at zero energy.

and nonbonding electrons around the antimony element resulting from this configurational change. This reordering, the presence of p_x and p_y orbitals at the Fermi energy, of quantal states can be understood as mixing the p-manifold in the distorted trigonal pyramidal geometry as overlapping among these states accumulates. Hence, charge transfer increases slightly in H_B-B_4Sb_4. Consequently, a metallic phase emerges in this haeckelite ultrathin film. However, we will see that the ground state electronic density realizes these physical and electronic properties.

We finish our discussion with the boron series of haeckelite thin films by noting the ground state charge densities of each film displayed in Fig. 5.8. From above we can see the emergence of our DFT predictions. For H-B_4N_4 there is extreme

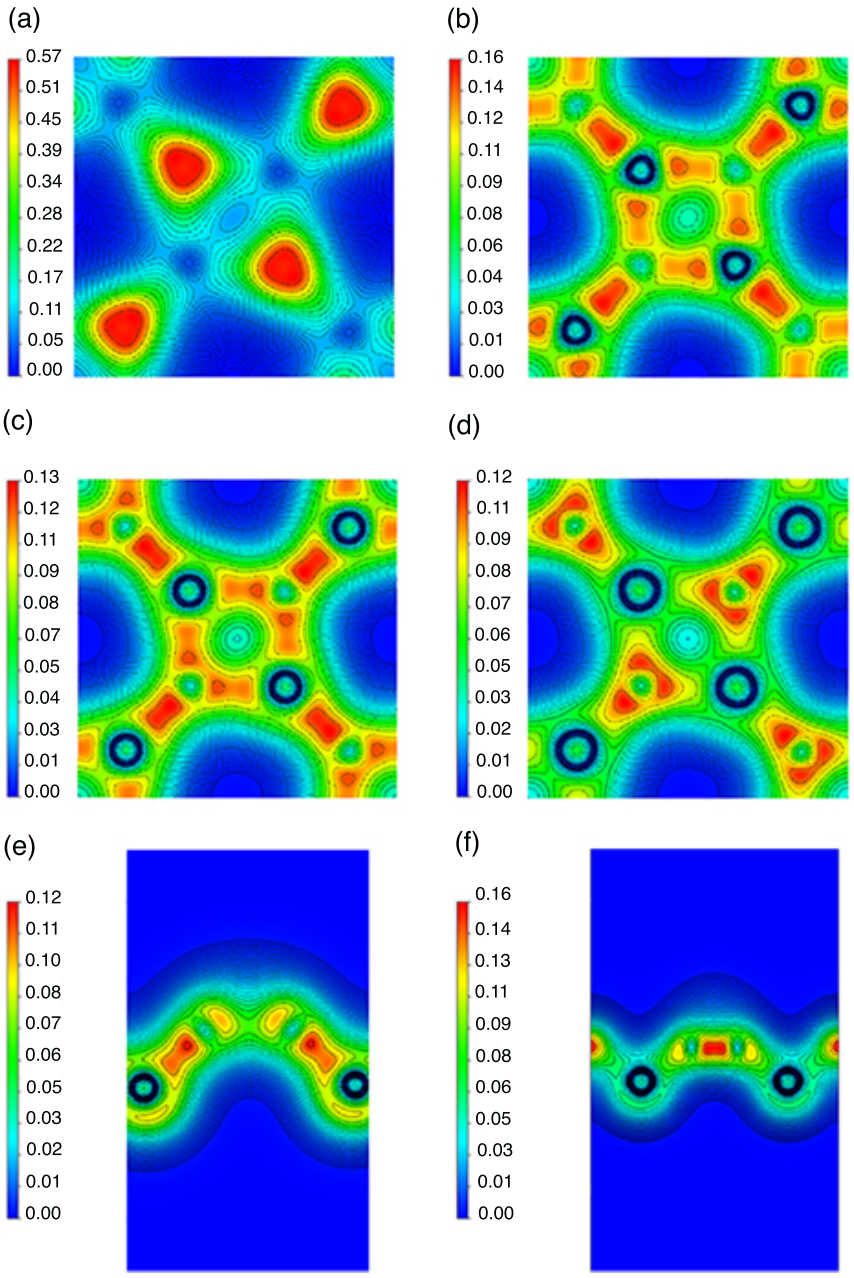

Figure 5.8. Crossectional slices of (001) in-plane charge density of the planar boron haeckelites (a)-(d) and (110) slices of the buckled nanosheets charge density (e)-(f). (a) H-B_4N_4, (b) H-B_4P_4, (c) H-B_4As_4, (d) H-B_4Sb_4, (e) H_B-B_4As_4 and (f) H_B-B_4Sb_4. Note the unit of charge is in absolute atomic units, e Bohr^{-3}.

charge localization suggesting a polar material, as expected from differences in electronegativity and charge transfer between boron and nitrogen. Thus, H-B_4N_4 can be characterized as a wide bandgap intrinsic semiconductor. Continuing with H-B_4P_4 we observe an immediate change in the distribution of charge density among the elements forming this material. Here H-B_4P_4 shows polarization between the boron and phosphorus, but some reorganization leads to lesser abstraction of charge from the boron element. Thus, H-B_4P_4 presents a polar-covalent sp^2 material with a lowering bandgap and lesser charge transfer between boron and phosphorus. Moreover, H-B_4As_4 shows similar charge delocalization between boron and arsenic elements as the overall elemental properties touched upon already vary only slightly. Hence, H-B_4As_4 bandgap lowers slightly and the amount of charge transfer varies little as well, forming an indirect bandgap semiconductor similar to H-B_4P_4. Additionally, the planar H-B_4Sb_4 cross-sectional charge density displays the charge transfer reversal already alluded too above, with charge localization appearing over the boron atoms, Fig 5.8d. Corresponding to this reversal of charge transfer, the subsequent properties discussed above become apparent, Table 5.2, forming a small indirect bandgap semiconductor. Finally, buckled haeckelite H_B-B_4As_4 and H_B-B_4Sb_4 have an interesting arrangement of electron charge density, where we can see the former, Fig. 5.8e, does not have appreciable charge density localized between boron atoms in the center of the figure, while the latter, Fig 5.8f, shows a hot spot of concentrated electron density. A consequence of this charge localization between the boron elements within the tetragonal ring induces very little charge localization between antimony and boron (Fig. 5.8f). Therefore, the electrons in this material are weakly bound and constitute a metallic phase. However, H_B-B_4As_4 shows greater charge build up between the boron and lone pair formation pointing axial or orthogonal to the material located on the arsenic elements to which the material remains semiconducting and of a sp^3 bonding network.

Hence, bandgap expansion occurs for H_B-B_4As_4, while a metallic phase forms in H_B-B_4Sb_4. However, the boron-boron bond that forms in H_B-B_4Sb_4, though a chemical peculiarity, vitiates this material in fact. First, this material forms a metallic ground state, hence the conduction band is accessible to valence electrons under ambient conditions. Second, because of the strong localization of electron charge density between vertices boron elements, weak bonding forms between boron and antimony. With the ratio of bonding types being three B-Sb to one B-B, the predominant bonding within this material is overall weak, Fig. 5.8f. Therefore, this material will likely decay under thermally driven agitation because of the charge inhomogeneity and accessible conduction states for H_B-B_4Sb_4. Consequently, H_B-B_4Sb_4 is unlikely to form in the buckled state. However, it is clear the lighter mass pnictogen congeners will likely form, and, in particular, H-B_4N_4 > H-B_4P_4 > H_B-B_4As_4 > H-B_4As_4 being the arrangement of stability predicted within the boron series. We exclude H-B_4Sb_4 and H_B-B_4Sb_4 because of likely instabilities associated with their formation. Moreover, only H-B_4N_4 and H-B_4P_4 will likely form true one-atom thick ultrathin films as no buckling was observed, while H-B_4As_4 does obtain a competing buckled ground state configuration.

5.4.2 Aluminum Series

5.4.2.1 Bulk Aluminum Pnictogen Crystals.

The aluminum haeckelite bulk crystals display different electronic ground state and structural properties contrasted against the boron bulk haeckelite series. Within the bulk aluminum series (Fig. 5.9), we observe the first few crystals having the same symmetry as that of the boron series, I4cm (C_{4v}^{10}). Thus, this metastable crystal has some structural regularity as seen in the bulk boron haeckelite crystals; however, this is the only similarity shared between these inorganic crystals. As expected, the bond lengths elongate as the counter ion, aluminum, increases in ionic radius. For H-Al_8N_8

we observe an approximately 0.3 Å increase in bond length from interchanging the boron for aluminum. Further, H-Al_8P_8 and H-Al_8As_8 bond lengths increase by 0.4 Å compared to the bulk boron crystals discussed above. Interestingly, within these crystals we observe greater charge transfer between the aluminum and pnictogen congeners, as shown in Table 5.3. In H-Al_8N_8 we observe the greatest charge transfer of 2.36 e/at., which is expected as the greatest electronegativity arises between these two combinations of elements. Thus, H-Al_8N_8 has the lowest cohesive energy at -5.646 eV/at. and the lowest formation energy of -1.255 eV/at. (Table 5.3). Similar ground state trends become apparent for both H-Al_8P_8 and H-Al_4As_4. Because the underlying differences in elemental properties become more moderate, the charge transfer from aluminum to each pnictogen congener decreases slightly to 2.04 and 1.89 for H-Al_8P_8 and H-Al_8As_8, respectively. Hence for H-Al_8P_8, we predict a rise in cohesive energy per atom to -4.042 eV, and consequently an increase in formation energy to -0.603 eV/at. Additionally, for H-Al_8As_8 the cohesive energy increases to -3.646 eV/at., while the formation energy is found to be -0.390 eV/at. Taking both the cohesive energy and formation energy into account, the aluminum bulk haeckelite structures discussed thus far show reasonable thermodynamic stability. Moreover, due to the increase charge transfer within this group, it is apparent this quantity serves to enhance the stability in these crystals.

Table 5.3. Bulk aluminum haeckelite pnictogen crystals. For each material we show the aluminum-pnictogen bond length $d(Al-PN)$ [Å], where we have enumerated as was done for the boron series, bandgap energy E_g [eV], charge transfer from aluminum to pnictogen Δq [e/at.], cohesive energy E_{Coh} [eV/at.], and the formation energy E_f [eV/at.]. Note, H-Al_8Sb_8 is discussed within the body of the text.

Material	$d(Al-PN)$	E_g	Δq	E_{Coh}	E_f
H-Al_8N_8	1.904, 1.945, 1.844	3.29	2.36	-5.646	-1.255
H-Al_8P_8	2.383, 2.403, 2.355	2.00	2.04	-4.042	-0.603
H-Al_8As_8	2.456, 2.501, 2.482	1.46	1.89	-3.646	-0.390

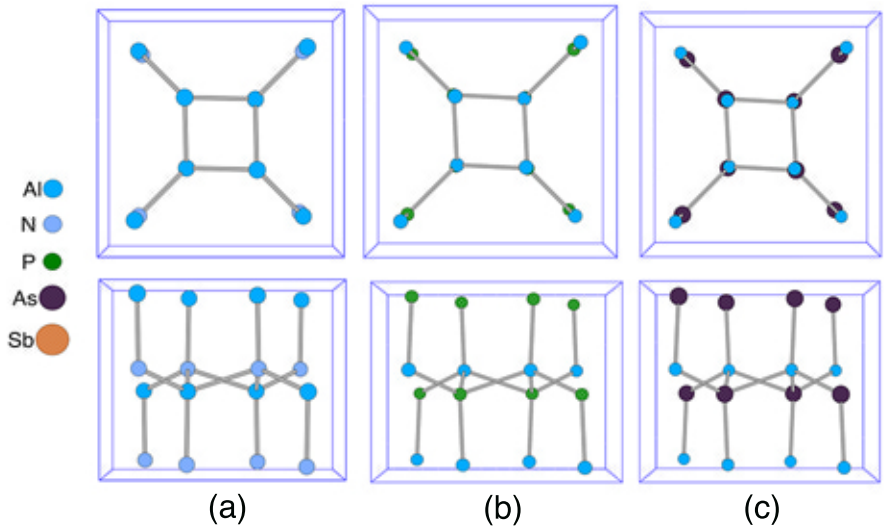

Figure 5.9. Bulk aluminum haeckelite ground state crystal structures. (a) H-Al_8N_8, (b) H-Al_8P_8, and (c) H-Al_8As_8.

We now turn to discuss the H-Al_8Sb_8 bulk haeckelite crystal structural and thermodynamic properties, which merits special attention as this crystal presented an unexpected bifurcation from observations made thus far. Within semilocal density functional theory, our optimization of this crystal lattice resulted in an all together different structure shown in Fig. 5.10. The overall symmetry of this inorganic crystal was found to be body-centered orthorhombic with space group Ibam (D_{2h}^{26}). The interlayer bond length was found to be 2.860 Å (label 4). The distorted tetragonal ring bond lengths, label 1 and 2, were found to be 2.773 Å and 2.921 Å, while the bond length within the octagonal ring, label 3, was found to be 2.857 Å (Fig. 5.10d). As compared to the lower atomic number congeners above, H-Al_8Sb_8 presents the longest bond lengths among the bulk haeckelite aluminum crystals. However, unlike H-Al_8N_8 to H-Al_8As_8 the coordination number changes from four to five. Consequently, the lattice forms into thin film arrangements of aluminum and antimony, and the local geometry switches from tetrahedral to square pyramidal, which is displayed for aluminum polyhedra in Fig. 5.10c. Interestingly, H-Al_8Sb_8 assembles into layers resembling the thin film H-Al_4Sb_4 to be discussed later. The cohesive energy

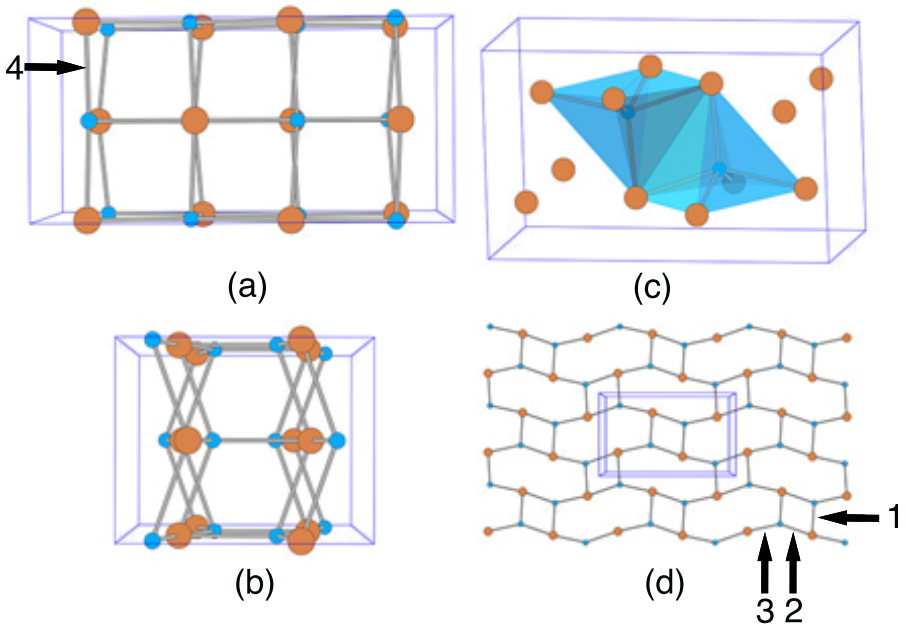

Figure 5.10. Bulk aluminum antimonide crystal structure. (a) (100) crystallographic view and (b) (010) crystallographic view. (c) A single thin layer of of H-Al_4Sb_4 forming the entire crystal structure. (d) Polyhedra of aluminum within the unit cell displaying the unique local five coordinate square pyramidal geometry. An expanded cell is displayed in the supplemental of this bulk crystal, Fig.S3.

per atom increases to -3.042 eV/at., and the formation energy was predicted to be -0.293 eV/at. Hence, this combination of elements will likely present a more stable crystal than H-B_8Sb_8. This is driven by charge transfer from aluminum to antimony of 1.09 e/at., whereas we observed the opposite charge transfer event in H-B_8Sb_8. This underscores the importance of charge transfer on thermodynamic stability for such inorganic crystals of the (4,8)-tessellation, which will be driven, in part, by charge localization over pnictogen centers.

The ground state electronic properties of the bulk aluminum haeckelite crystals will now be discussed. We observe decreasing bandgap energies for the bulk aluminum haeckelite series (Table 5.3). However, unlike the bulk boron haeckelite crystals, the bulk aluminum haeckelite crystals possess a direct bandgap at Γ points,

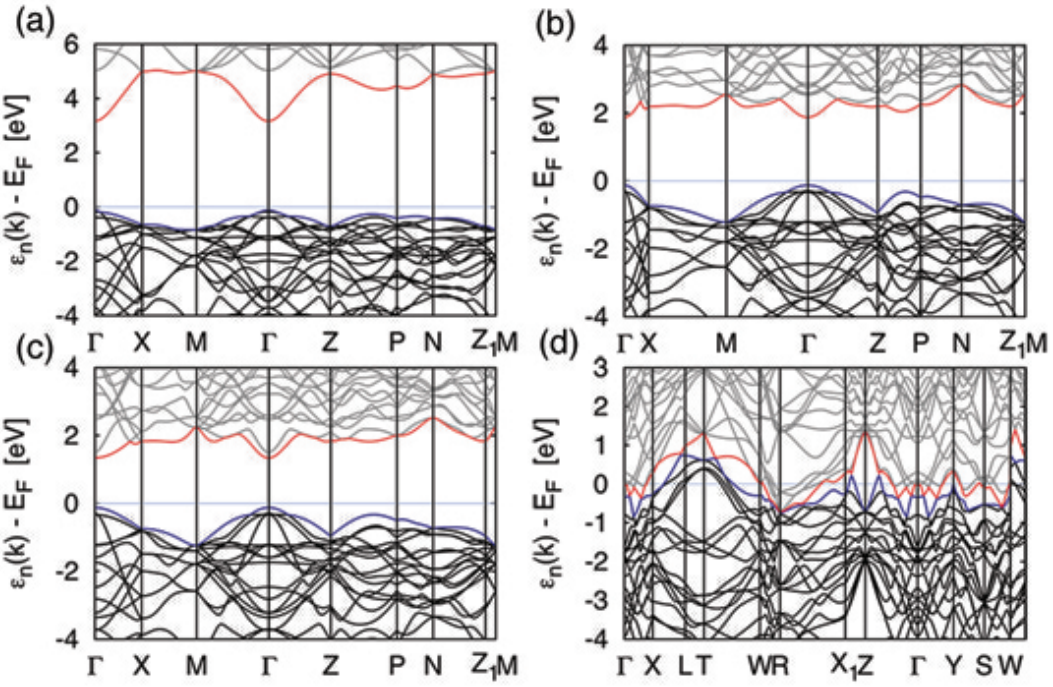

Figure 5.11. Bulk aluminum pnictogen dispersion curves. (a) H-Al_8N_8, (b) H-Al_8P_8, (c) H-Al_8As_8, and (d) H-Al_8Sb_8.

as shown in Fig. 5.11. Bandgaps extend from the UV to the IR, with H-Al_8N_8 obtaining a gap energy of 3.29 eV and H-Al_8P_8 and H-Al_8As_8 yielding 2.00 eV and 1.46 eV, respectively. In contradistinction to these bulk aluminum haeckelite crystals, H-Al_8Sb_8 forms a metallic phase (Fig. 5.11d). Interestingly, H-B_8Sb_8 remains a semiconductor, while H-Al_8Sb_8 becomes a metal and alters its ground state configuration. From the projected density of states (Fig. 5.12), we observe a strengthening of p_z and $p_x + p_y$ states near the Fermi energy for lighter mass pnictogen elements. For instance, H-Al_8N_8 shows large contributions of p-manifold electrons near the Fermi energy relative to the aluminum quantal states. Moreover, the prominence of the pnictogen p-manifold electrons, shown as red and green lines, diminishes as charge transfer lessens, Table 5.3. Consequently, for the least amount of charge transfer within the bulk aluminum haeckelite crytals, H-Al_8Sb_8, we see the smallest contribution of p-manifold states per eV, Fig. 5.12d. In fact, the provenance of the dispersion

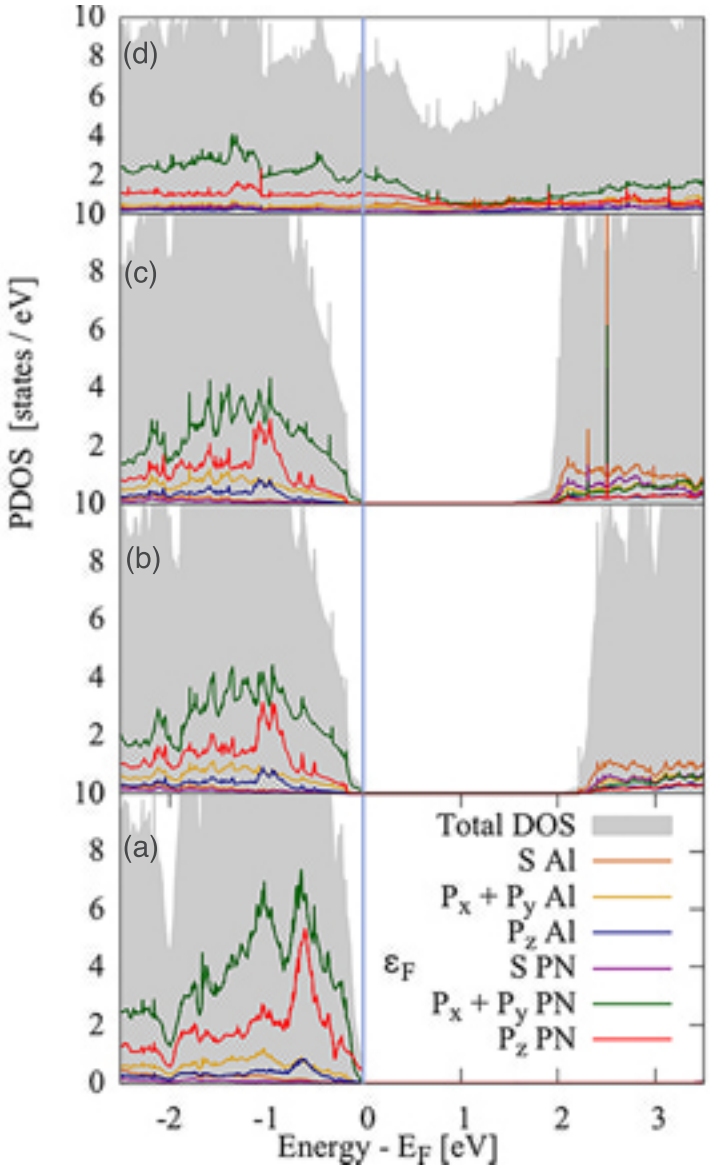

Figure 5.12. Projected density of states of bulk haeckelite aluminum crystals. (a) H-Al_8N_8, (b) H-Al_8P_8, (c) H-Al_8As_8, and (d) H-Al_8Sb_8. The vertical blue line marks the Fermi energy.

curves and projected density of states can be traced to the ground state electron density resulting from electron transfer, shown in Fig. 5.13. Similar to the bulk boron haeckelite electronic ground state, we observe the impact of the underlying elemental properties composing the bulk aluminum haeckelite crystals. For H-Al_8N_8 we observe the largest bandgap since the overall electronegativity differences are largest, thus this material presents polar bonding with a moderate bandgap, Fig. 5.13a. Continuing to H-Al_8P_8, the band edges contract as the elemental properties weaken between aluminum and phosphorus, and this periodic trend continues to H-Al_8As_8. Once H-Al_8Sb_8 is reached (Fig. 5.13d), we observe a more covalent environment as the antimony atoms withhold less electron density than the lighter pnictogen congeners. The electron density is found to center around the antimony element, but because of the strength of the shielding of electrons from antimony and the electrostatic attraction provided by aluminum, the electron density appears to be free like in the interstitial regions of the crystal. Hence, the metallic phase is supported within this unique inorganic crystal.

5.4.2.2 Haeckelite Aluminum Nanosheets.

In this section, we turn to the final haeckelite nanosheets forming the aluminum series of the (4,8)-tessellation motif. We first consider the thermodynamic stability of such ultrathin nanosheets, which are derived from the previously discussed bulk aluminum crystals. The optimized haeckelite aluminum nanosheets within semilocal density functional theory are displayed in Fig. 5.14. Panels a-d display thin films with P4/mbm (D^5_{4h}) symmetry, like the (4,8)-tessellated boron haeckelite nanosheets discussed in Fig. 5.5. Furthermore, we see similar bonding trends as a function of pnictogen, although perturbed by the presence of the larger aluminum atom, Table 5.4. In particular, we predict H-Al_4N_4 to have the shortest bond lengths of 1.763 Å and 1.832 Å forming a sp^2 haeckelite nanosheet. Moreover, for the other planar aluminum structures (Fig. 5.14b-d), we observe a similar bonding pattern, suggesting

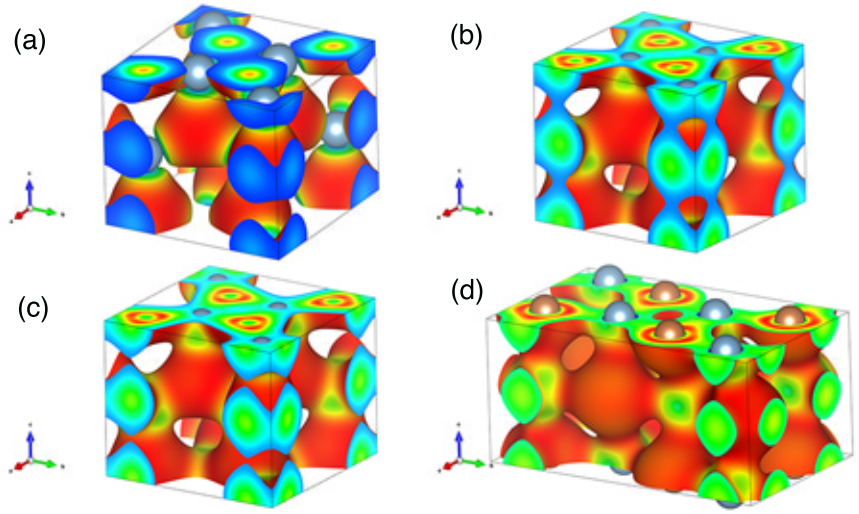

Figure 5.13. Isosurfaces of bulk aluminum haeckelite crystals. (a) H-Al_8N_8, (b) H-Al_8P_8, (c) H-Al_8As_8, and (d) H-Al_8Sb_8. Red regions are volumes of higher electron charge density whereas lighter colored regions display lesser electron charge density. For these bulk crystals, electron charge density tends to form over the pnictogen centers.

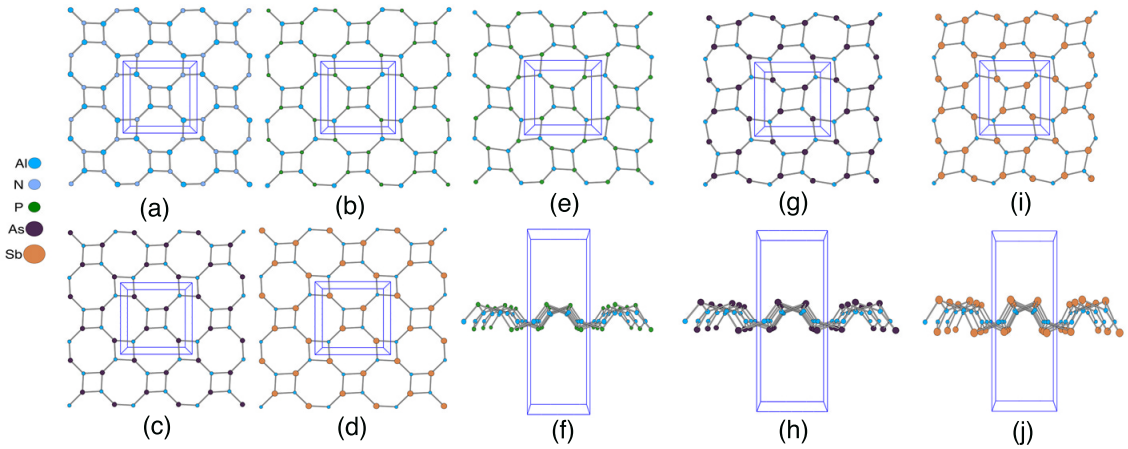

Figure 5.14. Planar and buckled (4,8)-tessellation of aluminum pnictide nanosheets. (a) H-Al_4N_4, (b) H-Al_4P_4, (c) H-Al_4As_4, (d) H-Al_4Sb_4, (e-f) H_B-Al_4P_4, (g-h) H_B-Al_4As_4, and (i-j) H_B-Al_4Sb_4.

that these cases too form sp^2 hybridized nanosheets with bond elongation escalating with larger pnictogen atomic number. Unlike the boron haeckelite nanosheets, however, we observe extreme differences in the electron transfer manifest in these planar aluminum (4,8)-nanosheets, Table 5.4. For H-Al_4N_4 we observe the most dramatic charge transfer of 3.00 e/at. determined from Bader analysis. Hence, the formation of this nanosheet leads to greater or complete abstraction of aluminum valence charge to nitrogen. For H-Al_4P_4 we observe lesser abstraction (although greater than that observed in H-B_4P_4) at 1.99 e/at. These amounts decrease to 1.86 and 1.55 e/at. for H-Al_4As_4 and H-Al_4Sb_4, respectively. As shown in Table 5.4, we observe a general increase in the cohesive energy with atomic number for these planar ultrathin nanosheets, ranging from -5.087 eV/at. for H-Al_4N_4 to -2.651 eV/at. for H-Al_4Sb_4. This suggests that heavier congeners are less stable than the lighter aluminum haeckelite nanosheets. Thus, the change in formation energy per atom for each aluminum haeckelite nanosheet generally increases within the planar structures. For H-Al_4N_4 and H-Al_4P_4, we observe similar energies of formation to produce the two-dimensional ultrathin film at 0.563 eV/at. and 0.565 eV/at. This figure-of-merit decreases slightly for H-Al_4As_4 to 0.558 eV/at., while H-Al_4Sb_4 was found to be 0.768 eV/at. The lower formation energy per atom to form H-Al_4As_4 likely occurs as aluminum and arsenic share similar ionic radii. The increase in the change of formation energy per atom, Table 5.4, can be accounted for by the increase in the stabilization of the bulk aluminum haeckelite crystal discussed in the previous section. As noted previously, the formation energy in the bulk haeckelite aluminum solids lowers, especially compared to the bulk boron haeckelite solids. Hence, the capriciousness in forming the two-dimensional one-atom thick aluminum nanosheets, Fig. 5.14a-d, becomes apparent; the formation energy per bulk aluminum crystal increases relative to aluminum nanosheets. Moreover, because of the charge transfer manifest in the bulk aluminum crystals, we can expect stronger bonding formed from this greater charge

disparity, which will further irritate their formation into planar haeckelite thin films. However, a consequence of charge localization around the pnictogen congeners within the planar motif is that the electrostatic attraction between ions increases, which promotes their stability in the planar configuration. Yet the buckled configurations of these haeckelite ultrathin films show greater stabilization similar to that observed with the buckled boron nanosheets.

Table 5.4. Aluminum haeckelite pnictide nanosheets thermodynamics stability. The 'B' subscript under the material heading expresses buckled cases. For each material we show the aluminum-pnictogen bond length $d(Al-PN)$ [Å], bandgap energy E_g [eV], charge transfer from aluminum to pnictogen Δq [e/at.], cohesive energy E_{Coh} [eV/at.], and the change in formation energy to form the nanosheet relative to bulk ΔE_f [eV/at.].

Material	$d(Al-PN)$	E_g	Δq	E_{Coh}	ΔE_f
H-Al_4N_4	1.763, 1.832	2.857	3.00	-5.087	0.563
H-Al_4P_4	2.251, 2.286	2.148	1.99	-3.479	0.565
H_B-Al_4P_4	2.285, 2.331	2.327	1.94	-3.577	0.465
H-Al_4As_4	2.338, 2.378	1.106	1.86	-3.090	0.558
H_B-Al_4As_4	2.395, 2.445	2.028	1.76	-3.250	0.395
H-Al_4Sb_4	2.550, 2.591	0.388	1.55	-2.651	0.768
H_B-Al_4Sb_4	2.627, 2.665	1.552	1.40	-2.856	0.561

Along with the formation of planar structures, a number of buckled aluminum nanosheets form, as shown in Fig. 5.14e-j. The symmetry of the buckled aluminum nanosheets was found to be P-421m (D^3_{2d}). Interestingly, for the aluminum nanosheets, we observe an addition to the buckled group (compared to the boron series), H_B-Al_4P_4. The buckled aluminum haeckelite nanosheets display a trigonal pyramidal geometry surrounding each pnictogen congener, while aluminum forms a quasi-trigonal planar geometry like we have observed for the buckled boron nanosheets. Again the buckling occurs within the tetragonal ring system composing the nanosheet to alleviate ring strain. Moreover, upon relaxation, the formation of corrugations becomes pronounced, while obeying the local geometries around the

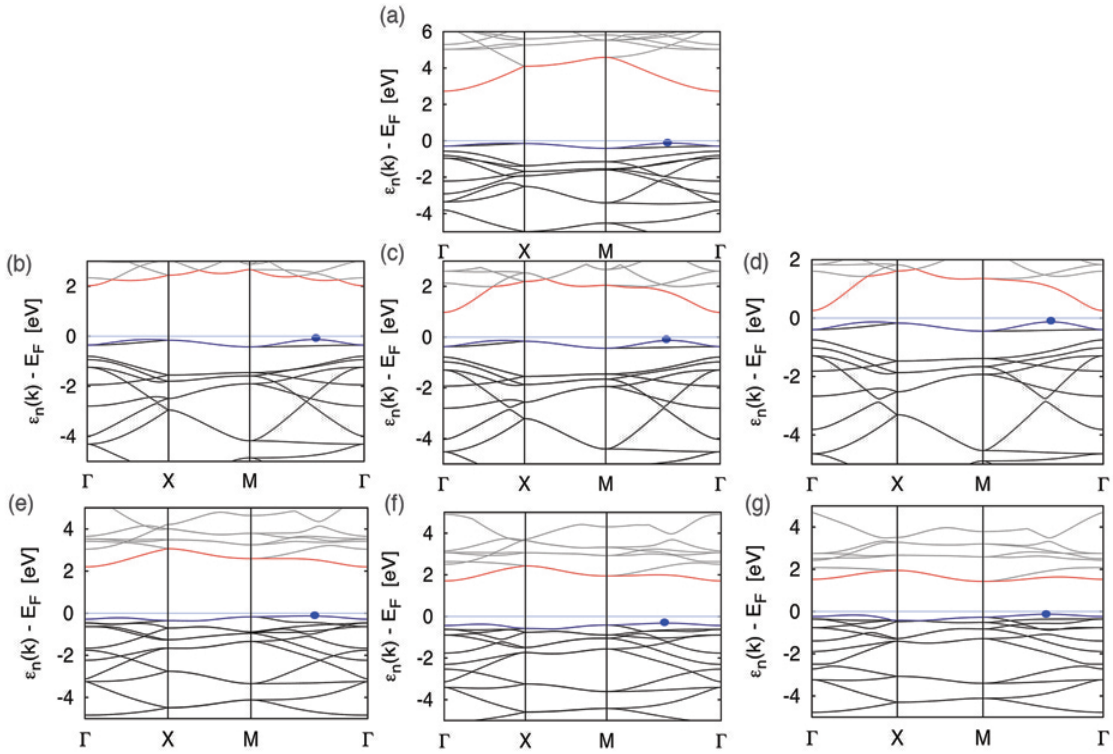

Figure 5.15. Dispersion curves of ground state haeckelite aluminum pnictide nanosheets. (a) H-Al_4N_4, (b) H-Al_4P_4, (c) H-Al_4As_4, (d) H-Al_4Sb_4, (e) H_B-Al_4P_4, (f) H_B-Al_4As_4, and (g) H_B-Al_4Sb_4. The blue dots on the subfigures mark the band extrema of the valence band maximum.

elements composing each nanosheet. Consequently, we observe interesting bonding patterns within this series. For H_B-Al_4P_4 we observe the shortest bond length increasing by approximately 0.034 Å and the longest increasing 0.045 Å compared to the planar polytype, Table 5.4. However, we observe the heavier aluminum haeckelite nanosheets H_B-Al_4As_4 and H_B-Al_4Sb_4 to have moderate bond elongation of 0.057 Å and 0.067 Å, and 0.077 Å and 0.074 Å compared to the planar configuration, respectively. Aside from the bonding within the buckled aluminum nanosheets, the charge transfer diminishes slightly compared to the planar ones (Table 5.4). For H_B-Al_4P_4 the charge transfer between aluminum and phosphorus lessens by 0.05 e/at. compared to the planar nanosheet. Analogously, H_B-Al_4As_4 charge transfer reduces by 0.1 e/at. and H_B-Al_4Sb_4 decreases by 0.15 e/at. These differences in charge transfer within the buckled aluminum series of haeckelite nanosheets are followed by lower cohesive energies, contrasted against the planar aluminum ultrathin nanosheets discussed previously. The cohesive energy for H_B-Al_4P_4 lowers by 0.097 eV/at. relative to the planar configuration, while for the heavier buckled H_B-Al_4As_4 and H_B-Al_4Sb_4, we observe decreases of 0.16 and 0.20 eV/at. These buckled structures alleviate the strain within the tetragonal ring. Since these structures are composed of eight member rings as well, their buckling accesses the configurational landscape that is possible with greater ring sizes. In fact, H_B-Al_4As_4 attains the lowest change in formation energy per atom forming this buckled nanosheet at 0.395 eV/at. And for H_B-Al_4P_4 the change in formation energy creating the buckled configuration is predicted to be 0.465 eV/at., while H_B-Al_4Sb_4 is found to be 0.561 eV/at. Consequently, these buckled nanosheets have correspondingly greater thermodynamic stability as shown by their lower change in formation energy to create the buckled aluminum nanosheets and decreased cohesive energy , Table 5.4. These structural and thermodynamic trends will be reflected in the ground state electronic structures for both planar and buckled haeckelite aluminum nanosheets.

The ground state electronic structures of the planar aluminum haeckelite are presented in Fig. 5.15a-d. In the aluminum haeckelite nanosheets, we observe the formation of intrinsic indirect bandgap semiconductors similar to the boron nanosheets discussed above. Unlike the (4,8)-boron nanosheets, the aluminum ultrathin nanosheets support only a single set of band extrema, which are found to occur along M-Γ direction. Moreover, bandgap trends observed for the aluminum haeckelite nanosheets decreases in a similar fashion as the boron haeckelite nanosheets and extend over the visible and IR. The largest bandgap observed in the aluminum nanosheet series is 2.857 eV for H-Al_4N_4, Table 5.4. This is to be expected, as we have already noted that this inorganic thin film forms a polar material to which the greatest charge transfer occurs. Furthermore, the projected density of states for H-Al_4N_4, Fig. 5.16a, shows sharp van Hove singularities near the Fermi energy originating from nitrogen valence p_z state. The significant formation of p_z states can be attributed to the large charge transfer from aluminum and the reduction of dimensionality to a two-dimensional thin film. However, unlike the planar boron haeckelite structures discussed previously, we do not predict the formation of a conduction band van Hove singularity. In fact, around 3 eV we see the incipient formation of conduction band states that gradually rise upward instead of a sharp critical feature in the atomic PDOS (Fig. 5.16a). Further, with H-Al_4P_4 the bandgap lowers to 2.148 eV, and we observe the similar p_z channel forming near the Fermi energy, which is, again, driven by the charge transfer from aluminum elements and reducing the dimensionality of the material. And like H-Al_4N_4 we see no notable critical point at the conduction band edge of the PDOS, Fig. 5.16b. Hence, the optical response to external electromagnetic stimuli will lessen compared to boron haeckelite nanosheets. Within the latter heavier pnictogen elements arsenic and antimony, we observe band further contraction at Γ to 1.106 eV and 0.388 eV, respectively. Additionally, the PDOS trends observed for lighter mass pnictogens extend to the heavier ones; we observe

van Hove singularities near the Fermi energy in the valence band extremum and a gradual increase in the DOS near the conduction band minimum for both materials. Hence these aluminum nanosheets should display weaker light matter interactions contrasted against the boron haeckelite nanosheets that support these critical features in the density of states. An apparent chemical trend emerges within this series that, as noted already, can be understood from the differences in elemental properties between aluminum and the pnictogen congeners. Hence, the largest differences in electronegativity emerge within this series, and the electrostatic attraction between ions forming the aluminum thin films increases. Consequently, the bandgap within the planar aluminum nanosheets overall have larger bandgaps than the boron versions (with the exception of H-B_4N_4). Thus, these materials exhibit polar sp^2 hybridized nanosheets with properties unique and separate from the boron planar nanosheets. These ground state material properties are an emblematic feature for the planar cases; however, the bandgaps open larger when the planar polytype buckles, as discussed below.

In the buckled cases, Fig. 5.15e-g, we observe band extrema lying along the M-Γ direction as well, although the conduction band minimum for H_B-Al_4Sb_4 switches from Γ to M. Note that the valence band maximum along Γ-X is close to the reciprocal direction M-Γ; however, strictly speaking this is a local maximum. For H_B-Al_4P_4, we observe a change in the bandgap, increasing approximately 0.18 eV relative to the planar configuration bandgaps, Table 5.4. The bandgap expansion for heavier H_B-Al_4As_4 and H_B-Al_4Sb_4 increases by 0.92 eV and 1.16 eV, respectively. As noted above, the buckled configuration forms such that the pnictogen becomes quasi-trigonal pyramidal and the aluminum becomes trigonal planar. This distortion around the square ring alters the interaction of quantal states between the aluminum and pnictogen elements such that the entire p-manifold is found around the Fermi energy as seen in the projected density of states (Fig. 5.16e-g). In fact, we can see that the $p_x + p_y$

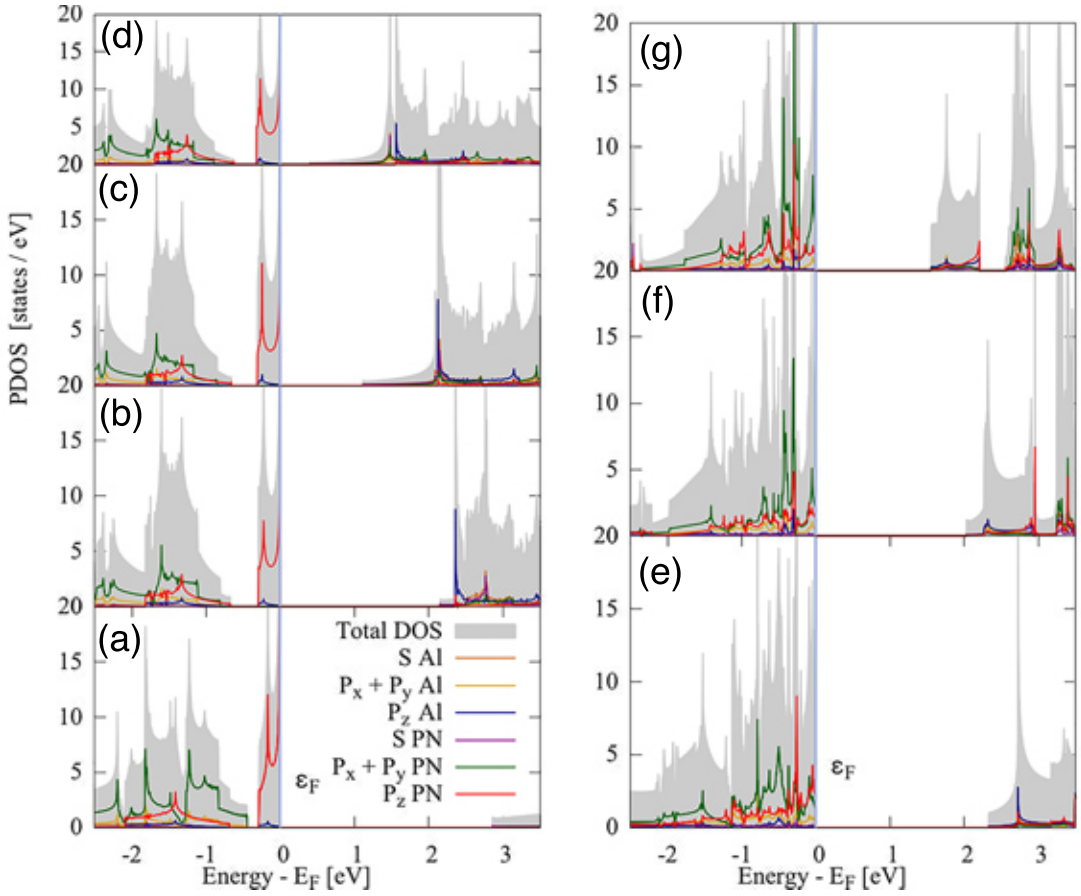

Figure 5.16. Projected density of states of aluminum pnictide nanosheets. (a) H-Al_4N_4, (b) H-Al_4P_4, (c) H-Al_4As_4, (d) H-Al_4Sb_4, (e) H_B-Al_4P_4, (f) H_B-Al_4As_4, and (g) H_B-Al_4Sb_4. (a)-(d) are planar aluminum pnictide nanosheet PDOS, and (e)-(g) are the buckled aluminum pnictide nanosheet PDOS. The vertical blue line marks the Fermi energy at zero energy.

states grow in prominence near the Fermi energy, thus mixing of these orbital states forces open a larger bandgap within the buckled polytype. Hence, within the buckled aluminum nanosheets greater mixing of p-manifold electrons slightly lowers charge transfer from aluminum to the pnictogen elements. This quantum interaction forms the sp^3 hybridized buckled motif, lowering the energy and raising the bandgap of these aluminum haeckelite nanosheets compared to the planar versions. Incidentally, within the bandstructures of the buckled aluminum haeckelite nanosheets, Fig. 5.14e-g, the lowest conduction band and highest valence band show moderately smooth dispersion across the Brillouin zone. This could lead to improved light-matter interactions for those bands that track similarly between the valence and conduction states. However, because of the appreciable increase in charge transfer (relative to the boron nanosheets) within these buckled aluminum nanosheets, their absorption will likely be hyperchromic in the absorption spectrum and lower in intensity. This conjecture will hold true for the planar aluminum nanosheets as well. These electronic grounds states can be realized by observing the pseudo-charge density slices of each nanosheet.

Cross-sections of the ground state charge densities reveal the underlying electronic and structural properties of each aluminum haeckelite nanosheet, Fig. 5.17. The elemental properties are conspicuous within the planar aluminum series. For H-Al_4N_4, we observe the most disparate organization of ground state charge density (Fig. 5.17a). Most of the charge is found localized over the nitrogen element, and thus, this material forms a stable polar sp^2 two-dimensional crystal. Upon substituting phosphorus for nitrogen, the degree of charge localization reduces (Fig. 5.17b), but we can still see that the electrons localize heavily around the pnictide. Hence, the charge transfer from the aluminum element to phosphorus supports the material having a modest bandgap, as would be expected for a polar-covalent material.

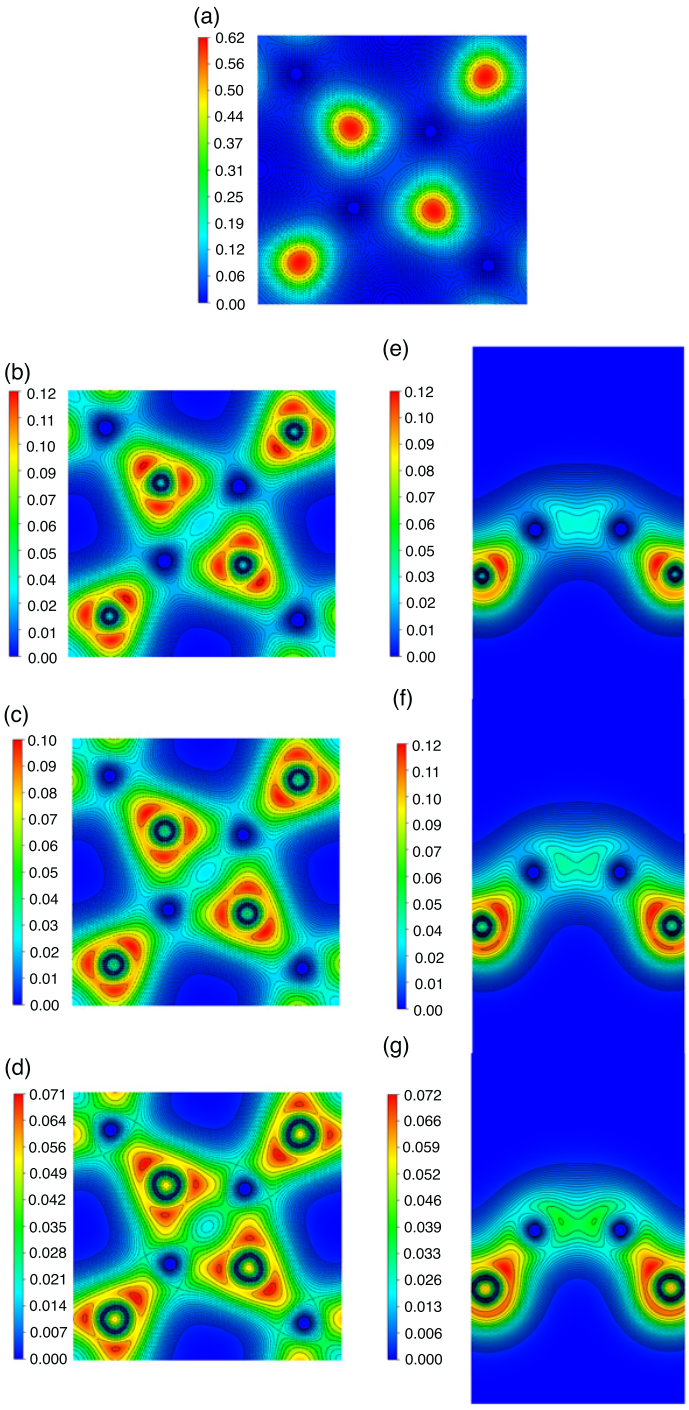

Figure 5.17. Ground state electronic charge density cross-sections of aluminum haeckelite nanosheets presented as in Fig. 5.8. (a) H-Al_4N_4, (b) H-Al_4P_4, (c) H-Al_4As_4, (d) H-Al_4Sb_4, (e) H_B-Al_4P_4, (f) H_B-Al_4As_4 , and (g) H_B-Al_4Sb_4.

Proceeding to the heavier planar nanosheets, Fig. 5.17c-d, we observe a gradual reduction in the charge localization around the arsenic and antimony atoms, where the most concentrated charge regions begin to spread closer to the aluminum ions. The organization of electron density is similar to that of phosphorus, which suggests these planar aluminum nanosheets are polar and sp^2-unsaturated. Consequently, the gap structure within the bandstructures stays open, and the energy gap within the planar aluminum nanosheets generally remains larger than that of the boron structures. Therefore, as alluded to above, the elemental properties are more dissimilar within the aluminum series to which we observe the greatest polarization of charge density, larger bandgaps, and similar thin-film formation energies. However, as shown in Fig. 5.17e-g, when the planar nanosheets buckle, the ground state charge density reorganizes around the pnictogen congeners. Interestingly, the buckled configuration charge density shows only a diminutive redistribution of charge around the pnictogen, where there appears to be appreciable charge density axially fixed away from the nanosheet. These are the locations of lone-pairs formed in the buckled configuration (Fig. 5.17e-g). This suggests the sp^3 character of the buckled motif for the aluminum haeckelite nanosheets. Moreover, these lone-pairs could certainly be involved in cooperative chemical transformations serving as a nucleophilic source for surface-absorbate reactions. Conversely, the aluminum atoms could serve as electrophiles due to their deprivation of charge density. For H_B-Al_4Sb_4, we note the aluminum-aluminum bond doesn't form in the nanosheet (recall boron-boron did). The absence of this unusual bonding feature can be understood in terms of the polarization of charge density in the ground state around the antimony atom. The electronegativity difference between aluminum and antimony favors the latter element, which reduces diagonal charge density build-up between the vertice alumina on the tetragonal ring.

5.5 Conclusions

In this article, we have elucidated the thermodynamic and ground state electronic properties of bulk and ultrathin haeckelite nanostructures composed of boron/aluminum − group V elements. Additionally, we have observed the formation of an unexpected metallic five-coordinate aluminum antimonide crystal, H-Al_8Sb_8. We have shown that these bulk haeckelite crystals could form metastable structures to which the ultrathin film may be mechanically formed. Hence, the stability of forming the unique (4,8)-tessellation can be achieved for those ultrathin films with low change in formation energy relative to bulk, or low cohesive energies. H-B_4N_4 shows the greatest promise of forming based on these criteria, but we put forward that H-B_4P_4, H-B_4As_4, H_B-B_4As_4, and most of the aluminum haeckelite nanosheets with the exception of H-Al_4Sb_4 could be formed; the latter are likely to be refractory and adopt various configurations at ambient conditions. In particular, the existence of buckled configurations within both the boron and aluminum series suggests that those particular nanosheets will likely form deviations from planarity should experimental synthesis be attempted. Thus, such suspended thin films may likely form buckled configurations upon interfacial interaction with substrates. Furthermore, in order to form such materials a combination of synthetic strategies may be necessary. For example, a combination of on-surface synthesis and encapsulation of an inert thin film over a substrate to form a nanoreactor would be most efficacious.[14] Conseqently, with the observations made herein, only H-B_4N_4, H-B_4P_4, and H-Al_4N_4 will remain truly two-dimensional, as no buckling within these nanosheets was found due to appreciable charge transfer and strong polarized bonds. Moreover, should their synthesis be achieved, these ultrathin nanosheets would likely exhibit the electronic properties of an indirect bandgap semiconductor, but with larger bandgaps as the presence of exact-exchange interactions was not accounted for. Hence, the presence of the optical gaps could lead to their use as a photoactive material in light-driven applications

spanning a broad range of photon energies. And due to the stability of the aforementioned haeckelite nanomaterials, with the variation of their bandgaps, it is possible that they may find utility as photovoltaics or light-emitting diodes. Moreover, many physical aspects concerning these novel haeckelite nanomaterials were not discussed within this article, e.g., multilayer polymorphs, excitonic effects, phonon spectra, p heterostructures, etc. Thus, we hope this fundamental article will invigorate scientific inquiry into the experimental synthesis and theoretical elucidation of the haeckelite bulk and ultrathin nanosheets, as this is an open question at present.

5.6 Supplemental Information

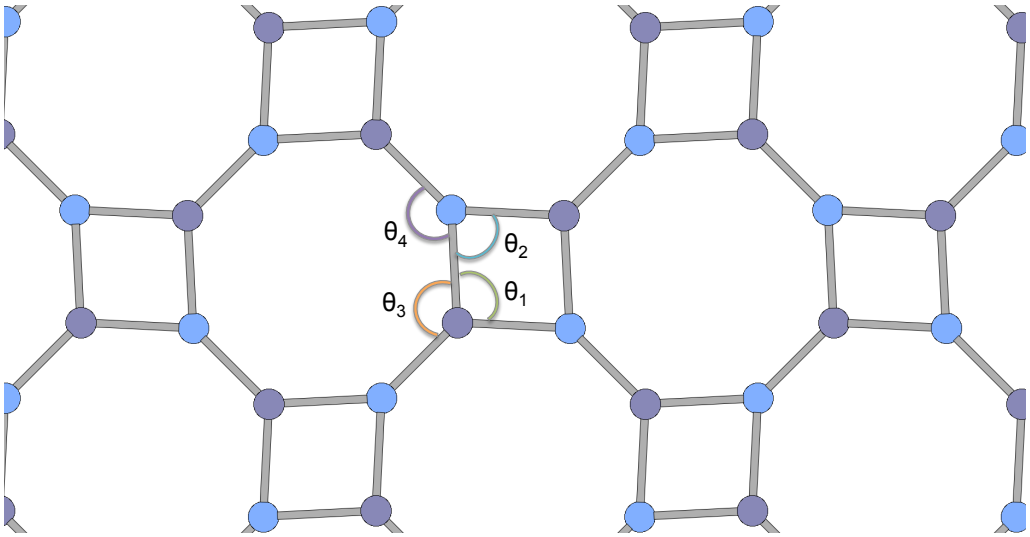

Figure 5.18. Angles listed in Table S1 for all haeckelite nanosheets and bulk haeckelite crystals.

Table 5.5. Haeckelite crystal structure data for all materials presented within the main text. All lattice constants are given in angstrom, Å. α, β, and γ refer to crystal cell angles (degrees) of bulk haeckelite crystals.

Material	a	b	c	θ_1	θ_2	θ_3	θ_4	α	β	γ
H-B_8N_8	5.013	5.013	4.229	–	–	–	–	90.00	90.00	90.00
H-B_8P_8	6.303	6.303	5.322	–	–	–	–	90.00	90.00	90.00
H-B_8As_8	6.689	6.689	5.625	–	–	–	–	90.00	90.00	90.00
H-B_8Sb_8	7.352	7.352	6.150	–	–	–	–	90.00	90.00	90.00
H-B_4N_4	4.938	4.938	–	95.74	84.26	132.13	134.87	–	–	–
H-B_4P_4	6.350	6.350	–	89.53	90.47	135.24	134.77	–	–	–
H-B_4As_4	6.707	6.707	–	91.51	88.49	134.25	135.76	–	–	–
H_B-B_4As_4	5.784	5.784	–	102.94	63.52	127.54	109.11	–	–	–
H-B_4Sb_4	7.398	7.398	–	92.57	87.43	133.71	136.29	–	–	–
H_B-B_4Sb_4	6.264	6.264	–	102.36	49.81	125.53	110.31	–	–	–
H-Al_8N_8	6.167	6.167	5.006	–	–	–	–	90.00	90.00	90.00
H-Al_8P_4	7.649	7.648	6.375	–	–	–	–	90.00	90.00	90.00
H-Al_8As_8	7.961	7.960	6.646	–	–	–	–	90.00	90.00	90.00
H-Al_8Sb_8	6.754	11.099	5.376	–	–	–	–	90.00	90.00	90.00
H-Al_4N_4	6.154	6.154	–	93.78	86.22	133.11	136.89	–	–	–
H-Al_4P_4	7.749	7.750	–	95.46	85.54	132.27	137.73	–	–	–
H_B-Al_4P_4	6.843	6.844	–	95.08	74.07	130.82	110.63	–	–	–
H-Al_4As_4	8.057	8.057	–	95.64	84.36	132.18	137.81	–	–	–
H_B-Al_4As_4	6.925	6.925	–	95.46	71.19	130.30	105.76	–	–	–
H-Al_4Sb_4	8.782	8.782	–	95.85	84.15	132.08	137.92	–	–	–
H_B-Al_4Sb_4	7.296	7.295	–	97.48	67.14	129.06	101.87	–	–	–

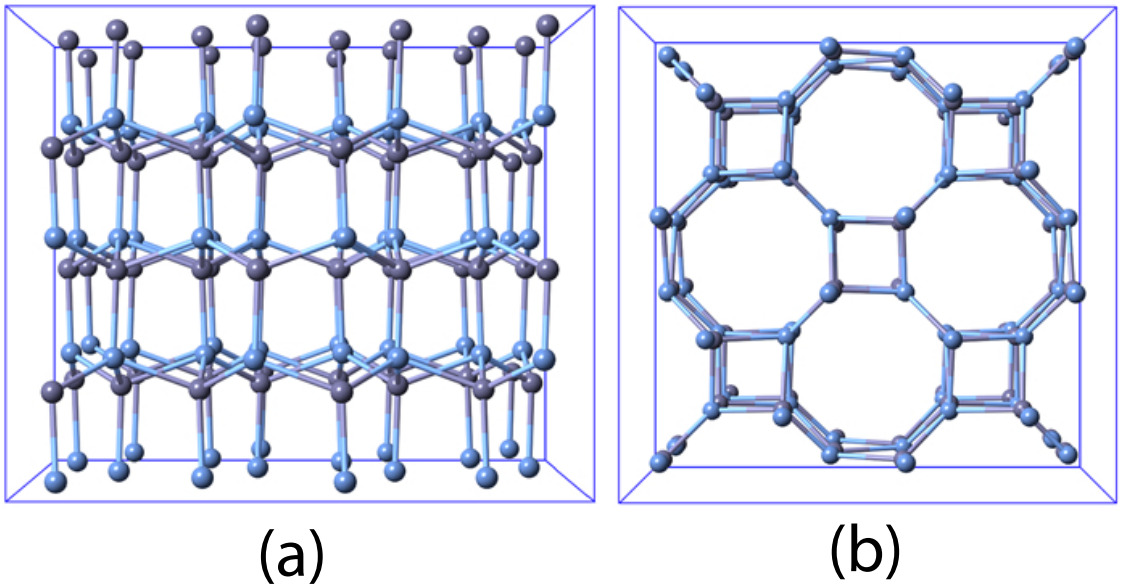

Figure 5.19. Bulk H-B_8N_8 shown in an expanded 2x2x2 cell along (a) (100) and (b) (001) crystallogrphic directions. This cell is a representative model of all bulk boron and aluminum haeckelite cyrstals, except for the bulk H-Al_8Sb_8. Note the color scheme of the elements for all figures in the supplemental is the same as that displayed in the manuscript.

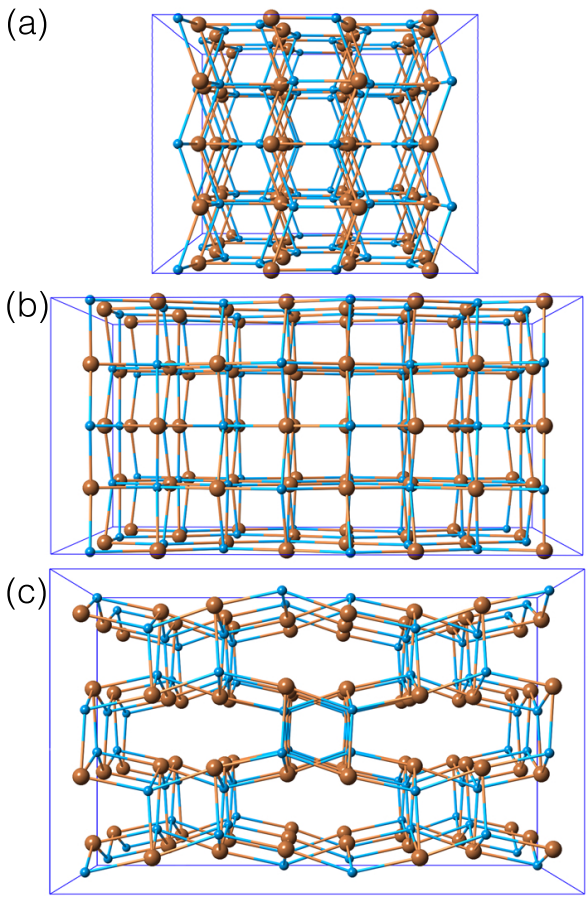

Figure 5.20. Bulk H-Al_8Sb_8 displayed in an expanded 2x2x2 cell along (a) (100), (b) (010), and (c) (001) crystallographic directions. We can see in this cell the unique bonding pattern accompanied with five coordinate alumina and antimony elements. Note the color scheme of the elements for all figures in the supplemental is the same as that displayed in the manuscript.

CHAPTER SIX

Exceptional Optical Response of Archimedean Boron and Group-V Ultrathin Nanosheets

This chapter published as: Paul A. Brown and Kevin L. Shuford. *J. Phys. Chem. C* **2017**,121, 44, 24489-24494

6.1 Abstract

The ascendency of ultrathin films have emerged as a boon for 21^{st}-century nanotechnologies that rely on flexibility, tunable properties, and active surface area. In this article we explore uncharted configurations with Archimedean (4,8)-tessellations that exhibit exceptional light-matter interactions captured with time-dependent density functional theory. We find that planar monolayers of haeckelite boron-pnictogen binary materials possess strong interband absorbance and absorption coefficients that rival existing ultrathin films. These observables were found to occur in the ultraviolet for the boron-nitride nanosheet and in the infrared region of the electromagnetic spectrum for heavier pnictogens, suggesting a route for photocapture of high density solar photons. Moreover, we find the buckled haeckelite boron arsenide supports a similar, yet slightly decreased, optical response that is blue-shifted from its planar configuration. The strong optical response of these ultrathin films emerges from their unique bandstructures, localization of π-electrons in the ground state, Van Hove singularities at band extrema, and complementary elemental properties. Consequently, the (4,8) haeckelite motif demonstrates that many two-dimensional films with distinctly different lattice tessellations from that of established ultrathin materials could have a significant impact on the field.

6.2 Introduction

Since the first isolation of graphene in 2004, the field of ultrathin film research has grown rapidly with new discoveries every year.[6,7,229,260] Most of the scientific vigor has concentrated on a number of hexagonal ultrathin films – such as transition metal dichalcogenides (TMDCs), boron-nitride, and graphene – whose designer heterostructures have been fabricated to form an array of novel device architectures.[229,260] These proof-of-concept devices have displayed exceptional light-matter interactions surpassing established technologies.[260] For instance, heterostructures composed of a GaTe/MoS_2 device boasted a 60% external quantum efficiency displaying efficient carrier separation.[261] Also, because of its low density of states and low optical absorption coefficient, graphene-based optoelectronic devices have been assembled with GaS, InSe, TMDCs, black phosphorus and others.[262–266] With the ability to tune light-matter interactions with local gating, number of layers, and material flexibility, such single junction devices hold a great deal of promise for emerging nanotechnologies of the 21^{st}-century – in particular photovoltaics, light-emitting diodes, and field-effect tunneling transistors.[260] However, much of the scientific research has been focused on the aforementioned subgroup of ultrathin films, while a vast ocean of configurationally distinct nanomaterials, whose properties may be more efficacious than existing ultrathin films, have yet to be explored in great detail.

In this article we focus on the optical response of a new class of ultrathin film – the Archimedean haeckelite nanosheets, whose constituents are composed of binary, boron pnictogen combinations. Archimedean haeckelite nanosheets are semiregular polygonal structures that form from four to eight membered fused polynuclear ring structures.[250,267–274] Such materials display an interesting array of intrinsic indirect semiconducting and metallic behavior. In particular, the boron series of haeckelite nanosheets were found to have double extrema in their bandstructure.[272] This fortuitous bandstructure forms from hybridization of s- and p-electrons of the boron

and pnictogen elements within a (4,8)-tessellated configuration, yielding one-atom thick planar sp^2 hybridized crystalline nanosheets. The haeckelite boron-pnictogen ultrathin films display strong light matter interactions that arise from their unique bandstructures. Consequently, these particular structures have tremendous optical response even though haeckelite crystals are technically indirect bandgap semiconductors, albeit very close to a direct bandgap. More importantly, we predict strong optical response in the infrared region for heavier pnictogen elements, where optoelectronic applications are most critical estimated from the well known Shockley-Queisser limit.[275] And we will show that these materials exhibit annular valence and conduction band extrema that are responsible for their exceptional optical response. Thus, such configurationally distinct materials may have a real impact in both extended theoretical investigations and experimental strategies for synthesis and elucidation of fundamental properties.

6.3 Theoretical Methods

The Archimedean boron haeckelite series was studied within density functional theory using the Vienna ab initio simulation package (VASP) (*vasp.5.4.1*).[114] First, the haeckelite boron pnictogen monolayers were optimized with the semilocal Perdew-Burke-Ernzerhof (PBE) functional following the procedure reported elsewhere.[272] We study the optical response by computing the complex dielectric functions with a screened hybrid corrected exchange-correlation functional of Heyd-Scuseria-Ernzerhof (HSE06) to correct the gap structure (within 15-16 % of the experimental bandgap) and then introduce these orbitally-corrected Kohn-Sham states into time-dependent Hartree-Fock to capture electron-hole contributions in the spectra.[47,52,53,276,277] Paier et al. have shown that excitonic features can be described well with this approach to within 3% of the expected optical response compared to experiment.[276] The complex dielectric functions were computed on a Monkhorst-Pack grid sampling of 18 x 18 x 1 with default cutoff. A Gaussian smearing function was applied with a finite

temperature smearing width of 0.01 eV for the partial occupancies.[216] The band-structures and projected density of states were computed with this approach. We compute the electron-hole interaction within time-dependent Hartree-Fock including seven valence and eight virtual states explicitly, while increasing the number of bands to ninety six total bands for all spectra.[276,278] Each spectra presented below was computed on a fine grid of 5000 points up to 10 eV in photon energy. The complex dielectric response is captured via a Dyson expansion over irreducible polarizability, where the dynamically screened bare Coulomb potential is approximated through the sum over Coulomb and effective frequency dependent nonlocal exchange-correlation kernel.[276,278] From this computational approach, the excitonic features can be indirectly captured for semiconducting materials rather than resorting to computing the more laborious Bethe-Salpeter equation.[276,278]

The absorbance in this article is determined from the following expression

$$A(E) = 1 - e^{-p\alpha(E)\Delta z}, \tag{6.1}$$

where Δz is the thickness of a material (taken to be the unit cell thickness) and p is the number of passes of light (p is one for first pass absorption).[103] Here α is the absorption coefficient given as

$$\alpha(E) = \frac{\omega}{cn}\epsilon_2(E), \tag{6.2}$$

where E is the photon energy, c the speed of light, n is the refractive index taken to be unity for vacuum, and $\epsilon_2(E)$ is the imaginary portion of the frequency-dependent complex dielectric function.[103]

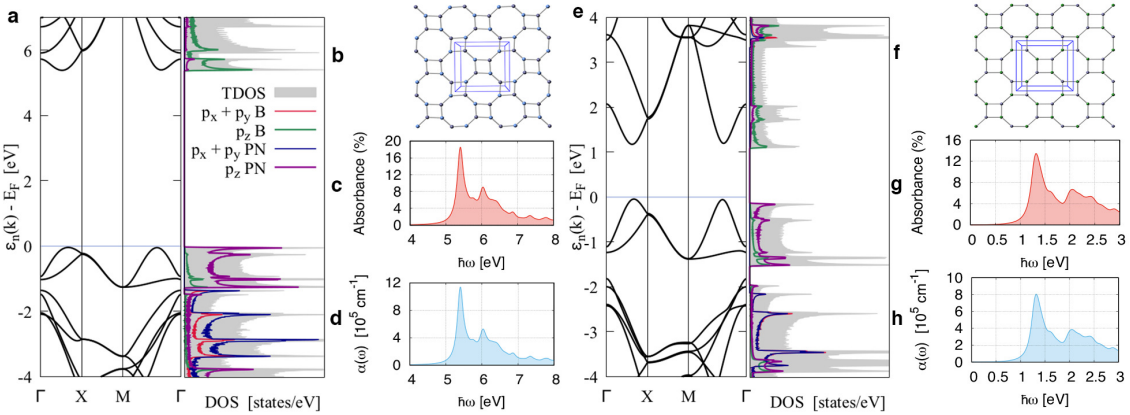

Figure 6.1. Hybrid band structure, PDOS, and optical response of H-BN and H-BP. (a) & (e) HSE06 band structure and projected density of states, (b) & (f) ultrathin film optimized structures, (c) & (g) absorbance spectrum from Eqn. 6.1, and (d) & (h) absorption coefficient from Eqn. 6.2 for H-BN and H-BP respectively.

6.4 Results and Discussion

Figure 6.1a-c shows the result of our computational approach for H-BN (haeckelite boron nitride). The overall cohesive energy of monolayer of H-BN was found to be -6.78 eV with a formation energy change *relative to bulk* at 0.050 eV.[272] For H-BN we observe a bandgap of approximately 5.44 eV, which is 0.56 eV lower than its hexagonal counterpart h-BN.[262] Moreover, the bandstructure of H-BN displays two extrema along the M−Γ and Γ−X directions, Fig. 6.1a. A conspicuous sharp peak emerges in the absorbance spectrum (Fig. 6.1c), which corresponds to the fundamental gap for H-BN, and can be attributed to the interband transition from the double extrema. A second peak emerges from the $X_{15v,16v} \longrightarrow X_{15c,16c}$ interband transition around 6.2 eV. In the PDOS for H-BN, the formation of Van Hove singularities (VHs) ensures a strong optical response observed in the absorbance spectrum. These VHs are characterized by sharp peaks in the PDOS, Fig. 6.1a & 6.1e, and are responsible for a build up of the joint density of states. Located near the Fermi energy, the pnictogen contributes the majority of states per eV (purple line), while at the conduction band extrema the boron element (green line) forms the majority of empty states per

eV. Thus, computed absorbance displays a strong absorption around the bandgap energy of nearly 18.5% and a maximum absorption coefficient of 1.14 x 10^6 cm^{-1}. Compared to other computed absorption coefficients,[279] such as those for MoS_2 of 1-1.5 x 10^6 cm^{-1}, our values suggest comparable photoresponsivity at the onset of absorption in H-BN.

Replacing the pnictogen element nitrogen with phosphorus results in an entirely different yet strong absorption that shifts from the ultraviolet to infrared, Fig. 6.1e-h. Moreover, the cohesive energy in the monolayer rises to -4.71 eV with a change in formation energy relative to bulk at 0.48 eV.[272] Substituting a phosphorus into the haeckelite lattice results in a lowering of the bandgap to approximately 1.25 eV (Fig. 6.1e). Moreover, the double extrema still form two valleys of well defined parabolicity, and again we see the VHs observed in H-BN appear at the band extrema for H-BP. Hence, interband transitions from the valence band edge to the conduction band yield a strong peak at the fundamental gap in the absorbance spectrum for H-BP, Fig. 6.1g. Furthermore, a shoulder appears at about 2 eV and extends across the entire visible region of the electromagnetic spectrum. This peak emerges from a transition between $X_{15v,16v} \longrightarrow X_{15c,16c}$ as was observed for H-BN. These observations are intrinsic to the planar (4,8)-tessellation of boron and group-V elements. Moreover, proceeding from the onset of absorption, we see the absorbance extends into the deep infrared and across the visible, Fig. 6.1g. Consequently, H-BP demonstrates powerful optical response in a region critical to photovoltaic devices. From the absorbance spectrum, we see the strongest absorbance around the fundamental bandgap approaching 13.47% with an optical absorption coefficient of 0.80 x 10^6 cm^{-1}, which is competitive with TMDCs.[279] It is interesting to note that these haeckelite structures are less dense per unit cell than TMDCs (TMDCs are 4 times more dense per unit cell). Hence, within the infrared region of the electromagnetic spectrum, H-BP exhibits a strong optical response compared to existing thin films. Moreover, these

Archimedean nanosheets may be layered to tune the bandgap of the material. This approach can mitigate atmospheric scattering in the IR allowing for better control of free carrier formation from absorption of solar photons.

In order to estimate the maximum short circuit photocurrent resulting from solar emission, the absorbed photon flux, J_{abs}^{max}, is determined as

$$J_{abs}^{max} = e \int_{E_g}^{\infty} dE \; A(E) \cdot J_{ph}(E), \tag{6.3}$$

where A(E) is the absorbance of each haeckelite nanosheet (Eqn. 6.1), J_{ph} is the incident photon flux (photons/cm^2·s·eV), where we introduce AM 1.5G solar spectrum for J_{ph}, E is the photon energy, and e converts the photon flux to current density per photon energy (mA/cm^2·eV).[279] The absorbed photon flux for each material indicates the upper limit of short-circuit electrical current density, J_{abs}^{max} (mA/cm^2), available for conversion of photons to free carriers as electrical current in a photovoltaic device.[279] It is important to note that the maximum photocurrent determined from Eqn. 6.3 represents the maximum current under ideal conditions, and does not capture the influence of carrier scattering on the fate of free carriers resultant from excitation. From Table 6.1 we see that H-BP has a notable photocurrent of 2.53 mA/cm^2, which is quite large compared against established materials like silicon. However, this value is less than that reported for TMDCs like MoS_2 at 3.9 mA/cm^2 or even larger 4.6 mA/cm^2 for $MoSe_2$.[279] The lower photocurrent reported here can be attributed to the peak position of H-BP being coincident with a dip in the solar irradiance around 950 nm. Hence, H-BP photocurrent is limited by a lower incident photon flux, $J_{ph}(E)$, from notable atmospheric losses. However, as noted above, the optical gap of two-dimensional materials can be tuned by adding more layers, hence the optical response of H-BP could be red shifted to better align with incident solar spectral irradiance.

For the H-BAs monolayer, we found two configurations to be stable, the planar and buckled geometries shown in Fig. 6.2b & 6.2f. The planar and buckled

Table 6.1. Hybrid corrected (HSE06) bandgaps of haeckelite monolayers and maximum absorbed photocurrent, J_{abs}^{max}, under AM1.5G solar illumination assessed from Eqn. 6.3. Included below are established materials employed as active layers for photocurrent generation.

Material	$E_g[eV]$	$J_{abs}^{max}(mA/cm^2)$
H-BN	5.44	–
H-BP	1.25	2.53
H-BAs	1.15	2.49
H_B-BAs	1.96	0.61
Si	1.11	0.1^a
P3HT	1.95	0.2^a
GaAs	1.42	0.3^a

[a] J_{abs}^{max} determined from literature absorption coefficients at 1 nm thickness (see Ref [279]).

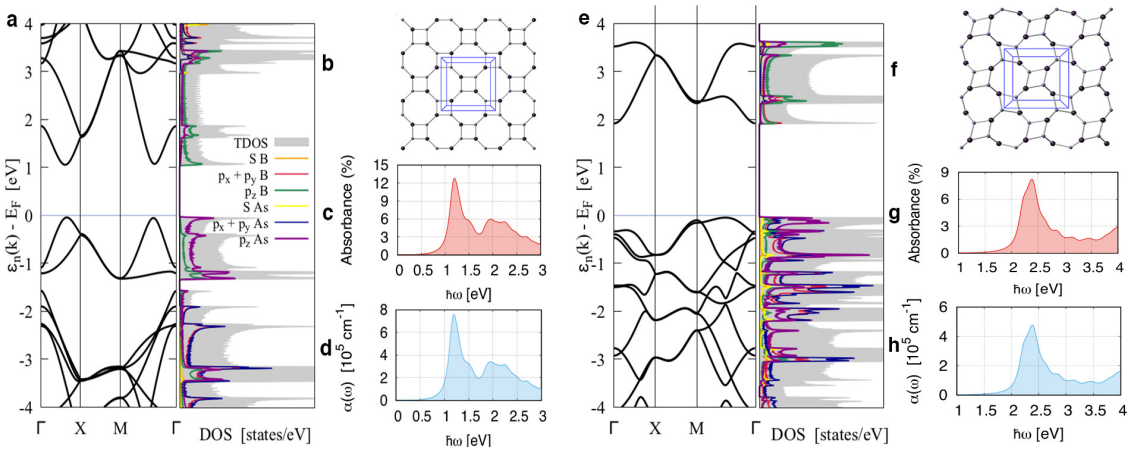

Figure 6.2. Hybrid band structure, PDOS, and optical response of H-BAs. (a) & (e) are the HSE06 band structures and projected density of states, (b) & (f) optimized structures of H-BAs and H_B-BAs, (c) & (g) absorbance spectra computed from Eqn. 6.1, and (d) & (h) absorption coefficients determined from Eqn. 6.2. We have added the s-channel to highlight the presence of s-electrons apparent in H_B-BAs.

haeckelite boron arsenide monolayers were found to have cohesive energies of -3.96 eV and -4.16 eV with the change in formation energy relative to bulk at 0.80 eV and 0.37 eV, respectively.[272] In planar H-BAs the double extrema remain present, and the fundamental gap lowers to approximately 1.15 eV. Thus, the salient optical trends observed within a planar configuration continues when phosphorus is substituted with the larger arsenic element. Furthermore, the formation of VHs can be observed in the PDOS (Fig. 6.2a; purple line marks states contributed by As, green line denotes states contributed by B), supporting strong optical response around 1.15 eV in the infrared. The global line shape of the absorbance resembles H-BP but with a slight decrease at the fundamental gap. Moreover, planar H-BAs exhibits strong optical absorbance of approximately 12.5% and absorption coefficient of 0.75 x 10^6 cm^{-1} (Fig. 6.2c,d). Consistent with this moderate change in the optical constants, the maximum open circuit photocurrent was found to be 2.49 mA/cm^2, Table 6.1. Thus, within the planar configuration H-BAs displays slightly reduced yet strong infrared absorbance. However, upon buckling, H-BAs forms the H_B-BAs structure, where the local geometries around each elemental constituent begin to resemble sp^3 hybridization. Consequently, the bandstructure is altered with an increased gap of 0.8 eV, Fig. 6.2e. Further, the H_B-BAs bandgap structure becomes increasingly indirect. This is driven by mixing additional p-state as well as s-state contributions to the valence band edge near the Fermi energy. Notice in the PDOS (Fig. 6.2e) the red and blue lines marking (p_x, p_y)-states approaching the Fermi level. This causes the H_B-BAs dielectric response to weaken and display a strong polarization shift to higher photon energy. The shift from infrared to visible is evident in the absorbance spectrum (Fig. 6.2g). H_B-BAs displays sizable response in the visible region near 2.38 eV, where the absorbance of H_B-BA rises to approximately 8.5% with an absorption coefficient of 0.48 x 10^6 cm^{-1}. This strong polarization emerges from interband transitions along M$-\Gamma$ ($\pi \rightarrow \pi^*$), where the valence band edge tracks the conduction

band edge closely resulting in a build up of joint density of states. More absorbance appears at higher ultraviolet energies resulting from greater sp^3 hybridization and $\sigma \rightarrow \pi^*$ transitions (not observable here). Further, we can see in Fig. 6.2e that the appearance of s-state contributions from both elements near the Fermi energy becomes more pronounced compared to the planar configuration H-BAs. Because of the reduction of the optical constants for H_B-BAs the maximum open circuit photocurrent lowered by 1.88 mA/cm^2 to 0.61 mA/cm^2. Nevertheless, the maximum photocurrent for H_B-BAs remains above existing photoactive materials listed in Table 6.1, even though it forms a buckled configuration. We shall see that the optical response of the planar Archimedean nanosheets can be attributed to a unique band-edge topology.

To better understand how indirect semiconductor haeckelite nanosheets can have such strong light-matter interactions, we further examined their electronic properties rendered in three dimensions. As a representative case for planar configurations, Fig. 6.3 displays the results for H-BP. From this illustration we can see the source of the enhanced light-matter response. For planar haeckelite monolayers, annuli-shaped extrema form in both the valence and conduction band. This topology extends across the entire Brillouin zone. The high symmetry points mark the line integration used to construct the bandstructures, Fig. 6.3c-d. Moving from Γ to X we can see a rise in the VBM or dip in the CBM. Continuing from X to M the dispersion rises along the high symmetry (100)-crystallographic face. Finally, moving from M to Γ we observe the second rise in the VBM or dip in the CBM. This pattern is reflected in the bandstructures presented above. Consequently, the opportunity for optical transitions to occur improves dramatically, as there exist greater numbers of allowed interband transitions via the selection rule $k_v \simeq k_c$, ensuring conservation of momentum. Hence, these $\pi \rightarrow \pi^*$ transitions occur all along the band edges of both the VBM and CBM (arrows Fig. 6.3b). Therefore, the unique band topology could be critical to enhancing light-matter interactions for emerging ultrathin films. This electronic

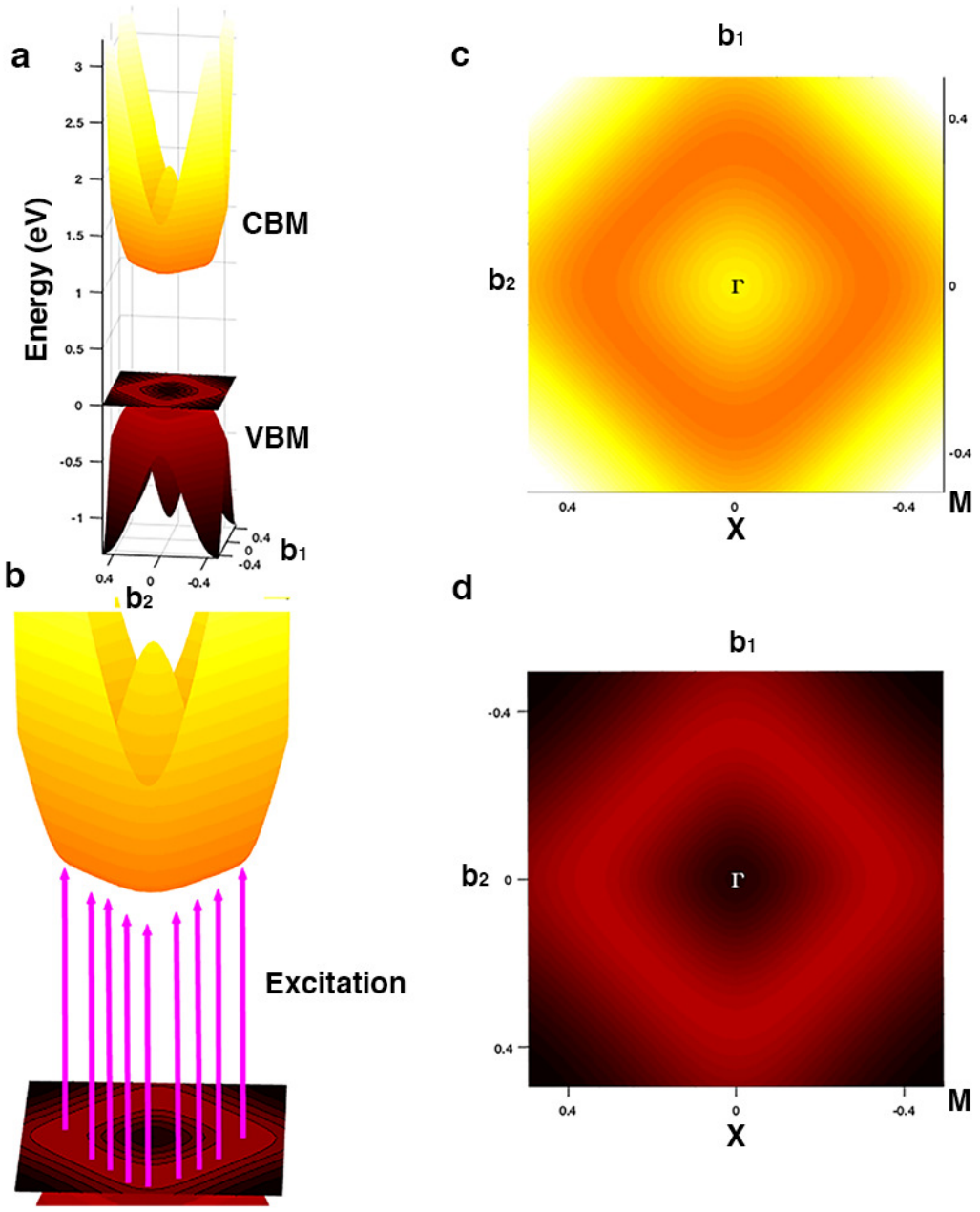

Figure 6.3. Reduced zone illustration of three-dimensional bands of H-BP monolayer. (a) Projection of H-BP valence band maximum (VBM) and conduction band minimum (CBM), (b) Optical interband transitions shown as arrows between VBM to CBM along an annulus geometry, (c) CBM of H-BP and (d) VBM of H-BP with high symmetry points labeled.

behavior, acute in the Archimedean structures presented here, has been observed for group IV-VI materials, albeit with less symmetry.[280] The symmetry of the bands can be attributed to the centrosymmetrism of the planar haeckelite materials. Moreover, because of the inversion symmetry of the planar haeckelite boron pnictogen monolayers, these structures display effectively equal bandgaps at multiple points in the Brillouin zone. Interestingly, in relation to reports elsewhere,[280] the band characters within these haeckelite monolayers bear similarities to group IV-VI materials in that each anion contributes to a large density of states (hence large effective mass) to the top-most valence band, and each cation contributes a large density of states to the bottom-most conduction band. Accordingly, the planar haeckelite nanosheets joint density of states is sizeable, which supports an increased propensity of optical excitation across the double bandgap, and thus, greater absorption coefficients for each monolayer nanosheet.

6.5 Conclusions

In conclusion, we have shown that the optical response of haeckelite boron pnictogen binary materials is exceptionally strong. For H-BN we observed a strong UV-absorber that is enhanced with respect to its h-BN counterpart.[260] Moreover, substituting phosphorus results in infrared absorption, which was found to be quite strong. We also observed, within the planar configuration, substituting arsenic results in little change in the overall optical response; however, buckling leads to altered electronic and optical properties. This was attributed to the change in hybridization around the Fermi energy and the diminution of the double extrema observed in the planar configurations. Hence, the buckled geometries present reduced optical response relative to planar nanosheets but still larger than established materials. Therefore, these configurationally distinct monolayer materials exhibit competitive light-matter interactions within the (4,8)-tessellation. The combination of complementary elements of the periodic table, localization (conjugation) in the ground state,

Van Hove singularities at the band edges, and the formation of symmetric annuli in the bandstructure promotes strong optical response. Hence, the optical response of these unique ultrathin films suggest the possibility of an unexplored and vast configurational space under confined conditions that could result in powerful new electronic materials currently just beyond the experimental horizon.[281]

6.6 Supplemental Information

Below we have included additional figures to highlight the resulting ground state planar configurations versus the nonplanar corrugated structure, see Ref. [17] of the main text. In Fig. 6.4, we show all of the resulting optimized structures where the central square ring was *plucked* above the plane of the nanosheet. This particular structural deformation was chosen as the smaller square ring likely contains high ring strain. Consonant with the high ring strain of the square ring, the octagonal ring likely has greater configurational plasticity, hence the choice is complementary in both energetics and configurationally accessible entropy. However, the resulting configurations, Fig 6.4(b), 6.4(d), & 6.4(f), displayed planar structures with the exception of H_B-BAs. Furthermore, a 2x2-supercell of H-BP was distorted again by forcing phosphorus to obtain a trigonal pyramidal geometry, Fig. 6.5(a), since H-BP is similar to H-BAs in terms of chemical bonding. However, upon relaxation the planar structure reformed.

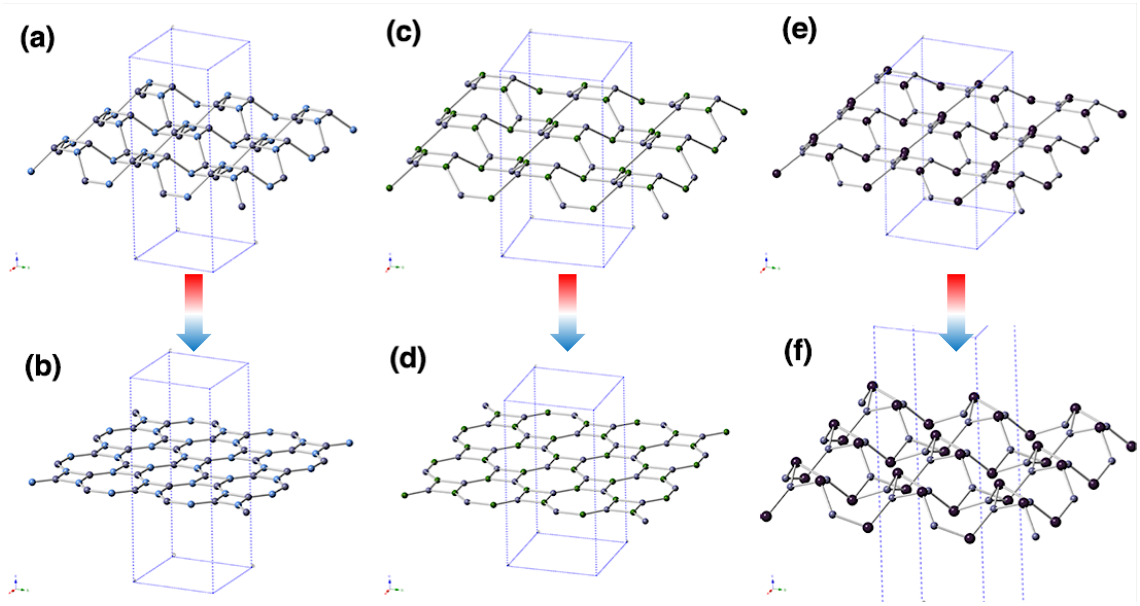

Figure 6.4. Displayed are the originally perturbed structures (upper panels) of monolayer haeckelite materials presented in the main text, and the resulting optimized ground state structures (lower panels). Each structure was distorted around the square ring where there is likely a source of high ring strain in an effort to uncover addional low energy configurations. (a)-(b) H-BN, (c)-(d) H-BP, and (e)-(f) H_B-BAs.

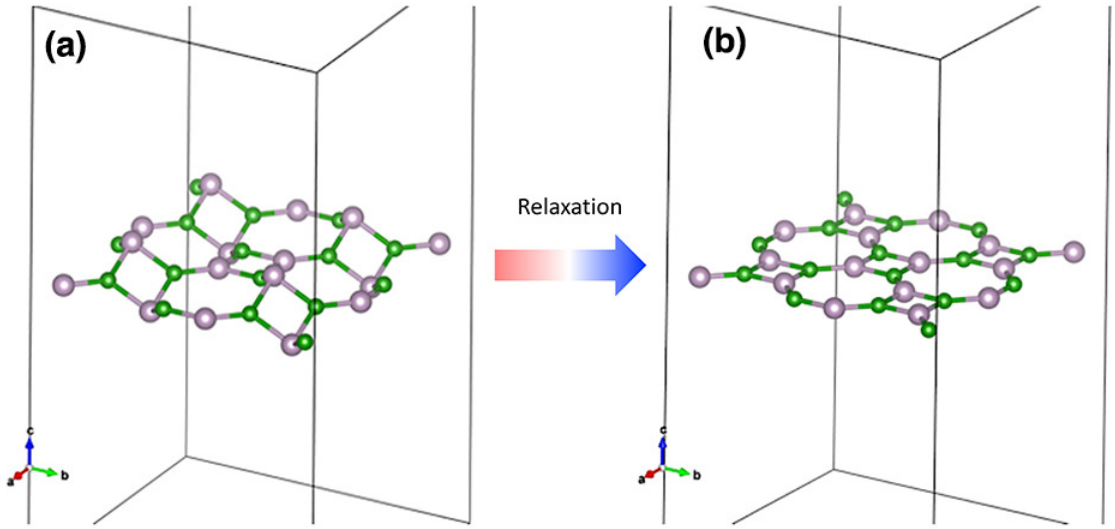

Figure 6.5. An alternative distortion was applied to monolayer of H-BP after optimization in Ref [17] of the main article to check planarity. (a) displays a trigonal pyramidal distortion around the phosphorus elements as the initial configuration, and (b) shows the final optimized planar structure reported in the main article.

CHAPTER SEVEN

Strain-Induced Semimetal-to-Semiconductor Transition and Indirect-to-Direct Band Gap Transition in Monolayer 1T-TiS_2

This chapter published as: Chengyong Xu; Paul A. Brown; and Kevin L. Shuford. RSC Adv., **2015**,5, 83876-83879

7.1 Abstract

We have investigated the effect of uniform plane strain on the electronic properties of monolayer 1T-TiS_2 using first-principles calculations. In the absence of strain, we find monolayer TiS_2 is a semimetal, with a small overlap of the valence band maximum and the conduction band minimum. The band overlap increases under compression; however under tensile, monolayer 1T-TiS_2 experiences a transition from a semimetal to a semiconductor as a band gap emerges. Moreover, the electronic properties change from an indirect to a direct band gap upon application of greater tensile strain. Thus one can modulate the properties of monolayer TiS_2 by applying the appropriate strain, thereby providing a route towards control in optoelectronic devices.

7.2 Introduction

Transition metal disulfides crystallize in layered forms. Within each layer, metal and sulfur atoms are held together by strong bonding interactions such that the metal atomic plane is sandwiched between two sulfur atomic planes. Normal to the planes, the individual layers are bound by weak van der Waals forces. These layers can be separated to form two-dimensional crystals composed of one to several layers by various synthetic routes.[282–284] Among the transition metal sulfides, TiS_2 is of particular interest due to its intriguing electronic, structural, and optical properties.[285,286] Moreover, these properties facilitate a synergistic coupling to other

materials that has been reported to improve electro- and photocatalytic activity of hydrogen evolution reactions.[287,288]

It is well known that strain can modulate the band structure of low dimensional materials. For example, monolayer MoX_2 (X = S, Se, and Te) experiences an indirect-to-direct band gap transition and a semiconductor-to-metal transition under mechanical strain due to the relocation of the conduction band minimum.[289] In this letter, we present a density functional theory investigation on monolayer TiS_2 under strain and report equally drastic changes to its electronic properties. Upon increasing tensile strain, the material evolves from a semimetal into a small band gap semiconductor. Concurrently, we observe a transition in the band gap from indirect to direct (and then back to indirect). This provides a way to tune the electronic properties of monolayer TiS_2 in a precise fashion by controlling the extent of strain on the monolayer.

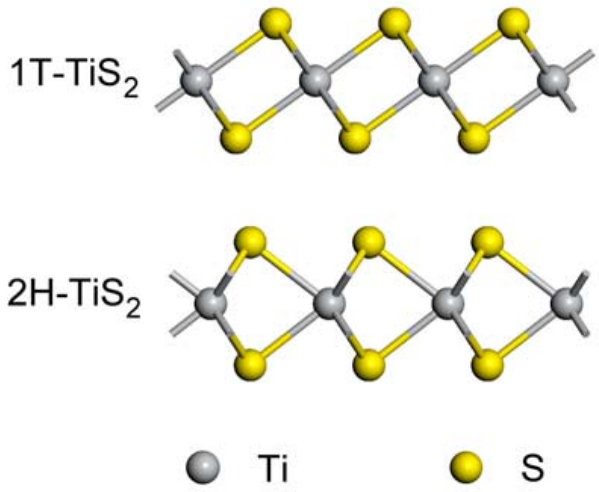

Figure 7.1. Schematic structure of 1T- and 2H-TiS_2. The 1T phase is 0.142 eV/atom lower in energy.

7.3 Computational Methods

The energy and electronic properties of monolayer TiS_2 were calculated using VASP[290] with the projector augmented wave pseudopotentials[291] and GGA-PBE[292] exchange-correlational functionals. The kinetic energy cutoff was set to 400 eV in the plane-wave basis set. The primary unit cell of monolayer TiS_2 was constructed with 20 Å of vacuum to eliminate possible image interactions. All layered structures were relaxed on a well-converged 25×25×1 Monkhorst-Pack[293] k-point grid until the Hellmann-Feynmann forces on every ion falls under 0.001 eV/Å. Strain on the monolayer was simulated by scaling the atomic positions of the relaxed structure by the appropriate factors along the lattice vector directions $\mathbf{a}_1$ and $\mathbf{a}_2$. The system was then allowed to relax again within the scaled unit cell. Calculations of the electronic properties followed on a 41×41×1 k-point grid. Bader analysis was used to quantify the charge transfer between atoms.[294] Calculations on bulk TiS_2 were also performed and found to be in good agreement with previous reports (see Supplemental Information for description and band structure).

We begin by presenting the properties of unstrained monolayer TiS_2. It consists of three atomic layers, where the titanium layer is sandwiched between two sulfur layers. TiS_2 favors the 1T structure, as opposed to the 2H structure (see Fig. 7.1). We have compared the energies of monolayer TiS_2 in the 2H and 1T phases, and find 1T-TiS_2 is 0.142 eV per atom lower in energy. All results from this point forward are on the 1-T phase. Figures 7.2c and 7.3b show the band structure and density of states (DOS) of monolayer TiS_2. The primary feature is the Fermi energy (E_F) crosses the valence and conduction bands. The valence band maximum (VBM) is located at Γ 0.109 eV above E_F, while the conduction band minimum (CBM) is located at M 0.104 eV above E_F. As observed from the relative position of the VBM and CBM, there is an energetic overlap of 5 meV suggesting the semimetallic nature of monolayer TiS_2. The angular moment resolved DOS of monolayer TiS_2 can be divided into

four main groups with respect to their energies. The first group between -13.6 and -11.9 eV mainly stems from the s states of sulfur and has a sharp peak at -11.91 eV. These states lie far below E_F and have little influence on the properties of monolayer TiS_2. The second group lies between -5.2 eV and E_F, and consists primarily of S-p states and to a lesser extent Ti-d. The third group is located between E_F and 1.8 eV, including hybridization between mainly Ti-d states with some S-p states. The second and third groups meet at E_F, where an inversion of their primary character occurs. The fourth group lies between 2.6 and 3.9 eV, and the hybridization is similar to that of the third group.

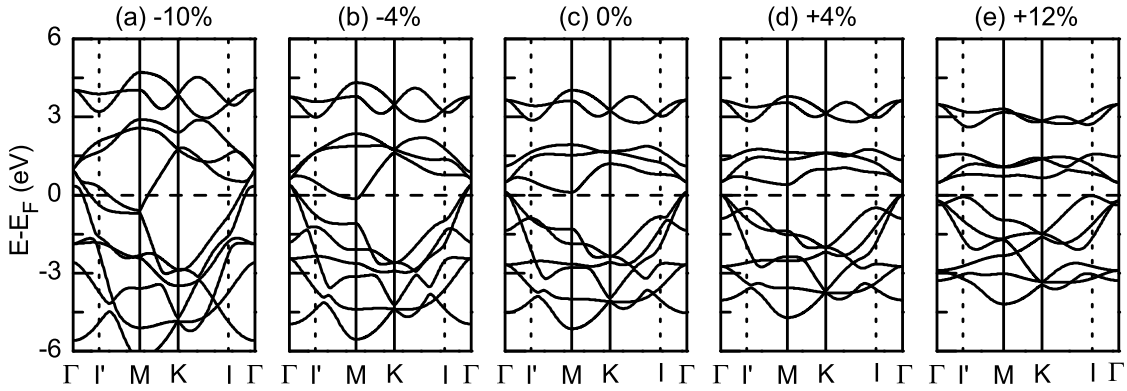

Figure 7.2. Band structures of monolayer 1T-TiS_2 under strain. Panels (a)-(e) correspond to strains of -10%, -4%, 0%, +4%, and +12%, respectively. The Fermi energy is denoted by a horizontal dashed line at zero energy. The I' and I points in the first Brillouin zone marked by dotted lines are not points with high symmetry.

Since the DOS and energy overlap at E_F is quite small (Figs. 7.2c and 7.3b), a slight disturbance in the structure may alter the electronic properties substantially. Indeed, strain on other two-dimensional materials – such as graphene,[295] 2H-MoS_2,[296,297] and ZrS_2,[298] – can adjust the relative position of the valence and conduction band edges. We have calculated the case of compression (negative strain) and tensile (positive strain) of monolayer TiS_2. Under slight compression (-4%, Fig. 7.2b), the VBM at Γ is shifted up while the CBM at M is shifted down with respect to E_F.

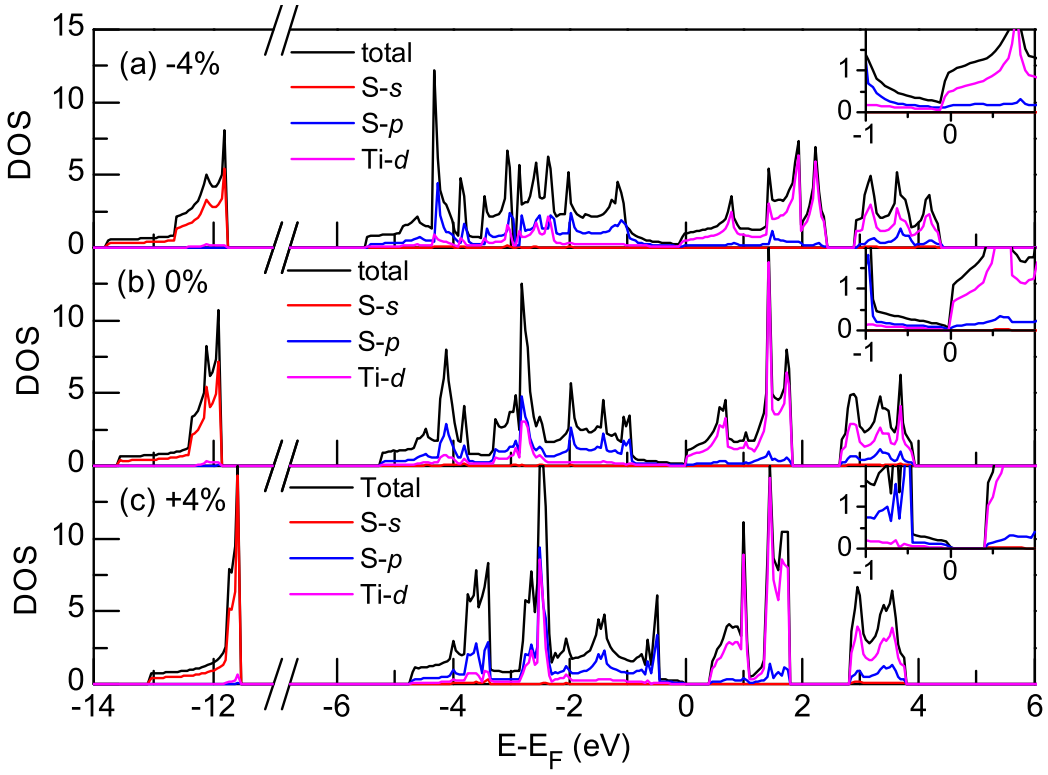

Figure 7.3. Density of states of monolayer 1T-TiS_2 under strain. Panels (a), (b), and (c) are under -4%, 0%, and +4% strain, respectively. The insets show the DOS near E_F.

The corresponding DOS at -4% strain is not altered in hybridization components, but the four groups are broadened energetically. Most notably, the second and third groups expand into each other's energy range near E_F. As a result, the overlap of conduction and valence bands is enlarged, making monolayer TiS_2 more semimetallic. Increasing compression further shifts the the lowest conduction band at the Γ point down. As a consequence, the conduction and valence bands at Γ get closer as compression increases and finally converge energetically when compression is -8%. At this point, the material can be understood as a metal, as part of the original conduction and valence bands are degenerate (Fig. 7.2a)

We have investigated the geometric variations and charge transfer in strained monolayer TiS_2 to further understand the effects of strain on this material. The results are presented in Table 7.1. Under compression, the distance between Ti and S atoms is shortened while fewer electrons are transferred from Ti to S, implying covalent bonding is increasing more rapidly than ionic attraction. Compared to zero strain, there is a redistribution of electrons from S_{3p} states towards Ti_{4d}, which is shown in the DOS as an expansion of the third group (mainly Ti_{4d} state) into the range of the second group (largely S_{3p} state). As a consequence, the second group and third group in the DOS merge into each other. In the corresponding band structure, this is manifested as more overlap of valence and conduction bands.

When a positive strain, or tensile, is applied to monolayer TiS_2, the VBM and CBM are shifted away from each other energetically as shown in Fig. 7.2d,e. The band structure for +4% strain displays the features of an indirect band gap semiconductor. In this case, the VBM and CBM are still located at Γ and M points, respectively; however, the energetic overlap has disappeared because the conduction bands are shifted upward. The corresponding DOS (Fig. 7.3c) is again very similar to the others in component and hybridization. However under +4% strain, the energy distribution of each of the four groups is narrower and the overall range is condensed. Also,

Table 7.1. The effect of strain on the geometry and band gap of monolayer 1T-TiS_2. The complete data set is provided in the Supporting Information. Negative (Positive) strain means compression (tensile). d_{Ti-S} is the bond length between nearest Ti and S atoms, h_{S-S} represents the interlayer height between upper and lower S atomic planes, and CT means charge transfer from Ti to S atoms. Negative band gap indicates overlapping of valence and conduction bands. VB-CB denotes the transition point from valence to conduction bands, and Ind/Dir refers to whether the transition of VB-CB is indirect or direct.

strain (%)	d_{Ti-S} (Å)	h_{S-S} (Å)	CT (e)	band gap (eV)	VB-CB	Ind/Dir
-10	2.368	3.150	1.528	—	—	—
-8	2.378	3.091	1.566	—	—	—
-4	2.400	2.968	1.639	-0.521	Γ-M	Ind
0	2.427	2.851	1.702	-0.005	Γ-M	Ind
+4	2.459	2.737	1.741	0.401	Γ-M	Ind
+6	2.476	2.677	1.752	0.567	Γ-Γ	Dir
+9	2.500	2.581	1.769	0.641	Γ-Γ	Dir
+10	2.508	2.547	1.771	0.601	I-Γ	Ind
+15	2.548	2.354	1.778	0.431	I-Γ	Ind
+20	2.586	2.125	1.768	0.389	I-Γ	Ind

the second and third groups are now separated from each other, and the conduction band no longer crosses E_F. So we see an energy gap emerges, and a semimetal-to-semiconductor transition occurs under tensile. As shown in Fig. 7.2d, the Γ and M points of the lowest conduction band are shifted upward at different rates in response to strain, with Γ shifting slower than M. Consequently, the CBM moves from M to Γ as the tensile strain reaches +6%, resulting in a direct band gap of 0.567 eV. Therefore, the semiconductor type changes from an indirect to direct band gap. Tensile also disproportionately affects the energetics of the valence bands. As the strain increases from 0%, two new points I' (about 39% from Γ to M) and I (about 34% from Γ to K) are shifted upward in energy rapidly, with I being higher. When strain reaches +10%, the I point exceeds the Γ point to become the VBM, while the CBM remains at the Γ point. Consequently, monolayer TiS_2 changes from a direct band gap ($\Gamma \rightarrow \Gamma$) to an indirect gap ($I \rightarrow \Gamma$), as shown in Fig. 7.2e for +12% strain. To summarize the effect of strain, we find monolayer TiS_2 is a semimetal under

compression, an indirect semiconductor when strain is between 0 and +6% as well as above +10%, and a direct semiconductor when strain is in the range from +6% to +10%.

Contrary to compression, TiS_2 under tensile strain has extended Ti-S bonds and more electron transfer (Table 7.1), suggesting ionic attraction plays a more important role. In this way, electrons are localized around atoms to a greater degree and become less itinerant. Therefore, the separation between the valence and conduction bands is enlarged. The energetic overlap is removed and a band gap appears. The band gap increases with strain until it reaches a maximum of 0.641 eV at +9% tensile. This is accompanied by an increase in charge transfer. Beyond this strain the band gap decreases, and charge transfer oscillates slightly while generally trending down. When strain is larger than +16%, the band gap remains almost constant in the range between 0.383 eV and 0.389 eV.

7.4 Conclusions

In summary, we have investigated the effect of strain on the electronic properties of monolayer 1T-TiS_2. We find the monolayer is a semimetal in the absence of strain. The semimetallic nature increases with compression and is accompanied by more overlap of the valence and conduction bands. Under tensile, however, the energetic overlap is removed and a semimetal-to-semiconductor transition occurs. The transition between valence and conduction bands is a Γ-Γ direct one when strain is between +6% and +10%. Outside of this range of tensile strain, an indirect transition is predicted. The change of electronic properties with respect to strain can be explained from the geometry and charge transfer. These results establish the relationship between the properties of 1T-TiS_2 and strain, which may find utility in future electronic devices.

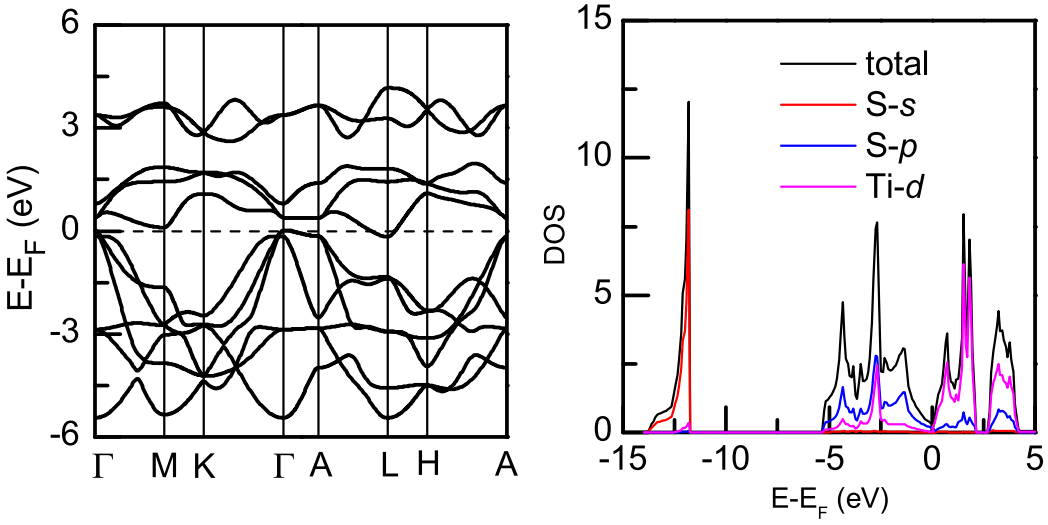

Figure 7.4. Band structure and DOS of bulk 1T-TiS_2.

Table 7.2. The effect of partial strain on the geometric and band gap of monolayer 1T-TiS_2. The complete data are listed in Supporting Information. Negative (Positive) strain means compression (tensile). d_{Ti-S} is the bond length between nearest Ti and S atoms, h_{S-S} represents the interlayer height between upper and lower S atomic planes, and CT means charge transfer from Ti to S atom. Negative band gap suggests overlapping of valence and conduction bands. VB-CB denotes the transition point from valence to conduction bands, and Ind/Dir refers to whether the transition of VB-CB is indirect or direct.

strain (%)	d_{Ti-S} (Å)	h_{S-S} (Å)	CT (e)	bandgap (eV)	VB-CB	Ind/Dir
-10	2.368	3.150	1.528	—	—	—
-9	2.373	3.120	1.546	—	—	—
-8	2.378	3.091	1.566	—	—	—
-7	2.382	3.058	1.608	-1.004	Γ-M	Ind
-6	2.387	3.024	1.613	-0.833	Γ-M	Ind
-5	2.394	2.999	1.626	-0.670	Γ-M	Ind
-4	2.400	2.968	1.639	-0.521	Γ-M	Ind
-3	2.407	2.939	1.656	-0.379	Γ-M	Ind
-2	2.413	2.909	1.673	-0.246	Γ-M	Ind
-1	2.420	2.879	1.685	-0.121	Γ-M	Ind
0	2.427	2.851	1.702	-0.005	Γ-M	Ind
+1	2.435	2.822	1.721	0.106	Γ-M	Ind
+2	2.443	2.794	1.732	0.211	Γ-M	Ind
+3	2.451	2.766	1.742	0.309	Γ-M	Ind
+4	2.459	2.737	1.741	0.401	Γ-M	Ind
+5	2.467	2.708	1.746	0.487	Γ-M	Ind
+6	2.476	2.677	1.752	0.567	Γ-Γ	Dir
+7	2.484	2.646	1.759	0.594	Γ-Γ	Dir
+8	2.492	2.614	1.762	0.618	Γ-Γ	Dir
+9	2.500	2.581	1.769	0.641	Γ-Γ	Dir
+10	2.508	2.547	1.771	0.601	I-Γ	Ind
+11	2.516	2.511	1.779	0.550	I-Γ	Ind
+12	2.524	2.474	1.777	0.507	I-Γ	Ind
+13	2.532	2.436	1.777	0.470	I-Γ	Ind
+14	2.540	2.396	1.779	0.440	I-Γ	Ind
+15	2.548	2.354	1.778	0.431	I-Γ	Ind
+16	2.555	2.311	1.775	0.400	I-Γ	Ind
+17	2.563	2.267	1.778	0.389	I-Γ	Ind
+18	2.571	2.222	1.773	0.383	I-Γ	Ind
+19	2.578	2.174	1.771	0.384	I-Γ	Ind
+20	2.586	2.125	1.768	0.389	I-Γ	Ind

CHAPTER EIGHT

Conclusion and Future Work

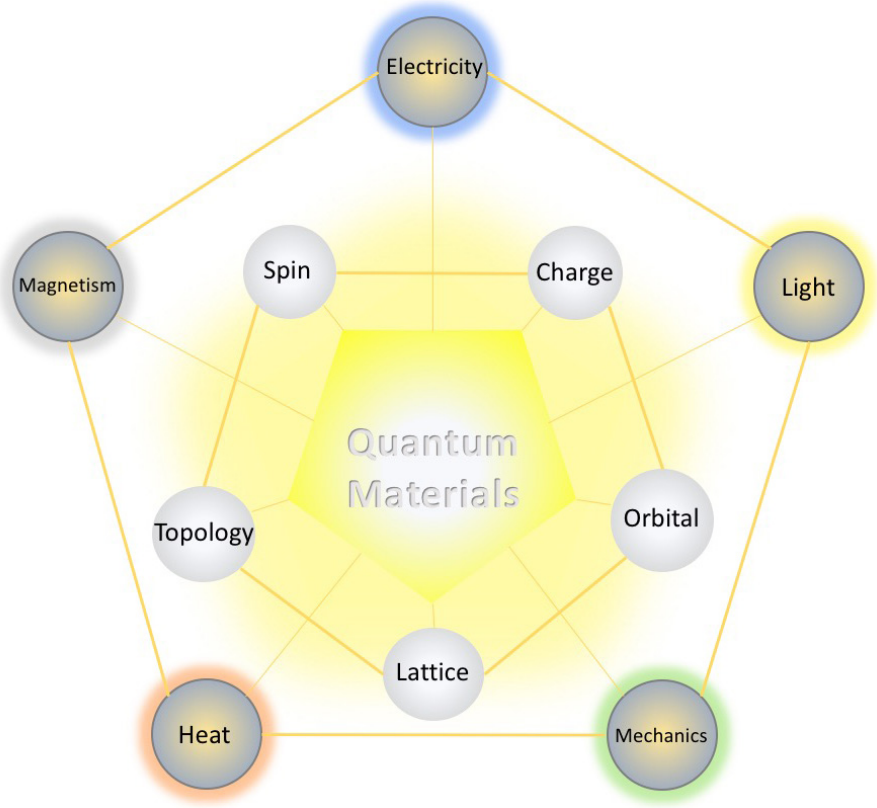

Figure 8.1. The quantum-materials pursuit. This figure contains the crucial internal degrees of freedom (inner pentagon) for tuning the material properties. The outer-pentagon displays the desired material response properties utilized by mankind. Adapted from Ref[29].

Ultrathin films are an extreme form of matter, wherefore along a single crystallographic direction all of the material is found. This body of research extends across existing and theorized ultrathin films, where advanced computational techniques provide the essential quantum picture of the electronic ground and excited state material properties. From the preceding chapters it is clearly demonstrated that the *tuning*

of material properties can generate entirely new material properties not supported in the original crystal. Furthermore, leveraging the degrees-of-freedom, e.g., spin, charge, orbital, lattice, and topology for a crystalline system provides an expedient path forward for fabricating new materials out of old materials. The extreme changes in the electronic properties of the ultrathin films discussed in previous chapters is possible because of the paucity of electrons that can be accommodated in the two-dimensional plane. Therefore, the sensitivity to intrinsic or extrinsic dopants, lattice tessellations, and mechanical deformations make it possible to alter ultrathin films dramatically to meet the societal demands of the 21^{st}-century. This manuscript forms a portion of a new epoch, the Quantum age, Figure 8.1. This age will be marked by many discoveries of new ultrathin films, which will beckon new nanotechnologies that could be coupled with existing technologies to bolster performance. Moreover, controlling the degrees-of-freedom of materials, such as ultrathin films, could make the possibility of materials on demand a reality.

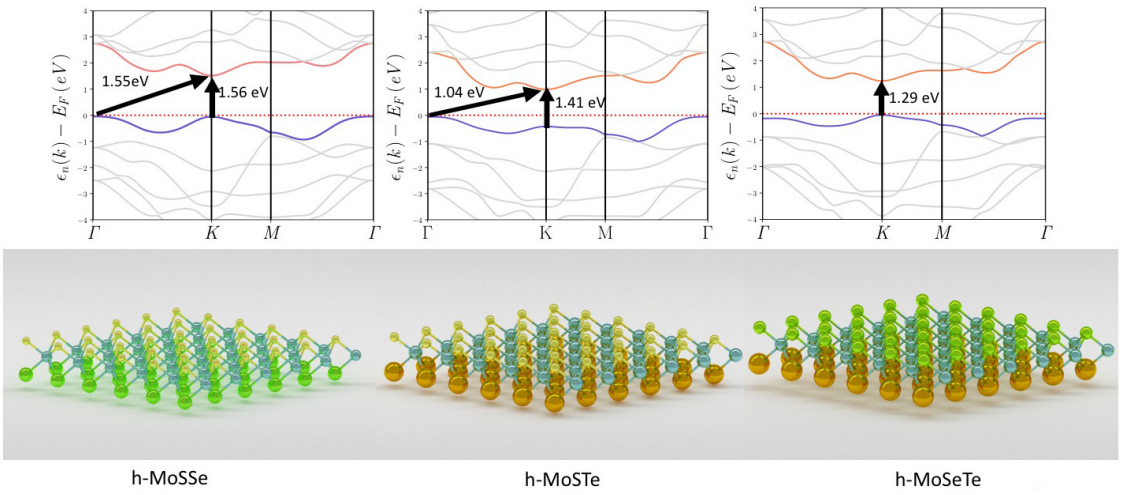

Figure 8.2. Janus transition metal dichalcogenides. Newly synthesized heteroleptic TMDs feature a permanent dipole moment offering the possibility of piezoelectric properties or strong Förster energy resonance transfer opening new possibilities for this group of ultrathin films.

The current and future directions of research in ultrathin films will continue to surround nanometer control of layer thickness and composition, Figure 8.1. Furthermore, most ultrathin films typically feature a hexagonal crystal, which is likely rooted in nature's preference to crystallize in a hexagonal form in two-dimensions.[120,299] However, this dissertation envisions a larger notion expounded in Chapter 5 and Chapter 6, and inspires two grand questions: what is configurationally and chemically accessible in two-dimensions? In other words, what structural complexity is possible in two-dimensions? And what is the chemical and physical taxonomy of two-dimensional ultrathin films? The former question points to the deep connection between the lattice and the orchestration of fermionic states. The latter question points to the categorification of material properties rooted in the first question, that is, the structure-function relationship. The first question addresses all possible two-dimensional tessellations that may be formed, if not already found in nature, then synthetically. From the group of configurationally distinct ultrathin films, the second question addresses their material properties, and; hence, classifies the potential application of novel nanosheets. However, this reductionist approach will likely face challenges. For one, condensed matter is non-reductionist, in that, it is difficult to presume that the sum of the parts of microscopic matter form the whole. Consequently, divesting patterns from the staggering data formed from the above questions will inevitably be difficult. Nevertheless, an understanding of material behavior in two-dimensions as a function of element and lattice could offer some insight and countless discoveries. For instance, a recent synthesis of a Cairo pentagonal $PdSe_2$ nanosheet was achieved, where the nanosheet forms regular pentagons as the major structural motif.[28] Furthermore, a combined experimental and theoretical study may in fact have already discovered a (4,8)-tessellated bulk crystal of ZnO (Figure 5 in cited article).[300] These results point to the potential of increased complexity where

regular, semi-regular, and irregular polygonal motifs could become the norm. Therefore, the two posed questions above will inevitably be explored as a new direction of scientific inquiry as the branch grows from the seminal trunk, the isolation and discovery of graphene back in 2004.[6]

Most recently, research on Janus (two-faced sentinel that guards the state in times of conflict) TMDs has been pursued. In Figure 8.2 a series of Janus TMDs and their bandstructures are presented. Interestingly, these heteroleptic TMDs feature, with a molybdenum metal ion, a MoXY stoichiometry with two different chalcogens populating opposite faces.[301–306] To date only MoSSe has been successfully synthesized and characterized. These TMD nanosheets carry a permanent dipole moment resulting from disproportionate electronegativity between the sulfur and selenium atoms bound to molybdenum metal ion, Figure 8.2. Interestingly, the overall hexagonal structures is retained, even at high preparation temperatures, where each variant of Janus TMD forms a direct gap semiconducting nanosheet (MoSSe and MoSeTe) or an indirect gap semiconductor (MoSTe). Moreover, h-MoSSe was found to have an equilibrium lattice constant of 3.24 Å, which is within less than 1 % error of the experimental lattice constant of 3.23 Å.[301] Interestingly, that lattice constant prediction was made with GGA PBE, which is impressive considering a 4d element is present. Because of the presence of a permanent dipole moment in Janus TMDs, these ultrathin films could fine useful applications as a piezoelectric material used in sensing applications for example. Moreover, because the dipole is fixed within the nanosheet, alignment with additional layers could result in ultrafast resonant energy transfer or charge transfer to a tandem material, such as silicon for photovoltaics. These heteroleptic ultrathin films will likely inspire new variants utilizing the durable TMD itself to diversify the new Janus family of ultrathin films.

Similar to the chalcogen based TMDs, highlighted above, the transition metal dipnictides (TMPs) could also form a fruitful direction of research. Only MoN_2 has

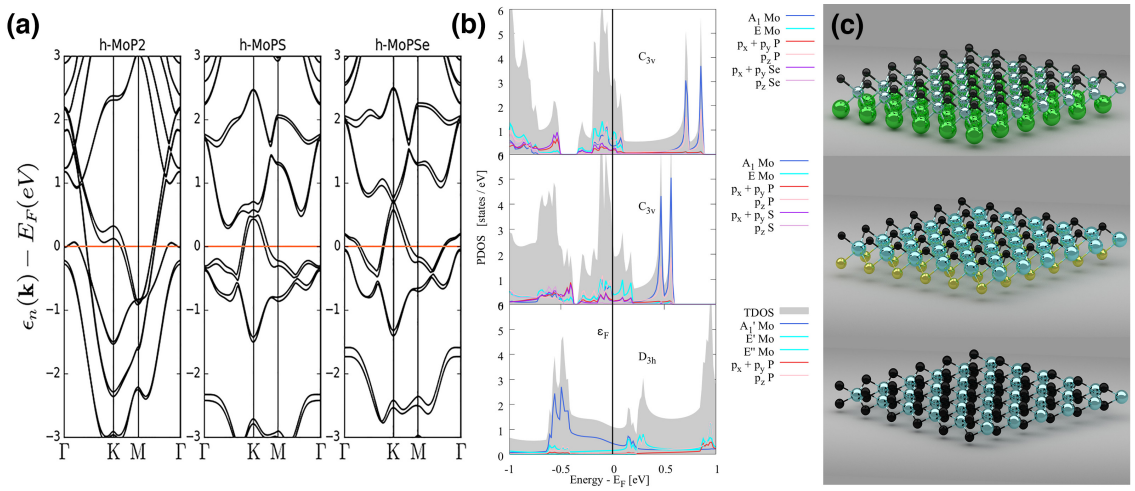

Figure 8.3. Newly theorized Janus transition metal dipnito-chalcogenides (h-MoPX, X=P,S,Se) featuring a phosphorus ligand. (a) displays the spin-orbit ground state bandstructures of each nanosheet (Fermi energy is set to zero, red line). All of the h-MoPX form ferromagnetic ground states. (b) projected density of states of each h-MoPX, and (c) equilibrium ground state structures of h-MoPX. Interestingly, each nanosheet h-MoPX features a magnetization and dipole moment, which suggest these ultrathin films are possibly multiferroic or half-metallicity.

been realized recently, suggesting that subsequent pnictogens might be fabricated in the near future.[307] In this respect the author has already theorized MoP_2, Figure 8.3, and the newly transition metal pnicto-chalcogenides (TMPDs). Each nanosheet supports a net magnetization (magnetic dipole) and polarization (electric dipole) suggesting that the Janus TMPDs are multiferroic or half-metallic nanosheets. In Figure 8.4, the spin-orbit charge density differences show clearly that the net magnetization results from the d_{z^2} orbital on the Mo-atom for MoP_2, but $p-d$ coupling appears in the Janus TMPDs. In fact, from the projected density of states the d_{z^2} orbital mixes with additional d-manifold states deforming the orbital (Figure 8.3(b)), where the mixing is mediated by enhanced coupling to chalcogen p-orbitals polarizing Mo d-orbitals. Hence, the magnetic ground state is synergistically established permitting phosphorus p_z-angular momentum to grow in prominence at the Fermi energy, see Figure 8.3(b). Furthermore, a general trend emerges where the magnetization

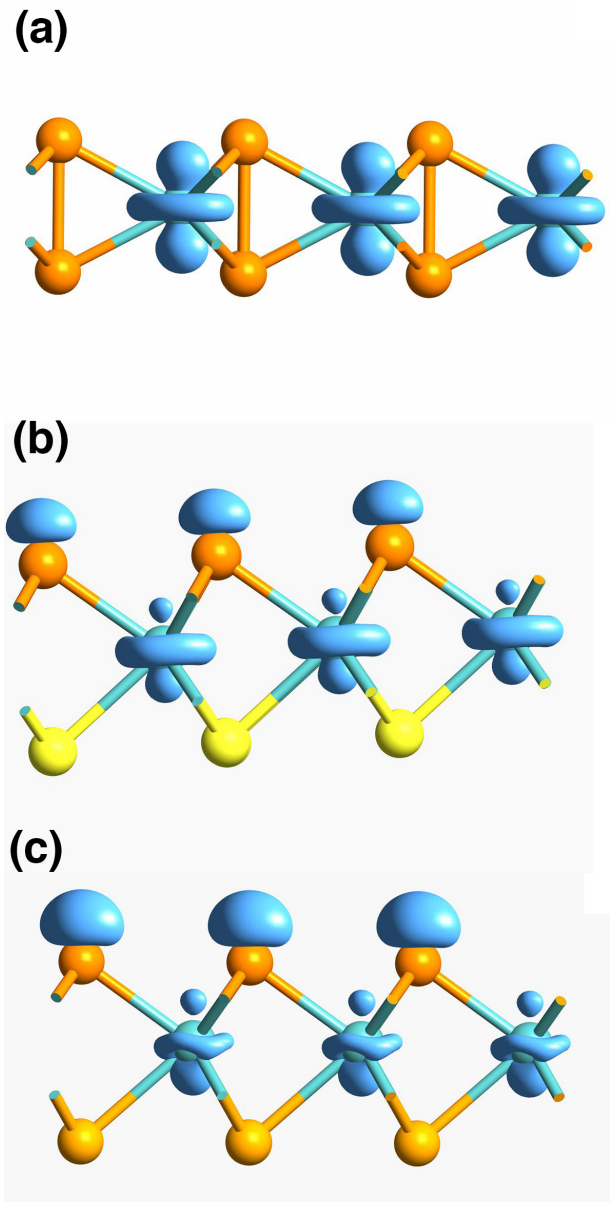

Figure 8.4. Spin-orbit charge density differences for h-MoPX ultrathin films. (a) h-MoP_2, (b) h-MoPS, and (c) h-MoPSe. Note the color of phosphorus is dark orange, yellow is sulfur, orange is selenium, and molybdenum light blue as above. Here the p-d magnetism between the phosphorus atom and molybdenum d_{z^2} can be readily seen (b) & (c). Note the perturbation of the Mo d_{z^2} in the presence of phosphorus and chalcogen atoms, yet in MoP_2 d_{z^2} is unperturbed with the homoleptic TMP seen in (a). Note the appearance of a cross-layer P-P bond. This is mostly rendering, but some weak density can be observed in the charge density difference.

tends to rise slightly proceeding to the heavier selenium element, where phosphorus-molybdenum orbital angular momenta become more prominent at the Fermi energy. Further analysis of heteroleptic ultrathin films is an open question, but comparing the Janus TMDs and Janus TMPDs, the small change in element can have have a significant impact on the ground state electronic properties. These ultrathin films, like the haeckelites, are ahead of their time, but all of the ultrathin films discussed herein carry potentially important material properties useful to society. In order to address the challenges highlighted in the introduction, scientist will be forced to trek an intellectual landscape never before explored. This exploration, of sorts, may just unmask the imperceptibility of *emergent* phenomena replete in nature and lead to new expansions in civilization as a whole.

APPENDICES

APPENDIX A

The Local-Spin Density Approximation & Generalized Gradient Approximation

Typically, approximations to the many-body problem based on the density are formed with the inclusion of spin, or spin-densities. Within the main text the formulations presented are spin-compensated, but the more general case treats each spin-fermion separately, and, in fact, better approximations can be obtained using spin-uncompensated Kohn-Sham equations, so this has become standard practice. We define the spin-generalized case for the local spin density approximation (LSDA), which is equivalent to the LDA, but the density becomes $n(r) = n_\uparrow(r) + n_\downarrow(r)$ and we include the relative spin-polarization, $\zeta(r) = \frac{n_\uparrow(r) - n_\downarrow(r)}{n(r)}$. The spin-densities take the form, $n_\sigma(r) = \frac{n(r)}{2}(1 + \sigma\zeta(r))$, where $\sigma = \uparrow, \downarrow$.[308,309] The effect of spin on the terms forming the Kohn-Sham equation (Equation 2.30) forms the well known spin-scaling relations for the noninteracting kinetic energy,

$$T_S[n_\uparrow, n_\downarrow] = \frac{1}{2}(T_S^{unpol}[2n_\uparrow] + T_S^{unpol}[2n_\downarrow]), \tag{A.1}$$

where the polarized noninteracting Kohn-Sham kinetic energy is the sum of unpolarized noninteracting kinetic energy of each spin contribution.[308,309] Likewise, the exchange energy per particle has the same form,

$$E_X[n_\uparrow, n_\downarrow] = \frac{1}{2}(E_X^{unpol}[2n_\uparrow] + E_X^{unpol}[2n_\downarrow]), \tag{A.2}$$

hence the spin-polarized exchange energy is a sum of each exchange energy spin-density.[308,309] Using the relative spin-polarization and spin-densities above and using

the UEG exchange energy we have

$$\epsilon_X[n,\zeta] = \epsilon_X^{unpol}[n]\Big(\frac{(1+\zeta^{4/3})+(1-\zeta^{4/3})}{2}\Big), \tag{A.3}$$

therefore the LSDA for the exchange energy takes the form,

$$E_X^{LSDA}[n] = -C_X \int d^3r n(r)^{4/3}\Big(\frac{(1+\zeta^{4/3})+(1-\zeta^{4/3})}{2}\Big). \tag{A.4}$$

The correlation energy for LSDA is given in Appendix B. The combination of $E_X^{LSDA}[n]$ and Perdew-Zunger or Vosko-Wilkes-Nusair correlation permits a general formulation of spin-density functional theory in common use. The correlation energy can be interpolated over the relative spin-polarization between paramagnetic (P) and ferromagnetic (F) ground states,

$$E_C^{LSDA}[n] = \int d^3r n(r)\epsilon_C^{UEG,i}(r_S), \tag{A.5}$$

which is the spin-correlation energy given in Appendix B.[308] Consequently, the exchange-correlation energy per particle includes a functional dependence on the spin-polarization, $\zeta(r)$, hence $E_{XC}[n](r) \mapsto E_{XC}[n,\zeta](r)$. This dependence is also included in the GGA formulation.

The generalized gradient approximation employed in this text utilizes PBE functional.[85] The correlation energy employed for PBE was adapted from the PW91 GGA earlier using the *ansatz*,

$$E_C^{PBE}[n_\uparrow, n_\downarrow] = \int d^3r n(r)[\epsilon_C^{UEG}[r_S,\zeta] + H(r_S,\zeta,t_S)], \tag{A.6}$$

which contains the contribution of the UEG correlation and an additional term chosen to obey certain constraints on the correlation energy whilst adhering to constraints

obeyed within LSD,

$$H(r_S,\zeta,t_S) = c_0\phi^2 ln\Big\{1+\frac{\beta_{MB}}{c_0}t_S^2\Big[\frac{1+At_S^2}{1+At_S^2+(At_S^2)^2}\Big]\Big\}, \tag{A.7}$$

where $t_S = \frac{|\nabla n|}{2\phi k_S n}$ is a reduced density gradient including Thomas-Fermi screening, k_S, $A = \frac{\beta_{MD}}{c_0}(e^{-\epsilon_C^{LDA}(r_S,\zeta)/c_0\phi^3}-1)^{-1}$, the spin-scaling factor $\phi(\zeta) = [(1+\zeta)^{2/3} + (1-\zeta)^{2/3}]/2$, and $\beta_{MD} = 0.066725$.[2,40,85] This form of H is chosen to obey several gradient conditions or limits, which include the slowly varying limit for $t \to 0$, rapidly varying limit $t \to \infty$, and uniform scaling to the high density limit.[85] In the slowly varying limit $t \to 0$, $H \to c_0\phi^3 ln\Big\{1+\frac{\beta_{MD}}{c_0}t_S^2\Big\} \to \beta_{MD}\phi^3 t_S^2$, which matches the leading order term in the GEA.[40] The rapidly varying limit $t \to \infty$, $H \to c_0\phi^3 ln\Big\{e^{-\epsilon_C^{LDA}(r_S,\zeta)/c_0\phi^3}\Big\} \to -\epsilon_C^{LDA}(r_S,\zeta)$, where the LDA correlation is recovered insuring the non-positivity of correlation. And the uniform scaling for $r_S \to 0$ at constant $s(r)$, $H \to c_0\phi^3 ln(t^2) \to -c_0\phi^3 ln(r_S)$ which cancels the leading singularity in the correlation of the UEG, see Appendix B Equation B1. Because Equation 2.81 retains these limits, PBE-correlation obeys similar constraints within LDA.[82] The exchange energy per electron in PBE this has the following form,

$$E_X^{PBE}[n] = \int d^3r n(r) e_X^{UEG}(n(r)) F_X(n,s(r),\zeta), \tag{A.8}$$

where $e_X^{UEG}(n(r)) = \frac{-3e^2k_F}{4\pi}$ and the enhancement factor in PBE-exchange is,

$$F_X(n,s(r)) = 1+\kappa-\frac{\kappa}{1+\mu s^2/\kappa}, \tag{A.9}$$

here $\kappa = 0.804$, $\mu = 0.21951$, and s is the density gradient. This form of exchange obeys the spin-scaling relation Equation 2.29, recovers LSDA linear response, and obeys the Lieb-Oxford bound (shown in Chapter 2).[85] In the above expression, Equations A.7-A.9 are supplied to Equation 2.44 of Chapter 2.

APPENDIX B

The Correlation Energy

As noted in the text of Chapter 2.2.3, the correlation energy per particle $E_C[n]$ is only true unknown term in the Kohn-Sham equations, Equations 2.17-2.18-2.34. Here we will expand upon the discussion of the correlation potential and provide some insight into the approximated/parameterized correlation potential commonly employed in DFT.

The correlation energy is known in two limits, that is the high density ($r_S \to 0$) and low density ($r_S \to \infty$) limits.[310,311] The Wigner-Seitz radius, $r_S = (3/4\pi)^{1/3} n(r)^{-1/3}$, is the average spherical distance between electrons.[40] In the high density limit the correlation energy per electron

$$\epsilon_C[r_S] = c_0 ln(r_S) - c_1 + c_2 r_S ln(r_S) - c_3 r_S + ..., \tag{B.1}$$

determined from perturbation expansion of the uniform electron gas.[310] Here the coefficients were found to be $c_0 = 0.031091$ and $c_1 = 0.046644$.[40] In the low density regime the correlation energy per electron was found to be,

$$\epsilon_C[r_S] = -\frac{d_0}{r_S} + \frac{d_1}{r_S^{3/2}} + ..., \tag{B.2}$$

which is determined from the zero-point vibrational energy and Madelung electrostatic energies of the uniform electron gas.[40,311] Here $d_0 \approx 0.896$ and $d_1 \approx 1.325$.[311,312] Both of these two expressions have enabled for interpolations between them to derive new $\epsilon_C[n]$. Two notable parameterizations for the correlation energy are the Perdew-Zunger and Vosko-Wilkes-Nusair correlation energies. In the Perdew-Zunger parameterization the correlation energy was fitted to highly accurate quantum Monte

Carlo data,

$$\epsilon_C[r_S] = \begin{cases} \gamma_i(1+\beta_1^i\sqrt{r_S}+\beta_2^i r_S)^{-1} & \forall r_S \geq 1 \\ A_i ln(r_S) + B_i + C_i r_S ln(r_S) + D_i r_S & \forall r_S < 1 \end{cases}$$

, where the constants appearing in the expression are found in Ref[42]. Note, $i = P, F$, for paramagnetic and ferromagnetic spin-polarized ground states. From the Perdew-Zunger correlation energy, the potential energy for Equation 2.34 can be approximated via, $v_c^i[n] = \epsilon_C^i[n] + n(r)\frac{\partial r_S}{\partial n}\frac{\partial \epsilon_C^i[r_S]}{\partial r_S}$, permitting full solution to the Kohn-Sham equations. Another parameterization was provided by Vosko, Wilkes, and Nusair, where their approximation to the correlation energy followed a similar approach to Perdew-Zunger, and took the form,

$$\epsilon_C[r_S] = \frac{A}{2}\Big[ln\frac{x}{X(x)} + \frac{2b}{Q}arctan\Big(\frac{Q}{2x+b}\Big) - \frac{bx_0}{X(x_0)}\Big[ln\frac{(x-x_0)^2}{X(x)} + \frac{2(b+2x_0)}{Q}arctan\Big(\frac{Q}{2x+b}\Big)\Big]\Big], \tag{B.3}$$

where $x = \sqrt{r_S}$, $X(x) = x^2 + bx + c$, $Q = (4c - b)^{1/2}$, $A = 0.0621814$, $b = 13.07020$,$c = 42.7198$,$c = 42.7198$,and $x_0 = -0.0409286$.[67,79] This expression can be inserted into the same expression as the Perdew-Zunger for the effective Kohn-Sham potential energy to fully solve Equation 2.34. Hence, ultimately the correlation energy is an approximated quantity interpolated on a spin-polarized ground state of a UEG.

APPENDIX C

Adiabatic Connection

The adiabatic connection theorem provides an elegant way of *turning* on the exchange-correlation within a many-body system. This can be accomplished with the aid of the Hellmann-Feynman theorem for the expectation of the total energy,

$$\epsilon_n(\lambda) = \frac{\langle\psi_n(\lambda)|\hat{H}_{KS}|\psi_n(\lambda)\rangle}{\langle\psi_n(\lambda)|\psi_n(\lambda)\rangle}, \tag{C.1}$$

where the parameter $\lambda \in [0,1]$, which will be passed to the electron-electron interaction. Applying the Hellmann-Feynman theorem to Equation 2.1 results in the expression,

$$\epsilon_n(1) - \epsilon_n(0) = \int_0^1 d\lambda \frac{\langle\psi_n(\lambda)|\frac{\partial\hat{H}_{KS}}{\partial\lambda}|\psi_n(\lambda)\rangle}{\langle\psi_n(\lambda)|\psi_n(\lambda)\rangle}. \tag{C.2}$$

Including the parameter λ into the Kohn-Sham Hamiltonian via the Levy-Lieb constrained search formula, $F_{KS}[n] = \inf_{|\psi\rangle\in\mathcal{G}}\langle\psi|\hat{H}_{e,kin} + \lambda V_{ee}|\psi\rangle$. The expressions for the λ-dependent energy will be useful for constructing the adiabatic connection theorem for the Kohn-Sham Hamiltonian, and; furthermore, we will see that approximations to the exchange-correlation energy will rest on approximations of the exchange-correlation hole.

As noted in Chapter 1, the Levy-Lieb functional is related to the Hohenberg-Kohn functional via, $F_{LL}[n] = T[n] + U_H[n] + \tilde{E}_{XC}[n]$. Note that I have added a tilde over the exchange-correlation energy to suggest that this is *exact*, whereas in the Kohn-Sham functional of the Levy-Lieb functional will contain the approximate exchange-correlation energy per particle. Hence, $F_{LL}[n] = T_S[n] + E_{XC}[n]$. Equating

the two expressions and solving for the exchange-correlation energy,

$$E_{XC}[n] = F_{LL}[n] - T_S[n] - \frac{1}{2}\frac{e^2}{4\pi\epsilon_0}\sum_{\sigma\sigma'}\int\int d^3r d^3r' \frac{n_\sigma(r)n_{\sigma'}(r')}{|r-r'|}, \tag{C.3}$$

where the last term is the Hartree energy. As mentioned above, the Levy-Lieb functional will contain a interaction parameter, λ, where the electron-electron interaction will be gradually switched on. Hence, $F^\lambda_{LL}[n] = \inf_{|\Psi\rangle\in\mathcal{G}}\langle\Psi_\lambda[n]|T_S[n] + \lambda V_{ee}[n]|\Psi_\lambda[n]\rangle$. In this form of the Levy-Lieb functional the functional dependence of the many-body wavefunction depends on the density as required by the Hohenberg-Kohn theorems of Chapter 1. However, to ensure conservation of electron density a Lagrange-multiplier is added to the Levy-Lieb functional, which takes on the form,

$$E_{XC}[n] = F^\lambda_{LL}[n] + \int d^3r(v_\lambda(r_i) - \frac{E_\lambda}{N})\langle\Psi_\lambda[n]|\hat{n}|\Psi_\lambda[n]\rangle - U_H[n], \tag{C.4}$$

where the variation of $F^\lambda_{LL}[n]$ leads to an eigenvalue expression of the form,

$$H_\lambda|\Psi_\lambda\rangle = (T_S[n] + \lambda V_{ee}[n] + \sum_i v_\lambda(r_i)) = E_\lambda|\Psi_\lambda\rangle. \tag{C.5}$$

The $v_\lambda(r_i)$ counteracts the electron-electron potential energy of the electrons, such that, when the interaction is scaled to zero, $\lambda = 0$, the $V_{ee}[n]$ term vanishes and the single-particle potential energy dominates ensuring electron density conservation. With Equation C.5 in hand we can apply the Hellmann-Feynman theorem to determine the exchange-correlation energy per electron in terms of the interaction parameter, λ. Therefore,

$$\begin{aligned}\frac{\partial E_\lambda}{\partial\lambda} &= \langle\Psi_\lambda[n]|\frac{\partial H_\lambda}{\partial\lambda}|\Psi_\lambda[n]\rangle \\ &= \langle\Psi_\lambda[n]|V_{ee}[n]|\Psi_\lambda[n]\rangle + \int d^3r n(r)v_\lambda(r),\end{aligned} \tag{C.6}$$

and noting that $E_\lambda = F^\lambda_{LL}[n] + \langle\Psi_\lambda[n]|\sum_i v_\lambda(r_i)|\Psi_\lambda[n]\rangle$, it follows,

$$\frac{\partial F^\lambda_{LL}[n]}{\partial\lambda} = \langle\Psi_\lambda[n]|V_{ee}[n]|\Psi_\lambda[n]\rangle. \tag{C.7}$$

Equation C.7 can be implemented into the expression C.3 we have

$$E_{XC}[n] = \int_0^1 d\lambda\langle\Psi_\lambda[n]|V_{ee}[n]|\Psi_\lambda[n]\rangle - U_H[n]. \tag{C.8}$$

This expression can be simplified further by expanding the pair-spin density, Chapter 1, and canceling the Hartree energy that follows, where the final expression leads to a simple expression for the exchange-correlation energy per particle scaled over the interaction parameter, λ,

$$E_{XC}[n] = \frac{1}{2}\frac{e^2}{4\pi\epsilon_0}\int_0^1 d\lambda\int\int d^3r d^3r'\frac{n_\sigma(r)n^\lambda_{XC}(r,r')}{|r-r'|}, \tag{C.9}$$

where the exchange-correlation hole has the form, $n^\lambda_{XC}(r,r') = [g^\lambda_{\sigma\sigma'}(r,r') - 1]n_{\sigma'}(r')$, as alluded to in Chapter 1. This expression is shown in Equation 2.37 of Chapter 1. Equation C.9 is a simpler form for the exchange-correlation energy, and generally forms the starting point for approximations applied to this term to solve the Kohn-Sham field equations. In fact, Equation C.9 has a spherical dependence, $u = |r-r'|$, on the exchange-correlation hole density, as an approximation of course, which takes a simpler form,

$$\begin{aligned} E_{XC}[n] &= \frac{1}{2}\frac{e^2}{4\pi\epsilon_0}\sum_{\sigma\sigma'}\int d^3r n(r)\int du 4\pi\frac{n^{SA}_{\sigma\sigma'}(u)}{u} \\ &= \frac{1}{2}\frac{e^2}{4\pi\epsilon_0}\int du\frac{\langle n_{XC}(u)\rangle}{u}. \end{aligned} \tag{C.10}$$

Here we have moved the integration over space into the spherical average of the exchange-correlation hole, $\langle n_{XC}(u)\rangle$. The 4π results from integration over all spherical

space, and now any approximation that is made to $E_{XC}[n]$ must simply capture the spherical dependence of the exchange and correlation hole densities at average spherical distances, u.

APPENDIX D

Collaborations

Complementing this body of work is also a series of collaborations that have not been explicitly included. These collaborative projects were completed and published elsewhere with Dr. Caleb D. Martin's group with his counsel. Furthermore, an earlier collaboration with the Chambliss group for the comparison of computed and experimental molecular cross-sections was conducted. These projects were essential, for they have provided the opportunity to interface with the experimentalist and their observations.

Additional Works:

- Barnard, Jonathan; Brown, Paul A.; Shuford, Kevin L.; Martin, Caleb D. *Angew. Chem. Int. Ed.* **2015**, 54, 12083-12086

- Brown, Paul A.; Martin, Caleb D.; Shuford, Kevin L. *under revision* **2018**

BIBLIOGRAPHY

(1) School, F. Jacob's ladder. Musee du Petit Palais, 84000 Avignon, c.1490; Palais des Archevques, Place du Palais des Papes

(2) Martin, R. *Electronic Structure: Basic Theory and Practical Methods*, 1st ed.; 0; Cambridge University Press: The Edinburgh Building, Cambridge CB2 8RU, UK, 2004; Vol. 0

(3) Engel, E.; Dreizler, R. M. *Density Functional Theory, An Advanced Course*, 1st ed.; Theoretical and Mathematical Physics; Springer-Verlag Berlin Heidelberg: Springer Heidelberg Dordrecht London New York, 2011; Vol. 0

(4) Baskin, Y.; Meyer, L. Lattice Constants of Graphite at Low Temperatures. *Phys. Rev.* **1955**, *100*, 544–544

(5) `http://cccbdb.nist.gov/expdata.asp`, Accessed: 6-01- 2015

(6) Novoselov, K. S.; Geim, A. K.; Morozov, S. V.; Jiang, D.; Zhang, Y.; Dubonos, S. V.; Grigorieva, I. V.; Firsov, A. A. Electric Field Effect in Atomically Thin Carbon Films. *Science* **2004**, *306*, 666–669

(7) Novoselov, K. S.; Jiang, D.; Schedin, F.; Booth, T. J.; Khotkevich, V. V.; Morozov, S. V.; Geim, A. K. Two-dimensional atomic crystals. *Proc. Natl. Acad. Sci. U.S.A.* **2005**, *102*, 10451–10453

(8) Geim, A.; Novoselov, K. The rise of graphene. *Nature Mater.* **2007**, *6*, 183–191

(9) Britnell, L.; Ribeiro, R. M.; Eckmann, A.; Jalil, R.; Belle, B. D.; Mishchenko, A.; Kim, Y.-J.; Gorbachev, R. V.; Georgiou, T.; Morozov, S. V.; Grigorenko, A. N.; Geim, A. K.; Casiraghi, C.; Neto, A. H. C.; Novoselov, K. S. Strong Light-Matter Interactions in Heterostructures of Atomically Thin Films. *Science* **2013**, *340*, 1311–1314

(10) Fiori, G.; Bonaccorso, F.; Iannaccone, G.; Palacios, T.; Neumaier, D.; Seabaugh, A.; Banerjee, S. K.; Colombo, L. Electronics based on two-dimensional materials. *Nature Nanotech.* **2014**, *9*, 768–779

(11) Restrepo, O. D.; Krymowski, K. E.; Goldberger, J.; Windl, W. A first principles method to simulate electron mobilities in 2D materials. *New J. Phys.* **2014**, *16*, 105009

(12) Bonaccorso, F.; Colombo, L.; Yu, G.; Stoller, M.; Tozzini, V.; Ferrari, A. C.; Ruoff, R. S.; Pellegrini, V. Graphene, related two-dimensional crystals, and hybrid systems for energy conversion and storage. *Science* **2015**, *347*, 1246501

(13) Ponraj, J. S.; Xu, Z.-Q.; Dhanabalan, S. C.; Mu, H.; Wang, Y.; Yuan, J.; Li, P.; Thakur, S.; Ashrafi, M.; Mccoubrey, K.; Zhang, Y.; Li, S.; Zhang, H.; Bao, Q. Photonics and optoelectronics of two-dimensional materials beyond graphene. *Nanotechnology* **2016**, *27*

(14) Deng, D.; Novoselov, K. S.; Fu, Q.; Zheng, N.; Tian, Z.; Bao, X. Catalysis with two-dimensional materials and their heterostructures. *Nature Nanotech.* **2016**, *11*, 218–230

(15) Luo, B.; Liu, G.; Wang, L. Recent advances in 2D materials for photocatalysis. *Nanoscale* **2016**, *8*, 6904–6920

(16) Si, C.; Sun, Z.; Liu, F. Strain engineering of graphene: a review. *Nanoscale* **2016**, *8*, 3207–3217

(17) Wang, Z.; Zhu, W.; Qiu, Y.; Yi, X.; von dem Bussche, A.; Kane, A.; Gao, H.; Koski, K.; Hurt, R. Biological and environmental interactions of emerging two-dimensional nanomaterials. *Chem. Soc. Rev.* **2016**, *45*, 1750–1780

(18) Choi, W.; Choudhary, N.; Han, G. H.; Park, J.; Akinwande, D.; Lee, Y. H. Recent development of two-dimensional transition metal dichalcogenides and their applications. *Materials Today* **2017**, *20*, 116 – 130

(19) Tan, C.; Cao, X.; Wu, X.-J.; He, Q.; Yang, J.; Zhang, X.; Chen, J.; Zhao, W.; Han, S.; Nam, G.-H.; Sindoro, M.; Zhang, H. Recent Advances in Ultrathin Two-Dimensional Nanomaterials. *Chem. Rev.* **2017**, *117*, 6225–6331

(20) Mannix, A. J.; Zhou, X.-F.; Kiraly, B.; Wood, J. D.; Alducin, D.; Myers, B. D.; Liu, X.; Fisher, B. L.; Santiago, U.; Guest, J. R.; Yacaman, M. J.; Ponce, A.; Oganov, A. R.; Hersam, M. C.; Guisinger, N. P. Synthesis of borophenes: Anisotropic, two-dimensional boron polymorphs. *Science* **2015**, *350*, 1513–1516

(21) Tao, L.; Cinquanta, E.; Chiappe, D.; Grazianetti, C.; Fanciulli, M.; Dubey, M.; Molle, A.; Akinwande, D. Silicene field-effect transistors operating at room temperature. *Nat. Nanotech.* **2015**, *10*, 227–231

(22) Zhu, F.-F.; Chen, W.-J.; Xu, Y.; Gao, C.-L.; Guan, D.-D.; Liu, C.-H.; Qian, D.; Zhang, S.-C.; Jia, J.-F. Epitaxial growth of two-dimensional stanene. *Nature Mater.* **2015**, *14*, 1020–1025

(23) Gong, C.; Li, L.; Li, Z.; Ji, H.; Stern, A.; Xia, Y.; Cao, T.; Bao, W.; Wang, C.; Wang, Y.; Qiu, Z.; Cava, R.; Louie, S.; Xia, J.; Zhang, X. Discovery of intrinsic ferromagnetism in two-dimensional van der Waals crystals. *Nature* **2017**, *546*, 265–269

(24) Pan, J.; Lany, S.; Qi, Y. Computationally Driven Two-Dimensional Materials Design: What Is Next? *ACS Nano* **2017**, *11*, 7560–7564

(25) Huang, B.; Clark, G.; Navarro-Moratalla, E.; Klein, D.; Cheng, R.; Seyler, K.; Zhong, D.; Schmidgall, E.; McGuire, M.; Cobden, D.; Yao, W.; Xiao, D.; Jarillo-Herrero, P.; Xu, X. Layer-dependent ferromagnetism in a van der Waals crystal down to the monolayer limit. *Nature* **2017**, *546*, 270–273

(26) Liu, X.; Watanabe, K.; Taniguchi, T.; Halperin, B.; Kim, P. Quantum Hall drag of exciton condensate in graphene. *Nature Phys.* **2017**, *13*, 746–750

(27) Li, J.; Taniguchi, T.; Watanabe, K.; Hone, J.; Dean, C. Excitonic superfluid phase in double bilayer graphene. *Nature Phys.* **2017**, *13*, 751–755

(28) Oyedele, A. D. et al. $PdSe_2$: Pentagonal Two-Dimensional Layers with High Air Stability for Electronics. *J. Amer. Chem. Soc.* **2017**, *139*, 14090–14097

(29) Tokura, Y.; Kawasaki, M.; Nagaosa, N. Emergent functions of quantum materials. *Nature Phys.* **2017**, *13*, 1056–1068

(30) Jin, J.; Fu, X.; Liu, Q.; Liu, Y.; Wei, Z.; Niu, K.; Zhang, J. Identifying the Active Site in Nitrogen-Doped Graphene for the VO^{2+}/VO_2^+ Redox Reaction. *ACS Nano* **2013**, *7*, 4764–4773

(31) Zheng, Y.; Jiao, Y.; Li, L. H.; Xing, T.; Chen, Y.; Jaroniec, M.; Qiao, S. Z. Toward Design of Synergistically Active Carbon-Based Catalysts for Electrocatalytic Hydrogen Evolution. *ACS Nano* **2014**, *8*, 5290–5296

(32) Wang, H.; Xie, M.; Thia, L.; Fisher, A.; Wang, X. Strategies on the Design of Nitrogen-Doped Graphene. *J. Phys. Chem. Lett.* **2014**, *5*, 119–125

(33) Lv, J.-J.; Li, Y.; Wu, S.; Fang, H.; Li, L.-L.; Song, R.-B.; Ma, J.; Zhu, J.-J. Oxygen Species on Nitrogen-Doped Carbon Nanosheets as Efficient Active Sites for Multiple Electrocatalysis. *ACS Appl. Mater. & Interfaces* **2018**, *10*, 11678–11688

(34) Ji, L.; Wang, J.; Teng, X.; Dong, H.; He, X.; Chen, Z. N,P-Doped Molybdenum Carbide Nanofibers for Efficient Hydrogen Production. *ACS Appl. Mater. & Interfaces* **2018**, *10*, 14632–14640

(35) Jin, H.; Guo, C.; Liu, X.; Liu, J.; Vasileff, A.; Jiao, Y.; Zheng, Y.; Qiao, S.-Z. Emerging Two-Dimensional Nanomaterials for Electrocatalysis. *Chem. Rev.* **0**, *0*, null

(36) Jung, N.; Kim, N.; Jockusch, S.; Turro, N. J.; Kim, P.; Brus, L. Charge Transfer Chemical Doping of Few Layer Graphenes: Charge Distribution and Band Gap Formation. *Nano Lett.* **2009**, *9*, 4133–4137

(37) Marx, D.; Hutter, J. *Ab Initio Molecular Dynamics: Basic Theory and Advanced Methods*, 1st ed.; 0; Cambridge University Press: The Edinburgh Building, Cambridge CB2 8RU, UK, 2009; Vol. 0

(38) Kohn, W. Nobel Lecture: Electronic structure of matter-wave functions and density functionals. *Rev. Mod. Phys.* **1999**, *71*, 1253–1266

(39) Phillips, P. *Advanced Solid State Physics*, 2nd ed.; 0; Cambridge University Press: The Edinburgh Building, Cambridge CB2 8RU, UK, 2012; Vol. 0

(40) edited by Carlos Fiolhais,; Marques, M. A. L.; Nogueira, F. *A Primer in Density Functional Theory*, 1st ed.; Lecture Notes in Physics; Springer-Verlag Berlen Heidelberg: Springer-Verlag Berlen Heidelberg New York, 2003; Vol. 620

(41) Perdew, J. P.; Zunger, A. Self-interaction correction to density-functional approximations for many-electron systems. *Phys. Rev. B* **1981**, *23*, 5048–5079

(42) Perdew, J.; Chevary, J.; Vosko, S.; Jackson, K.; Pederson, M.; Singh, D.; Fiolhais, C. Atoms, Molecules, Solids, and Surfaces: Applications of the Generalized Gradient Approximation for Exchange and Correlation. *Phys. Rev. B* **1992**, *46*, 6671

(43) Perdew, J. P.; Burke, K.; Ernzerhof, M. Erratum: Generalized Gradient Approximation Made Simple. *Phys. Rev. Lett.* **1997**, *78*, 1396

(44) Ernzerhof, M.; Scuseria, G. E. Assessment of the PerdewBurkeErnzerhof exchange-correlation functional. *J. Chem. Phys.* **1999**, *110*, 5029–5036

(45) Heyd, J.; Scuseria, G. E. Assessment and validation of a screened Coulomb hybrid density functional. *J. Chem. Phys.* **2004**, *120*, 7274–7280

(46) Heyd, J.; Scuseria, G. E. Efficient hybrid density functional calculations in solids: Assessment of the HeydScuseriaErnzerhof screened Coulomb hybrid functional. *J. Chem. Phys.* **2004**, *121*, 1187–1192

(47) Heyd, J.; Scuseria, G. E.; Ernzerhof, M. Erratum: Hybrid functionals based on a screened Coulomb potential [J. Chem. Phys. 118, 8207 (2003)]. *J. Chem. Phys.* **2006**, *124*, 219906

(48) Sun, J.; Ruzsinszky, A.; Perdew, J. P. Strongly Constrained and Appropriately Normed Semilocal Density Functional. *Phys. Rev. Lett.* **2015**, *115*, 036402

(49) Sun, J.; Remsing, R. C.; Zhang, Y.; Sun, Z.; Ruzsinszky, A.; Peng, H.; Yang, Z.; Paul, A.; Waghmare, U.; Wu, X.; Klein, M. L.; Perdew, J. P. Accurate first-principles structures and energies of diversely bonded systems from an efficient density functional. *Nat. Chem.* **2016**, *8*, 831–836

(50) Sander, T.; Maggio, E.; Kresse, G. Beyond the Tamm-Dancoff approximation for extended systems using exact diagonalization. *Phys. Rev. B* **2015**, *92*

(51) Maggio, E.; Kresse, G. Correlation energy for the homogeneous electron gas: Exact Bethe-Salpeter solution and an approximate evaluation. *Phys. Rev. B* **2016**, *93*

(52) Paier, J.; Marsman, M.; Hummer, K.; Kresse, G.; Gerber, I.; Angyan, J. Screened hybrid density functionals applied to solids. *J. Chem. Physics* **2006**, *124*

(53) Sander, T.; Kresse, G. Macroscopic dielectric function within time-dependent density functional theory-Real time evolution versus the Casida approach. *J. Chem. Phys.* **2017**, *146*, 064110

(54) Hohenberg, P.; Kohn, W. Inhomogeneous Electron Gas. *Phys. Rev.* **1964**, *136*, B864–B871

(55) Levy, M. Universal variational functionals of electron densities, first-order density matrices, and natural spin-orbitals and solution of the v-representability problem. *Proc. Nat. Acad. Sci.* **1979**, *76*, 6062–6065

(56) Levy, M. Electron densities in search of Hamiltonians. *Phys. Rev. A* **1982**, *26*, 1200–1208

(57) edited by Reiner M. Dreizler,; de Providencia, J. *Density Functional Methods In Physics*, 1st ed.; 0; Springer: 233 Spring Street New York, N.Y. 10013, 2013; Vol. 0

(58) edited by A. Shimony,; Feshbach, H. *Physics as Natural Philosophy*, 1st ed.; 0; MIT Press: One Rogers Street Cambridge MA 02142-1209, 1982; Vol. 0

(59) Lieb, E. H. Density functionals for coulomb systems. *Int. J. Quantum Chem.* **1983**, *24*, 243–277

(60) Gilbert, T. L. Hohenberg-Kohn theorem for nonlocal external potentials. *Phys. Rev. B* **1975**, *12*, 2111–2120

(61) Kohn, W.; Sham, L. J. Self-Consistent Equations Including Exchange and Correlation Effects. *Phys. Rev.* **1965**, *140*, A1133–A1138

(62) Hartree, D. R. The Wave Mechanics of an Atom with a Non-Coulomb Central Field. Part I. Theory and Methods. *Mathematical Proceedings of the Cambridge Philosophical Society* **1928**, *24*, 89110

(63) Slater, J. C. The Self Consistent Field and the Structure of Atoms. *Phys. Rev.* **1928**, *32*, 339–348

(64) Fock, V. Näherungsmethode zur Lösung des quantenmechanischen Mehrkörperproblems. *Zeitschrift für Physik* **1930**, *61*, 126–148

(65) Slater, J. C. A Simplification of the Hartree-Fock Method. *Phys. Rev.* **1951**, *81*, 385–390

(66) Szabo, A.; Ostlund, N. *Modern Quantum Chemistry: Introduction to Advanced Electronic Structure Theory*; Dover Books on Chemistry; Dover Publications, 1989

(67) Parr, R.; Yang, W. *Density-Functional Theory of Atoms and Molecules*; International Series of Monographs on Chemistry; Oxford University Press, USA, 1994

(68) Ernzerhof, M.; Perdew, J. P.; Burke, K. In *Density Functional Theory I: Functionals and Effective Potentials*; Nalewajski, R. F., Ed.; Springer Berlin Heidelberg: Berlin, Heidelberg, 1996; pp 1–30

(69) Langreth, D. C.; Perdew, J. P. Exchange-correlation energy of a metallic surface: Wave-vector analysis. *Phys. Rev. B* **1977**, *15*, 2884–2901

(70) Gunnarsson, O.; Lundqvist, B. I. Exchange and correlation in atoms, molecules, and solids by the spin-density-functional formalism. *Phys. Rev. B* **1976**, *13*, 4274–4298

(71) Cohen, A. J.; Mori-Snchez, P.; Yang, W. Challenges for Density Functional Theory. *Chem. Rev.* **2012**, *112*, 289–320

(72) Kubo, R. The fluctuation-dissipation theorem. *Rep. Prog. Phys.* **1966**, *29*, 255

(73) Burke, K.; Perdew, J. P.; Wang, Y. In *Electronic Density Functional Theory: Recent Progress and New Directions*; Dobson, J. F., Vignale, G., Das, M. P., Eds.; Springer US: Boston, MA, 1998; pp 81–111

(74) Burke, K.; Perdew, J. P.; Ernzerhof, M. Why semilocal functionals work: Accuracy of the on-top pair density and importance of system averaging. *J. Chem. Phys.* **1998**, *109*, 3760–3771

(75) Dirac, P. A. M. Note on Exchange Phenomena in the Thomas Atom. *Mathematical Proceedings of the Cambridge Philosophical Society* **1930**, *26*, 376385

(76) Hedin, L.; Lundqvist, B. I. Explicit local exchange-correlation potentials. *J. Phys. C* **1971**, *4*, 2064

(77) von Barth, U.; Hedin, L. A local exchange-correlation potential for the spin polarized case. i. *J. Phys. C* **1972**, *5*, 1629

(78) Gunnarsson, O.; Lundqvist, B. I.; Wilkins, J. W. Contribution to the cohesive energy of simple metals: Spin-dependent effect. *Phys. Rev. B* **1974**, *10*, 1319–1327

(79) Vosko, S. H.; Wilk, L.; Nusair, M. Accurate spin-dependent electron liquid correlation energies for local spin density calculations: a critical analysis. *Can. J. Phys.* **1980**, *58*, 1200–1211

(80) Lieb, E. H.; Oxford, S. Improved lower bound on the indirect Coulomb energy. *Int. J. Quantum Chem.* **1981**, *19*, 427–439

(81) Levy, M.; Perdew, J. P. Hellmann-Feynman, virial, and scaling requisites for the exact universal density functionals. Shape of the correlation potential and diamagnetic susceptibility for atoms. *Phys. Rev. A* **1985**, *32*, 2010–2021

(82) Staroverov, V. N.; Scuseria, G. E.; Tao, J.; Perdew, J. P. Tests of a ladder of density functionals for bulk solids and surfaces. *Phys. Rev. B* **2004**, *69*, 075102

(83) Chan, G. K.-L.; Handy, N. C. An extensive study of gradient approximations to the exchange-correlation and kinetic energy functionals. *J. Chem. Phys.* **2000**, *112*, 5639–5653

(84) Perdew, J. P.; Burke, K. Comparison shopping for a gradient-corrected density functional. *Int. J. Quantum Chem.* **1996**, *57*, 309–319

(85) Perdew, J. P.; Burke, K.; Ernzerhof, M. Generalized Gradient Approximation Made Simple. *Phys. Rev. Lett.* **1996**, *77*, 3865–3868

(86) Perdew, J.; Chevary, J.; Vosko, S.; Jackson, K.; Pederson, M.; Singh, D.; Fiolhais, C. Erratum: Atoms, Molecules, Solids, and Surfaces: Applications of the Generalized Gradient Approximation for Exchange and Correlation. *Phys. Rev. B* **1993**, *48*, 4978

(87) Perdew, J. P.; Yue, W. Accurate and simple density functional for the electronic exchange energy: Generalized gradient approximation. *Phys. Rev. B* **1986**, *33*, 8800–8802

(88) Perdew, J. P.; Yue, W. Erratum: Accurate and simple density functional for the electronic exchange energy: Generalized gradient approximation. *Phys. Rev. B* **1989**, *40*, 3399–3399

(89) Perdew, J. P.; Burke, K.; Wang, Y. Generalized gradient approximation for the exchange-correlation hole of a many-electron system. *Phys. Rev. B* **1996**, *54*, 16533–16539

(90) Giuliani, G.; Vignale, G. *Quantum Theory of the Electron Liquid*; Masters Series in Physics and Astronomy; Cambridge University Press, 2005

(91) Perdew, J. John Perdew talk entited *The SCAN functional* covering meta-GGA SCAN and particular intial estimates of SCANs performance delivered at the Centre Européen de Calcul Atomique et Moléculaire (CECAM). Lecture delivered at CECAM, Ecole Polytechnique Fédérale de L ausanne Batochime (BCH) 1015 Lausanne Switzerland, 2017

(92) Grimme, S. Semiempirical GGA-type density functional constructed with a long-range dispersion correction. *J. Comput. Chem.* **2006**, *27*, 1787–1799

(93) Grimme, S.; Antony, J.; Ehrlich, S.; Krieg, H. A consistent and accurate ab initio parametrization of density functional dispersion correction (DFT-D) for the 94 elements H-Pu. *J. Chem. Phys.* **2010**, *132*, 154104

(94) Tkatchenko, A.; DiStasio, R. A.; Car, R.; Scheffler, M. Accurate and Efficient Method for Many-Body van der Waals Interactions. *Phys. Rev. Lett.* **2012**, *108*, 236402

(95) Tkatchenko, A.; Scheffler, M. Accurate Molecular Van Der Waals Interactions from Ground-State Electron Density and Free-Atom Reference Data. *Phys. Rev. Lett.* **2009**, *102*, 073005

(96) Kerber, T.; Sierka, M.; Sauer, J. Application of semiempirical long-range dispersion corrections to periodic systems in density functional theory. *J. Comput. Chem.* **2008**, *29*, 2088–2097

(97) Bučko, T.; Lebégue, S.; Hafner, J.; Ángyán, J. G. Improved Density Dependent Correction for the Description of London Dispersion Forces. *J. Chem. Theory Comput.* **2013**, *9*, 4293–4299

(98) Bučko, T.; Lebégue, S.; Ángyán, J. G.; Hafner, J. Extending the applicability of the Tkatchenko-Scheffler dispersion correction via iterative Hirshfeld partitioning. *J. Chem. Phys.* **2014**, *141*, 034114

(99) Bultinck, P.; Alsenoy, C. V.; Ayers, P. W.; Carb-Dorca, R. Critical analysis and extension of the Hirshfeld atoms in molecules. *J. Chem. Phys.* **2007**, *126*, 144111

(100) Bučko, T.; Lebégue, S.; Gould, T.; Ángyán, J. G. Many-body dispersion corrections for periodic systems: an efficient reciprocal space implementation. *J. Phys. Cond. Matter* **2016**, *28*, 045201

(101) Ambrosetti, A.; Reilly, A. M.; Jr., R. A. D.; Tkatchenko, A. Long-range correlation energy calculated from coupled atomic response functions. *J. Chem. Phys.* **2014**, *140*, 18A508

(102) Steinmann, S. N.; Corminboeuf, C. Comprehensive Benchmarking of a Density-Dependent Dispersion Correction. *J. Chem. Theory Comput.* **2011**, *7*, 3567–3577

(103) Bernardi, M.; Grossman, J. C. Computer calculations across time and length scales in photovoltaic solar cells. *Energy Environ. Sci.* **2016**, *9*, 2197–2218

(104) Perdew, J. P.; Ernzerhof, M.; Burke, K. Rationale for mixing exact exchange with density functional approximations. *J. Chem. Phys.* **1996**, *105*, 9982–9985

(105) Perdew, J. P.; Yang, W.; Burke, K.; Yang, Z.; Gross, E. K. U.; Scheffler, M.; Scuseria, G. E.; Henderson, T. M.; Zhang, I. Y.; Ruzsinszky, A.; Peng, H.; Sun, J.; Trushin, E.; Görling, A. Understanding band gaps of solids in generalized Kohn–Sham theory. *Proc. Nat. Acad. Sci.* **2017**, *114*, 2801–2806

(106) Krukau, A. V.; Vydrov, O. A.; Izmaylov, A. F.; Scuseria, G. E. Influence of the exchange screening parameter on the performance of screened hybrid functionals. *J. Chem. Phys.* **2006**, *125*, 224106

(107) Janesko, B. G.; Henderson, T. M.; Scuseria, G. E. Screened hybrid density functionals for solid-state chemistry and physics. *Phys. Chem. Chem. Phys.* **2009**, *11*, 443–454

(108) Burke, K. Kerion Burke talk entited *Kohn-Sham equations* covering Kohn-Sham equations and particular contributions to this expression delivered at the Centre Européen de Calcul Atomique et Moléculaire (CECAM). Lecture delivered at CECAM, Ecole Polytechnique Fédérale de Lausanne Batochime (BCH) 1015 Lausanne Switzerland, 2017

(109) Bloch, F. Über die Quantenmechanik der Elektronen in Kristallgittern. *Zeitschrift für Physik* **1929**, *52*, 555–600

(110) Simon, S. *The Oxford Solid State Basics*; OUP Oxford, 2013

(111) Ashcroft, N.; Mermin, N. *Solid State Physics*; HRW international editions; Holt, Rinehart and Winston, 1976

(112) Marder, M. *Condensed Matter Physics*; Wiley, 2015

(113) Blöchl, P. E. Projector augmented-wave method. *Phys. Rev. B* **1994**, *50*, 17953–17979

(114) Kresse, G.; Joubert, D. From ultrasoft pseudopotentials to the projector augmented-wave method. *Phys. Rev. B* **1999**, *59*, 1758–1775

(115) Scholes, G. D.; Rumbles, G. Excitons in nanoscale systems. *Nature Mater.* **2006**, *5*, 920

(116) Runge, E.; Gross, E. K. U. Density-Functional Theory for Time-Dependent Systems. *Phys. Rev. Lett.* **1984**, *52*, 997–1000

(117) Fetter, A.; Walecka, J. *Quantum Theory of Many-particle Systems*; Dover Books on Physics; Dover Publications, 2003

(118) Harl, J. The linear response function in density functional theory. 2008; Dissertation, University of Vienna. Fakultät für Physik

(119) Pines, D.; Nozières, P. *The Theory of Quantum Liquids: Normal Fermi liquids*; The Theory of Quantum Liquids; W.A. Benjamin, 1966

(120) Martin, R.; Reining, L.; Ceperley, D. *Interacting Electrons: Theory and Computational Approaches*; Cambridge University Press, 2016

(121) Gajdo, M.; Hummer, K.; Kresse, G.; Furthmüller, J.; Bechstedt, F. Linear optical properties in the projector-augmented wave methodology. *Phys. Rev. B* **2006**, *73*, 045112

(122) Adler, S. L. Quantum Theory of the Dielectric Constant in Real Solids. *Phys. Rev.* **1962**, *126*, 413–420

(123) Wiser, N. Dielectric Constant with Local Field Effects Included. *Phys. Rev.* **1963**, *129*, 62–69

(124) Dresselhaus, M. *SOLID STATE PHYSICS PART II Optical Properties of Solids*; 2009

(125) YU, P.; Cardona, M. *Fundamentals of Semiconductors: Physics and Materials Properties*; Graduate Texts in Physics; Springer Berlin Heidelberg, 2010

(126) Jackson, J. *Classical electrodynamics*, 3rd ed.; Wiley, 1975

(127) Sólyom, J. *Fundamentals of the Physics of Solids: Volume 3 - Normal, Broken-Symmetry, and Correlated Systems*; Theoretical Solid State Physics: Interaction Among Electrons; Springer Berlin Heidelberg, 2010

(128) Onida, G.; Reining, L.; Rubio, A. Electronic excitations: density-functional versus many-body Green's-function approaches. *Rev. Mod. Phys.* **2002**, *74*, 601–659

(129) Geim, A. K. Graphene: Status and Prospects. *Science* **2009**, *324*, 1530–1534

(130) Muszynski, R.; Seger, B.; Kamat, P. V. Decorating Graphene Sheets with Gold Nanoparticles. *J. Phys. Chem. C* **2008**, *112*, 5263–5266

(131) Kamat, P. V. Graphene-Based Nanoarchitectures. Anchoring Semiconductor and Metal Nanoparticles on a Two-Dimensional Carbon Support. *J. Phys. Chem. Lett.* **2010**, *1*, 520–527

(132) Zhao, L. et al. Visualizing Individual Nitrogen Dopants in Monolayer Graphene. *Science* **2011**, *333*, 999–1003

(133) Batzill, M. The surface science of graphene: Metal interfaces, CVD synthesis, nanoribbons, chemical modifications, and defects. *Surf. Sci. Rep.* **2012**, *67*, 83–115

(134) Yang, Y.; Xiao, Y.; Ren, W.; Yan, X. H.; Pan, F. Half-metallic chromium-chain-embedded wire in graphene and carbon nanotubes. *Phys. Rev. B* **2011**, *84*, 195447

(135) Castro Neto, A. H.; Guinea, F.; Peres, N. M. R.; Novoselov, K. S.; Geim, A. K. The electronic properties of graphene. *Rev. Mod. Phys.* **2009**, *81*, 109–162

(136) Kaloni, T.; Kahaly, M. U.; Faccio, R.; Schwingenschlgl, U. Modelling magnetism of C at O and B monovacancies in graphene. *Carbon* **2013**, *64*, 281 – 287

(137) Singh, N.; Kaloni, T. P.; Schwingenschlgl, U. A first-principles investigation of the optical spectra of oxidized graphene. *Appl. Phys. Lett.* **2013**, *102*, 023101

(138) Kaloni, T. P.; Cheng, Y. C.; Schwingenschlgl, U. Fluorinated monovacancies in graphene: Even-odd effect. *Europhys. Lett.* **2012**, *100*, 37003

(139) Yang, X.-F.; Wang, A.; Qiao, B.; Li, J.; Liu, J.; Zhang, T. Single-Atom Catalysts: A New Frontier in Heterogeneous Catalysis. *Acc. Chem. Res.* **2013**, *46*, 1740–1748

(140) Sun, S. et al. Single-atom Catalysis Using Pt/Graphene Achieved through Atomic Layer Deposition. *Sci. Rep.* **2013**, *3*

(141) Wu, X.; Sprinkle, M.; Li, X.; Ming, F.; Berger, C.; de Heer, W. A. Epitaxial-Graphene/Graphene-Oxide Junction: An Essential Step towards Epitaxial Graphene Electronics. *Phys. Rev. Lett.* **2008**, *101*, 026801

(142) Wei, Z.; Wang, D.; Kim, S.; Kim, S.-Y.; Hu, Y.; Yakes, M. K.; Laracuente, A. R.; Dai, Z.; Marder, S. R.; Berger, C.; King, W. P.; de Heer, W. A.; Sheehan, P. E.; Riedo, E. Nanoscale Tunable Reduction of Graphene Oxide for Graphene Electronics. *Science* **2010**, *328*, 1373–1376

(143) Torrisi, F.; Hasan, T.; Wu, W.; Sun, Z.; Lombardo, A.; Kulmala, T. S.; Hsieh, G.-W.; Jung, S.; Bonaccorso, F.; Paul, P. J.; Chu, D.; Ferrari, A. C. Inkjet-Printed Graphene Electronics. *ACS Nano* **2012**, *6*, 2992–3006

(144) Zhang, S. B.; Wei, S.-H.; Zunger, A. Intrinsic n-type versus p-type doping asymmetry and the defect physics of ZnO. *Phys. Rev. B* **2001**, *63*, 075205

(145) Gierz, I.; Riedl, C.; Starke, U.; Ast, C. R.; Kern, K. Atomic Hole Doping of Graphene. *Nano Lett.* **2008**, *8*, 4603–4607

(146) Susi, T.; Kotakoski, J.; Arenal, R.; Kurasch, S.; Jiang, H.; Skakalova, V.; Stephan, O.; Krasheninnikov, A. V.; Kauppinen, E. I.; Kaiser, U.; Meyer, J. C. Atomistic Description of Electron Beam Damage in Nitrogen-Doped Graphene and Single -Walled Carbon Nanotubes. *ACS Nano* **2012**, *6*, 8837–8846

(147) Nicholls, R. J.; Murdock, A. T.; Tsang, J.; Britton, T. J., Jude an d Pennycook; Koós, A.; Nellist, P. D.; Grobert, N.; Yates, J. R. Probing the Bonding in Nitrogen-Doped Graphene Using Electron Energy Loss Spectrosc opy. *ACS Nano* **2013**, *7*, 7145–7150

(148) Robertson, A. W.; Warner, J. H. Atomic resolution imaging of graphene by transmission electron microscopy. *Nanoscale* **2013**, *5*, 4079–4093

(149) Lv, R. et al. Nitrogen-doped graphene: beyond single substitution and enhanced molecular sensing. *Sci. Rep.* **2012**, *2*, 1–8

(150) Kondo, T.; Honma, Y.; Oh, J.; Machida, T.; Nakamura, J. Edge states propagating from a defect of graphite: Scanning tunneling spectroscopy measurements. *Phys. Rev. B* **2010**, *82*, 153414

(151) Robertson, A. W.; Montanari, B.; He, K.; Allen, C. S.; Wu, Y. A.; Harrison, N. M.; Kirkland, A. I.; Warner, J. H. Structural Reconstruction of the Graphene Monovacancy. *ACS Nano* **2013**, *7*, 4495–4502

(152) Denis, P. A. Band gap opening of monolayer and bilayer graphene doped with aluminium, silicon, phosphorus, and sulfur. *Chem. Phys. Lett.* **2010**, *492*, 251 – 257

(153) Denis, P. A. Concentration dependence of the band gaps of phosphorus and sulfur doped graphene. *Comput. Mater. Sci.* **2013**, *67*, 203 – 206

(154) mei Wang, H.; xia Wang, H.; Chen, Y.; jie Liu, Y.; xiang Zhao, J.; hai Cai, Q.; zhang Wang, X. Phosphorus-doped graphene and (8, 0) carbon nanotube: Structural, electronic, magnetic properties, and chemical reactivity. *Appl. Surf. Sci.* **2013**, *273*, 302 – 309

(155) Singh, R.; Kroll, P. Magnetism in graphene due to single-atom defects: dependence on the concentration and packing geometry of defects. *J. Phys. Condens. Matter* **2009**, *21*, 196002

(156) Hou, Z.; Wang, X.; Ikeda, T.; Terakura, K.; Oshima, M.; Kakimoto, M.-a. Electronic structure of N-doped graphene with native point defects. *Phys. Rev. B* **2013**, *87*, 165401

(157) Fujimoto, Y.; Saito, S. Formation, stabilities, and electronic properties of nitrogen defects in graphene. *Phys. Rev. B* **2011**, *84*, 245446

(158) Hou, Z.; Wang, X.; Ikeda, T.; Terakura, K.; Oshima, M.; Kakimoto, M.-a.; Miyata, S. Interplay between nitrogen dopants and native point defects in graphene. *Phys. Rev. B* **2012**, *85*, 165439

(159) Paek, E.; Pak, A. J.; Kweon, K. E.; Hwang, G. S. On the Origin of the Enhanced Supercapacitor Performance of Nitrogen-Doped Graphene. *J. Phys. Chem. C* **2013**, *117*, 5610–5616

(160) Lambin, P.; Amara, H.; Ducastelle, F.; Henrard, L. Long-range interactions between substitutional nitrogen dopants in graphene: Electronic properties calculations. *Phys. Rev. B* **2012**, *86*, 045448

(161) Rani, P.; Jindal, V. K. Designing band gap of graphene by B and N dopant atoms. *RSC Adv.* **2013**, *3*, 802–812

(162) Üzengi Aktürk, O.; Tomak, M. Lithium and antimony adsorbed on graphene studied by first-principles calculation s. *Appl. Surf. Sci.* **2011**, *258*, 800 – 805

(163) Aktürk, O. U.; Tomak, M. Bismuth doping of graphene. *Appl. Phys. Lett.* **2010**, *96*, 081914 1–3

(164) Tsetseris, L.; Wang, B.; Pantelides, S. T. Substitutional doping of graphene: The role of carbon divacancies. *Phys. Rev. B* **2014**, *89*, 035411

(165) Kresse, G.; Furthmüller, J. Efficient iterative schemes for ab initio total-energy calculations using a plane-wave basis set. *Phys. Rev. B* **1996**, *54*, 11169–11186

(166) Blöchl, P. E.; Jepsen, O.; Andersen, O. K. Improved tetrahedron method for Brillouin-zone integrations. *Phys. Rev. B* **1994**, *49*, 16223–16233

(167) Methfessel, M.; Paxton, A. T. High-precision sampling for Brillouin-zone integration in metals. *Phys. Rev. B* **1989**, *40*, 3616–3621

(168) Tkatchenko, A.; Scheffler, M. Accurate Molecular Van Der Waals Interactions from Ground-State Electron Density and Free-Atom Reference Data. *Phys. Rev. Lett.* **2009**, *102*, 073005

(169) Amara, H.; Latil, S.; Meunier, V.; Lambin, P.; Charlier, J.-C. Scanning tunneling microscopy fingerprints of point defects in graphene: A theoretical prediction. *Phys. Rev. B* **2007**, *76*, 115423

(170) Ugeda, M. M.; Brihuega, I.; Guinea, F.; Gómez-Rodríguez, J. M. Missing Atom as a Source of Carbon Magnetism. *Phys. Rev. Lett.* **2010**, *104*, 096804

(171) Yazyev, O. V.; Helm, L. Defect-induced magnetism in graphene. *Phys. Rev. B* **2007**, *75*, 125408

(172) Yazyev, O. V. Emergence of magnetism in graphene materials and nanostructures. *Rep. Prog. Phys.* **2010**, *73*, 056501

(173) Palacios, J. J.; Ynduráin, F. Critical analysis of vacancy-induced magnetism in monolayer and bilayer graphene. *Phys. Rev. B* **2012**, *85*, 245443

(174) Kumazaki, H.; S. Hirashima, D. Nonmagnetic-Defect-Induced Magnetism in Graphene. *J. Phys. Soc. Jpn* **2007**, *76*, 064713

(175) Lee, C.-C.; Yamada-Takamura, Y.; Ozaki, T. Competing magnetism in π electrons in graphene with a single carbon vacancy. *ArXiv e-prints* **2013**,

(176) Lieb, E. H. Two theorems on the Hubbard model. *Phys. Rev. Lett.* **1989**, *62*, 1201–1204

(177) Li, R.; Wei, Z.; Gou, X.; Xu, W. Phosphorus-doped graphene nanosheets as efficient metal-free oxygen reduction electrocatalysts. *RSC Adv.* **2013**, *3*, 9978–9984

(178) Cruz-Silva, E.; Barnett, Z. M.; Sumpter, B. G.; Meunier, V. Structural magnetic and transport properties of substitutionally doped graphene nanoribbons from first principles. *Phys. Rev. B* **2011**, *83*, 155445

(179) Berger, C.; Song, Z.; Li, X.; Wu, X.; Brown, N.; Naud, C.; Mayou, D.; Li, T.; Hass, J.; Marchenkov, A. N.; Conrad, E. H.; First, P. N.; de Heer, W. A. Electronic Confinement and Coherence in Patterned Epitaxial Graphene. *Science* **2006**, *312*, 1191–1196

(180) Balandin, A. A.; Ghosh, S.; Bao, W.; Calizo, I.; Teweldebrhan, D.; Miao, F.; Lau, C. N. Superior Thermal Conductivity of Single-Layer Graphene. *Nano Lett.* **2008**, *8*, 902–907

(181) Kamat, P. V. Graphene-Based Nanoassemblies for Energy Conversion. *J. Phys. Chem. Lett.* **2011**, *2*, 242–251

(182) Lin, Y.-M.; Jenkins, K. A.; Valdes-Garcia, A.; Small, J. P.; Farmer, D. B.; Avouris, P. Operation of Graphene Transistors at Gigahertz Frequencies. *Nano Lett.* **2009**, *9*, 422–426

(183) Sordan, R.; Traversi, F.; Russo, V. Logic gates with a single graphene transistor. *Appl. Phys. Lett.* **2009**, *94*, 073305

(184) Meric, I.; Han, M. Y.; Young, A. F.; Ozyilmaz, B.; Kim, P.; Shepard, K. L. Current saturation in zero-bandgap, topgated graphene field-effect transistors. *Nature Nanotech.* **2008**, *3*, 654–659

(185) Schwierz, F. Graphene transistors. *Nature Nanotech.* **2010**, *5*, 487–496

(186) Latil, S.; Henrard, L. Charge Carriers in Few-Layer Graphene Films. *Phys. Rev. Lett.* **2006**, *97*, 036803

(187) Abergel, D.; Apalkov, V.; Berashevich, J.; Ziegler, K.; Chakraborty, T. Properties of graphene: a theoretical perspective. *Adv. Phys.* **2010**, *59*, 261–482

(188) Boukhvalov, D. W.; Katsnelson, M. I.; Lichtenstein, A. I. Hydrogen on graphene: Electronic structure, total energy, structural distortions and magnetism from first-principles calculations. *Phys. Rev. B* **2008**, *77*, 035427

(189) Liu, H.; Liu, Y.; Zhu, D. Chemical doping of graphene. *J. Mater. Chem.* **2011**, *21*, 3335–3345

(190) McCann, E. Asymmetry gap in the electronic band structure of bilayer graphene. *Phys. Rev. B* **2006**, *74*, 161403

(191) Castro, E. V.; Novoselov, K. S.; Morozov, S. V.; Peres, N. M. R.; dos Santos, J. M. B. L.; Nilsson, J.; Guinea, F.; Geim, A. K.; Neto, A. H. C. Biased Bilayer Graphene: Semiconductor with a Gap Tunable by the Electric Field Effect. *Phys. Rev. Lett.* **2007**, *99*, 216802

(192) Tang, K.; Qin, R.; Zhou, J.; Qu, H.; Zheng, J.; Fei, R.; Li, H.; Zheng, Q.; Gao, Z.; Lu, J. Electric-Field-Induced Energy Gap in Few-Layer Graphene. *J. Phys. Chem. C* **2011**, *115*, 9458–9464

(193) Son, Y.-W.; Cohen, M.; Louie, S. Half-metallic graphene nanoribbons. *Nature* **2006**, *444*, 347–349

(194) Singh, A. K.; Zhuang, H. L.; Hennig, R. G. *Ab initio* synthesis of single-layer III-V materials. *Phys. Rev. B* **2014**, *89*, 245431

(195) Ohta, T.; Bostwick, A.; Seyller, T.; Horn, K.; Rotenberg, E. Controlling the Electronic Structure of Bilayer Graphene. *Science* **2006**, *313*, 951–954

(196) Zhou, S.; Gweon, G.-H.; Fedorov, A.; First, P.; De Heer, W.; Lee, D.-H.; Guinea, F.; Castro Neto, A.; Lanzara, A. Substrate-induced bandgap opening in epitaxial graphene. *Nature Mater.* **2007**, *6*, 770–775

(197) Fazel, Y.; Christo, K.; Churamani, G.; Li, S.; Hemtej, G.; Theodorian, B.; M., A. P.; Nikhil, K. Tunable Bandgap in Graphene by the Controlled Adsorption of Water Molecules. *Small* **2010**, *6*, 2535–2538

(198) Böttcher, S.; Weser, M.; Dedkov, Y. S.; Horn, K.; Voloshina, E. N.; Paulus, B. Graphene on ferromagnetic surfaces and its functionalization with water and ammonia. *Nanoscale Res. Lett.* **2011**, *6*, 214

(199) Mishra, A. K.; Ramaprabhu, S. Carbon dioxide adsorption in graphene sheets. *AIP Advances* **2011**, *1*, 032152

(200) Yavari, F.; Castillo, E.; Gullapalli, H.; Ajayan, P. M.; Koratkar, N. High sensitivity detection of NO2 and NH3 in air using chemical vapor deposition grown graphene. *Appl. Phys. Lett.* **2012**, *100*, 203120

(201) Ling, P. H.; imek Petr,; Zdenk, S.; Martin, P. Halogenation of Graphene with Chlorine, Bromine, or Iodine by Exfoliation in a Halogen Atmosphere. *Chem.A Eur. J.* **2013**, *19*, 2655–2662

(202) Antonova, I. V.; Kotin, I. A.; Soots, R. A.; Volodin, V. A.; Prinz, V. Y. Tunable properties of few-layer graphene N -methylpyrrolidone hybrid structures. *Nanotechnology* **2012**, *23*, 315601

(203) Ragoussi, M.-E.; Katsukis, G.; Roth, A.; Malig, J.; de la Torre, G.; Guldi, D. M.; Torres, T. Electron-Donating Behavior of Few-Layer Graphene in Covalent Ensembles with Electron-Accepting Phthalocyanines. *J. Amer. Chem. Soc.* **2014**, *136*, 4593–4598

(204) Hao, R.; Qian, W.; Zhang, L.; Hou, Y. Aqueous dispersions of TCNQ-anion-stabilized graphene sheets. *Chem. Commun.* **2008**, 6576–6578

(205) de Oliveira, I. S. S.; Miwa, R. H. Organic molecules deposited on graphene: A computational investigation of self-assembly and electronic structure. *J. Chem. Phys.* **2015**, *142*, 044301

(206) Chan, K. T.; Neaton, J. B.; Cohen, M. L. First-principles study of metal adatom adsorption on graphene. *Phys. Rev. B* **2008**, *77*, 235430

(207) Brown, P. A.; Xu, C.; Shuford, K. L. Periodic Trends of Pnictogen Substitution into a Graphene Monovacancy: A First-Principles Investigation. *Chem. Mater.* **2014**, *26*, 5735–5744

(208) Quhe, R.; Ma, J.; Zeng, Z.; Tang, K.; Zheng, J.; Wang, Y.; Ni, Z.; Wang, L.; Gao, Z.; Shi, J.; Lu, J. Tunable band gap in few-layer graphene by surface adsorption. *Sci. Rep.* **2013**, *3*

(209) Chen, J.-H.; Jang, C.; Adam, S.; Fuhrer, M.; Williams, E.; Ishigami, M. Charged-impurity scattering in graphene. *Nature Phys.* **2008**, *4*, 377–381

(210) Chen, J.-H.; Cullen, W. G.; Jang, C.; Fuhrer, M. S.; Williams, E. D. Defect Scattering in Graphene. *Phys. Rev. Lett.* **2009**, *102*, 236805

(211) Chu, S. W.; Baek, S. J.; Kim, D. C.; Seo, S.; Kim, J. S.; Park, Y. W. Charge transport in graphene doped with diatomic halogen molecules (I_2, Br_2) near Dirac point. *Synthetic Metals* **2012**, *162*, 1689 – 1693

(212) Aoki, M.; Amawashi, H. Dependence of band structures on stacking and field in layered graphene. *Solid State Commun.* **2007**, *142*, 123 – 127

(213) Wu, X.; Vargas, M. C.; Nayak, S.; Lotrich, V.; Scoles, G. Towards extending the applicability of density functional theory to weakly bound systems. *J. Chem. Phys.* **2001**, *115*, 8748–8757

(214) Dion, M.; Rydberg, H.; Schröder, E.; Langreth, D. C.; Lundqvist, B. I. Van der Waals Density Functional for General Geometries. *Phys. Rev. Lett.* **2004**, *92*, 246401

(215) Lee, K.; Murray, E. D.; Kong, L.; Lundqvist, B. I.; Langreth, D. C. Higher-accuracy van der Waals density functional. *Phys. Rev. B* **2010**, *82*, 081101

(216) Monkhorst, H. J.; Pack, J. D. Special points for Brillouin-zone integrations. *Phys. Rev. B* **1976**, *13*, 5188–5192

(217) Charlier, J.-C.; Gonze, X.; Michenaud, J.-P. Graphite Interplanar Bonding: Electronic Delocalization and van der Waals Interaction. *Europhys. Lett.* **1994**, *28*, 403

(218) Städele, M.; Majewski, J. A.; Vogl, P.; Görling, A. Exact Kohn-Sham Exchange Potential in Semiconductors. *Phys. Rev. Lett.* **1997**, *79*, 2089–2092

(219) Tang, W.; Sanville, E.; Henkelman, G. A grid-based Bader analysis algorithm without lattice bias. *J. Phys. Conden. Matter* **2009**, *21*, 084204

(220) Yaya, A.; Ewels, C. P.; Suarez-Martinez, I.; Wagner, P.; Lefrant, S.; Okotrub, A.; Bulusheva, L.; Briddon, P. R. Bromination of graphene and graphite. *Phys. Rev. B* **2011**, *83*, 045411

(221) Chen, Y.; Ye, D.; Wu, M.; Chen, H.; Zhang, L.; Shi, J.; Wang, L. Break-up of Two-Dimensional MnO2 Nanosheets Promotes Ultrasensitive pH-Triggered Theranostics of Cancer. *Adv. Mater.* **2014**, *26*, 7019–7026

(222) Rudenko, A. N.; Keil, F. J.; Katsnelson, M. I.; Lichtenstein, A. I. Adsorption of diatomic halogen molecules on graphene: A van der Waals density functional study. *Phys. Rev. B* **2010**, *82*, 035427

(223) Ijäs, M.; Havu, P.; Harju, A. Fracturing graphene by chlorination: A theoretical viewpoint. *Phys. Rev. B* **2012**, *85*, 035440

(224) Liu, X.-Y.; Zhang, J.-M.; Xu, K.-W. Chlorine molecule adsorbed on graphene and doped graphene: A first-principle study. *Phys. B: Conden. Matter* **2014**, *436*, 54 – 58

(225) Fan, X.; Liu, L.; Kuo, J.-L.; Shen, Z. Functionalizing Single- and Multi-layer Graphene with Br and Br_2. *J. Phys. Chem. C* **2010**, *114*, 14939–14945

(226) Ghosh, S.; Yamijala, S. R. K. C. S.; Pati, S. K.; Rao, C. The interaction of halogen molecules with SWNTs and graphene. *RSC Adv.* **2012**, *2*, 1181–1188

(227) Tongay, S.; Hwang, J.; Tanner, D. B.; Pal, H. K.; Maslov, D.; Hebard, A. F. Supermetallic conductivity in bromine-intercalated graphite. *Phys. Rev. B* **2010**, *81*, 115428

(228) Castro Neto, A. H.; Guinea, F.; Peres, N. M. R.; Novoselov, K. S.; Geim, A. K. The electronic properties of graphene. *Rev. Mod. Phys.* **2009**, *81*, 109–162

(229) Geim, A. K.; Grigorieva, I. V. Van der Waals heterostructures. *Nature* **2013**, *499*, 419–425

(230) Zhang, H. Ultrathin Two-Dimensional Nanomaterials. *ACS Nano* **2015**, *9*, 9451–9469

(231) Zhuang, H. L.; Hennig, R. G. Electronic structures of single-layer boron pnictides. *Appl. Phys. Lett.* **2012**, *101*, 153109

(232) Zhuang, H. L.; Singh, A. K.; Hennig, R. G. Computational discovery of single-layer III-V materials. *Phys. Rev. B* **2013**, *87*, 165415

(233) Magoulas, I.; Kalemos, A. An ab initio study of the electronic structure of boron arsenide, BAs. *J. Chem. Phys.* **2013**, *139*, 154309

(234) Singh, A. K.; Hennig, R. G. Computational synthesis of single-layer GaN on refractory materials. *Appl. Phys. Lett.* **2014**, *105*, 051604

(235) Wang, Q.; Sun, Q.; Jena, P.; Kawazoe, Y. Potential of AlN Nanostructures as Hydrogen Storage Materials. *ACS Nano* **2009**, *3*, 621–626

(236) Chen, Q.; Hu, H.; Chen, X.; Wang, J. Tailoring band gap in GaN sheet by chemical modification and electric field: Ab initio calculations. *Appl. Phys. Lett.* **2011**, *98*, 053102

(237) Blonsky, M. N.; Zhuang, H. L.; Singh, A. K.; Hennig, R. G. Ab Initio Prediction of Piezoelectricity in Two-Dimensional Materials. *ACS Nano* **2015**, *9*, 9885–9891

(238) Singh, A. K.; Mathew, K.; Zhuang, H. L.; Hennig, R. G. Computational Screening of 2D Materials for Photocatalysis. *J. Phys. Chem. Lett.* **2015**, *6*, 1087–1098

(239) Yoon, J.; Jo, S.; Chun, I.; Jung, I.; Kim, H.-S.; Meitl, M.; Menard, E.; Li, X.; Coleman, J. J.; Paik, U.; Rogers, J. A. GaAs photovoltaics and optoelectronics using releasable multilayer epitaxial assemblies. *Nature* **2010**, *465*, 329–333

(240) Jiao, Y.; Zhou, L.; Ma, F.; Gao, G.; Kou, L.; Bell, J.; Sanvito, S.; Du, A. Predicting Single-Layer Technetium Dichalcogenides (TcX_2, X = S, Se) with Promising Applications in Photovoltaics and Photocatalysis. *ACS Appl. Mater. & Interfaces* **2016**, *8*, 5385–5392

(241) Braun, A.; Vossier, A.; Katz, E. A.; Ekins-Daukes, N. J.; Gordon, J. M. Multiple-bandgap vertical-junction architectures for ultra-efficient concentrator solar cells. *Energy Environ. Sci.* **2012**, *5*, 8523–8527

(242) Taniyasu, Y.; Kasu, M.; Makimoto, T. An aluminium nitride light-emitting diode with a wavelength of 210 nanometres. *Nature* **2006**, *441*, 325–328

(243) Razeghi, M. High-power laser diodes based on InGaAsP alloys. *Nature* **1994**, *369*, 631–633

(244) Avramescu, A.; Lermer, T.; Müller, J.; Tautz, S.; Queren, D.; Lutgen, S.; Strauβ, U. InGaN laser diodes with 50 mW output power emitting at 515 nm. *Appl. Phys. Lett.* **2009**, *95*, 071103

(245) Yoshida, H.; Yamashita, Y.; Kuwabara, M.; Kan, H. A 342-nm ultraviolet AlGaN multiple-quantum-well laser diode. *Nature Photon.* **2008**, *2*, 551–554

(246) Cotal, H.; Fetzer, C.; Boisvert, J.; Kinsey, G.; King, R.; Hebert, P.; Yoon, H.; Karam, N. III-V multijunction solar cells for concentrating photovoltaics. *Energy Environ. Sci.* **2009**, *2*, 174–192

(247) Lee, S.-M.; Kwong, A.; Jung, D.; Faucher, J.; Biswas, R.; Shen, L.; Kang, D.; Lee, M. L.; Yoon, J. High Performance Ultrathin GaAs Solar Cells Enabled with Heterogeneously Integrated Dielectric Periodic Nanostructures. *ACS Nano* **2015**, *9*, 10356–10365

(248) Tsipas, P.; Kassavetis, S.; Tsoutsou, D.; Xenogiannopoulou, E.; Golias, E.; Giamini, S. A.; Grazianetti, C.; Chiappe, D.; Molle, A.; Fanciulli, M.; Dimoulas, A. Evidence for graphite-like hexagonal AlN nanosheets epitaxially grown on single crystal Ag(111). *Appl. Phys. Lett.* **2013**, *103*, 251605

(249) Al Balushi, Z. Y. et al. Two-dimensional gallium nitride realized via graphene encapsulation. *Nature Mater.* **2016**, *advance online publication*, doi.org/10.1038/nmat4742

(250) Camacho-Mojica, D. C.; López-Urías, F. GaN Haeckelite Single-Layered Nanostructures: Monolayer and Nanotubes. *Sci. Rep.* **2015**, *5*, 17902

(251) Rocquefelte, X.; Rignanese, G.-M.; Meunier, V.; Terrones, H.; Terrones, M.; Charlier, J.-C. How to Identify Haeckelite Structures: A Theoretical Study of Their Electronic and Vibrational Properties. *Nano Letters* **2004**, *4*, 805–810

(252) Nie, S. M.; Song, Z.; Weng, H.; Fang, Z. Quantum spin Hall effect in two-dimensional transition-metal dichalcogenide haeckelites. *Phys. Rev. B* **2015**, *91*, 235434

(253) Xu, L.; Yu, Y.; Lin, J.; Zhou, X.; Tian, W. Q.; Nieckarz, D.; Szabelski, P.; Lei, S. On-surface synthesis of two-dimensional imine polymers with a tunable band gap: a combined STM, DFT and Monte Carlo investigation. *Nanoscale* **2016**, *8*, 8568–8574

(254) Dienstmaier, J. F.; Medina, D. D.; Dogru, M.; Knochel, P.; Bein, T.; Heckl, W. M.; Lackinger, M. Isoreticular Two-Dimensional Covalent Organic Frameworks Synthesized by On-Surface Condensation of Diboronic Acids. *ACS Nano* **2012**, *6*, 7234–7242

(255) Dong, L.; Liu, P. N.; Lin, N. Surface-Activated Coupling Reactions Confined on a Surface. *Acc. Chem. Res.* **2015**, *48*, 2765–2774

(256) Basagni, A.; Sedona, F.; Pignedoli, C. A.; Cattelan, M.; Nicolas, L.; Casarin, M.; Sambi, M. MoleculesOligomersNanowiresGraphene Nanoribbons: A Bottom-Up Stepwise On-Surface Covalent Synthesis Preserving Long-Range Order. *J. Amer. Chem. Soc.* **2015**, *137*, 1802–1808

(257) Curtarolo, S.; Setyawan, W.; Wang, S.; Xue, J.; Yang, K.; Taylor, R. H.; Nelson, L. J.; Hart, G. L.; Sanvito, S.; Buongiorno-Nardelli, M.; Mingo, N.; Levy, O. AFLOWLIB.ORG: A distributed materials properties repository from high-throughput ab initio calculations. *Comput. Mater. Sci.* **2012**, *58*, 227 – 235

(258) Yu, M.; Trinkle, D. R. Accurate and efficient algorithm for Bader charge integration. *J. Chem. Phys.* **2011**, *134*, 064111

(259) Henkelman, G.; Arnaldsson, A.; Jónsson, H. A fast and robust algorithm for Bader decomposition of charge density. *Comput. Mater. Sci.* **2006**, *36*, 354 – 360

(260) Novoselov, K. S.; Mishchenko, A.; Carvalho, A.; Castro Neto, A. H. 2D materials and van der Waals heterostructures. *Science* **2016**, *353*

(261) Wang, F.; Wang, Z.; Xu, K.; Wang, F.; Wang, Q.; Huang, Y.; Yin, L.; He, J. Tunable GaTe-MoS2 van der Waals pn Junctions with Novel Optoelectronic Performance. *Nano Lett.* **2015**, *15*, 7558–7566

(262) Xia, F.; Wang, H.; Xiao, D.; Dubey, M.; Ramasubramaniam, A. Two-dimensional material nanophotonics. *Nature Photon.* **2014**, *8*, 899–907

(263) Hu, P.; Wang, L.; Yoon, M.; Zhang, J.; Feng, W.; Wang, X.; Wen, Z.; Idrobo, J. C.; Miyamoto, Y.; Geohegan, D. B.; Xiao, K. Highly Responsive Ultrathin GaS Nanosheet Photodetectors on Rigid and Flexible Substrates. *Nano Lett.* **2013**, *13*, 1649–1654

(264) Tamalampudi, S. R.; Lu, Y.-Y.; Kumar U., R.; Sankar, R.; Liao, C.-D.; Moorthy B., K.; Cheng, C.-H.; Chou, F. C.; Chen, Y.-T. High Performance and Bendable Few-Layered InSe Photodetectors with Broad Spectral Response. *Nano Lett.* **2014**, *14*, 2800–2806

(265) Wang, Q. H.; Kalantar-Zadeh, K.; Kis, A.; Coleman, J. N.; Strano, M. S. a. Electronics and optoelectronics of two-dimensional transition metal dichalcogenides. *Nature Nanotech.* **2012**, *7*, 699–712

(266) Buscema, M.; Groenendijk, D. J.; Blanter, S. I.; Steele, G. A.; van der Zant, H. S. J.; Castellanos-Gomez, A. Fast and Broadband Photoresponse of Few-Layer Black Phosphorus Field-Effect Transistors. *Nano Lett.* **2014**, *14*, 3347–3352

(267) Dai, J.; Li, Z.; Yang, J. Boron K_4 crystal: a stable chiral three-dimensional sp^2 network. *Phys. Chem. Chem. Phys.* **2010**, *12*, 12420–12422

(268) Terrones, H.; Terrones, M. Electronic and vibrational properties of defective transition metal dichalcogenide Haeckelites: new 2D semi-metallic systems. *2D Mater.* **2014**, *1*, 011003

(269) Zhu, X.; Monahan, N. R.; Gong, Z.; Zhu, H.; Williams, K. W.; Nelson, C. A. Charge Transfer Excitons at van der Waals Interfaces. *J. Am. Chem. Soc.* **2015**, *137*, 8313–8320

(270) Fthenakis, Z. G.; Lathiotakis, N. N. Graphene allotropes under extreme uniaxial strain: an ab initio theoretical study. *Phys. Chem. Chem. Phys.* **2015**, *17*, 16418–16427

(271) Kolobov, A. V.; Fons, P.; Tominaga, J.; Hyot, B.; Andr, B. Instability and Spontaneous Reconstruction of Few-Monolayer Thick GaN Graphitic Structures. *Nano Lett.* **2016**, *16*, 4849–4856

(272) Brown, P. A.; Shuford, K. L. Archimedean (4,8)-tessellation of haeckelite ultrathin nanosheets composed of boron and aluminum-group V binary materials. *Nanoscale* **2016**, *8*, 19287–19301

(273) Takahashi, L.; Takahashi, K. Structural stability and electronic properties of an octagonal allotrope of two dimensional boron nitride. *Dalton Trans.* **2017**, *46*, 4259–4264

(274) Li, X.; Puretzky, A. A.; Sang, X.; KC, S.; Tian, M.; Ceballos, F.; Mahjouri-Samani, M.; Wang, K.; Unocic, R. R.; Zhao, H.; Duscher, G.; Cooper, V. R.; Rouleau, C. M.; Geohegan, D. B.; Xiao, K. Suppression of Defects and Deep Levels Using Isoelectronic Tungsten Substitution in Monolayer $MoSe_2$. *Adv. Funct. Mater.* **2017**, *27*, 1603850–n/a, 1603850

(275) Shockley, W.; Queisser, H. J. Detailed Balance Limit of Efficiency of pn Junction Solar Cells. *J. Appl. Phys.* **1961**, *32*, 510–519

(276) Paier, J.; Marsman, M.; Kresse, G. Dielectric properties and excitons for extended systems from hybrid functionals. *Phys. Rev. B* **2008**, *78*

(277) Garza, A. J.; Scuseria, G. E. Predicting Band Gaps with Hybrid Density Functionals. *J. Phys. Chem. Lett.* **2016**, *7*, 4165–4170

(278) Sottile, F.; Olevano, V.; Reining, L. Parameter-Free Calculation of Response Functions in Time-Dependent Density-Functional Theory. *Phys. Rev. Lett.* **2003**, *91*, 056402

(279) Bernardi, M.; Palummo, M.; Grossman, J. C. Extraordinary Sunlight Absorption and One Nanometer Thick Photovoltaics Using Two-Dimensional Monolayer Materials. *Nano Lett.* **2013**, *13*, 3664–3670

(280) Shi, G.; Kioupakis, E. Anisotropic Spin Transport and Strong Visible-Light Absorbance in Few-Layer SnSe and GeSe. *Nano Lett.* **2015**, *15*, 6926–6931

(281) Millan, J. A.; Ortiz, D.; van Anders, G.; Glotzer, S. C. Self-Assembly of Archimedean Tilings with Enthalpically and Entropically Patchy Polygons. *ACS Nano* **2014**, *8*, 2918–2928

(282) Zeng, Z.; Yin, Z.; Huang, X.; Li, H.; He, Q.; Lu, G.; Boey, F.; Zhang, H. Single-Layer Semiconducting Nanosheets: High-Yield Preparation and Device Fabrication. *Angew. Chem. Int. Ed.* **2011**, *50*, 11093–11097

(283) Zheng, J.; Zhang, H.; Dong, S.; Liu, Y.; Nai, C. T.; Shin, H. S.; Jeong, H. Y.; Liu, B.; Loh, K. P. Single-Layer Semiconducting Nanosheets: High-Yield Preparation and Device Fabrication. *Nat. Commun.* **2014**, *5*, 2995

(284) Biener, M. M.; Biener, J.; Friend, C. M. Novel Synthesis of Two-Dimensional TiS_2 Nanocrystallites on Au(111). *J. Chem. Phys.* **2005**, *122*, 034706

(285) Tan, C.; Zhang, H. Two-Dimensional Transition Metal Dichalcogenide Nanosheet-Based Composites. *Chem. Soc. Rev.* **2015**, *44*, 2713–2731

(286) Wan, C.; Gu, X.; Dang, F.; Itoh, T.; Wang, Y.; Sasaki, H.; Kondo, M.; Koga, K.; Yabuki, K.; Snyder, G. J.; Yang, R.; Koumoto, K. Flexible n-Type Thermoelectric Materials by Organic Intercalation of Layered Transition Metal Dichalcogenide TiS_2. *Nature Mat.* **2015**, *14*, 622–627

(287) Zeng, Z.; Tan, C.; Huang, X.; Bao, S.; Zhang, H. Growth of Noble Metal Nanoparticles on Single-Layer TiS_2 and TaS_2 Nanosheets for Hydrogen Evolution Reaction. *Energy Environ. Sci.* **2014**, *7*, 797–803

(288) Gupta, U.; Rao, B. G.; Maitra, U.; Prasad, B. E.; Rao, C. N. R. Visible-Light-Induced Generation of H_2 by Nanocomposites of Few-Layer TiS_2 and TaS_2 with CdS Nanoparticles. *Chem. Asian J.* **2014**, *9*, 1311–1315

(289) Johari, P.; Shenoy, V. B. Tuning the Electronic Properties of Semiconducting Transition Metal Dichalcogenides by Applying Mechanical Strains. *ACS Nano* **2012**, *6*, 5449–5456

(290) Kresse, G.; Furthmüller, J. Efficient Iterative Schemes for Ab Initio Total-Energy Calculations using a Plane-Wave Basis Set. *Phys. Rev. B* **1996**, *54*, 11169–11186

(291) Blöchl, P. E. Projector Augmented-Wave Method. *Phys. Rev. B* **1994**, *50*, 17953–17979

(292) Perdew, J. P.; Burke, K.; Ernzerhof, M. Generalized Gradient Approximation Made Simple. *Phys. Rev. Lett.* **1996**, *77*, 3865–3868

(293) Monkhorst, H. J.; Pack, J. D. Special Points for Brillouin-Zone Integrations. *Phys. Rev. B* **1976**, *13*, 5188–5192

(294) Tang, W.; Sanville, E.; Henkelman, G. A. A Grid-Based Bader Analysis Algorithm without Lattice Bias. *J. Phys.: Condens. Matter* **2009**, *21*, 084204

(295) Ni, Z. H.; Yu, T.; Lu, Y. H.; Wang, Y. Y.; Feng, Y. P.; Shen, Z. X. Uniaxial Strain on Graphene: Raman Spectroscopy Study and Band-Gap Opening. *ACS Nano* **2008**, *2*, 2301–2305

(296) Johari, P.; Shenoy, V. B. Tuning the Electronic Properties of Semiconducting Transition Metal Dichalcogenides by Applying Mechanical Strains. *ACS Nano* **2012**, *6*, 5449–5456

(297) Dong, L.; Dongare, A. M.; Namburu, R. R.; Oapos;Regan, T. P.; Dubey, M. Theoretical Study on Strain Induced Variations in Electronic Properties of 2H-MoS_2 Bilayer Sheets. *Appl. Phys. Lett.* **2014**, *104*, 053107

(298) Li, Y.; Kang, J.; Li, J. Indirect-to-Direct Band Gap Transition of the ZrS_2 Monolayer by Strain: First-Principles Calculations. *RSC Adv.* **2014**, *4*, 7396–7401

(299) Wigner, E.; Seitz, F. On the Constitution of Metallic Sodium. *Phys. Rev.* **1933**, *43*, 804–810

(300) Tietze, T. et al. Interfacial dominated ferromagnetism in nanograined ZnO: A μSR and DFT study. *Sci. Rep.* **2015**, *5*

(301) Lu, A.-Y. et al. Janus monolayers of transition metal dichalcogenides. *Nat. Nanotech.* **2017**, *12*, 744–749

(302) Dong, L.; Lou, J.; Shenoy, V. B. Large In-Plane and Vertical Piezoelectricity in Janus Transition Metal Dichalchogenides. *ACS Nano* **2017**, *11*, 8242–8248

(303) Zhang, J.; Jia, S.; Kholmanov, I.; Dong, L.; Er, D.; Chen, W.; Guo, H.; Jin, Z.; Shenoy, V. B.; Shi, L.; Lou, J. Janus Monolayer Transition-Metal Dichalcogenides. *ACS Nano* **2017**, *11*, 8192–8198

(304) Li, F.; Wei, W.; Zhao, P.; Huang, B.; Dai, Y. Electronic and Optical Properties of Pristine and Vertical and Lateral Heterostructures of Janus MoSSe and WSSe. *J. Phys. Chem. Lett.* **2017**, *8*, 5959–5965

(305) Ji, Y.; Yang, M.; Lin, H.; Hou, T.; Wang, L.; Li, Y.; Lee, S.-T. Janus Structures of Transition Metal Dichalcogenides as the Heterojunction Photocatalysts for Water Splitting. *J. Phys. Chem. C* **2018**, *122*, 3123–3129

(306) Er, D.; Ye, H.; Frey, N. C.; Kumar, H.; Lou, J.; Shenoy, V. B. Prediction of Enhanced Catalytic Activity for Hydrogen Evolution Reaction in Janus Transition Metal Dichalcogenides. *Nano Lett.* **2018**, *18*, 3943–3949

(307) Wang, S. et al. A New Molybdenum Nitride Catalyst with Rhombohedral MoS_2 Structure for Hydrogenation Applications. *J. Amer. Chem. Soc.* **2015**, *137*, 4815–4822

(308) Burke, K. ABC of DFT. Online published manuscript of the technical details of DFT.http://dft.uci.edu/learnDFT.php, Department of Chemistry, University of California, Irvine, CA92697, 2007

(309) Oliver, G. L.; Perdew, J. P. Spin-density gradient expansion for the kinetic energy. *Phys. Rev. A* **1979**, *20*, 397–403

(310) Gell-Mann, M.; Brueckner, K. A. Correlation Energy of an Electron Gas at High Density. *Phys. Rev.* **1957**, *106*, 364–368

(311) Coldwell-Horsfall, R. A.; Maradudin, A. A. ZeroPoint Energy of an Electron Lattice. *J. Math. Phys.* **1960**, *1*, 395–404

(312) Wigner, E. On the Interaction of Electrons in Metals. *Phys. Rev.* **1934**, *46*, 1002–1011.